Theoretical Study of Electronic States of Chemical Bonds(Dissertation_全文)

AUTHOR(S):

Szarek, Pawel

Theoretical Study

of Electronic States of Chemical Bonds

Paweł Szarek

A PhD Thesis

Submitted in

DEPARTMENT OF MICRO ENGINEERING

KYOTO UNIVERSITY

2008 KYOTO, JAPAN

Summary

The interpretative mathematical model (consistent with postulates of Quantum Mechanics and valid for exact wavefunctions) of chemical bond should rely on observable quantities. The geometrical representation of bonding in real space is intimate and advantageous to our perception or world. Therefore theoretical description of Lewis ideas in geometrical space should arise from density distribution, since objects like molecular orbitals or valence bond structures (without physical significance) appear as intermediates upon solving the Schrödinger equation. The first Hohenberg-Kohn theorem binds electron density distribution with corresponding number of electrons N and external potential (i.e. distribution of nuclei), for a given ground state, providing complete chemical information about the system. The essential in chemistry a chemical bond concept by Lewis, despite its simplicity, urges one to search between atomic centers for a localized electron pairs and, following Pauling, to explore associated forces that lead to stabilization of an aggregate. This thesis attempts to bridge practical chemistry and quantum mechanics and seek for physical explanation for chemical bonding in terms of energy density and electronic stress tensor analysis.

The chapters introduce new non-classical bond orders based on electronic properties of stationary point of electron density, so called Lagrange point. The relations between forces acting on electron distribution, through electronic stress tensor and corresponding energy density are explained. The reactivity and stability is discussed in terms of local electronic chemical potential and interaction energy density. The stress tensor and local dielectric properties as well as hybrid variational-perturbational interaction energy decomposition scheme or Natural Bonding Orbitals theory are applied to unravel and discuss the chemical bonding nature. The simple chemical systems of homonuclear diatomic molecules, small organic molecules as well as larger systems like metal clusters and enzyme active sites are subjects of study.

How the mode of bonding affects stability and reactivity of molecule on the frame of nonrelativistic limit of the rigged quantum electrodynamics using new indices for description of bond properties related to bond orders have been characterized here. These indices are in close relation with tensorial interpretation of bond that among others allows discriminating covalent bonds using spindle structure concept. The real three-dimensional space representation of new interaction energy density utilized in this study contribute to better

understanding of interaction phenomena between atoms and molecules. The differences in reactivity and stabilities of molecules are expressed in the redistribution of interaction energy density.

The stress tensors are used widely for description of internal forces of matter. For some time it is also applied in quantum theory in studies of molecular properties in chemical systems. Electronic stress tensors measure effects caused by internal forces acting on electrons in molecules and particularly those between bonded atoms. Utilized here stress tensor originated bond orders express bond strengths in terms of these internal forces. The unique concept of energy density and electronic chemical potential based bond orders gives natural evaluation of interaction strength comparing with classical definition, considering delocalized nature of electrons. The relation to electronic energy causes that among others it may be used to predict relative stabilities of geometrical isomers or even conformers.

The local reactivity of hydrogenated Pt-clusters has been studied using Regional DFT method. We observed that antibond orbitals constitute the preferable binding site for H2. Those sites are characterized by lowered electronic chemical potential, strong directionality and exhibit electrophilic nature. The Pt—H2 sigma-complexes were formed only by occupation of the lowest chemical potential sites associated with σPtH* antibonds in saturated platinum clusters. The formation of sigma-complex caused mutual stabilization with trans Pt—H bond. Such activated H2 molecules on Pt-clusters in a sense resemble heme-O2 complex with interaction strength greater than phsisorbtion or hydrogen-bonding, however below chemisorption strength.

The origin of enzyme catalytic activity may be effectively explored within non-empirical theory of intermolecular interactions. The knowledge of electrostatic, exchange, delocalization and correlation components of the transition state and substrates stabilization energy arising from each enzyme active site residue allows to examine the most essential physical effects involved in enzymatic catalysis. Consequently, one can build approximate models of the catalytic activity in a systematic and legitimate manner. Whenever the dominant role of electrostatic interactions is recognized or assumed, the properties of an optimal catalytic environment could be simply generalized and visualized by means of catalytic fields that, in turn, aids the design of new catalysts. Differential transition state stabilization (DTSS) methodology has been applied herein to the phosphoryl transfer reaction catalyzed by cAMP-dependent protein kinase (PKA). The MP2 results correlate well with the available experimental data and theoretical findings indicating that Lys72, Asp166, and the two magnesium ions contribute -22.7, -13.3, -32.4 and -15.2 kcal/mol to differential transition

state stabilization, respectively. Although all interaction energy components except of electron correlation contribution are meaningful, the first order electrostatic term correlates perfectly with MP2 catalytic activity. Catalytic field technique was also employed to visualize crucial electrostatic features of an ideal catalyst and to compare the latter with the environment provided by PKA active site. The map of regional electronic chemical potential was used to analyze the unfavorable catalytic effect of Lys168. It was found that locally induced polarization on TS atoms thermodynamically destabilizes electrons pulling them to regions displaying higher electronic chemical potential.

[NiFe] hydrogenase has recently received attention as an enzyme for catalyzing hydrogen production. We review the theoretical investigations of the catalysis mechanism. The hydrogen production reaction occurs at the active site of the hydrogenase and the active site has several paramagnetic and several EPR-silent states, the structures of which are still controversial. Moreover, different catalysis mechanisms have been proposed. We review the proposed mechanisms focusing on the reaction paths.

Density functional calculations were performed for lanthanum-oxide clusters in order to study the local dielectric properties of such clusters using the dielectric constant defined at local points. An increase in coordination number brings about an increase in electron population on the central lanthanum atom, leading to an increase in the local dielectric constant.

Contents

Acknowledgements

There are many people who influenced and helped me in my work during the last three years. I wish to express my gratitude to them here.

Firstly I am very thankful to Professor Akitomo Tachibana for his warm hospitality and wisely guidance, numerous encouraging discussions, valuable advices and generous understanding.

The author is grateful to Professor Andrzej W. Sokalski for offering valuable advice and kind encouragement. I also wish to acknowledge Dr. Kentaro Doi for technical advice and many supports and Mrs. Edyta Dyguda-Kazimierowicz for editorial help and encouragement. I am indebted to Yuhui Cheng, Yingkai Zhang, and J. Andrew McCammon for the coordinates of PKA complexes as well as for the extensive discussion.

I owe much appreciation to my family, especially to my wife Mrs. Małgorzata Szarek for lasting encouragement and great help.

The studies in this thesis were supported by the Japanese Government – Monbukagakusho Scholarship through Kyoto University for which the author express his special gratitude.

The partial support by Special Coordination Funds for Promoting Science and Technology from the Ministry of Education, Culture, Sports, Science and Technology, Japan (MEXT), and the Center of Excellence for Research and Education on Complex Functional Mechanical Systems (COE Program of MEXT) is acknowledged. The part of work has been supported by Wroclaw University of Technology.

Author also acknowledge generous allocations of computer time provided by Fujitsu Primepower HPC2500 at the Academic Center for Computing and Media Studies, Kyoto University, Center for Computational Science, Okazaki, Japan, Wroclaw Supercomputer and Networking Center (WCSS) and Poznan Supercomputer and Networking Center (PCSS).

CHAPTER 1

Introduction.

The course of chemical processes depends on reactants environment, which is most often dominated by the influence of catalyst (general acid or base, transition metal species, biocatalysts etc.). Even though the reaction may be not catalyzed, the reactants might affect each other through intermolecular or intramolecular interaction that leads to conversion into a product or to display of particular properties. Such effects, either catalytic or not, might involve interatomic interactions of different nature and strength, like electron pairing, polarization, induction, charge transfer or simple electrostatic effects. All of these effects have common origin in electric field associated with charge density redistribution and fluctuations in molecules and quantum effects associated with electron wavefunctions. The theoretical knowledge on how electron distributions mutually affect interaction between atoms of different molecules (intermolecular) or within one molecule (intramolecular), based on *ab initio* methods provides fundamental information necessary/expedient for engineering of molecular processes and materials. The regional DFT rigged QED electronic stress tensor analysis of distribution of electrons in atoms and molecules is innovative tool aiding understanding of chemical bonding and giving new prospective. On first sight this concept might seem "strange", however a deeper reflection will bring one to conclusion that it is natural to explore the electronic structure of chemical bonding in terms of internal forces acting on electrons. The stress tensor subsumes such local indicators of "electron pairing" based on local kinetic energy density like electron localization function [1], local temperature of "nighness" functional [2], local entropy measures [3] or localized orbital locator [4]. The Bader's Atoms-In-Molecules theory [5] show some analogies with theory presented here. However the fundamental difference between these two methods is the means in which electrons are treated: topological analysis of charge density by Bader and dynamical approach which takes into account quantum mechanical forces acting on electron distribution.

The first section of this book (chapters 2 and 3) introduce new, non-classical bond order indices based on local electronic energy density and local chemical potential derived from electronic stress tensor. The idea and role of stationary point of charge density, defined by dynamical forces acting on electrons in molecules, in bonding region, so called "Lagrange point" is explained. In Chapter 2 systematic analysis of bond orders of simple diatomic, homonuclear molecules, the properties associated with Lagrange point, was made. Along with new bond orders, changes in the energy density due to interaction between bonding atoms are locally pictured in real tri-dimentional space representation and confronted against corresponding deformation of charge density. Next chapter provides extended discussion of bonding in terms of stress tensor and new bond orders using simple organic molecules as an example. Different aspects of bonding are considered like different multiplicity of bonds (different number of electron pairs in corresponding Lewis structure), conjugation and hyperconjugation effects as well as the stability of isomers and conformers, substitution effects and the dependency of electronic properties on electronegativity of bonded atoms. The correlation of new indices with interatomic distance and with commonly used overlap or population based bond orders was made. The stability of the method against different theory levels is discussed as well. Author in these chapters introduce and methodize new ideas in order to make a survey (benchmark) for further studies.

The tensorial analysis of interactions in molecules has been extended to transition metal species in Chapter 4, where hydrogenated Pt-clusters are analyzed. The study focuses on platinum catalytic properties associated with hydrogen chemistry in context of hydrogen storage materials. The reactive regions on molecular surface represented by interface surface of kinetic energy density (defining turning point for electrons) are characterized by displayed chemical potential. The author examined how presence of reactive regions affects HOMO-LUMO gap in clusters. The Pt—H interactions were characterized using energy density and chemical potential bond orders and natural bonding orbitals (NBO) analysis. The correlation between bond strengths determined by energy density bond order and the donor acceptor interactions estimated from NBO second-order perturbation theory stabilization has been found. Additionally interaction of dihydrogen species with Pt atoms was studied by hybrid variational-perturbational interaction energy decomposition of MP2 interaction energy and by real space visualization of Rigged QED interaction energy density.

In Chapter 5 the phosphoryl transfer reaction catalyzed by protein kinase A has been analyzed in terms of the ability of individual active site components to preferentially stabilize the transition state. Further decomposition of DTSS energy has allowed for elucidation of the

major interaction energy components influencing the catalytic activity of PKA. Finally, catalytic fields have been derived and compared to the catalytic surroundings provided by PKA. The knowledge of electrostatic, exchange, delocalization and correlation components of the transition state and substrates stabilization energy arising from each enzyme active site residue allows to examine the most essential physical effects involved in enzymatic catalysis. Consequently, one can build approximate models of the catalytic activity in a systematic and legitimate manner. Whenever the dominant role of electrostatic interactions is recognized or assumed, the properties of an optimal catalytic environment could be simply generalized and visualized by means of catalytic fields that, in turn, aids the design of new catalysts. Differential transition state stabilization (DTSS) methodology has been applied herein to the phosphoryl transfer reaction catalyzed by cAMPdependent protein kinase (PKA). The map of regional electronic chemical potential on kinetic energy density interface surface around transition state was used to analyze the unfavorable catalytic effect of Lys168 residue.

Next, the theoretical studies of catalytic mechanism of [NiFe] hydrogenase have been reviewed comparing proposed mechanisms and focusing on transition states. Several groups have investigated the catalytic system of [NiFe] hydrogenase and their findings are not yet consistent. Analysis of the transition states, which can not be studied experimentally because they are extremely short lived, was given and the activation energy barrier were determined. The reaction cycles in QM and QM/MM models of Desulfovibro gigas and Desulfovibro Miazaki F enzymes were considered and H_2 production cycle was proposed. The electron transfer during catalytic process was considered with anionic and dianionic complexes. The H_2 molecule is very small reactant that immediately binds to metal centre and dissociate, thus for all reaction steps hydrogen atoms seemed to be strongly bonded to the active site and do not interact directly with surrounding residues. The electronic interaction in the H_2 production process was expressed in terms of the quantum energy densities based on the regional DFT. The low spin and high spin models were confronted and the chemical interactions within active site for reaction steps of hydrogen production were discussed by means of kinetic energy density, electronic stress tensor and energetic barriers.

The final chapter presents quantum chemical calculations performed for several small cluster models of lanthanoid monoxide and several tetrahydroxides using regional DFT method. The calculations of small clusters shed a light on chemical bonding characteristic between oxygen and metal atoms. Furthermore a large-scale model has been studied using combined quantum mechanics/molecular mechanics (QM/MM) method. Using electron wavefunctions the local electronic properties such as electronic stress tensor density and local

dielectric constant were calculated. The local dielectric properties are related to the polarization of the system induced by the electric displacement of the external field. The relation between local dielectric constant and chemical bonding properties were determined based on the same electron wavefunction.

References

[1] (a) A. D. Becke and K. E. Edgeecombe, *J.Chem.Phys.* **92**, 5397 (1990), (b) M. Kohout, *Int. J. Quantum Chem.* **97**, 651 (2004), (c) A. Savin, n, A. D. Becke, J. Flad, R. Nesper, H. Preuss, and H. G. Vonschnering, *Angew. Chem.* **30**, 409 (1991), (d) A. Savin, R. Nesper, S. Wengert, and T. F. Fassler, *Angew. Chem.* **36**, 1809 (1997).

[2] P. W. Ayers, R. G. Parr, and A. Nagy, *Int. J. Quantum Chem.* **90**, 309 (2002).

[3] P. K. Chattaraj, E. Chamorro, and P. Fuentealba, *Chem. Phys. Lett.* **314**, 114 (1999).

[4] (a) H. L. Schmider and A. D. Becke, *J.Mol.Struc.Theochem* **527**, 51 (2000), (b) H. L. Schmider and A. D. Becke, *J. Chem. Phys.* **116**, 3184 (2002).

[5] R. F. W. Bader, *Atoms in Molecules: A Quantum Theory*. (Clarendon, Oxford, 1990).

CHAPTER 2

The field theoretical study of chemical interaction in terms of the Rigged QED: new reactivity indices.

Introduction

Recently developed novel field theory of regional energy density decomposition in real space [1] (an infinitely small regional energy decomposition scheme) [2] allows one to recognize how the electronic energy density is associated with the electron density and visualization of the chemical interaction in real space is now possible. Using the electronic energy density, one can pick up any point in a chemical reaction system and find how the electronic energy E is assigned to that point. The integration of the electronic energy density in a small region gives the regional electronic energy contribution to the global electronic energy E. If the integration spans the whole space, then the integral gives the total E of system. The new energy density partitioning scheme that utilizes the Rigged Quantum Electrodynamics (QED) has been developed recently [1]. One obtains the energy densities as follows:

$$n_E(\vec{r}) = n_T(\vec{r}) + n_V(\vec{r}) + n_W(\vec{r}) \qquad (1.1a)$$

$$n_E(\vec{r}) = \left\langle \hat{H}(\vec{r}) \right\rangle,\ n_T(\vec{r}) = \left\langle \hat{T}(\vec{r}) \right\rangle,\ n_V(\vec{r}) = \left\langle \hat{V}(\vec{r}) \right\rangle,\ n_W(\vec{r}) = \left\langle \hat{W}(\vec{r}) \right\rangle \qquad (1.1b)$$

the kinetic energy density $n_T(\vec{r})$, the external potential energy density $n_V(\vec{r})$, and the interelectron potential energy density $n_W(\vec{r})$. The all components are derived from the same density matrix and related to each other following the sum rule that leads to the total energy density $n_E(\vec{r})$.

The kinetic energy density obtained in this scheme provides a new outlook at the chemical bond by partitioning of space into mutually disjoint regions by using a concept of the electronic drop (R_D) and atmosphere (R_A) regions separated by the interface S [3]. The infinitely large positive electric potential of the bare nucleus influences the electron (in terms of classical and quantum mechanics as well) that has constant energy and can acquire infinitely large positive kinetic energy $n_T(\vec{r})$ at positions very near to nucleus (because the intramolecular electric field $E_{intra}(\vec{r})$ produced by the other electrons can not exceed that of the bare nucleus) [2]. Nevertheless the nucleus is surrounded by the surface of zero kinetic energy density ($n_T(\vec{r}) = 0$), within which the kinetic energy density is positive ($n_T(\vec{r}) > 0$), where the electron density is simply accumulated and classically allowed motion of electron is guaranteed. This region is called the electronic drop and denoted by R_D, while the complementary region is the region of the electronic atmosphere denoted by R_A, being separated by the electronic interface S:

$$n_T(\vec{r}) = -\frac{\hbar^2}{4m}\sum_i^{occ} \nu_i \left[\psi_i^*(\vec{r})\Delta\psi_i(\vec{r}) + \Delta\psi_i^*(\vec{r})\psi_i(\vec{r})\right] \qquad (1.2a)$$

$$\begin{aligned} R_D &: \quad n_T(\vec{r}) > 0 \\ R_A &: \quad n_T(\vec{r}) < 0 \\ S &: \quad n_T(\vec{r}) = 0 \end{aligned} \qquad (1.2b)$$

In the R_A the electron density is dried up and the motion of electrons is classically forbidden. The boundary S in between R_D and R_A gives a clear image of the intrinsic shape of the reactant atoms and molecules along the course of the chemical reaction coordinate. The kinetic energy density is a molecular property as a functional of electron density [1a,4]. While expectation values in the whole space of both conventional (regular DFT) and the Rigged QED kinetic energy density operators are the same, the density itself is different from each other [1b]. The interface surface S, that appears for the Rigged QED $n_T(\vec{r})$, is very important in chemical reaction systems as it allows specifying the turning point for electron [5].

The dynamical treatment, in the form of incorporation of the kinetic energy density of atomic nuclei (treated as external static source of force for electrons - Schrödinger field [6]), play important role in the Rigged QED in the chemical reaction systems since the local stress tensor density $\vec{\tau}^S(\vec{r})$, represented as force acting on a pair of electronic drop regions of reactants [3,7], have been applied to study the chemical reactivity [8]:

$$\vec{\tau}^S(\vec{r}) = \left\langle \hat{\vec{\tau}}^S(\vec{r}) \right\rangle \qquad (1.3a)$$

$$\tau^{Skl}(\vec{r}) = \frac{\hbar^2}{4m}\sum_i^{occ} \nu_i \left[\psi_i^*(\vec{r}) \frac{\partial^2 \psi_i(\vec{r})}{\partial x^k \partial x^l} - \frac{\partial \psi_i^*(\vec{r})}{\partial x^k}\frac{\partial \psi_i^*(\vec{r})}{\partial x^l} + \frac{\partial^2 \psi_i^*(\vec{r})}{\partial x^k \partial x^l}\psi_i(\vec{r}) - \frac{\partial \psi_i^*(\vec{r})}{\partial x^l}\frac{\partial \psi_i^*(\vec{r})}{\partial x^k} \right] \qquad (1.3b)$$

The eigenvalue is the principal stress and the eigenvector is the principal axis:

$$\left\langle \hat{\vec{\tau}}^S(\vec{r}) \right\rangle = \begin{bmatrix} \tau_{xx}^S(\vec{r}) & \tau_{xy}^S(\vec{r}) & \tau_{xz}^S(\vec{r}) \\ \tau_{yx}^S(\vec{r}) & \tau_{yy}^S(\vec{r}) & \tau_{yz}^S(\vec{r}) \\ \tau_{zx}^S(\vec{r}) & \tau_{zy}^S(\vec{r}) & \tau_{zz}^S(\vec{r}) \end{bmatrix} \xrightarrow{diag} \begin{bmatrix} \tau^{S11}(\vec{r}) & 0 & 0 \\ 0 & \tau^{S22}(\vec{r}) & 0 \\ 0 & 0 & \tau^{S33}(\vec{r}) \end{bmatrix} \qquad (1.4a)$$

$$\tau^{S11}(\vec{r}) \le \tau^{S22}(\vec{r}) \le \tau^{S33}(\vec{r}) \qquad (1.4b)$$

This new kind of force which acts on electrons is discriminated with the force on the nuclei. The covalent bond formation is characterized by a concept of the spindle structure, which is a geometrical object of a region where principal electronic tensile stress is positive along the line of principal axis of the electronic stress, that connects a pair of the R_D's of atoms or molecules (with predominant compressive stress inside) [7].

The stress is the surface force characterized by the dimension of force per area. The eigenvector of the stress tensor density dictates the local tensorial chemical force.

The eigenvalue of the stress tensor density gives a measure of the kinetic energy. If the local principal stress is positive, it is called the tensile stress, while if it is negative - compressive [7]. The compressive stress gives a positive contribution to the kinetic energy density, while the tensile stress provides a negative contribution because of negative eigenvalues (-1, -1, -1) of metric tensor g^{ij} [5]. Combination of the stress tensor and the spindle structure reveals new concept of tensorial chemical interaction energy density that includes the electronic spin angular momentum in the underling physics. The atomic electron density exhibits positive kinetic energy density, which leads to the formation of the electronic drop region R_D [3] and to the compressive stress [7]. This tendency should of course be intact in between ionic species interactions. The situation would change dramatically for covalent bond formation, where a pair of electrons should be bounded tightly and thereby creating tensile stress. Many systems show such generic feature, which is called spindle structure of covalent bond [6].

On the basis of the concept of the force density and the stress density (established in the quantum mechanics and QED), the force density operator $\hat{\vec{F}}^S(r)$, aside form the Lorentz force density operator $\hat{\vec{L}}^S(\vec{r})$, is composed of the tension density operator $\hat{\vec{\tau}}^S(\vec{r})$ given as the divergence of the stress tensor density operator $\hat{\vec{\tau}}^S(\vec{r})$:

$$\hat{\tau}^{Sk}(\vec{r}) = \partial_l \hat{\tau}^{Skl}(\vec{r}) \qquad (1.5)$$

$$\hat{\vec{F}}^S(r) = \hat{\vec{\tau}}^S(\vec{r}) + \hat{\vec{L}}^S(\vec{r}) \qquad (1.6)$$

Tension density operator represents purely quantum mechanical effects, for example, of electrons diffusing from an atomic nucleus. The Lorentz force density operator is of the usual classical form plus quantum mechanical exchange effects, for example, of electrons pulled back by the atomic nucleus. For the stationary state of charged particles the local force can vanish, when the equation of motions is equivalent to the local equilibrium condition and where the tension density (the tension of the field) exactly cancels the Lorentz force density (the Lorentz force exerted on the particle) at every point of space [3,5,7,9a]:

$$\left\langle \hat{\vec{\tau}}^S(\vec{r}) \right\rangle + \left\langle \hat{\vec{L}}^S(\vec{r}) \right\rangle = 0 \qquad (1.7)$$

The tension is integrable, and leads to the stress tensor, which itself has the dimension of the energy density:

$$[\text{stress}] = \frac{\text{force}}{\text{area}} = \frac{\text{energy}}{\text{volume}} = [\text{energy density}] \qquad (1.8)$$

Regional energy density

1. Bond line and Lagrange point

In the stress tensor analysis, one can visualize the propagation of local force in real space by tracing the congruence of the principal axes, leading to the bond line as the envelope, as shown in Figure 1a. The spindle structure accommodates a bundle of bond lines carrying tensile stress region in between a pair of compressive ones on the edges with a shape of bond if they connect a pair of R_D's.

In Bader's analysis topologically defined bond paths, bond critical points and electron cloud enclosed regions serve as regions of space carrying the information about bonding interaction and atomic regions [10]. The Rigged QED analysis at stationary point provides the chemical interaction characteristic with the Lagrange point $\vec{r}_{Lagrange}$ at which the tension (and also the Lorentz force) vanishes for electron to take a rest in course of the chemical bond, as shown in Figure1b. We suggest that $\vec{r}_{Lagrange}$ carries heavy load of interaction information, however it may be not complete. The $\vec{r}_{Lagrange}$ are common for all molecules and easy to identify. In contrast to Bader's AIM analysis [10] the Rigged QED characteristic point is determined by dynamical forces acting on electrons thus has mechanical origin instead of being a topological parameter.

Concluding, one obtains: i) a realization of boundaries of atoms or other electronic structural fragments as the R_D - drop regions of kinetic energy density separated with R_A , ii) a dynamical bond line dictating the local tensorial chemical force, and iii) a dynamical point $\vec{r}_{Lagrange}$ characterizing an interaction, where repulsive electronic tension cancels in space (in stationary state)[6]. The kinetic energy density can draw a shell structure of atoms. The tangential point of two atoms or molecules is called Lagrange point $\vec{r}_{Lagrange}$ and it is situated on the bond line that connects two R_D centers.

2. Non-relativistic limit of energy density

Tensorial analysis of bonding interactions has already been proved to be useful in determination of covalence and molecular shape [3]. Because the stress tensor has a dimension of the energy density, a completely new realization of the tensorial chemical

interaction energy density was obtained. The trace of the stress tensor density becomes [6] equivalent to two times the kinetic energy density in the non-relativistic limit. The integral of the trace of the stress tensor density gives a local picture of two times the kinetic energy density [6].

$$E_{Rigged\ QED} = \int d^3\vec{r} \left\langle \hat{H}_{Rigged\ QED}(\vec{r}) \right\rangle = \int d^3\vec{r} \left\langle m_e c^2 \hat{\bar{\psi}}(\vec{r})\hat{\psi}(\vec{r}) - \sum_{\alpha} \hat{T}_{\alpha}(\vec{r}) \right\rangle \qquad (2.1)$$

$$E_{\substack{non-relativistic \\ Rigged\ QED}} = \int d^3\vec{r} \left\langle \hat{H}_{\substack{non-relativistic \\ Rigged\ QED}}(\vec{r}) \right\rangle = -\frac{1}{2} \int d^3\vec{r} \left\langle \sum \hat{\tilde{\tau}}^{S\,k}_{\alpha\,k}(\vec{r}) \right\rangle \qquad (2.2)$$

The quantity calculated in this way corresponds to the total electronic energy E (when integration spans the whole space). Its local redistribution in space (ε - total energy density) can be drawn by using regional integration for infinitively small region of space [1]:

$$E = \int d^3\vec{r}\,\varepsilon^S_\tau(\vec{r}), \quad \varepsilon^S_\tau(\vec{r}) = \frac{1}{2}\tau^{S\,kk}(\vec{r}) \qquad (2.3)$$

3. Lagrange point vs. regional energy density

The total energy density in local picture reaches peak along the principal axis (bond line) in the $\vec{r}_{Lagrange}$ and for perpendicular axis leading through this point goes through the minima. It is not necessary condition that electron density would go through the extremum at $\vec{r}_{Lagrange}$ too, especially in many-atomic or heteroatomic systems. The b_ε value of ratios of energy densities at this point, calculated from equation below, where $\varepsilon^S_{\tau AB}(\vec{r}_{Lagrange})$ is the regional energy density at $\vec{r}_{Lagrange}$ for bond between *A* and *B*, and $\varepsilon^S_{\tau HH}(\vec{r}_{Lagrange})$ is regional energy density at $\vec{r}_{Lagrange}$ for σ bond in hydrogen molecule, is linked to bond order (defined in diatomic molecule as b = ½ (n - n*)) or more precisely to normalized interatomic strain (which may be compared to vacuum pressure) that glues atoms together, stabilizing given bonding interaction with respect to the properties of model pure single σ bond of hydrogen molecule.

$$b_\varepsilon = \frac{\varepsilon^S_{\tau AB}(\vec{r}_{Lagrange})}{\varepsilon^S_{\tau HH}(\vec{r}_{Lagrange})} \qquad (2.4)$$

Table 1 shows results for Lagrange points of carbon-carbon bond of C_2H_x molecules and model single bond of H_2 molecule, all calculated at MP2/6-311++G** level of theory using Gaussian03 [11] and MRDFT program [12]. The largest eigenvalue of stress is positive for all cases except etyn, for which it is slightly negative - this is due to the effect of large stabilization in the directions perpendicular to the bond line that cause the covering up of

tensile stress in the principal axis. The positive stress is delocalized from the $\vec{r}_{Lagrange}$ into the ring shaped region around bond axis. The two minor eigenvalues of stress tensor are negative and represent the compressive stress acting on bonding electrons in directions perpendicular to C—C line. The negativity of these eigenvalues is connected with atomic like stabilization, while positive stress is associated with electronic destabilization (or stabilization in sense of tight covalent bonding of valence electrons). The electron density at $\vec{r}_{Lagrange}$ correlates with increasing b_ε. The values of b_ε are in good agreement with bond orders in these molecules. The results for other C—C bonds in hydrocarbons i.e.: s-trans-1,3-buten ($b_\varepsilon = 1.274$ and 1.897 for single and double respectively) or $\vec{r}_{Lagrange}$ between C atoms in benzene molecule ($b_\varepsilon = 1.557$) also assume reasonable values that correlate with bond orders. It should be noted that negativity of the largest eigenvalue of stress at $\vec{r}_{Lagrange}$ does not necessary negate the covalence and spindle structure existence. Largest eigenvalue of stress tensor is negative for non-covalent interactions (metallic bonds, van der Waals complexes) or sometimes for very strong covalent bonds where short interatomic distance causes that positive principal stress is dominated by compressive stresses of atomic cores. The value for etyn molecule turns out to be negative as the total result of superimposed effects. The negativity of principal stress in this case might mean fluidity of electron density and potential to conduct (see next paragraph for more information). It is possible however to find the spindle structure when electronic "noise" in shape of all occupied orbitals except HOMO will be omitted [5].

4. Homonuclear diatomic molecules

The homonuclear diatomic molecules in ground states of main group elements, from first to fourth period, have been analyzed here with respect to the Lagrange point. The results are shown in Table 2. The calculations have been performed at HF/6-311++G** level of theory using Gaussian03 [11] and MRDFT program [12]. The regional total energy density as well as b_ε reflect periodicity of atomic properties and correlate with bond length and electron density at Lagrange points. Among the elements of first two groups one can notice that from Na_2 to Ca_2 the degeneracy of the largest eigenvalue occurs in contrast to the degeneracy of two minor eigenvalues of stress in other cases. There also appears another clear tendency, that among all metals and metalloids bonds the largest eigenvalue of stress in Lagrange point becomes negative. This indicates a kind of fluidity of bonding/valance electron density between species. There might be connection between such feature and band properties of metals and semiconductors however not studied yet.

The b_ε index does not give commonly used bond orders any more. While it still evaluates the bond strength and order, the magnitude for some bonds is either largely overestimated or underestimated comparing to results by Mayer's [13a-d] or Molecular Orbital theory [13e-h]. One can obtain more adequate results by taking dependency of electron redistribution into consideration since the electronic energy is associated with electron density [9]. The modified index takes also the interaction of electronic clouds of bonding species into account. In chemical reaction systems, the redistribution of electrons directly redefines the electronic energy as a unique functional of the electron density [3]. New parameter is calculated from equation below, where $n_{AB}(\vec{r}_{Lagrange})$ indicates electron density at $\vec{r}_{Lagrange}$ for given bond.

$$b_\mu = \frac{b_\varepsilon}{\left(n_{AB}(\vec{r}_{Lagrange})/n_{HH}(\vec{r}_{Lagranre})\right)} = \frac{\varepsilon^S_{\tau AB}(\vec{r}_{Lagranre})}{n_{AB}(\vec{r}_{Lagranre})} \cdot \left(\frac{\varepsilon^S_{\tau HH}(\vec{r}_{Lagranre})}{n_{HH}(\vec{r}_{Lagranre})}\right)^{-1} \qquad (2.5)$$

The *ε/n* ratio reflects energy that is attributed to one electron at given point in space. For particular interaction between two R_D's the $\vec{r}_{Lagrange}$ describes exclusively only that particular phenomenon (especially if one investigates bonding in composed, many-atomic system). One can easily compare normalized energy density (first, bond order related parameter) or such energy per one electron at atomic (or molecular) interfaces expressed by any interacting subsystem.

5. Linear response of regional chemical potential density

The regional energy decomposition scheme has been extended to infinitely small regional energy decomposition scheme thus leading to local electronic energy density $n_E(\vec{r})$ in real space as a unique functional of electron density $n(\vec{r})$ [1a-b,9,14]. In this sense $\varepsilon^S_{\tau AB}(\vec{r})$ constitutes very small, partial contribution (∂E) to total electronic energy, likewise $n_{AB}(\vec{r})$ makes small portion (∂N) of total electron number *N*, for given region of space of bond between *A* and *B*:

$$E_{AB} = \int d^3\vec{r}\,\varepsilon^S_{\tau AB}(\vec{r}), \quad N_{AB} = \int d^3\vec{r}\, n_{AB}(\vec{r}) \qquad (2.6)$$

However the ratio of energy density per electron density has a much deeper meaning and broader importance for chemical description of system at single point of space. The $\varepsilon^S_{\tau AB}(\vec{r})/n_{AB}(\vec{r})$ in Eq. (2.5) may be regarded as derivative versus number of electrons that exhibits the property of regional chemical potential (μ_R) [1a] at least under linear response approximation:

$$\mu_R = \left(\frac{\partial E_R}{\partial N_R} \right) \Leftrightarrow \frac{\varepsilon_{\tau AB}^{S}(\vec{r})}{n_{AB}(\vec{r})} \tag{2.7}$$

The original Onsager's local equilibrium hypothesis that does not includes quantum mechanical effects across region interfaces [15] has been modified, and the quantum mechanical nature of electron was taken into account by use of density functional theory [1a]. Introduction of quantum mechanical coherency of electrons that can tunnel from region R to the neighboring regions allow replacing all Hamiltonians (originally for each region) by one density functional theory Hamiltonian that covers the system as a whole. In the irreversible thermodynamic of Onsager, there is a gradient of chemical potentials and there is an inequality of regional chemical potentials between complementary regions. The introduced quantum mechanical interference effect, working through the interfaces that divide the regions, survives even in the limit of global chemical equilibrium [1a]. Arising chemical potential inequality principle predicts inequality in between either: i) the Gibbs chemical potential μ_G for electronic subsystem as a whole and the regional chemical potentials μ_R, or ii) the regional chemical potentials μ_R themselves [1a].

$$\mu_G = \mu_R + \sum_{R'(\neq R)} \alpha_{R'R} \tag{2.8}$$

$$\mu_R = \left(\frac{\partial E_R}{\partial N_R} \right)_{S,v,N_{R'(\neq R)}} \tag{2.9}$$

$$\alpha_{R'R} = \left(\frac{\partial E_{R'}}{\partial N_R} \right)_{S,v,N_{R'(\neq R)}} \tag{2.10}$$

The μ_R refers to regional contribution to the μ_G. The sum of $\alpha_{R'R}$ over the complementary regions *R*' to *R* expresses intrinsic Volta electric potential ϕ_R. For a pair of regions *R*' and *R* Volta contact potential difference is identified with the difference in the regional work function proved by Herring and Nichols [16].

$$\phi_R - \phi_{R'} = \Phi_{R'} - \Phi_R \tag{2.11}$$

The Φ_R denotes the intrinsic Herring-Nichols work function. In between a pair of regions in contact with each other, the Gibbs chemical potential is constant as a consequence of the chemical equilibrium. This leads to Herring-Nichols work function Φ_R defined as regional chemical potential.

$$\mu_G = -e\Phi_R - e\phi_R = -e\Phi_{R'} - e\phi_{R'} \tag{2.12}$$

$$-e\phi_R = \sum_{R'(\neq R)} \alpha_{R'R} \tag{2.13}$$

$$-e\Phi_R = \mu_R \qquad (2.14)$$

The thermodynamic extension of electronic energy density $n_E(\vec{r})$ gives observables in electrochemistry in shape of ϕ_R and Φ_R. Likewise in crystals where these quantities are dependent on surface morphologies or crystallographic orientations but have constant value of μ_G, same regional chemical potential inequality in space for atoms and molecules is a valuable source of chemical interaction information.

According to Ilya Prigogine an open system at stationary state organizes itself in a way to minimize total entropy production. The thermodynamic forces represented by gradients of intensive variables drive fluxes of the associated extensive quantities [1a]. The μ_G turns out to be electrochemical potential composed of ordinary chemical potential arising from short range interactions and the macroscopic scalar electric potential field ϕ representing long range electromagnetic interactions [17]. The two parts of the electrochemical potential play a different role in thermodynamics [17].

Figure 2 compares b_ε and b_μ indices with the molecular orbital theory bond orders [13e-h]. The modified index b_μ describes the actual bond orders more accurately. However this new index, due to underestimation, is now not applicable to the carbon-carbon bonds in hydrocarbons (Table 1). This is due to the effect caused by bonding to more then one atomic center, when electron density may redistribute over the whole, much larger molecular orbital that spans all the nuclei. In diatomic molecules, where available orbital space is limited comparing to polyatomic molecules, electron density accumulated around one particular bond, although may not exceed that for similar bond in polyatomic system, has more favorable energy (due to lower number of available/occupied MOs; i.e. carbon-carbon bond in C2 and hydrocarbons) thus this causes change in local chemical potential at $\vec{r}_{Lagrange}$ and related b_μ index.

6. Method and basis set dependency

The calculations of energy density data are based on the eigenvectors obtained from any ab initio method implemented in commercially available programs for quantum mechanical calculations and the same basis sets are used. The dependency on method and basis set have been checked by HF, MP2 and B3LYP calculations with STO-3G, 6-31G, 6-311G basis sets (with polarization and diffusion functions added or removed) using Gaussian 03 [11] and MRQED program [12]. The very small method and small basis set dependency have been observed. The results for Li_2 case have been summarized in Table 3. In case of

constant interatomic distance all methods give very similar results and the regional total energy density at HF and B3LYP levels correlate very well (1.000 and 0.995 respectively) with MP2 results for H_2 molecule.

7. Interaction energy density

The combination of supermolecular approach and non-relativistic limit of energy density leads to the formulation of new molecular interaction energy density of the chemical species (corrected for the basis set superposition error (BSSE) by using the dimer centered basis set for monomers [18]). This new energy density is divided into the regions where attractive or repulsive interaction terms are dominating, that in case of bonding interaction might be regarded as stabilization or destabilization in bonding regions respectively, as the effect of electron density rearrangement upon bond formation.

$$\Delta E_{AB} = E_{AB} - (E_A + E_B) \qquad (2.15)$$

The corresponding value of local molecular interaction energy density is defined as follows:

$$\Delta\varepsilon^S_{\tau AB}(\vec{r}) = \varepsilon^S_{\tau AB}(\vec{r}) - \left(\varepsilon^S_{\tau A}(\vec{r}) + \varepsilon^S_{\tau B}(\vec{r})\right) \qquad (2.16)$$

This approach has been applied recently to study hydrogen bond interactions for visualization of intermolecular effects between donor and acceptor pair [to be published].

Similarly to the regional total energy density and b_ε index it is possible to define ratio of molecular interaction energy densities.

$$b_{\Delta\varepsilon} = \frac{\Delta\varepsilon^S_{\tau AB}(\vec{r}_{Lagrange})}{\Delta\varepsilon^S_{\tau HH}(\vec{r}_{Lagrange})} \qquad (2.17)$$

The $b_{\Delta\varepsilon}$ represents the relative stability of given A—B bond comparing to single σ bond of hydrogen molecule. In other words the character (passive - quite stable, or aggressive – quite unstable) of interaction and tendency to undergo transformation from given stationary state is characterized. The change of this index with respect to the standard bond energies is presented in Figure 3. One can notice from data in Table 2 that the lowest value of $b_{\Delta\varepsilon}$ is attached to bond in Kr_2 molecule which is very weakly bonded. In contrast the most inert among molecules in Table 2 the N_2 has the highest value. This index describes how much the given bond is stabilized comparing to single H—H bond, in other words the effect of localization of bonding electrons in space in between nuclei is evaluated. For example Li_2 and Be_2 molecules have less stable but energetically favorable interaction at $\vec{r}_{Lagrange}$. The interaction in N_2 is estimated to be much stronger then in H_2 and electronic type interaction is exclusively localized in between nitrogen atoms. The negativity of this index would mean

destabilizing effects present at $\vec{r}_{Lagrange}$ (thus high reactivity) or indicate delocalization of bonding (attractive, electronic) interactions to the regions outside interatomic axis. In this case three-dimensional view is needed to fully illustrate bonding interaction character.

8. Energy density in real space

The electronic stress, kinetic energy density and interaction energy density may be represented in real space providing more detailed and prospective view that complements the information obtained from Lagrange point. In case of interaction energy density real space data is especially valuable showing the source of stability or weakness of molecules.

Figure 4 shows redistribution of interaction energy density in space while the electron density change in space is shown in Figure 5. The metal atoms from first group constitute bonds with wide stabilization regions (represented by blue isosurfaces) in between atoms and wide destabilization regions outside. The region of negative interaction energy density that stabilizes bond is in overlap with increased electron density regions (represented by red isosurfaces in Figure 5). The second group elements have bonds very similar to H_2 bond, where both atoms are buried in stabilization region that spreads around the whole molecule. However in case of these elements the negative interaction energy density region is redistributed over the much larger space and energetically unfavorable regions are limited only to doughnut structures surrounding the bond. One can notice that electron density increase between atoms is limited to small σ-like region while outside interatomic region it is widely redistributed. On the other hand the hydrogen molecule is closed in shell structure in which the center is formed by stabilized core of increased electron density. The N_2 and P_2 molecules show stability in "σ^*" shaped region surrounded by stabilization ring. The As_2 molecule, in contrast to former ones, innermost has σ like stabilization region submerged in bulk of destabilization. The negative interaction energy density regions usually cover the electron density increase regions. However this is not exactly the case for H_2 and N_2 molecules for which regions of favorable interaction also appear in place where electron density is decreased. This may have connection with greater stability (and lower reactivity, see $b_{\Delta\varepsilon}$ parameter in Table 2) of these molecules comparing to the other species from given group in periodic table.

In Figure 6 and Figure 7 is presented visualization of interaction energy density and electron density change for noble gases. The magnitude of interaction energy density is very small (almost in error limit) however one can notice for interatomic region that the stabilization effect occurs due to decrease of electron density in this region (in contrast to

other molecules where attractive interaction energy density comes in pair with increase of electron density). Among all noble gases species the Ne_2 is characterized by strongest interaction (greatest bi indices). The source of such stability might be explained by following issues. The Ne_2 has the shortest optimized interatomic distance of all presented noble-gases, very close to that in Na_2. Although the electron density at Lagrange point has been decreased about two orders more then for other noble-gases, still it's value is an order greater then others. The strong accumulation of electron density on atomic cores is also observed with very small and diffused destabilization in those regions.

Conclusions and discussion

The supermolecular approach when applied to diatomic molecules need to take into account the possible electronic configurations and orbitals orientations for atomic monomers. In case of diatomic species of 3rd, 4th, 6th and 7th group elements it is required more careful and detailed analysis which has not been applied on this stage yet. Some difficulties are originated from single determinant wave function, utilization of which causes not reasonable orientations of atomic orbitals of monomers in some atoms that do not correspond to ones in dissociation limit (configuration of maximum overlap in molecule). We need to revise our definition of atomic monomer in some cases. Nevertheless the method for obtaining the three-dimensional interaction energy density in present state is fully applicable to intermolecular interactions, in generic circumstances.

Lagrange point is the characteristic point of bond line that may represent bond properties using energy density data. The total energy density (calculated as the trace of stress tensor) is in close association with electronic and chemical properties of molecules. It is possible to characterize interactions and to evaluate their strengths and energy based bond orders using the energy density related indices. However we need more detailed study to find the source of difference between values of bond orders calculated in our method with commonly used ones. The correspondence of b_ε, b_μ and $b_{\Delta\varepsilon}$ indices describing reactivity with standard bond energies was found and only small basis set and immaterial method dependency of these indices have been inferred. However single point is not enough for full characterization of bonding interactions. The three-dimensional insight is much more informative. The differences in the redistribution of interaction energy densities are in close relation with activity of given molecule. Furthermore it may provide details on orbital interaction, spin state and stability of given compound.

It may seem strange that the values of the b_μ index calculated for noble-gas diatomic molecules are surprisingly large in some cases (the He_2, Ne_2, Ar_2, Kr_2 values are larger than Li_2, Na_2, K_2), while the b_ε index gives practically zeros. In fact all noble gases dimers have very low b_ε indices (except Ne_2 for which it is comparable to that of Na_2 or K_2), which indicates very weak bonding. However the greater b_μ index is associated with greater absolute value of local chemical potential of bonded atoms that is the potential of electrons to undergo physical or chemical change in the system. The similar points (competition between stabilization energy and chemical potential) may also apply to other species i.e. of fifth group (N_2, P_2, As_2) explaining it's reactivity and the deviation of b_ε from commonly used bond orders. In addition in presented set of molecules only noble gases have negative kinetic energy density at Lagrange point. The atoms and interatomic region of bonded molecules are embedded in positive kinetic energy density region. The noble gases atoms (positive kinetic energy density) are separated and surrounded by negative kinetic energy density without any connection in shape of positive region, which reflects a leading role of long range field (electrostatic or quantum in nature) effects for interaction between noble gases. Although we have found very little method dependency, the HF level is not suitable for noble gases calculations. The noble gases have one of the lowest bond order indices. The use of more sophisticated method and inclusion of higher dispersion and correlation effects should lead to more accurate results in this case.

Another unusual result is that the P_2 molecule shows substantially different figure of bond order from MO-based bond order. The Table 4 compares molecular orbitals energy densities in Lagrange point of three "triple bonded" molecules. The N_2 has the lowest energy in Lagrange Point for all highest occupied molecular orbitals, filled by valance electrons (except σ^*) and the lowest sum of energies of MO-s of core electrons. Second is carbon-carbon bond in C_2H_2 and P_2 at the end. Our bond orders give the same order of decreasing bond order. The interatomic distances are: 1.07[Å], 1.18[Å] and 1.85[Å] respectively. The electron density decreases with increasing distance. One should notice that our indices are deeply related to electron density accumulated in meta-stable position at Lagrange point and its energy not only in the total effect.

There are many discussions in literature about bonding itself and some researches even claim that there is no such thing as a chemical bond at all. The new indices, although reflect traditional bond orders, are carrying different information about interactions on the interfaces of quantum chemical subsystems. Thus we can not judge and recommend one of our new

indices as representative method to estimate bond order. Our indices satisfy the earlier definition of bond order (by IUPAC) as “index of the degree of bonding between two atoms relative to that of a single bond”. The bond order is provided by energy density associated with localized electron density, as the combined effect of all occupied molecular orbitals (which in some part corresponds also to molecular-orbital bond order definition). Since electronic energy density includes the electronic spin angular momentum in the underling physics, so does the energy density based bond order. However depending on the specific information one may use either one or all new indices to characterize molecules and chemical interactions.

References

[1] (a) Tachibana A (1999) Theor Chem Acc 102:188-195 (b) Tachibana A (1987) Int J Quantum Chem, Quantum Chem Symp 21:181-190 (c) Tachibana A (1996) Int J Quantum Chem 57:423-428; Tachibana A, Parr RG (1992) ibid. 41:527-555. (d) Tachibana A, Nakamura K, Sakata K, Morisaki T (1999) Int J Quantum Chem 74:669-679

[2] (a) Bingel WA (1963) Z Naturforsch A 18A:1249-1258; Bingel WA (1967) Theor Chim Acta 8:54-61. (b) Kato T (1957) Commun Pure Appl Math 10:151-171 (c) Pack RT, Brown WB (1966) J Chem Phys 45:556-559

[3] Tachibana A (2001) J Chem Phys 115:3497-3518

[4] (a) Hohenberg P, Kohn W (1964) Phys Rev 136:B864-B871 (b) Mermin ND (1965) Phys Rev A 137:1441-1443 (c) Parr RG, Yang W (1989) Density Functional Theory of Atoms and Molecules, Oxford University Press, New York

[5] Tachibana A (2002) Energy density in materials and chemical reaction systems. In: Sen KD (ed) Reviews in modern quantum chemistry: a celebration of the contributions of Robert Parr, vol 2. World Scientific, Singapore, pp 1327–1366

[6] Tachibana A (2005) J Mol Model 11:301–311

[7] Tachibana A (2004) Int J Quantum Chem 100:981–993

[8] Tachibana A (2003) Field energy density in chemical reaction systems. In: Brändas E, Kryachko E (eds) Fundamental perspectives in quantum chemistry: a tribute to the memory of Per-Olov Löwdin, vol 2. Kluwer, Dordrecht, pp 211–239

[9] (a) Tachibana A (1991) J Math Chem 7:95-110; Tachibana A (1994) String Model of Chemical Reactions. In: Conceptual Trends in Quantum Chemistry, Kryachko ES, Calais JL (eds), Kluwer, Dordrecht, pp 101–118 (b) Fukui K (1970) J Phys Chem 74:4161-4163; Fukui K (1981) Acc Chem Res 14:363-368 (c) Tachibana A (1999) Electronic energy density in chemical reaction systems. In: Fueno T (ed), The Transition State-A Theoretical Approach, Kodansha, Tokyo, pp 217–247

[10] Bader RFW (1990) Atoms in Molecules - A Quantum Theory, Oxford University Press, Oxford

[11], Frisch MJ, Trucks GW, Schlegel HB, Scuseria GE, Robb MA, Cheeseman JR, Montgomery JA, Vreven JrT, Kudin KN, Burant JC, Millam JM, Iyengar SS, Tomasi J, Barone V, Mennucci B, Cossi M, Scalmani G,

Rega N, Petersson GA, Nakatsuji H, Hada M, Ehara M, Toyota K, Fukuda R, Hasegawa J, Ishida M, Nakajima T, Honda Y, Kitao O, Nakai H, Klene M, Li X, Knox JE, Hratchian HP, Cross JB, Bakken V, Adamo C, Jaramillo J, Gomperts R, Stratmann RE, Yazyev O, Austin AJ, Cammi R, Pomelli C, Ochterski JW, Ayala PY, Morokuma K, Voth GA, Salvador P, Dannenberg JJ, Zakrzewski VG, Dapprich S, Daniels AD, Strain MC, Farkas O, Malick DK, Rabuck AD, Raghavachari K, Foresman JB, Ortiz JV, Cui Q, Baboul AG, Clifford S, Cioslowski J, Stefanov BB, Liu G, Liashenko A, Piskorz P, Komaromi I, Martin RL, Fox DJ, Keith T, Al-Laham MA, Peng CY, Nanayakkara A, Challacombe M, Gill PMW, Johnson B, Chen W, Wong MW, Gonzalez C, Pople JA, (2003) Gaussian 03, Revision C.02, Gaussian, Inc., Wallingford CT

[12] Nakamura K, Doi K, Tachibana A, MRDFT program; available on request via e-mail: akitomo@scl.kyoto-u.ac.jp

[13] (a) Mayer I (1983) Chem Phys Lett 97:270-274 (b) Mayer I (1985) Tcheoret Chim Acta (Berl.) 67:315-322 (c) Mayer I (1986) Int J Quantum Chem 29:73-84 (d) Mayer I (1986) Int J Quantum Chem 29:477-483 (e) Mulliken RS (1955) J Chem Phys 23:2343-2346 (f) Ruedenberg K (1962) Rev Mod Phys 34:326-376 (g) Roby KR (1974) Theor Chim Acta 33:105-113 (h) Coulson CA (1939) Proc Roy Soc A 169: 413-428

[14] Coulson CA (1961) Valence, 2nd ed., Clarendon Press, Oxford

[15] (a) Onsager L (1931) Phys Rev 37:405-426 (b) Onsager L (1931) Phys Rev 38:2265-2279

[16] Herring C, Nichols MH (1949) Rev Mod Phys 21:185-270

[17] Groot SR, Mazur P (1984) Non-Equilibrium Thermodynamics, Dover Publications Inc., Dover Ed edition, pp 339-345

[18] Boys SF, Bernardi F (1970) Mol Phys 19:553-556

[19] Atkins P, de Paula J (2006) Atkins' Physical Chemistry, 8th edition, Oxford University Press, New York, pp 1011-1012

[20] (a) Humphrey W, Dalke A, Schulten K (1996) J Molec Graphics 14:33-38, (b) http://www.ks.uiuc.edu/Research/vmd/

Table 1. The Lagrange point characteristics of C-C bonds - eigenvalues of stress tensor, electron density and regional total energy density (in atomic units). The b_ε ratio correlates with the bond orders of C-C bonds while modified index b_μ does not work for multiple bonds.

Molecule	The eigenvalues of stress tensor			Electron density	Total energy density	b_ε	b_μ
H_2	1.719E-01	-2.242E-01	-2.242E-01	2.643E-01	-1.383E-01	1.00	1.00
C_2H_6	6.020E-02	-1.641E-01	-1.641E-01	2.506E-01	-1.340E-01	0.97	1.02
C_2H_4	4.053E-02	-2.695E-01	-3.082E-01	3.458E-01	-2.686E-01	1.94	1.48
C_2H_2	-9.811E-03	-4.106E-01	-4.106E-01	3.969E-01	-4.155E-01	3.01	2.00

Table 2. Periodicity of the stress tensor and energy density related parameters at Lagrange point. Data in atomic units unless marked otherwise.

	H2	He2
3rd eigenvalue of stress tensor	0.1738	-0.000019
2nd eigenvalue of stress tensor	-0.2269	-0.000028
1st eigenvalue of stress tensor	-0.2269	-0.000028
Electron density	0.2660	0.000123
Regional total energy density	-0.1400	-0.000032
bε	1	0.00027
bμ	1	0.579
Electron density difference	0.1080	-2.60E-07
Interaction energy density	-0.0664	-4.36E-07
bΔε	1	6.57E-06
Interatomic distance [Å]	0.74	3.68

	Li2	Be2	B2	C2	N2	O2	F2	Ne2
3rd eigenvalue of stress tensor	-0.0008	-0.0149	-0.0045	0.0057	0.0908	0.3861	0.308	-0.000130
2nd eigenvalue of stress tensor	-0.001	-0.0159	-0.0571	-0.2011	-1.09	-0.9308	-0.4539	-0.000407
1st eigenvalue of stress tensor	-0.001	-0.0159	-0.0571	-0.2011	-1.09	-0.9308	-0.4539	-0.000407
Electron density	0.0129	0.0725	0.111	0.2008	0.7321	0.629	0.3563	0.001051
Regional total energy density	-0.0014	-0.0234	-0.0594	-0.1983	-1.0446	-0.7378	-0.2999	-0.000473
bε	0.010	0.167	0.424	1.416	7.462	5.270	2.142	0.00338
bμ	0.214	0.613	1.015	1.876	2.711	2.228	1.599	0.854
Electron density difference	0.0070	0.0326	-0.0446	-0.0814	0.1855	-0.1010	-0.0787	-1.14E-05
Interaction energy density	-0.0018	-0.0271	-	-	-0.7044	-	-	-2.15E-05
bΔε	0.027	0.408	-	-	10.615	-	-	0.000325
Interatomic distance [Å]	2.78	1.81	1.64	1.36	1.07	1.16	1.33	3.27

Table 2. Continued.

	Na2	Mg2	Al2	Si2	P2	S2	Cl2	Ar2
3rd eigenvalue of stress tensor	-0.0005	-0.0033	-0.0111	-0.0138	-0.0449	0.007	0.043	-0.000016
2nd eigenvalue of stress tensor	-0.0005	-0.0033	-0.0136	-0.0335	-0.1076	-0.1229	-0.0924	-0.000034
1st eigenvalue of stress tensor	-0.0007	-0.0064	-0.0136	-0.0335	-0.1076	-0.1229	-0.0924	-0.000034
Electron density	0.0084	0.0273	0.0459	0.0664	0.194	0.2013	0.157	0.000202
Regional total energy density	-0.0009	-0.0065	-0.0192	-0.0405	-0.1301	-0.1194	-0.0709	-0.000042
bε	0.006	0.046	0.137	0.289	0.929	0.853	0.506	0.00030
bμ	0.196	0.452	0.792	1.156	1.274	1.127	0.857	0.392
Electron density difference	0.0038	0.0076	-0.0168	-0.0285	0.0565	-0.0137	-0.0138	0
Interaction energy density	-0.0008	-0.0060	-	-	-0.1140	-	-	0.0022
bΔε	0.013	0.090	-	-	1.717	-	-	---
Interatomic distance [Å]	3.20	2.53	2.25	2.05	1.85	1.88	2.00	5.03

	K2	Ca2	Ga2	Ge2	As2	Se2	Br2	Kr2
3rd eigenvalue of stress tensor	-0.0002	-0.0015	-0.0071	-0.0139	-0.0334	-0.0083	0.0122	-0.000010
2nd eigenvalue of stress tensor	-0.0002	-0.0015	-0.0128	-0.0334	-0.0681	-0.0626	-0.0508	-0.000021
1st eigenvalue of stress tensor	-0.0003	-0.0019	-0.0154	-0.0334	-0.0681	-0.0626	-0.0508	-0.000021
Electron density	0.0044	0.0144	0.0518	0.0596	0.141	0.1339	0.1128	0.000154
Regional total energy density	-0.0004	-0.0033	-0.0096	-0.0202	-0.0650	-0.0597	-0.0354	-0.000021
bε	0.002	0.017	0.126	0.288	0.606	0.477	0.319	0.00019
bμ	0.145	0.322	0.648	1.287	1.143	0.947	0.752	0.324
Electron density difference	0.0019	0.0043	-0.0038	-0.0329	0.0263	-0.0216	-0.0081	-6.40E-07
Interaction energy density	-0.0003	-0.0020	-	-	-0.0442	-	-	-4.90E-07
bΔε	0.004	0.030	-	-	0.666	-	-	7.38E-06
Interatomic distance [Å]	4.20	3.35	2.54	2.18	2.06	2.15	2.29	5.58

Table 3. The method and basis set dependency of b_ε and b_μ for Li_2.

	STO-3G	6-31G	6-31++G	6-31G**	6-31++G**	6-311G	6-311++G	6-311G**	6-311++G**
R [Å]									
B3LYP	2.6888	2.7325	2.7334	2.7230	2.7254	2.7055	2.7056	2.7048	2.7050
HF	2.6964	2.8155	2.8218	2.8069	2.8145	2.7846	2.7847	2.7844	2.7846
MP2	2.6994	2.8109	2.8154	2.7821	2.7872	2.7698	2.7687	2.7485	2.7479
b_ε									
B3LYP	0.017	0.010	0.010	0.009	0.009	0.013	0.013	0.013	0.013
HF	0.016	0.008	0.008	0.008	0.007	0.011	0.011	0.010	0.010
MP2	0.017	0.008	0.008	0.008	0.008	0.011	0.011	0.011	0.011
b_μ									
B3LYP	0.252	0.168	0.170	0.170	0.167	0.220	0.220	0.214	0.214
HF	0.278	0.193	0.195	0.191	0.190	0.248	0.248	0.244	0.244
MP2	0.268	0.173	0.176	0.173	0.172	0.227	0.228	0.223	0.224

Table 4. The energy densities [au·bohr^{-3}] at Lagrange point $\vec{r}_{Lagrange}$ for highest occupied Molecular Orbitals. The core means sum of energy densities at $\vec{r}_{Lagrange}$ of core MO's. The valance electrons orbitals: σ - is sigma bonding MO, σ* - sigma antibonding MO, π – degenerated pi bonding MO.

MO	N_2	C_2H_2	P_2
π (HOMO)	-0.3174	-0.1440	-0.0320
π (HOMO)	-0.3174	-0.1440	-0.0320
σ	-0.5567	-0.2632	-0.0955
σ*	-0.0022	-0.0013	-0.0061
σ	-0.8912	-0.3849	-0.0929
core	-0.0050	-0.0038	-0.0017

Figure 1. The bond lines and Lagrange point $\vec{r}_{Lagrange}$; **a)** the eigenvectors of principal stress constitute the bond lines, **b)** the cancellation of tension defines Lagrange point (situated on a bond line), **c)** the eigenvectors of principal stress tensor arranged in bond lines in H_2 molecule, and **d)** tension cancellation in between atoms.

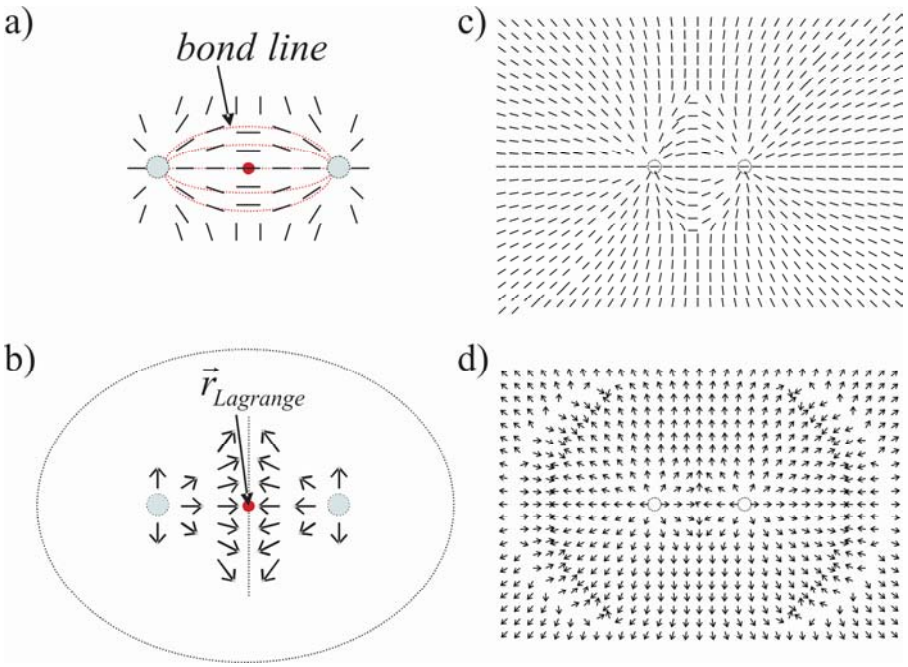

Figure 2. Comparison of MO theory bond orders (b=(n-n*)/2) – doted line. with b_ε (circles) and b_μ (squares). The molecules are ordered according to the increasing largest eigenvalue of stress tensor at Lagrange point.

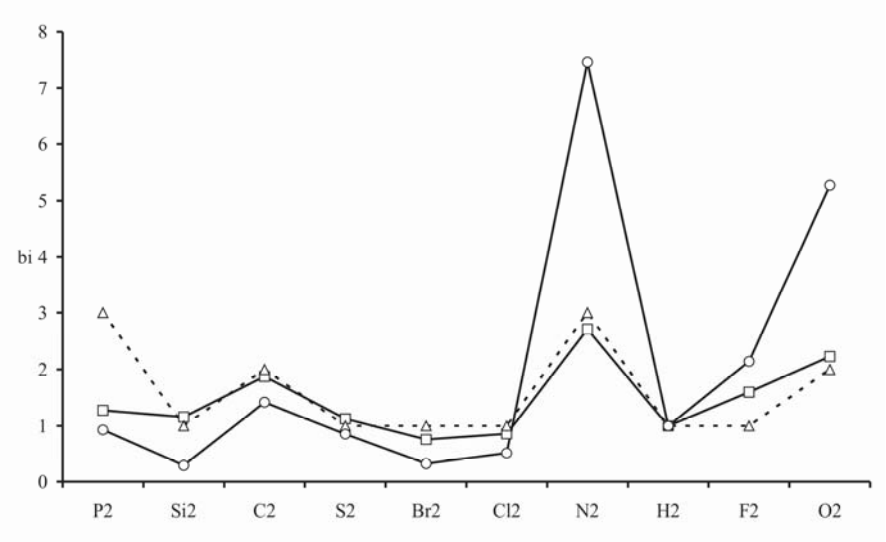

Figure 3. Correlation of b_ε (squares) and $b_{\Delta\varepsilon}$ (strokes) with standard bond energies [kJ·mol^{-1}] taken from literature [19] (doted line). The $b_{\Delta\varepsilon}$ has been normalized to level of H_2 standard bond energy. The molecules are ordered according to the increasing largest eigenvalue of stress tensor at Lagrange point (from left to right).

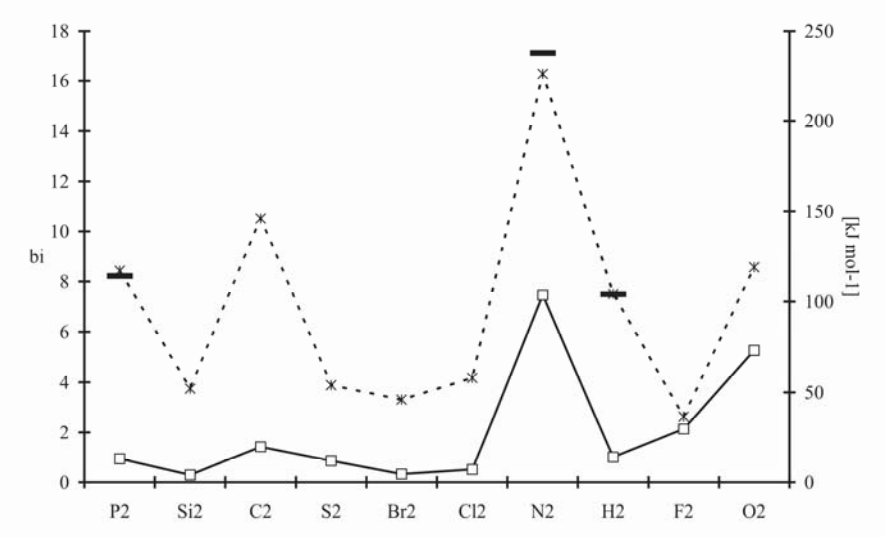

Figure 4. Interaction energy density. Black isosurfaces correspond to zero value of interaction energy density. The blue regions mark out the negative interaction energy density space $\Delta\varepsilon^{S}_{\tau AB}(\vec{r}) < 0$; in the complement space $\Delta\varepsilon^{S}_{\tau AB}(\vec{r}) > 0$. The diameter of cube is 20 bohr. The atoms represented by green CPKs. [20]

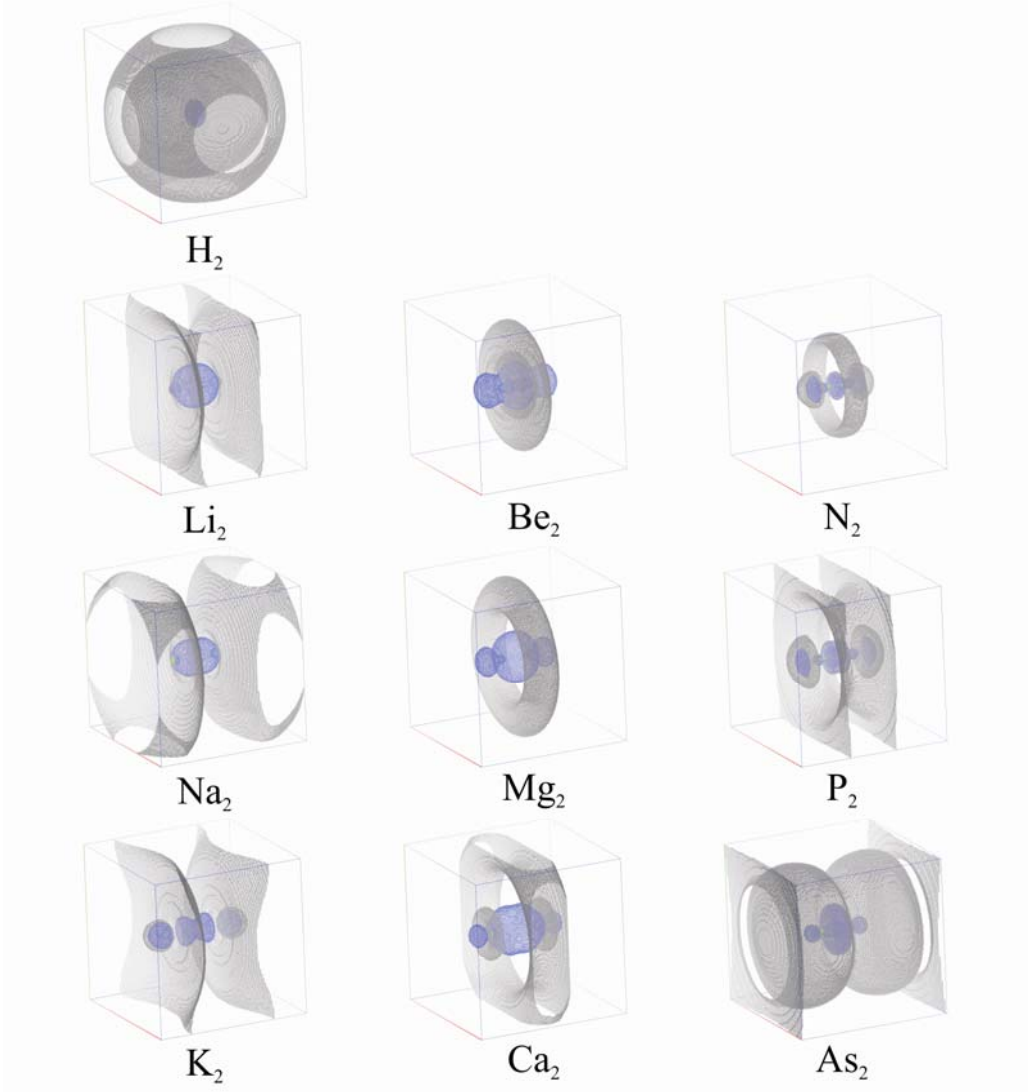

Figure 5. Electron density redistribution change calculated as difference of molecule and atoms electron densities. Black isosurfaces correspond to zero value. The red regions mark out the regions of increased electron density $\Delta n_{AB}(\vec{r}) > 0$; in the complement space $\Delta n_{AB}(\vec{r}) < 0$. The diameter of cube is 20 bohr. The atoms represented by green CPKs. [20]

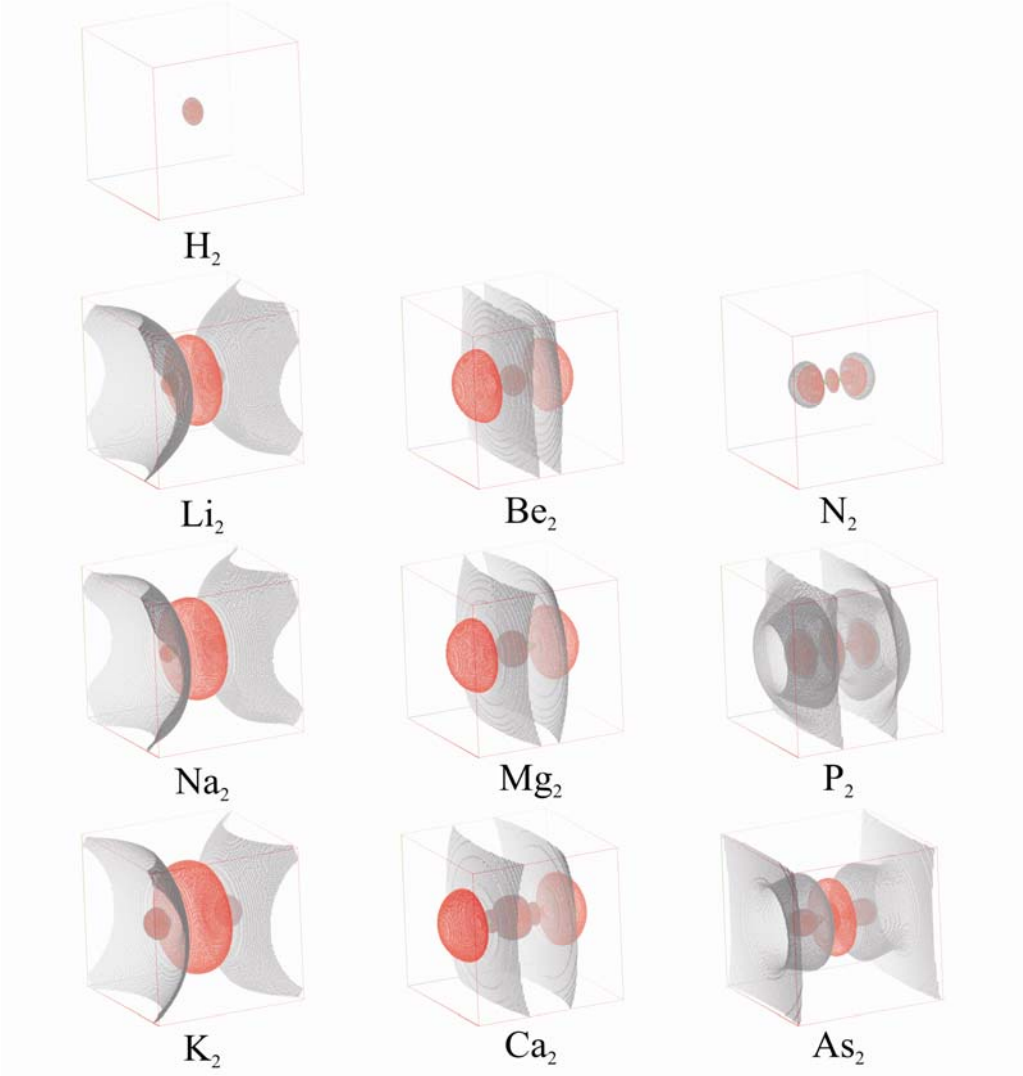

Figure 6. Interaction energy density - noble gases: the blue dots represent the negative interaction energy density space; the red dots – positive. The size of dots corresponds to the magnitude of energy density. The diameter of cube is 20 bohr. The atoms represented by black spheres. [19]

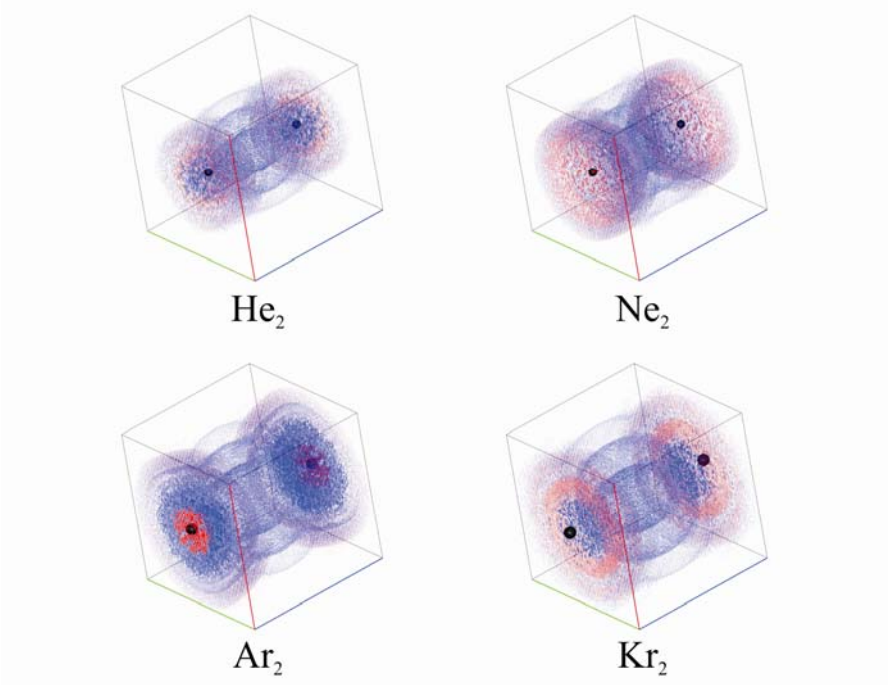

Figure 7. Electron density redistribution change (noble gases) calculated as difference of molecule and atoms electron densities. The red dots show increased electron density; the blue dots apply to decreased electron density. The size of dots corresponds to the magnitude of electron density change. The diameter of cube is 20 bohr. The atoms represented by black spheres. [19]

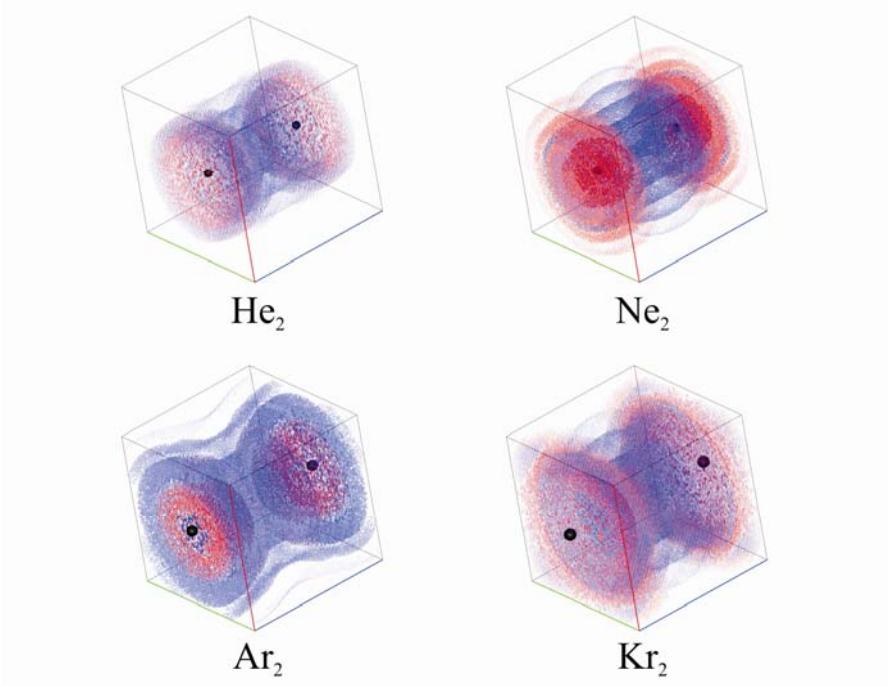

CHAPTER 3

Electronic Stress Tensor Description of Chemical Bonds Using Non-classical Bond Order Concept.

Introduction

Recently an examination of bond order gains much attention regarding studies of multiple bonded atoms (especially metals). One has in choice various definitions expressing classical bond order concept by quantum mechanical methods usually in terms of density [1,2] and overlap matrices [3] or natural resonance theory [4]. The bond order concepts have been reviewed recently by Mayer [5]. The original idea traces back to Lewis's shared electrons and assigning it to bonding, nonbonding or antibonding orbitals. However, due to disagreement between the experimental and theoretical results with simple Lewis-type structures for multiply bonded metal atoms [6,7], the use of non-classically oriented approaches is advised [8]. The delocalized nature of electron wavefunctions smeared over molecular orbitals makes the assignment of electron pairs to particular bond quite challenging. Besides, these pairs might feel different about different elements, thus a bonding pair between two atoms may not be equivalent to a pair between other two. New formulation of bond order concept [8] presented here refers to the electronic energy rather than to electrons them selves, thus it is more suitable for evaluation of bond strength. Bond order was introduced as an indicator of bond stability and essentially refers to bond strength relative to single bonds, thus new concept of bond order expressed in terms of electronic energy density is formally and naturally better to fulfill this role. Moreover this new indices allow one to have a closer look on redistribution of energy over the molecule and its partition between particular bonds.

1.1. Theory

The Regional DFT (RDFT) method [9-15] has been used for energy density calculations. The method allows assigning the electronic energy density associated with the electron density at discrete points of real space [16-19]. The sum of regional contributions gives global electronic energy E and integration over whole space leads to total energy. The kinetic energy density $n_T(\vec{r})$ obtained from energy density partitioning scheme within RDFT [9,20-23] divides space into the electronic drop R_D and atmosphere R_A regions separated by the interface S [10]. In the electronic drop region, where $n_T(\vec{r}) > 0$, the electron density is simply accumulated and classical motion of electrons is allowed. Contrary, the electron density is dried up and the motion of

electron is classically forbidden in the complementary region ($n_T(\vec{r}) < 0$) of the electronic atmosphere. The boundary S in between R_D and R_A encloses the molecular region of reactant atoms and molecules along the course of the chemical reaction coordinate. The kinetic energy density is defined as (Eq.1):

$$n_T(\vec{r}) = -\frac{\hbar^2}{4m}\sum_i^{occ} \nu_i \left[\psi_i^*(\vec{r})\Delta\psi_i(\vec{r}) + \Delta\psi_i^*(\vec{r})\psi_i(\vec{r})\right] \qquad (1)$$

$$\begin{aligned} R_D &: \quad n_T(\vec{r}) > 0 \\ R_A &: \quad n_T(\vec{r}) < 0 \\ S &: \quad n_T(\vec{r}) = 0 \end{aligned} \qquad (2)$$

where m is mass of electron, $\psi_i(\vec{r})$ is natural orbital and νi is occupation number of $\psi_i(\vec{r})$. The kinetic energy density is not positive definite in contrast to conventional positive-semidefinite representation [24-29]. The calculations [20-23] have not emphased which representation of kinetic energy density is appropriate. The expectation values integrated over whole space are the same [20]. However densities are different and the relevant differences are crucial for study of chemical systems. The $n_T(\vec{r}) = 0$ defines boundary, within which the intramolecular electric field produced by the other electrons does not exceed that of bare nucleus [10], thus the boundary defines the turning point for electron.

The stress tensors are used to describe the internal forces of matter. In molecules it characterizes internal distortion of electron density. The local stresses, represented as the force acting on a pair of electronic drop regions [10,14] of reactants, have been applied to study the chemical reactivity [13]. The electronic stress tensor is derived according to Eq.3:

$$\tau^{Skl}(r) = \frac{\hbar^2}{4m}\sum_i^{occ} \nu_i \left[\psi_i^*(\vec{r})\frac{\partial^2\psi_i(\vec{r})}{\partial x^k \partial x^l} - \frac{\partial\psi_i^*(\vec{r})}{\partial x^k}\frac{\partial\psi_i(\vec{r})}{\partial x^l} + \frac{\partial^2\psi_i^*(\vec{r})}{\partial x^k \partial x^l}\psi_i(\vec{r}) - \frac{\partial\psi_i^*(\vec{r})}{\partial x^l}\frac{\partial\psi_i(\vec{r})}{\partial x^k}\right] \qquad (3)$$

with indices *k,l*=1,2,3. The electronic stress tensor is second rank tensor given by 3x3 matrix (Eq.4) with components defined by Eq.3.

$$\left\langle \hat{\tilde{\tau}}_\alpha^S(\vec{r}) \right\rangle = \begin{bmatrix} \tau_{\alpha xx}^S(\vec{r}) & \tau_{\alpha xy}^S(\vec{r}) & \tau_{\alpha xz}^S(\vec{r}) \\ \tau_{\alpha yx}^S(\vec{r}) & \tau_{\alpha yy}^S(\vec{r}) & \tau_{\alpha yz}^S(\vec{r}) \\ \tau_{\alpha zx}^S(\vec{r}) & \tau_{\alpha zy}^S(\vec{r}) & \tau_{\alpha zz}^S(\vec{r}) \end{bmatrix} \xrightarrow{diag} \begin{bmatrix} \tau_\alpha^{S11}(\vec{r}) & 0 & 0 \\ 0 & \tau_\alpha^{S22}(\vec{r}) & 0 \\ 0 & 0 & \tau_\alpha^{S33}(\vec{r}) \end{bmatrix} \qquad (4)$$

$$\tau_{\alpha}^{S11}(\vec{r}) \le \tau_{\alpha}^{S22}(\vec{r}) \le \tau_{\alpha}^{S33}(\vec{r}) \qquad (5)$$

The eigenvalues of the stress tensor compose a set of invariant quantities that are the principal stresses. Their direction vectors (eigenvectors) are the principal directions. For surfaces normal to principal axes, the stress correspond to pushes (negative) or pulls (positive) perpendicular to the surfaces. The very low negative stress regions are associated with atomic core regions, where electron density is highly compressed. The covalent bond formation is characterized by a concept of spindle structure [14]. It is anticipated when the region, where principal electronic stress is positive (tensile stress), along the line of principal axis connecting a pair of the R_Ds of atoms or molecules (with predominant compressive stress). The electronic energy is given by first invariant of stress tensor. The half of trace over eigenvalues of stress tensor gives local contribution ($\varepsilon_{\tau}(\vec{r})$) to potential energy density of electrons (Eq.6).

$$\varepsilon_{\tau}^{S}(\vec{r}) = \tfrac{1}{2}\sum_{k}\tau_{\alpha}^{Skk}(\vec{r}), \qquad E = \int d^3\vec{r}\,\varepsilon_{\tau}^{S}(\vec{r}) \qquad (6)$$

It was shown in Ref. 15 that from the viral theorem follows (Eq. 7):

$$E_{Rigged\ QED} = \int d^3\vec{r}\left\langle \hat{H}_{Rigged\ QED}\right\rangle = \int d^3\vec{r}\left\langle m_e c^2\hat{\bar{\psi}}(\vec{r})\hat{\psi}(\vec{r}) - \sum_{a}\hat{T}_a(\vec{r})\right\rangle \qquad (7)$$

which in non-relativistic limit becomes (Eq. 8):

$$E_{\substack{non-relativistic\\ Rigged\ QED}} = \int d^3\vec{r}\left\langle \hat{H}_{\substack{non-relativistic\\ Rigged\ QED}}\right\rangle = -\int d^3\vec{r}\left\langle \sum_{a}\hat{T}_a(\vec{r})\right\rangle = -\tfrac{1}{2}\int d^3\vec{r}\left\langle \sum \hat{\bar{\tau}}_{\alpha k}^{Sk}(\vec{r})\right\rangle \qquad (8)$$

thus the integral over the trace of stress tensor density is equal to two times the kinetic energy density. The performance of other stress tensors [29-34] was not studied in context of this work (but were used to derive electronic pressure) so we can not advocate for any definition. However formulation of stress tensor directly translates into body forces that might represent different effects associated with charge distribution in molecules.

The total electronic force density operator is given by Eq.9:

$$\hat{\bar{F}}_{\alpha}^{S}(r) = \hat{\bar{\tau}}_{\alpha}^{S}(\vec{r}) + \hat{L}_{\alpha}^{S}(\vec{r}) \qquad (9)$$

where $\hat{L}_{\alpha}^{S}(\vec{r})$ is the Lorentz force density operator and $\hat{\bar{\tau}}_{\alpha}^{S}(\vec{r})$ is the tension density operator. Lorentz force density operator consist the classical form and quantum mechanical exchange effects. The tension density operator represents purely quantum mechanical effects. In the

stationary state of charged particles the local force vanish, since the tension density (the tension of the field) exactly cancels the Lorentz force density (the Lorentz force exerted on the particle) at every point of space (Eq.10) [10,12,14,35].

$$\left\langle \hat{\vec{\tau}}_{\alpha}^{S}(\vec{r}) \right\rangle + \left\langle \hat{\vec{L}}_{\alpha}^{S}(\vec{r}) \right\rangle = 0 \qquad (10)$$

The Lorentz force density operator is given by Eq. 11,

$$\hat{\vec{L}}(\vec{r}) = \hat{\vec{L}}_{e}(\vec{r}) + \sum_{a} \hat{\vec{L}}_{a}(\vec{r}) \qquad (11)$$

$$\hat{\vec{L}}_{e}(\vec{r}) = \hat{\vec{E}}(\vec{r})\hat{\rho}_{e}(\vec{r}) + \frac{1}{c}\hat{\vec{j}}_{e}(\vec{r}) \times \hat{\vec{B}}(\vec{r}) \qquad (12)$$

$$\hat{\vec{L}}_{a}(\vec{r}) = \hat{\vec{E}}(\vec{r})\hat{\rho}_{a}(\vec{r}) + \frac{1}{c}\hat{\vec{j}}_{a}(\vec{r}) \times \hat{\vec{B}}(\vec{r}) \qquad (13)$$

where $\hat{\vec{L}}_{e}(\vec{r})$ is the electronic Lorentz force density operator and $\hat{\vec{L}}_{a}(\vec{r})$ is the Lorentz force density operator of atomic nucleus *a* [15]. The tension is given as the divergence of the stress tensor density operator (Eq.14):

$$\hat{\tau}_{\alpha}^{Sk}(\vec{r}) = \partial_{l}\hat{\tau}_{\alpha}^{Skl}(\vec{r}) =$$
$$= \frac{\hbar^{2}}{4m}\sum_{i}^{occ} \nu_{i}\left[\psi_{i}^{*}(\vec{r})\frac{\partial \Delta\psi_{i}(\vec{r})}{\partial x^{k}} - \frac{\partial \psi_{i}^{*}(\vec{r})}{\partial x^{k}}\Delta\psi_{i}(\vec{r}) + \frac{\partial \Delta\psi_{i}^{*}(\vec{r})}{\partial x^{k}}\psi_{i}(\vec{r}) - \Delta\psi_{i}^{*}(\vec{r})\frac{\partial \psi_{i}(\vec{r})}{\partial x^{k}} \right] \qquad (14)$$

In stationary state between chemically bonded atoms, within electronic drop region, one can localize peculiar point (the Lagrange point $\vec{r}_{Lagrange}$) at which repulsive electronic tension (and also the Lorentz force) cancels itself in space thus local tension density is zero. [8]

1.2. Calculation method

The molecules were optimized at HF/6-311++G** level of theory using Gaussian 03 program package (G03) [36] unless specified different. The corresponding wave functions were used as input for RDFT code for electronic stress tensor and energy density calculations [37]. The NBO bond orders were calculated using G03 and Mayer's bond orders using APOST and BORDER programs [38,39].

1.3. The Nature of the Lagrange Point

Fig.1a shows absolute value of tension force density along interatomic axis in H_2 molecule and in hydrogen atom and Fig.1b shows tension density in the cross-section plane of H_2. The origin corresponds to the Lagrange point ($\vec{r}_{Lagrange}$) of H_2 molecule. Lagrange point exists in the molecule, between bonded hydrogen atoms, where bond lines (eigenvectors of stress) form an envelope connecting atomic centers [8]. It does not appear for single hydrogen atom or outside interatomic region of hydrogen molecule. Internal quantum forces are the greater the faster probability density is changing in space. At $\vec{r}_{Lagrange}$ internal quantum forces disappear (for stationary state). The Lagrange point is an attractor for fluxes, and is observed where density builds up (it is observed also at the atomic nuclei position) and the interference pattern forms ($\vec{r}_{Lagrange}$ results from intense interference). At Lagrange point net force is zero thus this point does not produce any acceleration/deceleration of electrons. It also implies zero energy density difference (no electronic "pressure" change) or zero momentum transfer. This is stationary point of charge density in interatomic region between bonded atoms.

Saddle point of electron density distribution does not have to indicate stationary point for electrons, since force exerted on particles might be non zero. The $\vec{r}_{Lagrange}$ has mechanical origin and is determined by dynamical forces acting on electrons in contrast to bond critical point (BCP) of AIM theory [29], which is a topological parameter. Sometimes these two points are equal (for bonds in very symmetric molecules), but it is not a rule. In particular cases, when bond critical point exists, the Lagrange point was not found, because "body" forces were not balanced (no stationary point), like between two hydrogen atoms in the bay region in phenanthrene [40].

The RQED Lagrange points in molecules are like Lagrange points in astrophysics (i.e. trojan asteroids, or Kordylewski clouds). However instead of gravitation, they are born from electromagnetic forces between atomic nuclei and much lighter electrons. The electromagnetic fields of two nuclei and electrons combined with orbital angular momentum (corresponding to centrifugal force in classical physics) are balanced at Lagrange points, allowing electron density to be stationary with respect to atomic nuclei. The reason for existence of Lagrange points in molecules is wavefunction interference and interelectron resonance. These features make Lagrange point a specific connector between two chemically bonded atoms. The molecular properties at this point provide reliable description of bond nature character.

Recently introduced bond order indices related to electronic stress tensor [8] are based on quantities calculated at $\vec{r}_{Lagrange}$, namely electronic energy density and electronic chemical potential [8]. The quantities for particular bond in a molecule are normalized by corresponding ones in H_2 molecule (as model, single, two-electron bond between two protons), calculated at the same level of theory (including method and basis set). The hydrogen molecule was chosen because it has no core electrons thus constitutes simplest chemical bond. The b_ε is the energy density bond order (Eq.15):

$$b_\varepsilon = \frac{\varepsilon^S_{\tau AB}(\vec{r}_{Lagrange})}{\varepsilon^S_{\tau HH}(\vec{r}_{Lagrange})} \tag{15}$$

and b_μ is the electronic chemical potential bond order (Eq.16):

$$b_\mu = \frac{b_\varepsilon}{\left(n_{AB}(\vec{r}_{Lagrange})/n_{HH}(\vec{r}_{Lagranre})\right)} = \frac{\varepsilon^S_{\tau AB}(\vec{r}_{Lagranre})}{n_{AB}(\vec{r}_{Lagranre})} \cdot \left(\frac{\varepsilon^S_{\tau HH}(\vec{r}_{Lagranre})}{n_{HH}(\vec{r}_{Lagranre})}\right)^{-1} \tag{16}$$

where $\varepsilon(\vec{r})$ to $n(\vec{r})$ ratio (of fractions of total electronic energy and total number of electrons) gives linear approximation to chemical potential [8] (local version of Parr's result [41]) at given point in space according to Eq.17 and Eq.18.

$$E_{AB} = \int d^3\vec{r}\,\varepsilon^S_{\tau AB}(\vec{r}), \quad N_{AB} = \int d^3\vec{r}\, n_{AB}(\vec{r}) \tag{17}$$

$$\mu_R = \left(\frac{\partial E_R}{\partial N_R}\right) \Leftrightarrow \frac{\varepsilon^S_{\tau AB}(\vec{r})}{n_{AB}(\vec{r})} \tag{18}$$

1.4. Atomic stabilization

The positiveness of the largest eigenvalue of stress is an indicator of covalent interaction between atoms when the spindle structure is formed [14]. The largest eigenvalue is resultant of effects along interatomic (principal) axis, while two minor eigenvalues measure effects through perpendicular plane. The electron pair sharing cause electron withdrawing effect along

interatomic axis, which results in positive stress. However a triple carbon-carbon bond in acetylene molecule, without doubt covalent, shows only negative eigenvalues in the interatomic region. Such feature might be attributed to atomic stabilization effect. The atomic cores are characterized by very low negative (compressive) stresses. At long interatomic distances, such as single covalent bond equilibrium distance, the separation of negative core regions is sufficient enough and perturbation in the bonding region is meaningless. As two atoms come closer the core regions may affect bonding region in significant manner (semi-united atom), finally covering up the positive stress coming from covalent interaction, like it has place in case of acetylene.

The two lower eigenvalues (degenerate for single and triple bonds and split for double and aromatic bonds) decrease in close to linear manner from single, through double to triple bond (Fig.2a). The two lower eigenvalues of double bond are not degenerate due to π symmetry plane. The degeneracy of two minor eigenvalues of electronic stress tensor show similar information like bond ellipticity defined in AIM theory [29]. Table 1 compares the largest eigenvalue of stress at Lagrange point of single, double and triple carbon-carbon bonds for a group of hydrocarbons. The largest eigenvalue would change linearly from about +0.06 in single bond to about +0.0 for triple bond, if there was no atomic stabilization, because there was no reason for which such significant deviation from linear behavior could occur. However the largest eigenvalue of stress is negative by about -0.033 which accounts for atomic stabilization.

The orbital-wise analysis of stress in carbon-carbon single to triple bonds indicates that the 3rd molecular orbital (first valence MO) and the 3rd HOMO are responsible for about 70-80% of total electronic stress at Lagrange point of carbon-carbon bond in $C_2H_{n=2,4,6}$ molecules. Moreover these two MOs do not change wavefunction phase (no nodal planes) in the interatomic region between carbon atoms. The MOs for valence electrons are shown in Fig.3. The largest eigenvalues of stress of corresponding orbitals are compared in Fig.2b. The 3rd HOMO eigenvalue show almost linear dependence, with small deviation for double bond (due to π symmetry), while 3rd MO eigenvalue significantly breaks linearity for triple bonds. The atomic stabilization, manifested by negative stress of triple covalent bond, might be attributed to low lying valence MOs, in case of $C_2H_{n=2,4,6}$ molecules the first valence MO. Intuitively one might expect that low lying orbitals having strong likeness to core levels should be involved in such effects.

Results and Discussion

To illustrate how new bond order indices perform, a group of simple organic compounds with most common functional groups had been tested. The derivatives of ethane, ethene and ethyne had been analyzed and the results compared with Mayer's [42] and NBO [43-45] bond orders.

Fig.4 (see also Fig. S1 in supporting data) shows correlation of bond orders with bond length of C-C bonds. The b_ε and b_μ bond orders correlate very well with bond lengths for single, double, triple and aromatic bonds while others have much worse coefficients (Tab.2). In general, when all bonds (single to triple) are considered together, the b_ε and b_μ indices again show very good correlation, with very similar coefficients, and the Wiberg index (b_W) and atom-atom overlap NAO bond order (b_{NAO}) coefficients are alike. The Mayer's and NLMO (b_{MO}) indices do not correlate with bond length, and assume negative values in certain cases. Some trends could be observed between energy density and NBO bond orders. The b_ε coincides with the Wiberg index and b_μ is always lower like atom-atom overlap NAO bond order values (Fig.4). The stress tensor rooted indices are usually higher then corresponding NBO bond orders.

Table 3 compares bond orders of several bonds from C_2H_5A molecules. In most cases b_μ assume values similar or very close to NBO or Mayer's bond orders and to classical values, indicating that electron chemical potential of particular bond is proportional to electron density or overlap in interatomic region. In few cases (C—F, C—O, N—H, N=O and O—H) the b_μ index breaks above trend. It suggests that these electron pairs have extra increased or decreased energy chemical potential. This index is related to electron chemical potential but also represents relative energy per electron at Lagrange point, thus ratio of chemical potentials corresponds to relative energy of electron associated with particular bond. The b_ε values significantly differ from other bond orders in many cases. This is because bonding electrons, recognized as electron pairs by classically oriented bond orders, bind two atoms with different strength, depending on the electronic energy. This index gives a measure of corresponding electronic energy and bond strength. The average trend of electron density might be described as increasing with decreasing energy. It means that the heavier is b_ε index the greater is also associated electron density, thus

(in correspondence with density or overlap based bond orders) stronger bond or in other words an energetically more favorable one.

Figures S2 and S3 (supporting data) plot new bond order indicators vs. NBO and Mayer's bond orders of various bonds. The Fig S2 (b_ε vs. b_μ) show decent resolution allowing to group bonds in classes (depending on bonding elements and effects of neighboring bonds, i.e. bonds in ethane derivatives have lower indices than ethane or ethyne). Figures S3 (a) and (b) (b_ε or b_μ vs. NBO and Mayer's) show poor resolution for most bond types, allowing only for rough classification. Moreover Mayer's and NLMO indices seem to introduce a lot of "noise" with largely dispersed values. The b_μ makes better correlation with all other indices than b_ε. Both indices correlate well with Wiberg and overlap-weighted NAO bond indices.

2.1. Does basis set affect bond orders?

The dependence of bond order indices against different basis sets implemented in Gaussian [36] had been tested. This comparison consists STO-3G minimal basis set, X-YZg, X-YZWg various split-valence, Pople basis sets, Dunning/Huzinaga valence (D95V) and full double-zeta (D95) [46] and Dunning's double- (cc-pVDZ) and triple-zeta (cc-pVTZ) correlation consistent basis sets [47,48]. The tested systems as well as reference H_2 molecules were optimized using particular basis set.

The b_ε index of covalent O—H bonds in $[H_2O]_2$ complex varies between 2.0 and 2.6 (Fig.5), however the range is much narrower (2.35~2.5) for most basis sets and only Dunning/Huzinaga D95, D95V and Dunning's correlation consistent double-zeta basis sets contribute to lower limit of index. The relevant bond order differences are in some part connected with different geometries obtained within particular basis set. One should note that these bond order indices correlate well with bond lengths and are sensitive to geometrical parameters of the system and in certain cases electronic properties, like atomic charges or spin densities, predicted at particular level of theory. However, despite foregoing differences in bond orders, the particular trends regarding bond orders i.e. of covalent O—H bonds of hydrogen bond donor and acceptor water molecules is well reproduced in all (except STO-3G) basis sets. Fig.5 and Fig.6 show significant deviations of results for basis sets having polarization functions only on heavy atoms. The diffuse functions do not cause similar problems and its effect is hardly noticeable in this case. Similar

trends and tendencies might be observed also for second - chemical potential weighted bond order index b_μ, however the values for corresponding bonds show much smaller dispersion.

The b_ε, b_μ and Mayer's indices show similar stability against different basis sets as shown in Tab.4. However, comparing with Mayer's bond orders of carbon-carbon bonds in $C_2H_{n=2,4,6}$ molecules, the b_ε (and also b_μ) is advantageous preserving the ratio of 1:2:3 for single, double and triple bonds in all basis sets (Fig.6), which turns out to be weakly conserved by Mayer's method especially in larger basis sets [49]. The NBO bond orders show almost no dependency on applied basis set. The Wiberg index and NAO bond order show remarkable stability and preserve very similar values within all considered basis sets, the ratio of bond orders is also conserved.

Concluding, utilization of double-zeta basis sets results in lower bond orders. Although there are differences between indices obtained with different basis sets, the trends within particular basis set are preserved and the ratios of indices between different multiple bonds are conserved.

2.2. Are b_ε and b_μ reproducing horizontal and vertical trends in Periodic Table?

The Fig.7a-c show bond orders of C—A bond in single substituted ethane, ethene and ethyne derivatives, where A was chosen from: CH_3, SiH_3, GeH_3, NH_2, PH_2, AsH_2, OH, SH, SeH, F, Cl and Br. For C—A bonds b_ε index is increasing with group number and decreasing with periods. A small exception is made by GeH_3 group in ethylgermane of which C—A bε index is greater then of bonds to elements from following groups of 4th period, placing its value near that of ethylsilane. The difference in bond orders of carbon bonds to elements of the same group but successive periods, namely difference in b_ε of 2nd and 3rd periods is much greater then between 3rd and 4th periods. The corresponding trend is stronger in following groups. The bμ index follows similar patterns, with exception that bμ bond orders of C—Ge bonds of germane species are higher than indices of C—Si bonds in corresponding silanes. This trend is more prominent among species with double and triple C to C bonds. This index reflects electronegativities of bounded partners (according to revised Pauling scale [50,51]). Such behavior is not surprising since electronegativity χ might be defined as the negative of electronic chemical potential (Eq.19) [52,53]:

$$\chi = -\mu = -\left(\frac{\partial E}{\partial N}\right)_v \qquad (19)$$

It was shown that bond orders express nature of bonded partners and bμ is related to elements electronegativities.

2.3. Conjugation and hyperconjugation effects in bond orders representation

The Tab.5 summarizes trends in bonding between carbon atoms when conjugation or hyperconjugation effects are present. One should notice that b_ε bond orders of single bonds in C_4H_n species, except terminal single bond in butyne, are higher than in ethane molecule, while double and triple bonds indices are lower than in ethene or ethyne molecules respectively. Moreover bond orders of multiple bonds in butadiene, butadiyne and vinylacetylene are also lower then the values of corresponding bonds in butene or butyne. In the series of hydrocarbons the predicted strength of carbon-carbon bonds (carbon-carbon bonds Tab.5) indicated by b_ε decreases in order:

a) triple bonds:

$$Ethyne > 1-Butyne > Butadiyne > Vinylacetylene \qquad (20)$$

b) double bonds:

$$Allene > Ethene > 1-Butene > Vinylacetylene > 1,3-Butadiene \qquad (21)$$

c) single bonds (middle):

$$Butadiyne > Vinylacetylene > 1,3-Butadiene > 1-Butyne > 1-Butene > n-Butane > Ethane > twisted\ Butane \qquad (22)$$

Furthermore the carbon-carbon single bond in s-trans-1,3-butadiene is stronger than in s-cis isomer. The above series indicate that conjugative πa→πb* or hyperconjugative πa→σb* donor-acceptor interactions lead to partial bond equalization strengthening adjacent single bond and weakening double and triple bonds, which is consistent with resonance picture and experiment. Although b_ε index (Tab.5) show no significant difference in strengths of double bonds of 1,3-butadiene isomers, the b_μ index (Tab.5) of s-cis isomer is higher then of s-trans. This behavior is consistent with natural resonance theory (NRT) bond orders trend for these molecules, which indicates 1.939 and 1.950 for double bonds in s-trans and s-cis species respectively [54]. Additionally associated conjugative stabilization (s-trans of -15.0 versus s-cis of -12.8 kcal/mol) [54], in these molecules correlates with single carbon-carbon bond strength indicated by b_ε bond order. The b_ε, b_μ (Tab.5) and NRT bond orders show good corelation also for allene molecule (with NRT bond order of C=C: 1.991) [54]. Greater bond orders of double bonds in allene then in

1,3-butadiene molecules does not indicate greater stability of the former molecule, which is the matter of reactivity dependent on many factors besides of electronic energy, and comes from interatomic contributions of all bonds in molecule, due to delocalized nature of electrons, as well as from atomic core regions. Table 6 shows sums of b_ε indices of 1,3-butadiene isomers, allene and propylene molecules. The "total" bond order is greater in more stable species. This is true for all bonds taken into account, likewise if only carbon-carbon bonds are summed, indicating the carbon chain as main source of stability.

The energy density and chemical potential derived bond orders are able to distinguish relative stability of different geometrical isomers or even conformers. For instance using bμ index one can tell which of butane conformers is more stable. The Δbμ for conformational change (Eq.23) is found to be -0.007, which implies that twisted butane molecule is less stable. The Δb_μ might be projected to enthalpy change (for reactions and processes with relatively small entropy contribution) thus interchange into "twisted" state is predicted to be slightly endothermic.

$$C_4H_{10\,"cis-like\ twisted"} \rightarrow C_4H_{10\,"normal"} \qquad \Delta b_\mu = -0.007 \qquad (23)$$

To estimate conjugation in diene and diyne we applied Kistiakowsky [55-58] method evaluating poliene stability by stepwise hydrogenation. The numbers over the arrows in reaction equations indicate a difference between b_μ bond orders of all bonds being broken (reactants) and bond orders of bonds being formed (products).

$$s-trans-1,3-Butadiene + H_2 \xrightarrow{-0.656} 1-Butene + H_2 \xrightarrow{-0.688} Butane \qquad (24)$$

$$1,3-Butadiyne + 2H_2 \xrightarrow{-1.182} 1-Butyne + 2H_2 \xrightarrow{-1.236} Butane \qquad (25)$$

According to the difference of Δb_μ of first and second hydrogenation step, the conjugation stabilization should be proportional to 0.032 and 0.054 (or -0.096 if corrected for atomic stabilization) for diene and diyne molecules respectively. As can be seen atomic stabilization accounts for strengthen of butadiyne bonding by 0.150. However interatomic regions by themselves point lack of conjugative stabilization or even destabilization in butadiyne.

These conclusions might be derived also from series, (Eq.20, 21 and 22) where stronger triple bonds of butadiyne than vinylacetylene or stronger double bonds of vinylacetylene than 1,3-butadiene indicate less partial bond equalization in former molecule and more in the latter, thus weaker and stronger conjugation, respectively. However the adjacent single C—C bonds are strengthen in contrasting manner suggesting stronger conjugation in butadiyne molecule, yet this

is misleading. The very presence of π bonds affects neighboring σ bonds by increasing their strengths. One may compare peripheral C—H bonds (and others) in the vincity of carbon-carbon σ and π bonds (Fig.8-10). Moreover the π bonds in 1,3-butadiene and vinylacetylene molecules are involved in hyperconjugative stabilization with C—H bonds around single C—C bond which is competitive to conjugation effects on the latter.

Similar reasoning can not follow from Mayer's bond order index, which yields unreasonable results of C4 hydrocarbons, like negative bond order of triple bond of vinylacetylene (Tab.5). Negative values are attributed to presence of diffuse functions [39], which in contrast have no noticeable adverse effect on b_ε and b_μ.

2.4. Orbital-wise contributions

The molecular orbitals involved in conjugation or hyperconjugation effects were recognized by orbital-wise analysis. Table 7 presents orbital-wise contributions to total bond orders of carbon-carbon bonds for selected C4 hydrocarbns. The greatest contribution to total bond order in s-trans-1,3-butadiene comes from 11th and 13th MOs for C=C and C–C bonds respectively. However the 5th and 14th MOs show significant contributions to all three carbon-carbon bonds and minor contribution to other bonds in molecule. These orbitals span all carbon atoms, thus associated electrons should have primary meaning for conjugation stabilization in s-trans-1,3-butadiene. In the s-cis isomer 10th and 13th MOs have the greatest impact on double and single bonds total bond orders, but the 5th and 14th are the ones that play the same role as in s-trans isomer. The vinylacetylene double, single and triple bonds have highest contributions from 10th, 7th and 6th MOs respectively. The 5th MO is the only one significantly contributing to all C to C bonds. The 12th MO could also be involved in conjugation effect. However its contribution to double bond is slightly below average which might mean not too favorable interaction between π orbitals (due to greater overlap of π* orbitals).

Conclusions

The current study is an extension to electronic stress tensor representation and analysis [8,14,15] of chemical interaction by means of Regional DFT. The stress tensors used to describe the internal forces of matter when applied to nano-scale systems, at quantum mechanical level,

can characterize effects related to internal distortion of electron density in molecules. The half of trace over eigenvalues of stress tensor gives local contribution to potential energy density of electrons. The very low negative stress regions associated with atomic cores may invoke significant perturbation in the bonding region at short interatomic distances. This atomic stabilization results from low lying valence MOs having strong likeness to atomic core levels. In contrast to similar analysis presented by other researchers [29], based on topological parameters, the RDFT defines dynamical point in chemical systems at stationary state. Internal quantum forces are the greater the steeper are the electron density changes in space. However at Lagrange point internal quantum forces disappear (for stationary state).This point, being an attractor for fluxes, is observed where density builds up and the interference pattern forms. The features of this stationary point of charge density in interatomic region make it a specific connector between two chemically bonded atoms.

Bond orders presented here refer to bond strength relative to bonds with order of one, and are expressed in terms of electronic energy density, thus have natural ability to fulfill this role. Moreover this new indices show the redistribution of energy over the molecule and its partition between particular bonds. The electrons, recognized as electron pairs by classically oriented bond orders, bind two atoms with different strength, depending on the electronic energy. A greater b_ε index, which is measure of this energy, is usually associated with higher electron density, thus (in correspondence with density or overlap based bond orders) stronger bond. The b_μ index reflects very well the electronegativities of bounded partners. The stress tensor rooted bond orders show very good correlation with bond lengths. Although stress tensor rooted indices are usually higher then corresponding NBO bond orders, it is found that b_ε bond order correlates with b_W while b_μ is related to b_{NAO}. The indices show small basis set dependence manifesting in differences between indices obtained in different basis sets, however the trends within particular basis set are preserved. These new measures allow for recognizing relative stabilities of geometrical isomers and even conformers. One can obtain reliable and informative description of interaction using molecular properties probed at Lagrange point.

The methods based on local kinetic energy density like AIM [29], ELF [59-62], LOL [63,64], analyze the electron density redistribution using $\nabla^2\rho(r)$. Despite it has proved to be important analytic tool, it is difficult to understand in simple physical terms (see Bader's explanation [29]). The other related methods (temperature of nighness [65], covariance methods

[66]) measure local correlation between electrons, thus local probability of electron pairing is given. The Pauling described chemical bond between two atoms as result of forces acting between them leading to formation of aggregate with sufficient stability [67]. The RQED studies the force exerted on electrons, as the intense variable coupled with energy, in terms of stress tensor. The methods [59-66] allow recognizing shell structures of atoms, and so is the RQED kinetic energy density, on very fundamental level, separating core from valence electron regions. The local temperature of nighness [65] is measure of kinetic energy and the stress tensor alike gives a measure of kinetic energy density with positive contribution from compressive stress and negative contribution of tensile stress, due to negative eigenvalues of metric tensor g^{ij}. Most of the mentioned methods need suitable reference system to define regions where electrons are especially localized. The stress tensor analysis provides such information explicitly from systems wavefunction, using tensile stress characterizing covalent interaction or Lagrange point - meta-stationary point of electron density, without relating to reference systems.

References

[1] I. Mayer, Chem. Phys. Lett 97, 270-274 (1983).

[2] I. Mayer, Int. J. Quantum. Chem. 23, 341-363 (1983).

[3] M. A. Natiello, J. A. Medrano, Chem. Phys. Lett. 105, 180-182 (1984).

[4] E. D. Glendening, F. J. Weinhold, Comp. Chem. 19, 610-627 (1998).

[5] I. Mayer, J. Comp. Chem. 28, 204-221 (2007).

[6] A. Sekiguchi, R. Kinjo, M. Ichinohe, Science 305, 1755-1757 (2004).

[7] M. Lein, A. Krapp, G. J. Frenking, Am. Chem. Soc. 127, 6290-6299 (2005).

[8] P. Szarek, A. Tachibana, J. Mol. Model. 13, 651-663 (2007).

[9] A. Tachibana, Theor. Chem. Acc. 102, 188–195 (1999).

[10] A. Tachibana, J. Chem. Phys. 115, 3497–3518 (2001).

[11] A. Tachibana, in Stress Induced Phenomena in Metallization, edited by S. P. Baker (American Institute of Physics, New York, 2002), p.205-211.

[12] A. Tachibana, in Reviews in modern quantum chemistry: a celebration of the contributions of Robert Parr, edited by K. D. Sen (World Scientific, Singapore, 2002), Vol 2, p.1327-1366.

[13] A. Tachibana, in Fundamental perspectives in quantum chemistry: a tribute to the memory of Per-Olov Löwdin, edited by E. Brändas, E. Kryachko (Kluwer, Dordrecht, 2003) Vol 2, p.211–239.

[14] A. Tachibana, Int. J. Quantum Chem. 100, 981–993 (2004).

[15] A. Tachibana, J. Mol. Model. 11, 301-311 (2005).

[16] W. A. Bingel, Z Naturforsch A 18A, 1249–1258 (1963).
[17] W. A. Bingel, Theor. Chim. Acta 8, 54–61 (1967).
[18] T. Kato, Commun. Pure. Appl. Math. 10, 151–171 (1957).
[19] R. T. Pack, W. B. Brown, J. Chem. Phys. 45, 556–559 (1966).
[20] A. Tachibana, Int. J. Quantum Chem. Quantum Chem. Symp. 21, 181–190 (1987).
[21] A. Tachibana, Int. J. Quantum Chem. 57, 423–428 (1996).
[22] A. Tachibana, R. G. Parr, Int. J. Quantum Chem. 41, 527–555 (1992).
[23] A. Tachibana, K. Nakamura, K. Sakata, T. Morisaki, Int. J. Quantum Chem. 74, 669–679 (1999).
[24] R.F.W. Bader and P.M. Beddall, J. Chem. Phys. 56, 3320- (1972)
[25] L. Cohen, J. Chem. Phys. 70, 788- (1979).
[26] L. Cohen, J. Chem. Phys. 80, 4277- (1984).
[27] S.K. Ghosh, M. Berkowitz, and R.G. Parr, Proc. Natl. Acad. Sci. 81, 8028- (1984).
[28] P.W. Ayers, R.G. Parr, and A. Nagy, Int. J. Quantum Chem. 90, 309- (2002)
[29] R. F. W. Bader, in Atoms in Molecules - A Quantum Theory (Oxford University Press, Oxford, 1990).
[30] R. F. W. Bader, J. Chem. Phys. 73, 2871 (1980).
[31] A. Holas and N. H. March, Phys. Rev. A 51, 2040 (1995).
[32] A. Nagy and N. H. March, Mol. Phys. 91, 597 (1997).
[33] L. J. Bartolotti and R. G. Parr, J. Chem. Phys. 72, 1593 (1980).
[34] S. K. Ghosh and M. Berkowitz, J. Chem. Phys. 83, 2976 (1985).
[35] A. Tachibana, J. Math. Chem. 7, 95–110 (1991).
[36] M. J. Frisch, G.W. Trucks, H.B. Schlegel, G.E. Scuseria, M.A. Robb, J.R. Cheeseman, J.A. Montgomery, JrT. Vreven, K.N. Kudin, J.C. Burant, J.M. Millam, S.S. Iyengar, J. Tomasi, V. Barone, B. Mennucci, M. Cossi, G. Scalmani, N. Rega, G.A. Petersson, H. Nakatsuji, M. Hada, M. Ehara, K. Toyota, R. Fukuda, J. Hasegawa, M. Ishida, T. Nakajima, Y. Honda, O. Kitao, H. Nakai, M. Klene, X. Li, J.E. Knox, H.P. Hratchian, J.B. Cross, V. Bakken, C. Adamo, J. Jaramillo, R. Gomperts, R.E. Stratmann, O. Yazyev, A.J. Austin, R. Cammi, C. Pomelli, J.W. Ochterski, P.Y. Ayala, K. Morokuma, G.A. Voth, P. Salvador, J.J. Dannenberg, V.G. Zakrzewski, S. Dapprich, A.D. Daniels, M.C. Strain, O. Farkas, D.K. Malick, A.D. Rabuck, K. Raghavachari, J.B. Foresman, J.V. Ortiz, Q. Cui, A.G. Baboul, S. Clifford, J. Cioslowski, B.B. Stefanov, G. Liu, A. Liashenko, P. Piskorz, I. Komaromi, R.L. Martin, D.J. Fox, T. Keith, M.A. Al-Laham, C.Y. Peng, A. Nanayakkara, M. Challacombe, P.M.W. Gill, B. Johnson, W. Chen, M.W. Wong, C. Gonzalez, J.A. Pople, (2003) Gaussian 03, Revision C.02, Gaussian, Inc., Wallingford CT.
[37] K. Doi, P. Szarek, K. Nakamura, M. Senami, A. Tachibana, Molecular Regional DFT program package Ver. 2 (Tachbana Lab., Kyoto University) Kyoto, 2007.
[38] I. Mayer, A. Hamza, Program "APOST", Ver. 1.07 (Chemical Research Center, Hungarian Academy of Sciences), Budapest, 2000-2004.
[39] I. Mayer, Program "BORDER", Version 1.0 (Chemical Research Center, Hungarian Academy of Sciences), Budapest, 2005.
[40] R.F.W.Bader, Chem. Eur. J. 12, 2896-2901 (2006)
[41] R.G. Parr, R.A. Donnelly, M. Levy, and W.E. Palke, J. Chem. Phys. 68, 3801- (1978).

[42] I. Mayer, Chem. Phys. Lett. 97, 270-274 (1983), ibid. 117, 396 (1985).
[43] K. B. Wiberg, Tetrahedron 24, 1083-1096 (1968).
[44] F. Weinhold, J. E. Carpenter, J. Mol. Struct. Theochem. 165, 189-202 (1980).
[45] A. E. Reed, P. v. R. Schleyer, Inorg. Chem. 27, 3969-3987 (1988); J. Am. Chem. Soc. 112, 1434-1445 (1990).
[46] Jr., T. H. Dunning; P. J. Hay, in Modern Theoretical Chemistry, edited by H. F. Schaefer III (Plenum, New York, 1976) Vol. 3, p.1-28.
[47] D. E. Woon, Jr. T. H. Dunning, J. Chem. Phys. 98, 1358-1371 (1993).
[48] R. A. Kendall, Jr., T. H. Dunning, R. J. Harrison, J. Chem. Phys. 96, 6796-6806 (1992).
[49] J. Baker, Theor. Chim. Acta 68, 221-229 (1985).
[50] L. Pauling, J. Am. Chem. Soc. 54, 3570-3582 (1932).
[51] A. L. Allred, J. Inorg. Nucl. Chem. 17, 215-221 (1961).
[52] R. P. Iczkowski, , J. L. Margrave, J. Am. Chem. Soc. 83, 3547-3551 (1961).
[53] R. G. Parr, R. A. Donnelly, M. Levy, W. E. Palke, J. Chem. Phys. 68, 3801-3807 (1978).
[54] F. Wienhold, C. Landis, in Valency and Bonding (Cambridge Univ. Press, 2005)
[55] G. B.Kistiakowsky, J. R. Ruhoff, H. A. Smith, W. E. Vaughan, J. Am. Chem. Soc. 58, 146-153 (1936).
[56] J. B. Conant, G. B. Kistiakowsky, Chem. Rev. 20, 181-194 (1937).
[57] J. B. Conn, G. B. Kistiakowsky, E. A. Smith, J. Am. Chem. Soc. 61, 1868-1876 (1939).
[58] W. Fang, D. W. Rogers, J. Org. Chem. 57, 2294-2297 (1992).
[59] A.D. Becke and K.E. Edgecombe, J. Chem. Phys. 92, 5397- (1990).
[60] M. Kohout, Int. J. Quant. Chem. 97, 651- (2004).
[61] A. Savin, A.D. Becke, J.Flad,R.Nesper,H. Preuss and H.G. Vonschnering, Angew. Chem, 30, 409- (1991).
[62] A. Savin, R, Nesper, S. Wengert and T.F. Fassler, Angev. Chem. 36, 1809- (1997).
[63] H.L. Schmider and A.D. Becke, J. Mol. Struc. Theochem, 527,51- (2000)
[64] H.L. Schmider and A.D. Becke, J. Chem. Phys., 116, 3184- (2002)
[65] P.W. Ayers, R.G. Parr and A. Nagy, Int. J. Quantum Chem. 90,309 (2002)
[66] P.W. Ayers, J. Chem. Sci. 117, 441- (2005)
[67] L. Pauling, The Nature of the Chemical Bond. Cornell University Press, Ithaca (1948)

Table 1. Largest eigenvalue of stress at Lagrange point for single, double and triple bonds in a group of hydrocarbons.

	Single	Double	Triple
Ethane	0.060		—
Ethene	—	0.034	—
Ethyne	—	—	-0.034
Propane	0.060	—	—
Propene	0.061	0.034	—
Propyne	0.059	—	-0.033
s-cis-Butadiene	0.060	0.035	—
s-trans-Butadiene	0.059	0.035	—
Vinylacetylene	0.058	0.035	-0.032
1-Buten	0.060	0.034	—
	0.061	—	—
1-Butyn	0.060	—	-0.032
	0.059	—	—
n-Butan	0.060	—	—
Butadiyn	0.054	—	-0.033

Table 2. The bond order versus bond length correlation coefficients of single, double, triple (of C_2H_nA, where n=1,3,5 and A are different functional groups) and aromatic (of phenyl group of $C_8H_{n=6,8,10}$) C to C bonds. Aberrations: b_ε, b_μ, b_{NAO}, b_{NLMO}, b_M, b_W – energy density, chemical potential, atom-atom overlap weighted NAO, natural localized orbital, Mayer's bond orders and Wiberg's index respectively.

	b_ε	b_μ	b_W	b_{NAO}	b_{NLMO}	b_M
C–C	-0.9884	-0.9931	-0.0099	-0.6456	-0.2049	-0.6352
C=C	-0.9870	-0.9916	-0.0067	-0.4478	0.0673	-0.4172
C≡C	-0.9103	-0.9699	-0.1342	-0.1040	0.1443	-0.0238
C⁻⁻C	-0.9913	-0.9881	-0.9660	-0.8653	-0.1635	-0.0608
In general*	-0.9821	-0.9823	-0.9738	-0.9820	-0.8702	-0.6569

Table 3. Stress tensor originated, NBO and Mayer's bond orders of different bonds in C_2H_5R molecules. The "av" subscript means arithmetical average over corresponding bonds of phenyl group. The number in superscript means successive hydrogen atom attached to particular heavy atom. The b_ε, b_μ, b_{NAO}, b_{NLMO}, b_M, b_W are energy density, chemical potential, atom-atom overlap weighted NAO, natural localized molecular orbital NLMO, Mayer's bond orders and Wiberg's index respectively.

Bond		b_ε	b_μ	b_W	b_{NAO}	b_{NLMO}	b_M
As–H1		0.595	0.944	0.973	0.734	0.883	0.987
As–H2		0.597	0.944	0.975	0.734	1.732	1.003
C–As		0.442	0.805	0.930	0.744	0.092	1.075
C–Br		0.457	0.818	0.993	0.721	-1.124	0.846
C–C	(H_3C-CH_3)	0.964	1.020	1.039	0.873	-0.712	0.815
C–C (av)	(-C_6H_5)	1.612	1.326	1.426	1.165	0.488	1.555
C–Cl		0.636	0.922	0.992	0.729	-1.091	0.903
C–F		1.711	1.523	0.809	0.644	0.602	0.939
C–Ge		0.457	0.853	0.846	0.749	0.231	1.018
C–H	C_2H_6	1.180	1.106	0.958	0.809	-0.029	0.994
C–H (av)	(-C_6H_5)	1.220	1.107	0.937	0.809	0.686	0.900
C≡N	(-CN)	4.879	2.378	2.918	1.985	0.736	2.689
C–N	(C_2H_5-NH_2)	1.316	1.192	1.002	0.841	0.460	0.943
C–N	(C_2H_5-NO_2)	1.216	1.142	0.870	0.739	-0.341	0.673
C=O	(-CHO)	4.075	2.099	1.847	1.355	1.856	2.015
C=O	(-COOH)	4.115	2.102	1.729	1.378	0.424	1.979
C–O	(C_2H_5-OH)	1.670	1.393	0.916	0.763	0.436	0.969
C–O	(-COOH)	2.297	1.594	1.001	0.906	0.832	1.146
C–P		0.566	0.850	0.948	0.769	0.324	0.521
C–S		0.603	0.873	1.010	0.782	-1.075	0.555
C–Se		0.449	0.802	0.992	0.750	0.133	1.001
C–Si		0.520	0.847	0.820	0.773	0.259	0.839
Ge–H1		0.536	0.950	0.936	0.769	0.778	0.952

Table 3. Continued.

Bond		b_ε	b_μ	b_W	b_{NAO}	b_{NLMO}	b_M
Ge–H2		0.536	0.950	0.936	0.769	-0.511	0.952
Ge–H3		0.537	0.950	0.939	0.769	1.616	0.961
N–H	(-NH_2)	1.843	1.346	0.876	0.755	0.557	0.972
N–O1	(-NO_2)	4.516	2.107	1.543	1.176	0.822	1.783
N–O2	(-NO_2)	4.533	2.109	1.556	1.179	-1.002	1.875
O–H	(-OH)	2.706	1.631	0.784	0.698	1.501	0.931
O–H	(-COOH)	2.628	1.601	0.748	0.660	1.368	0.899
P–H1		0.712	0.953	0.977	0.740	0.810	0.986
P–H2		0.714	0.954	0.979	0.741	1.744	0.947
Se–H		0.699	0.985	0.989	0.736	1.593	0.970
S–H		0.895	1.034	0.982	0.753	0.367	0.941
Si–H1		0.564	0.898	0.927	0.768	0.724	0.960
Si–H2		0.564	0.898	0.927	0.768	-0.488	0.960
Si–H3		0.565	0.899	0.930	0.770	1.653	0.958

Table 4. Comparison of bond orders variation in STO-3G, 6-31G $^{\#}$ and 6-311G $^{\#}$ basis sets ($^{\#}$ with diffuse and polarization functions added or removed):

	Average			Maximum Difference		
	b_M	b_ε	b_μ	b_M	b_ε	b_μ
C≡C	3.843	4.358	2.785	1.544	1.422	0.708
C=C	2.181	2.662	1.998	0.299	0.926	0.566
C–C	0.933	1.229	1.330	0.310	0.423	0.432

Table 5. The stress tensor rooted bond orders b_ε, b_μ and Mayer's bond order b_M of C—C bonds of C_2H_m and C_4H_n species (m = 2, 4,6 and n = 2,4,6,8,10).

Molecule	b_ε			b_μ			b_M		
	C1-C2	C2-C3	C3-C4	C1-C2	C2-C3	C3-C4	C1-C2	C2-C3	C3-C4
CH_3–CH_3	0.962	—	—	1.020	—	—	0.815	—	—
CH_2=CH_2	2.066	—	—	1.530	—	—	1.968	—	—
HC≡CH	3.362	—	—	2.110	—	—	3.798	—	—
CH_2=C=CH_2	2.203	2.203	—	1.608	1.608	—	1.805	1.805	—
CH_3–CH_2–CH_2–CH_3	0.965	0.967	0.965	1.018	1.016	1.018	0.714	0.892	0.714
CH_3–CH_2–CH=CH_2	0.971	1.015	2.065	1.020	1.035	1.530	0.739	0.716	1.854
CH_3–CH_2–C≡CH	0.953	1.127	3.321	1.013	1.101	2.105	0.718	1.396	-1.168
CH_2=CH–CH=CH_2 (s-cis)	2.036	1.129	2.036	1.517	1.089	1.517	2.000	1.104	2.000
CH_2=CH–CH=CH_2 (s-trans)	2.036	1.188	2.036	1.515	1.116	1.515	1.744	1.148	1.744
CH_2=CH–C≡CH	2.044	1.254	3.311	1.520	1.156	2.098	1.493	1.627	-1.644
HC≡C–C≡CH	3.317	1.456	3.317	2.099	1.255	2.100	2.837	1.526	2.837

Table 6. The total b_ε bond order of hydrocarbon isomers.

Molecule	$\sum b_\varepsilon$ (all bonds)	$\sum b_\varepsilon$ (C-C bonds)
s-cis-1,3-butadiene	12.490	5.201
s-trans-1,3-butadiene	12.515	5.260
allene	9.188	4.407
propyne	9.283	4.462

Table 7. Orbital-wise contributions to b_ε bond order.

MO	s-cis-1,3-butadien			s-trans-1,3-butadien			vinylacetylene		
	C=C	C-C	C=C	C=C	C-C	C=C	C=C	C-C	C≡C
1st	0.000	-0.002	0.000	0.000	-0.003	0.000	0.001	0.001	0.000
2nd	0.000	0.003	0.000	0.000	0.004	0.000	0.003	0.000	0.000
3rd	0.002	0.000	0.002	0.002	0.000	0.002	0.000	0.001	-0.009
4th	0.002	0.000	0.002	0.002	0.000	0.002	0.000	0.000	0.023
5th	0.232	0.130	0.232	0.223	0.147	0.223	0.347	0.170	0.252
6th	0.335	0.003	0.335	0.342	0.009	0.342	0.209	0.003	1.074
7th	0.032	0.219	0.032	0.027	0.236	0.027	0.030	0.335	0.140
8th	0.080	0.005	0.080	0.043	0.026	0.043	0.060	0.040	0.227
9th	0.093	0.139	0.093	0.323	0.050	0.323	0.110	0.217	0.415
10th	0.452	0.139	0.452	0.127	0.165	0.127	0.880	0.157	0.110
11th	0.235	0.001	0.235	0.551	0.075	0.551	0.014	0.187	0.076
12th	0.221	0.004	0.221	0.069	0.020	0.069	0.135	0.117	0.245
13th	0.030	0.386	0.030	0.003	0.352	0.003	0.060	0.025	0.499
14th	0.147	0.102	0.147	0.146	0.108	0.146	0.194	0.001	0.259
15th	0.178	0.000	0.178	0.177	0.000	0.177	—	—	—
∑	2.036	1.129	2.036	2.036	1.188	2.036	2.044	1.254	3.311
Average	0.136	0.075	0.136	0.136	0.079	0.136	0.146	0.090	0.236

Figure 1. Tension density [Hatree/bohr^3]. The origin corresponds to Lagrange point position in H_2 molecule; distance in [Å]:

a) tension density in H_2 molecule and in H atom along interatomic axis (z-axis), and for perpendicular directions (y-axis) going through Lagrange point ($r_{Lagrange}$) and through points at R1 and R2 outside interatomic region of H_2 at distance of half of the H—H bond length (y-axis*),

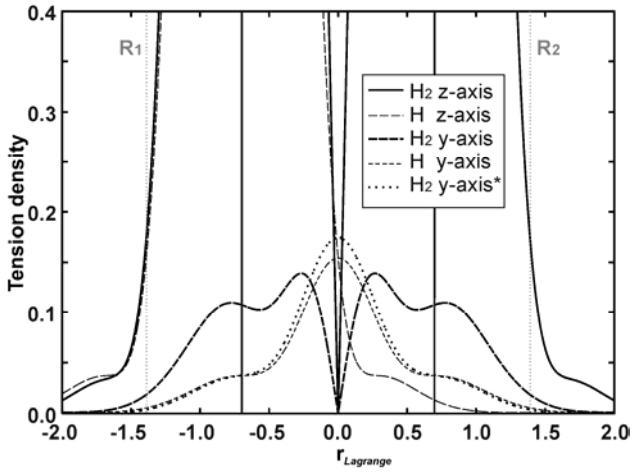

b) tension density in H_2 molecule, the cross-section plane through hydrogen atoms.

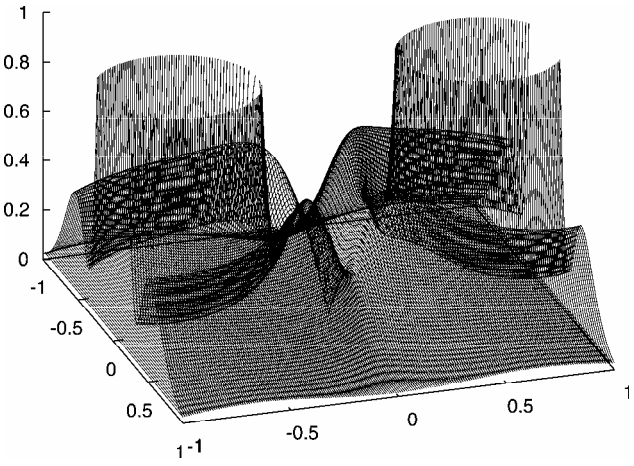

Figure 2. The eigenvalues of stress:

a) change of eigenvalues of stress with bond order,

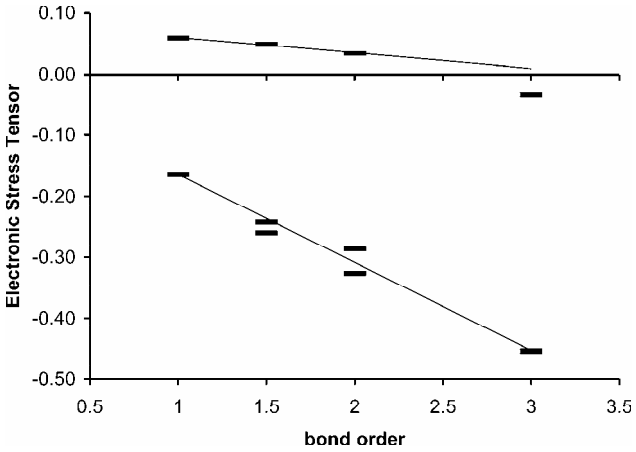

b) Largest eigenvalue of stress for two valence molecular orbitals.

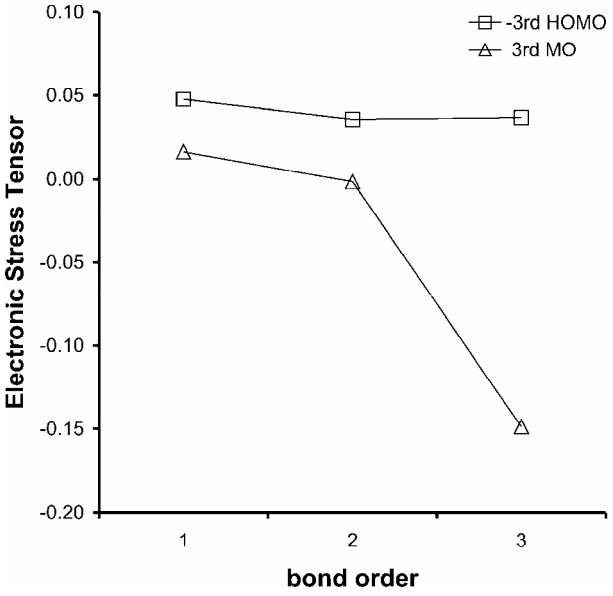

Figure 3. The valence electrons molecular orbitals of ethane (A1-E1), ethane (A2-E2) and ethyne (A3-E3). The "A" is the 3rd MO (first valence MO) and "E" is HOMO. The "A" and "C" MOs give 70-80% of total stress of carbon-carbon bond Lagrange point. The E3 and D3 MOs have the same symmetry and are perpendicular to each other.

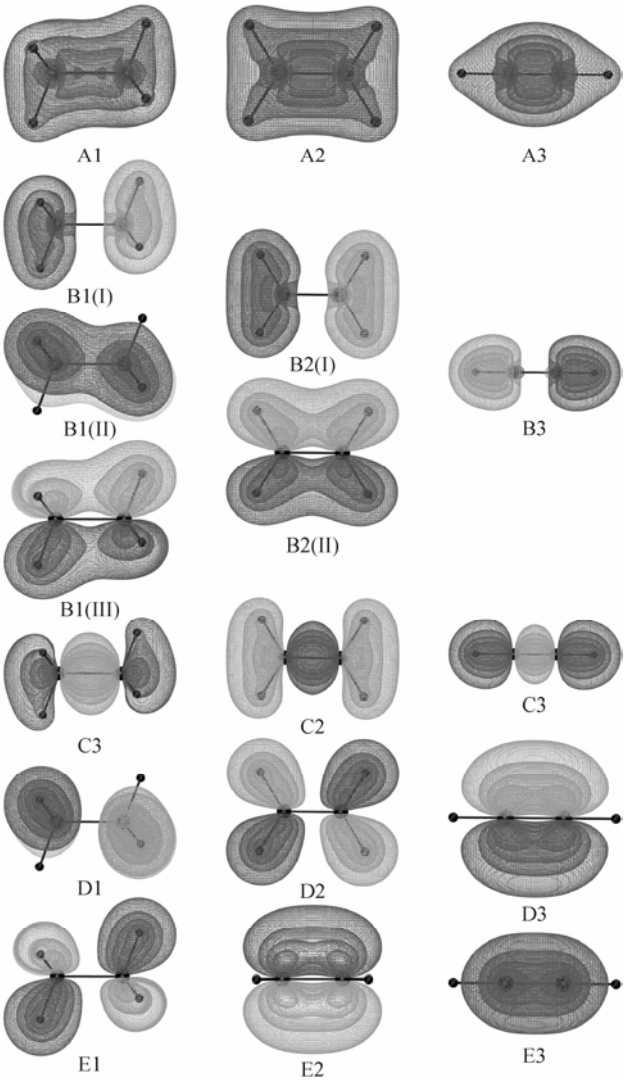

Figure 4. The correlation of carbon-carbon bond order indices with bond length for group of organic compounds (C_2H_nA - with different functional groups). The stress rooted bond orders bε and bμ are blue and pink dots, NBO bond orders: Wiberg's indexes (yellow dot), atom-atom overlap NAO bond order (blue ring) and NLMO bond orders (brown ring), and Mayer's bond order is represented by green rings.

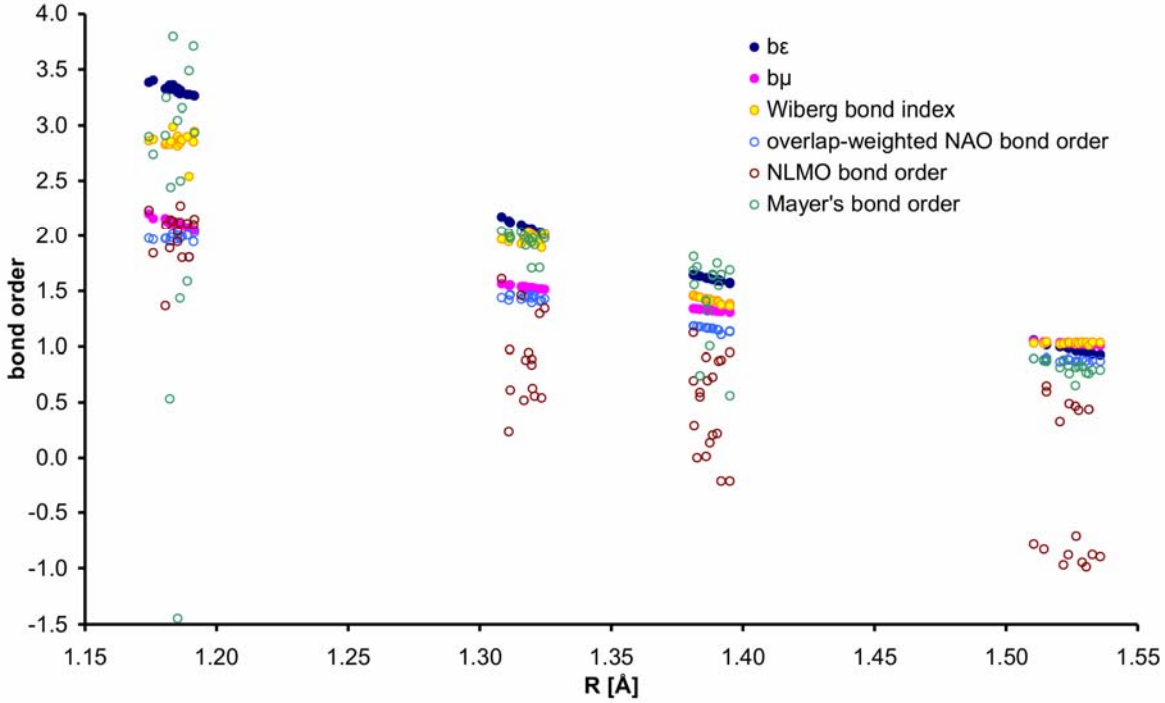

Figure 5. Basis set dependence of b_ε and b_μ bond orders of the O—H bonds for two water molecules connected by hydrogen bond.

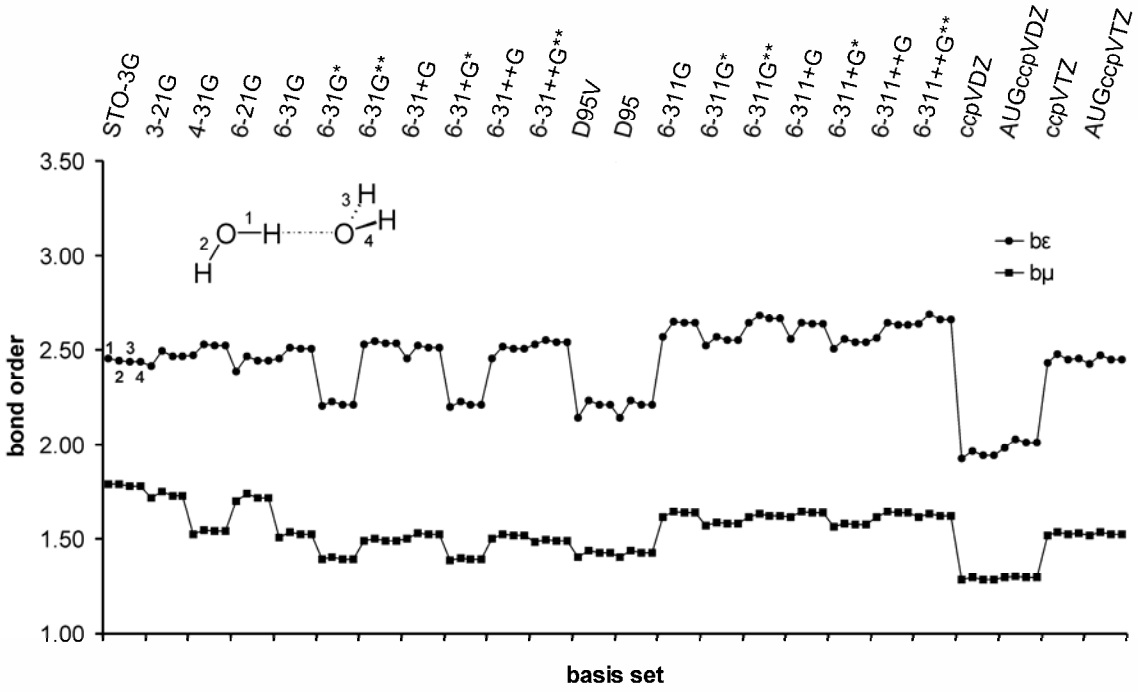

Figure 6. Basis set dependence of b_ε, b_μ and Mayer's bond orders, the C to C bonds of $C_2H_{n=2,4,6}$.

a) single bond

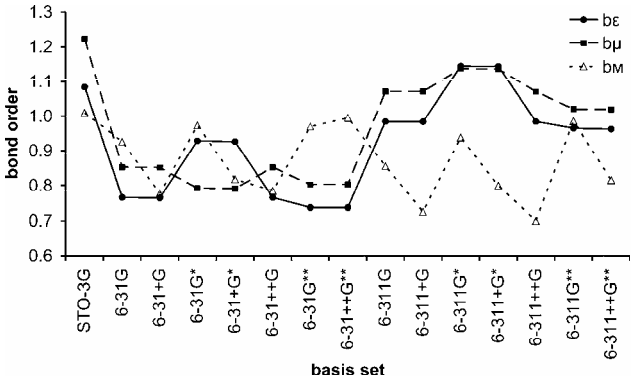

b) double bond

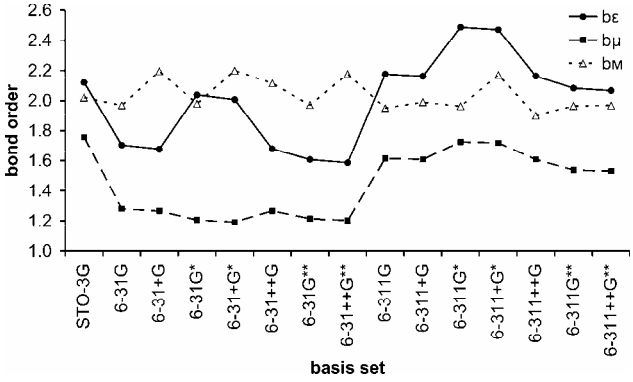

c) triple bond.

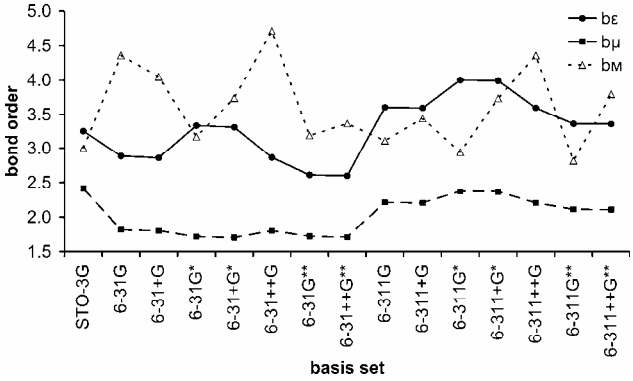

Figure 7. The periodic trends of bond orders for C—A bonds in $C_2H_nAH_m$ (where n=1,3,5, and A is chosen from: C to F, Si to Cl, Ge to Br atoms, with m=3,2,1,0 respectively).

a) ethane substitutions,

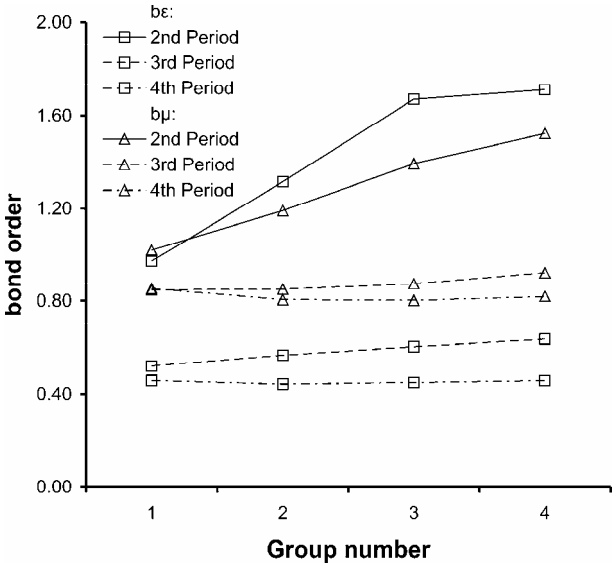

b) ethene substitutions,

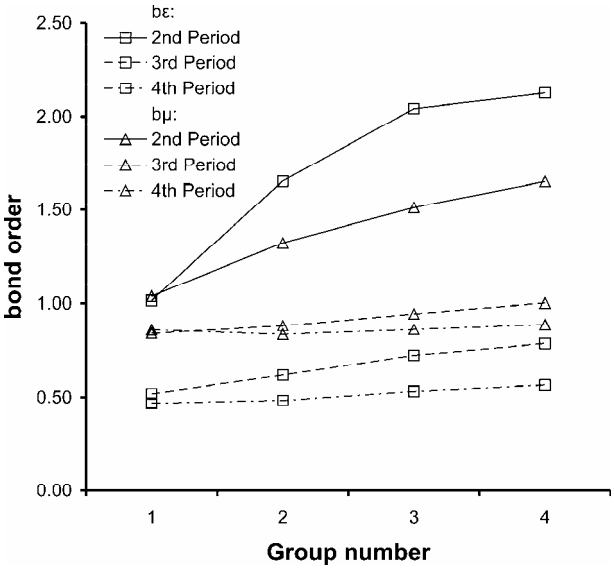

c) ethyne substitutions.

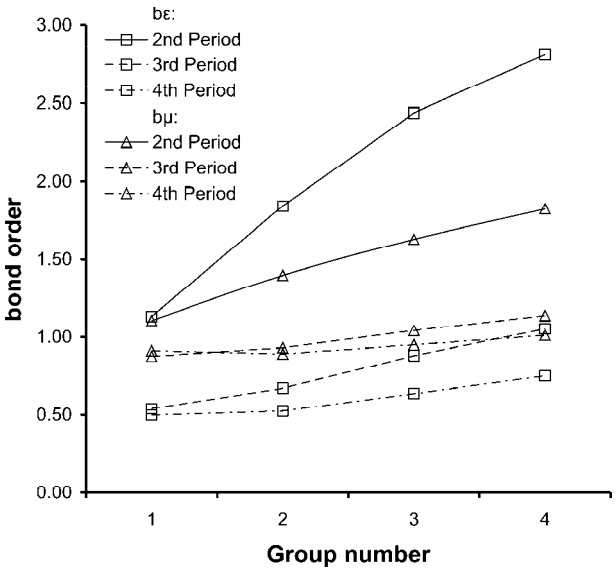

Figure 8. The electronic stress tensor rooted bond orders of bonds in C_2H_5A molecules (A is H, CH_3, CHO, COOH, CN, C_6H_5, SiH_3, GeH_3, NH_2, NO_2, PH_2, AsH_2, OH, SH, SeH, F, Cl, Br).

a) energy density based bond order b_ε, Wiberg index in parenthesis,

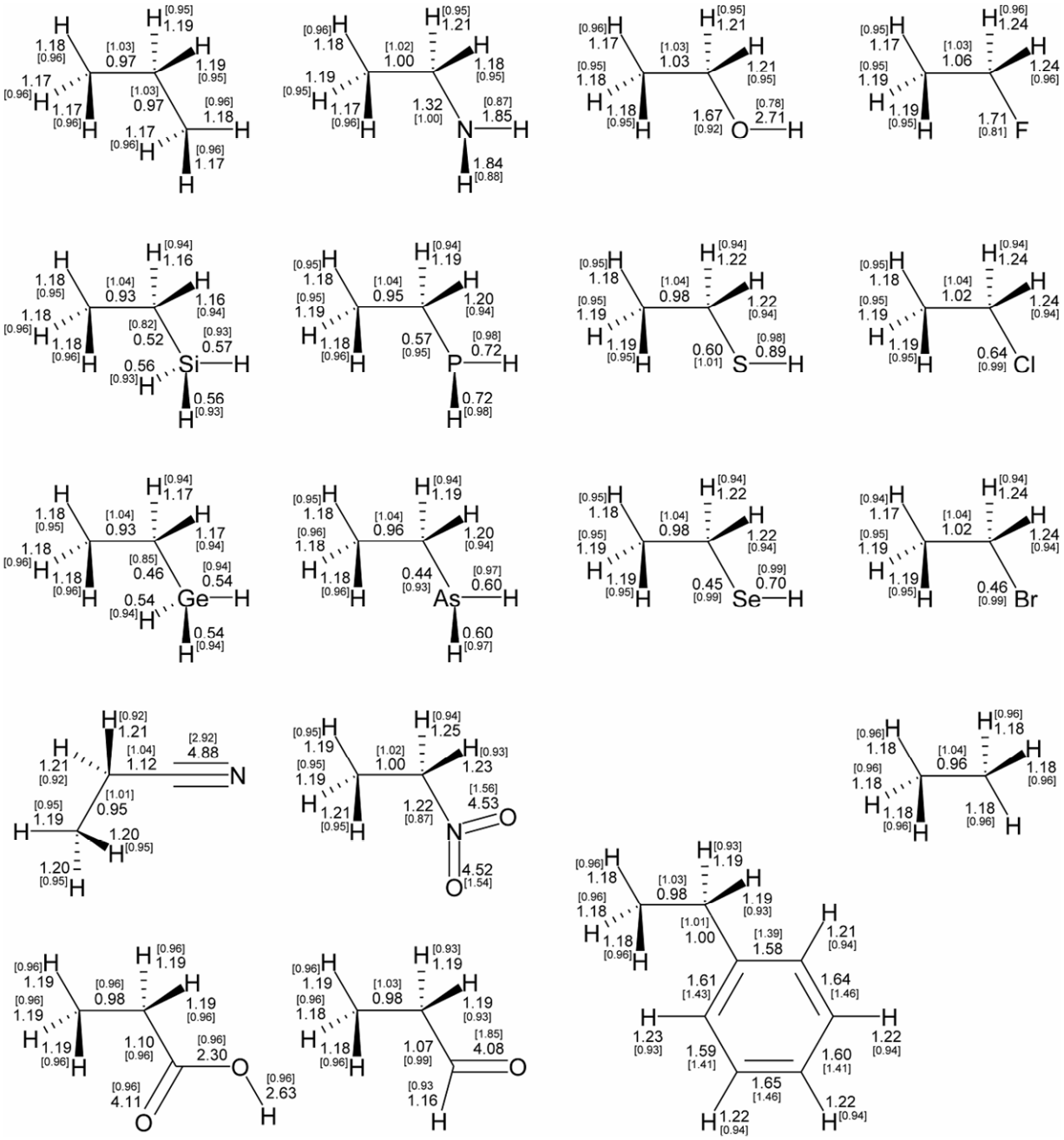

b) electronic chemical potential based bond order b_μ, overlap-weighted NAO bond order in parenthesis.

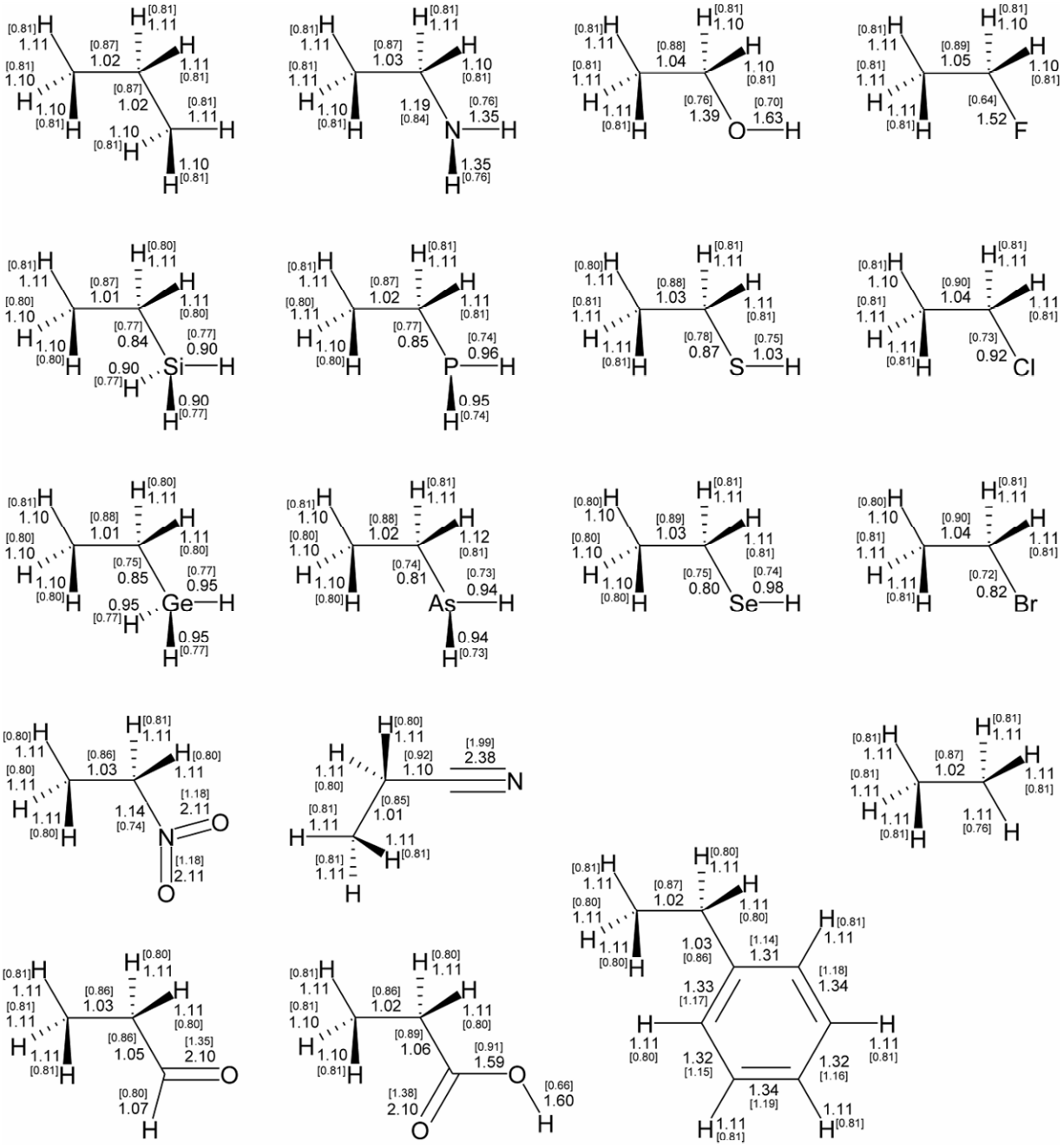

Figure 9. The electronic stress tensor rooted bond orders of bonds in C_2H_3A molecules (A is H, CH_3, CHO, COOH, CN, C_6H_5, SiH_3, GeH_3, NH_2, NO_2, PH_2, AsH_2, OH, SH, SeH, F, Cl, Br).

a) energy density based bond order b_ε, Wiberg index in parenthesis,

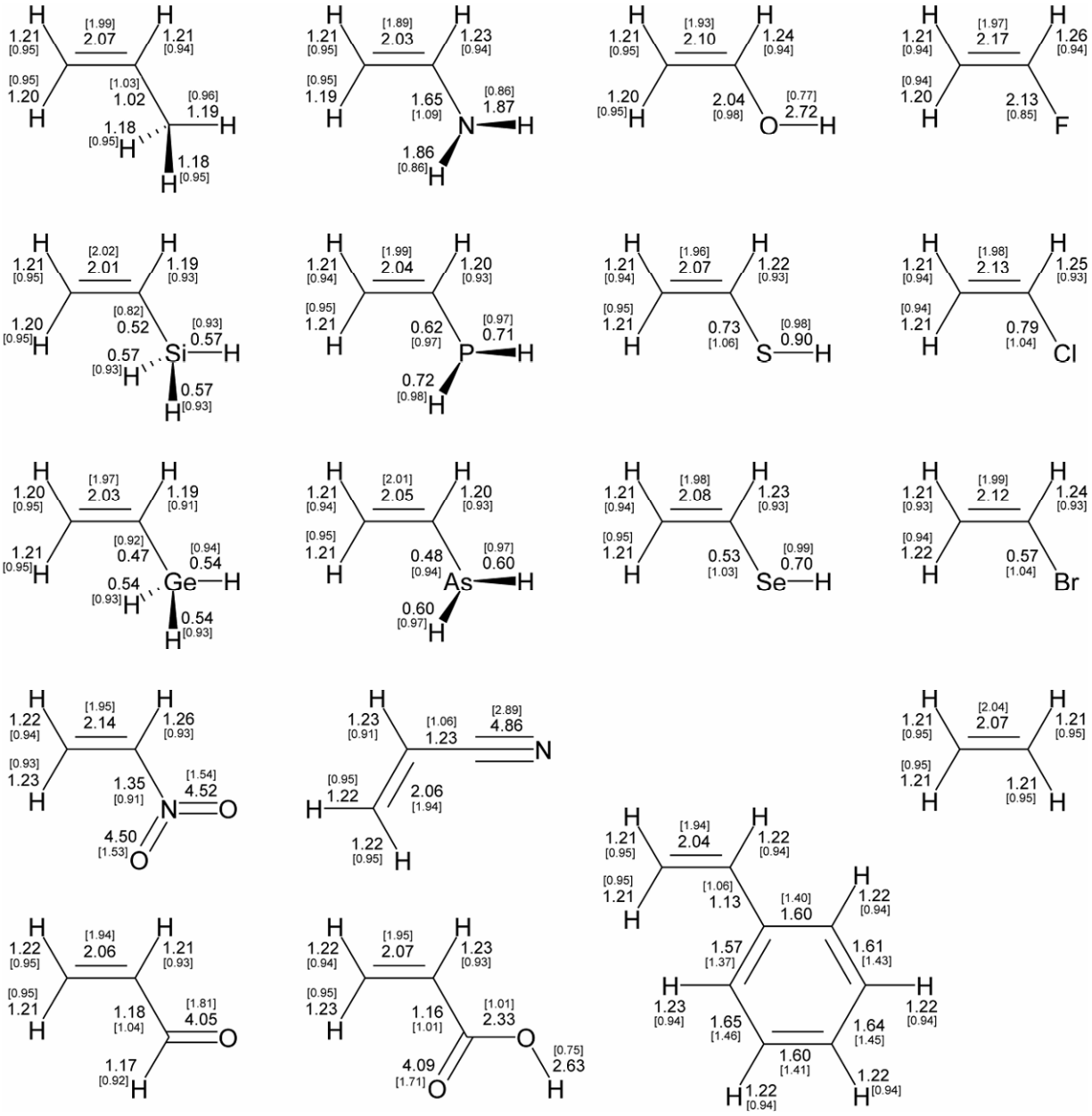

b) electronic chemical potential based bond order b_μ, overlap-weighted NAO bond order in parenthesis.

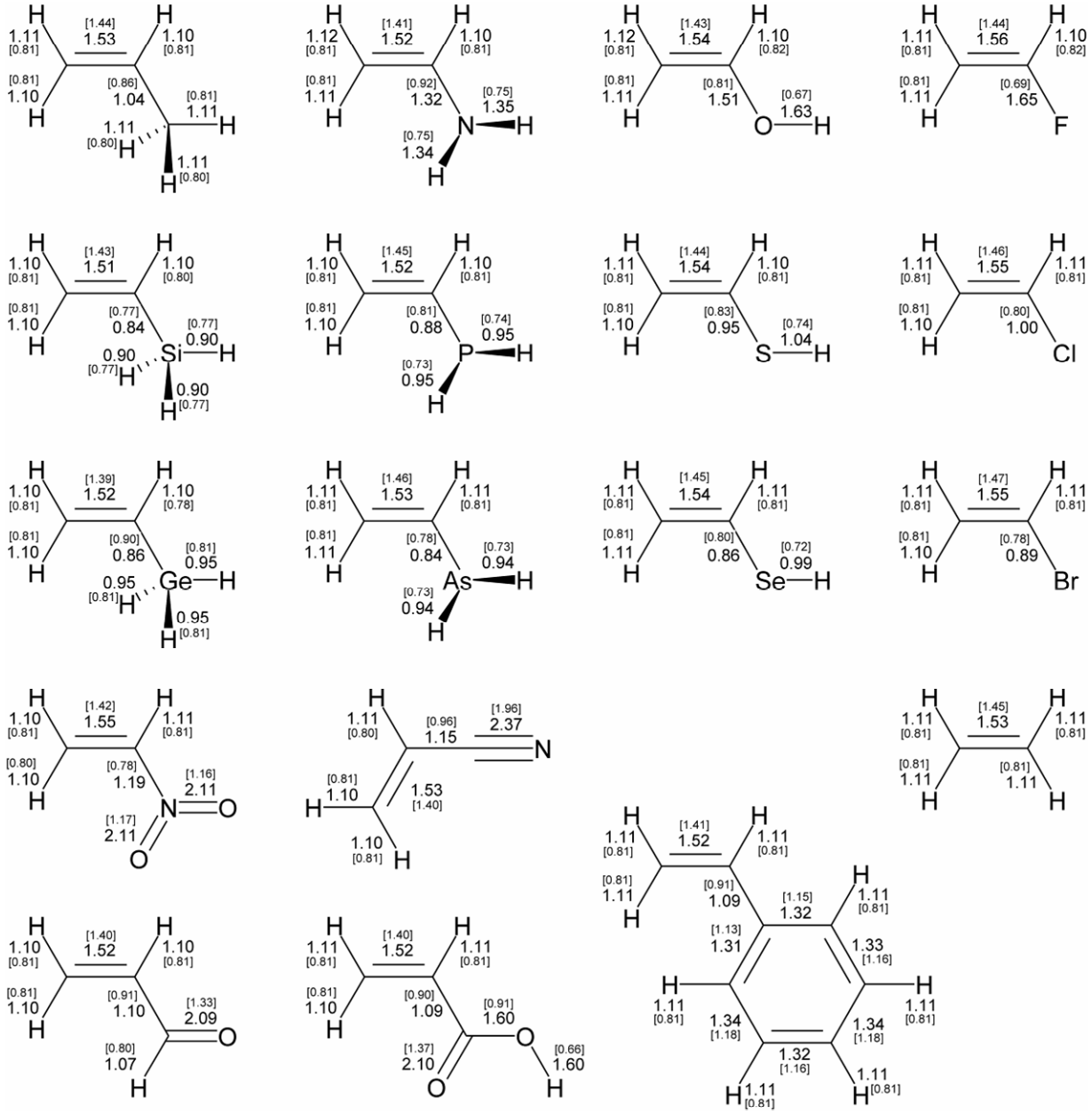

Figure 10. The electronic stress tensor rooted bond orders of bonds in C_2HA molecules (A is H, CH_3, CHO, COOH, CN, C_6H_5, SiH_3, GeH_3, NH_2, NO_2, PH_2, AsH_2, OH, SH, SeH, F, Cl, Br).

a) energy density based bond order b_ε, Wiberg index in parenthesis,

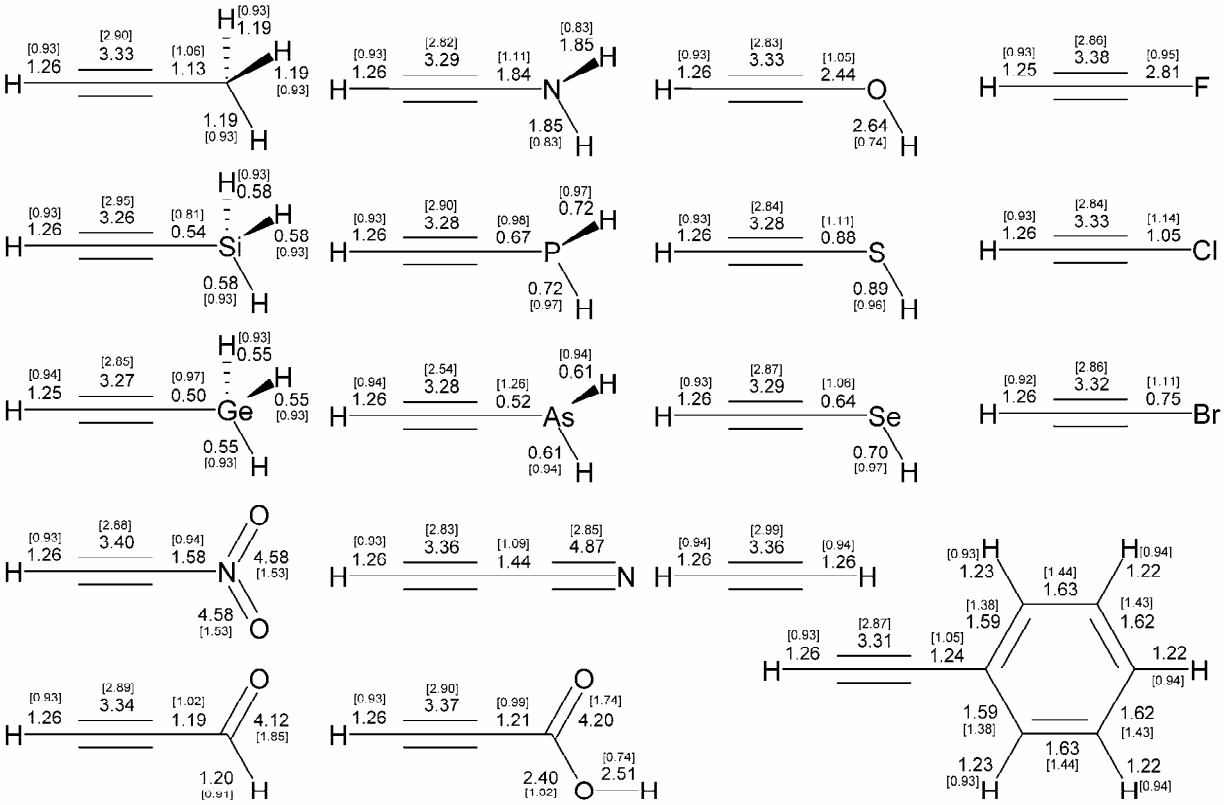

b) electronic chemical potential based bond order b_μ, overlap-weighted NAO bond order in parenthesis.

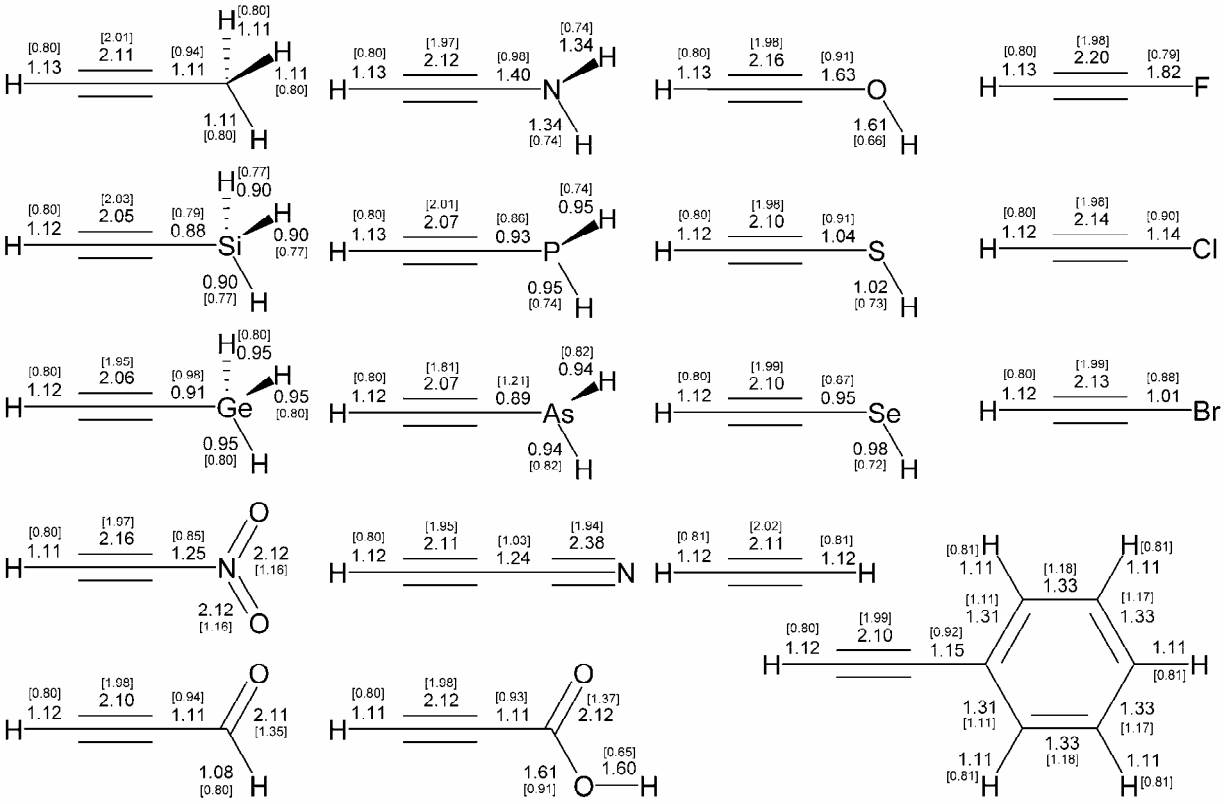

CHAPTER 4

On reversible bonding of H2 molecules on Pt-clusters.

Introduction

The hydrogen is expected to substitute the fossil fuel and to be cost-effective, renewable, and clean alternative energy source. Yet the mass production and storage of hydrogen turn out to be essential problem. The technical targets of these tasks were specified by the U.S. Department of Energy (DOE) [1]. Thus far utilized methods and materials can not sufficiently fulfill the expectations [1-4]. The classes of new materials are studied [4-10] however their properties, although promising, are still not in the target zone. The characterization of nature and strength of hydrogen interaction with promising materials is fundamental for successful development of satisfactory novel applicable technologies.

Among variety of tested materials metal clusters attract particular attention. The hydrides are long known as one of the stabilizing ligands of metal clusters. Some features of these “macro atoms”, like: high surface area to volume ratio, their electronic structures, high density of edges, corners and other reactive centers, leading to the greatly improved catalytic activity and aggressive chemical reactivity, makes them potentially important in hydrogen economy.

The simple way of understanding the properties of solid matter, especially concerning the irregularities of structure, is to study the clusters containing increasing number of atoms. These nano-dimensional materials are intermediate state between molecules and a bulk solid and they may share properties of both resulting in very peculiar physical and chemical properties compared to macro-scale. The dominant role is played by effects related to the quantization of energy for the electrons in solids with great reductions in particle size.

The properties of transition metals, particularly platinum possessing high resistance to chemical attack, excellent high-temperature characteristics, and stable electrical properties makes it desirable in industrial applications. Moreover the platinum is important catalyst in hydrogenation and dehydrogenation reactions. However its application in fuel cell implies additional restrictions regarding the amount of platinum required (and thus cost). Even though the study of Pt-materials is important, providing understanding of hydrogen chemistry, thus will contribute to development of cheaper, yet effective materials.

Theory

The energy density at macroscopic level can be used to express energy stored in capacitor (for electric field) or energy stored in inductor (for magnetic fields). The field energy (energy density) in chemical systems at atomic or molecular level is related to electromagnetic waves. The electromagnetic waves are associated with both the electric and magnetic fields that play a role in the transport of energy. The corresponding energy density, of the electromagnetic field, might be obtained within Regional DFT (RDFT) method [11-17] as the invariance of electronic stress tensor due to non-relativistic limit of RQED energy density [12,15].

The electronic stress tensor (Eq.1, k,l=1,2,3) [12,16] that reflects internal distortion of electron density and the intensity of total internal forces within a molecule (which results in relevant flow of electric charge through particular region), in local picture allows to study the chemical reactivity [15,18]. The electronic stress tensor, as second rank tensor is given by 3x3 matrix (Eq.1).

$$\left\langle \hat{\vec{\tau}}_{\alpha}^{S}(\vec{r}) \right\rangle = \begin{bmatrix} \tau_{\alpha xx}^{S}(\vec{r}) & \tau_{\alpha xy}^{S}(\vec{r}) & \tau_{\alpha xz}^{S}(\vec{r}) \\ \tau_{\alpha yx}^{S}(\vec{r}) & \tau_{\alpha yy}^{S}(\vec{r}) & \tau_{\alpha yz}^{S}(\vec{r}) \\ \tau_{\alpha zx}^{S}(\vec{r}) & \tau_{\alpha zy}^{S}(\vec{r}) & \tau_{\alpha zz}^{S}(\vec{r}) \end{bmatrix} \xrightarrow{diag} \begin{bmatrix} \tau_{\alpha}^{S11}(\vec{r}) & 0 & 0 \\ 0 & \tau_{\alpha}^{S22}(\vec{r}) & 0 \\ 0 & 0 & \tau_{\alpha}^{S33}(\vec{r}) \end{bmatrix} \tag{1}$$

$$\tau_{\alpha}^{S11}(\vec{r}) \le \tau_{\alpha}^{S22}(\vec{r}) \le \tau_{\alpha}^{S33}(\vec{r}) \tag{2}$$

with matrix elements:

$$\tau^{Skl}(r) = \frac{\hbar^2}{4m} \sum_{i}^{occ} \nu_i \left[\psi_i^*(\vec{r}) \frac{\partial^2 \psi_i(\vec{r})}{\partial x^k \partial x^l} - \frac{\partial \psi_i^*(\vec{r})}{\partial x^k} \frac{\partial \psi_i(\vec{r})}{\partial x^l} + \frac{\partial^2 \psi_i^*(\vec{r})}{\partial x^k \partial x^l} \psi_i(\vec{r}) - \frac{\partial \psi_i^*(\vec{r})}{\partial x^l} \frac{\partial \psi_i(\vec{r})}{\partial x^k} \right] \tag{3}$$

The principal stresses characterize compressive (negative) and tensile (positive) tendencies of charge density in space. The atomic core regions are associated with highly compressive stresses while tensile stress, present in a form of "spindle structure" [16] of interatomic region, indicates covalent bond. The local contribution to electronic energy ($\varepsilon_{\tau}(\vec{r})$, Eq.4) is given by half of the trace over the eigenvalues of electronic stress tensor [14].

$$\varepsilon_\tau^S(\vec{r}) = \tfrac{1}{2}\sum_k \tau_\alpha^{Skk}(\vec{r}), \qquad E = \int d^3\vec{r}\,\varepsilon_\tau^S(\vec{r}) \tag{4}$$

The energy density partitioning scheme [11,19-22] utilized in RDFT leads to three related energy components, derived from the same density matrix. The total energy density is decomposed into the external potential and the interelectron potential energy densities and the kinetic energy density. The former plays particularly important role in the characterization of space of chemical systems. The relevant kinetic energy density ($n_T(\vec{r})$, Eq.5, m is mass of electron, $\psi_i(\vec{r})$ is natural orbital and v_i is occupation number of $\psi_i(\vec{r})$) is non-positively defined, and sub-sections the real space of chemical moieties into electronic drop (R_D: $n_T(\vec{r}) > 0$) and atmosphere (R_A: $n_T(\vec{r}) < 0$) regions separated by interface surface (S: $n_T(\vec{r}) = 0$) [12].

$$n_T(\vec{r}) = -\frac{\hbar^2}{4m}\sum_i^{occ} v_i\left[\psi_i^*(\vec{r})\Delta\psi_i(\vec{r}) + \Delta\psi_i^*(\vec{r})\psi_i(\vec{r})\right] \tag{5}$$

The S surface of $n_T(\vec{r})$ (defining the turning point for electrons) encloses the molecular regions of reactants and defines the boundaries of separate chemical species, since in the R_A region the classical movement of electrons is denied.

Under the linear approximation the ratio of local energy density and corresponding electron density (understood as very small regional contributions to total values ($\partial E / \partial N$)) gives the electronic chemical potential at particular point in space [23].

$$\mu_R = \left(\frac{\partial E_R}{\partial N_R}\right) \Leftrightarrow \frac{\varepsilon_{\tau AB}^S(\vec{r})}{n_{AB}(\vec{r})} \tag{6}$$

$$E_{AB} = \int d^3\vec{r}\,\varepsilon_{\tau AB}^S(\vec{r}), \quad N_{AB} = \int d^3\vec{r}\, n_{AB}(\vec{r}) \tag{7}$$

The electronic chemical potential represents the effective potential experienced by associated electron density. The chemical potential also measures the tendency of particles to diffuse (a function of spatial location). Particles diffuse from regions with high chemical potential to regions with low chemical potential. This makes the gradient of chemical potential en effective electric field. The electron density is stationary where gradient of chemical potential is zero (all forces are balanced).

The total electronic force (Eq.8), defined within RDFT, is composed of Lorentz force and tension force [12,14,16,24]. For stationary state of charged particles total force becomes zero, thus tension is balanced by Lorentz force at every point in space. The eigenvalue of tension force density operator, given as the divergence of the stress tensor density operator

(Eq.9), at stationary state, between chemically bonded atoms, can locally vanish at the Lagrange point [23].

$$\left\langle \hat{\vec{\tau}}_{\alpha}^{S}(\vec{r}) \right\rangle + \left\langle \hat{\vec{L}}_{\alpha}^{S}(\vec{r}) \right\rangle = 0 \tag{8}$$

$$\hat{\tau}_{\alpha}^{Sk}(\vec{r}) = \partial_{l}\hat{\tau}_{\alpha}^{Skl}(\vec{r}) =$$
$$= \frac{\hbar^2}{4m}\sum_{i}^{occ}\nu_i\left[\psi_i^{*}(\vec{r})\frac{\partial\Delta\psi_i(\vec{r})}{\partial x^k} - \frac{\partial\psi_i^{*}(\vec{r})}{\partial x^k}\Delta\psi_i(\vec{r})\right. \tag{9}$$
$$\left. + \frac{\partial\Delta\psi_i^{*}(\vec{r})}{\partial x^k}\psi_i(\vec{r}) - \Delta\psi_i^{*}(\vec{r})\frac{\partial\psi_i(\vec{r})}{\partial x^k}\right]$$

This peculiar stationary point of charge density in interatomic region provides reliable characteristics of bond properties 18,23. The non-classical bond order measures 23 were based on electronic properties calculated at Lagrange point. The b_{ε} - the energy density bond order (Eq.10), and b_{μ} – chemical potential bond order (Eq.11) were introduced:

$$b_{\varepsilon} = \frac{\varepsilon_{\tau AB}^{S}(\vec{r}_{Lagrange})}{\varepsilon_{\tau HH}^{S}(\vec{r}_{Lagrange})} \tag{10}$$

$$b_{\mu} = \frac{b_{\varepsilon}}{\left(n_{AB}(\vec{r}_{Lagrange})/n_{HH}(\vec{r}_{Lagranre})\right)} = \frac{\varepsilon_{\tau AB}^{S}(\vec{r}_{Lagranre})}{n_{AB}(\vec{r}_{Lagranre})}\cdot\left(\frac{\varepsilon_{\tau HH}^{S}(\vec{r}_{Lagranre})}{n_{HH}(\vec{r}_{Lagranre})}\right)^{-1} \tag{11}$$

which are the respective quantities at Lagrange point of particular bond relatively to H_2 molecule as reference value calculated at the same level of theory.

The hybrid variational-perturbational interaction energy decomposition scheme [25] with counterpoise correction [26] was applied to obtain the MP2 interaction energy components (Eq.12), where $\Delta E_{EL}^{(1)}$ is electrostatic energy, $\Delta E_{EX}^{(1)}$ stays for exchange energy arising from overlap of charge distributions and Pauli exclusion principle, $\Delta E_{DEL}^{(R)}$ is delocalization component associated with relaxation of electronic clouds upon interaction and ΔE_{CORR} is the second-order correlation energy. The sum of successive components gives interaction energy at gradually increasing levels of theory.

$$\Delta E = \Delta E_{EL}^{(1)} + \Delta E_{EX}^{(1)} + \Delta E_{DEL}^{(R)} + \Delta E_{CORR}$$
$$\text{——————} MP2 \text{——————}$$
$$\text{————} SCF \text{————} \tag{12}$$
$$\text{———} HL \text{———}$$
$$\text{—} EL \text{—}$$

The two-body interaction energy density [23] calculated as a difference of energy densities of dimmer (AB) and monomers (A and B, without relaxation) in dimmer centered basis set (Eq.13):

$$\Delta\varepsilon_{AB}(\vec{r}) = \varepsilon_{AB}(\vec{r}) - (\varepsilon_{A}(\vec{r}) + \varepsilon_{B}(\vec{r})) \qquad (13)$$

shows regions where electronic energy becomes lower due to interaction, thus attractive and repulsive trends of charge density between atoms of considered system are visualized.

Calculation Methods

Recently reported hydrogenated Pt-clusters [27] were further studied here using RDFT method [11-17]. The structures were reoptimized by Gaussian03 [28] calculations employing the generalized gradient approximation of exchange-correlation energy with Wang and Perdew [29] (PW91PW91) parameterization in standard 6-31G** basis set for hydrogen atoms and LanL2DZ [30] 18-electron effective core potential for Pt atoms. Although the double precision numerical (DNP) basis set corresponds to Gaussian 6-31G** basis set [31-34] obtained structures were essentially different in particular cases. The RMS of atoms positions of initial [27] and G03 reoptimized structures are shown in Table 1. These differences in geometries (predominantly related to H atoms) result from the presence of polarization functions on H atoms, since optimalization using D95/LanL2DZ or 6-31G/LanL2DZ (H/Pt atoms respectively) lead to almost identical geometry like initial structures [27]. The 6-31G** basis set was employed, due to the inclusion of polarization functions in basis sets is important for calculating the equilibrium geometries [35] particularly when studying processes involving hypervalent molecules, 3c/2e interactions, σ-complexes and agostic interactions [36-38]. Moreover the difference in geometries might be related to small energetical barriers between local minima structures owning to very low activation energies for H_2 chemisorption [28]. The vibrational frequencies were calculated to confirm obtaining of true minimum structures. The energy density calculations were done with RDFT program package [39] using electron wavefunctions from Gaussian calculations. The visualizations of molecular structures and energy density isosurfaces were done using PyMol [40] and VMD [41] programs.

Results and Discussion

The electronic properties of Pt-clusters under full saturation are now discussed. We will focus on G03 structures since all properties (except presence of σ-bonded dihydrogen species) are shared also by initial structures [27].

Bond Order Analysis

The RQED bond orders show redistribution/dissipation of energy in a molecule and indicate bond strength in terms of energy density associated with stationary point of electron density between atoms. The relevant point is the highest energy density tangential point between atoms, since starting from Lagrange point, the energy density gets lower while moving through ward a nucleus. Figure 1 (and Fig. S1) shows relation between bond orders and bond lengths. The bonds in range about 1.5~2.5Å correspond to Pt—H bonds, while those above this range to Pt—Pt bonds and those around 0.8Å to H—H bonds. The bond types can be easily recognized from $b_\varepsilon(r)$ or $b_\mu(r)$ dependency. Moreover b_μ allows to distinguish between terminal two-center (2c) bonds and multicentre (>2c, like 3c/2e), electron deficient Pt—H bonds. The smooth trend changes around R=1.9Å because gradient of b_μ for multicentre bonds is greater than for two-center bonds. The terminal Pt—H bonds have the greatest average strength and the most effective electric potential (measured by b_μ). The b_ε and b_μ bond orders correlate very well with interatomic distance. The coefficients for b_ε and b_μ bond orders are similar or better than those of Wiberg index (b_W) and NAO overlap weighted bond orders (b_{NAO}), for Pt—H (b_ε: -0.96, b_μ: -0.98, b_W: -0.93, b_{NAO}: -0.96) and Pt—Pt (b_ε: -0.98, b_μ: -0.97, b_W: -0.55, b_{NAO}: -0.64) bonds.

Figure 2 presents average bond orders dependency on cluster size. The Pt—Pt bonds average strength is decreasing with increasing cluster size and hydrogen loading. In general, bigger clusters also have weaker terminal Pt—H bonds, however the b_ε bond order exhibits a slightly increasing tendency in clusters Pt5 to Pt9. The Pt—H 3c/2e bonds are stronger in larger clusters. The bond order indices of adsorbed H_2 molecules in Pt_2H_{10}, Pt_2H_{12} and Pt_5H_{20} clusters are lower than in isolated H_2 molecule (by definition 1.0), thus corresponding bond strength as well as associated chemical potential are weaker. Figure 3 shows optimized structures, bonding pattern and bond orders in Pt-clusters. The tables listing all bonds bond orders, as well as structures with atoms numbering can be found in supplementary data (Tab. S1 and Fig. S2).

The bridge, tri-fold and four-fold bonding of hydrogen atoms might be explained in terms of bond orders and NBO analysis [42,43]. The structure, bε bond orders and atoms identifiers of Pt_3H_{12} cluster are shown on Fig.4. According to NBO analysis the 3c/2e bridging H atom is bonded via donor-acceptor interaction between hydrogen's (H(11)) s-orbital and σ_{PtH}* antibonds (of terminal Pt(2)−H(7) and Pt(3)−H(4) bonds, with $s_H \rightarrow \sigma_{PtH}$* 95.5 kcal·mol^{-1} and 134.4 kcal·mol^{-1} of NBO second-order perturbation theory stabilization respectively). Simultaneously the backward interaction comes from σ_{PtH} orbitals with leading stabilizations, from σ_{PtH} backdonation to s-orbital of bridging hydrogen, of 15.2 kcal·mol^{-1} and 24.6 kcal·mol^{-1} respectively. In accord with estimated stabilizations the Pt(3)−H(11) bond strength (measured by b_ε) is higher than that of Pt(2)−H(11) and Pt(3)−H(4) strength is lower than of Pt(2)−H(7) bond. Similarly the tri-fold bonded hydrogen atoms are stabilized by two way ($s_H \rightarrow \sigma_{PtH}$* and $\sigma_{PtH} \rightarrow s_H$) interactions, where H(6) is stabilized by 72.8 (Pt(1)−H(8)), 59.3 (Pt(3)−H(10)) and 49.3 (Pt(2)−H(5)) kcal·mol^{-1} through $s_H \rightarrow \sigma_{PtH}$* donation, and 14.6 (Pt(3)−H(10)), 13.8 (Pt(1)−H(8)) and 9.0 (Pt(2)−H(5)) kcal·mol^{-1} through $\sigma_{PtH} \rightarrow s_H$ backdonation, while H(15) is stabilized by 79.7 (Pt(1)−H(9)), 73.8 (Pt(3)−H(14)) and 24.8 (Pt(2)−H(12)) kcal·mol^{-1} through $s_H \rightarrow \sigma_{PtH}$*, and 16.5 (Pt(3)−H(14)), 14.7 (Pt(1)−H(9)) and 3.6 (Pt(2)−H(12)) kcal·mol^{-1} through $\sigma_{PtH} \rightarrow s_H$ interaction. Relevant stabilizations are reflected by b_ε that shows the lowest strengths for Pt(2)—H(6) and Pt(2)—H(15) bonds and the highest of Pt(2)—H(5) and Pt(2)—H(12). It was previously shown that hydrogen is capable to form multicentre bonds in solids [44-48]. In Pt_8H_{30} cluster an atypical "four-fold" bonded H atom (four Largange points related to the Pt−H bonds) has been found. Such high coordination numbers for hydrogen are rare but have been reported for clusters [48]. The similar $s_H \rightarrow \sigma_{PtH}$* stabilizing interactions were determined (with major stabilizations [kcal·mol^{-1}]: 75.5 Pt(4)H(37), 60.7 Pt(8)H(25), 21.9 Pt(5)H(20) and almost equivalent contributions of 8.8 Pt(1)H(26) and 8.0 Pt(1)H(17) antibonds). However major back donations occurred from σ_{PtH} bonds (62.6 kcal·mol^{-1} Pt(4)H(37), 39.1 kcal·mol^{-1} Pt(8)H(25)), but also from Pt lone pairs (21.4 kcal·mol^{-1} Pt(5), 15.5 kcal·mol^{-1} Pt(1)). The b_ε shows strongest bonding through Pt(4)—H(38)—Pt(8) centers associated donor-acceptor cooperative interactions, indicating that involvement of σ_{PtH}* and σ_{PtH} orbitals (for retrodative stabilization) results in stronger bonding of H atom than engaging σ_{PtH}* and Pt lone pair. Recently it was shown that the antibonding orbitals on metal centers are sensed by hydrogen atom as they were non-bonding

[49]. The calculated stretching frequencies of Pt—H(38) bonds (994.9 cm^{-1} ~ 1306.7 cm^{-1}) are lower than those of two centre Pt—H bonds (~2100 cm^{-1}).

The RQED Energy Density and MO analysis

Figure 5 presents chemical potential (μ) mapped on interface surface of kinetic energy density around Pt-clusters. The regions of higher chemical potential around hydrogen atoms are associated with reduced electron density. However there also appear electron density deficient regions with lower chemical potential near surface exposed Pt atoms. These regions occur only in small clusters (up to five Pt atoms) and were not found on the interface surface of larger clusters.

The Pt—H bonds are characterized by presence of spindle structure, which indicates covalent interaction (the largest eigenvalue of stress is shown in Fig. S3, the corresponding eigenvector has been omitted for sake of clarity). The regions of lower electronic chemical potential on interface surface in proximity of Pt atoms coincide with non-spindle structure arisen tensile stress regions, as result of strong electric potential of poorly shielded Pt nucleus (marking strengthen acceptor properties of σ_{PtH}* of trans Pt—H bond and lone pair donating property). The electronic chemical potential is the effective potential experienced by electrons. The low μ means poor shielding and strong electric potential of nucleus. Therefore regions of low electronic chemical potential are "electrophilic" centres (where the electronic energy is very favourable). Contrary regions of higher chemical potential can be recognized as "nucleophilic", relatively to other parts of the molecule that will favour deflection of electron density to neighbouring regions with lower μ.

We had looked closer to these spots, of lower chemical potential, in $Pt_2H_{n=8,10,12}$ clusters and found that these are reactive regions, able to stabilize H_2 molecule ligands via synergistic, σ-bond interactions. However, due to its nature (as discussed below), these also can be the electrophilic centres responsible for poisoning of Pt that can be corroded by cyanides, halogens, sulphur, and caustic alkalis. Under low saturation a H_2 coordination leads to H—H bond breaking and formation of H—Pt—H hydrides, which is in tact with one of the possible reaction pathways of H_2 side-on cleavage on Pt [27,50]. Supported further by chemical potential redistribution on bare Pt-clusters, where on-top binding sites on Pt show moderate lower chemical potential (figures in supporting data, Fig.S4) associated with low electron density and tensile stress resulting from withdrawing of electronic charge from lone pairs. However upon high saturation, H_2 molecules symmetrically bind to Pt-clusters and remain dimmerized. Figure 6 compares properties of $Pt_2H_{n=8,10,12}$ clusters. The H_2

coordination or insertion depends on the relative strengths of Pt—H and H—H bonds. The dihydrogen ligand b_ε bond order is higher than any geminal or vicinal Pt—H bond, while b_μ index is similar to that of 3c/2e Pt—H—Pt bridging bonds. After H_2 coordination on Pt the non-spindle structure tensile stress diminishes and only residual positive stresses remain between Pt and dihydrogen's H atoms (a pro-spindle structure). Simultaneously electronic chemical potential on interface surface around Pt—H_2 becomes high. Due to similarity of chemical potentials of electrons the concerning Pt—Pt bonds are likely to be inserted with bridging hydrogen.

The H—H ligand bond lengths (~0.81Å) are found to be slightly elongated relative to "free" H2. Pt—H_2 distances are long (~1.92 Å) relative to Pt—H terminal (~1.58 Å) and bridging (~1.86 Å) bonds, however are in typical range (1.8 - 2.3 Å) for a σ-complex interactions [45,46]. The calculated interaction energy (Table 2) also agrees with estimated usual stabilization of 10-20 kcal•mol-1 [51,53-55]. The HOMO-LUMO separation energies, listed in Table 3, show that from Pt_2H_8 to Pt_2H_{12} reactivity of the cluster is decreasing as H_2 occupies low μ sites and the relevant MO energy gap increases.

The orbital-wise analysis provided information on the MOs with the greatest contribution to bε bond order of H—H bond. The shapes of these orbitals are presented in Figure 7, they indicate interaction of d-type orbitals of Pt and σ-bond of H_2. In all cases relatively low energy valence electrons molecular orbitals are involved in coordination of H_2 ligand. The natural bond order analysis of Pt_2H_{12} showed lowered occupancy (1.84696e) of H_2 σ-bond and synergistic donation into the in-plane Pt—H σ* antibond orbital (yielding 52.4 kcal·mol^{-1} of stabilization estimated from NBO second-order perturbation theory). The delocalization results in slight elongation of Pt—H bond *trans* to dihydrogen (1.53Å vs. 1.51Å in Pt_2H_8). Back donation occurs from d Pt lone pair to σ_{HH}* antibond (8.4 kcal·mol^{-1} stabilization). The b_ε bond order shows that relevant Pt—H bond has significantly decreased strength comparing to corresponding bond in Pt_2H_8 (or to "free" trans Pt—H bond on second Pt atom in Pt_2H_{10}). However binding H_2 at both sites strengthens the Pt—H as well as H—H bonds, associated with limited σ-donation and backdonation. The calculated interaction energy density (Fig. 8) shows lowering of energy (stabilization due to compression) in Pt—H_2 and trans Pt—H bonding regions and raise (destabilization due to expansion) in Pt lone pair orbital, connected with migration of electron density to electron deficient, but higher μ region in the process of backdonation. The differences in interaction energies (Tab.2) of H_2 ligand with Pt-cluster illustrate the important role of backdonation in σ-complex stabilization, where reduced backdonation results in less favourable interaction energy. The decomposition of

MP2 interaction energy unravelled the exchange energy as leading term being about twice time greater than electrostatic or delocalization terms, there is also significant contribution from correlation component, which might be attributed to the rearrangements of charge density on Pt atoms. It is evident that both H—H bond breaking and stabilization of σ-bond complex requires sharing electrons with vacant orbital associated with Pt centre as well as at least small backbonding [51].

In case of Pt_2H_{12} (but applies also to other clusters) molecular-H_2 complex of metal hydride and $Pt_2H_8(H_2)_2$ notation seems to be more proper. Besides $Pt_2H_8(H_2)_{n=1,2}$ the $Pt_4H_{16}(H_2)$ and $Pt_5H_{18}(H_2)_{n=1,2}$ clusters were obtained (data not included), where (H_2) denotes σ-bond complex of dihydrogen ligand. These σ-complexes were formed at sites on Pt atoms with Pt—H bond in trans position to H_2 ligand and exhibiting the lowest chemical potential. The H_2 molecules at sites with trans Pt—Pt bond, with a little higher μ were found to be physisorbed. The synergistic (cooperative) H_2 coordination described here shows remarkable similar principles to Dewar-Chatt-Duncanson model for olefin coordination [51]. The calculated lowering of H—H vibrational frequencies (3484~3570 cm^{-1} vs. 4386 cm^{-1} in isolated H_2) correlate with experimental [56] and theoretical findings [57] for such complexes. The intramolecular H—H stretching frequencies are smaller than those of physisorbed H_2 (~4200 cm^{-1} in Pt_4H_{20} or Pt_5H_{24}). Such sigma-bonded Pt—H_2 complexes (or Kubas interactions [51]), are desirable for fast kinetics, due to intermediate binding energies between physisorption and chemisorption.

Conclusions

Reversible bonding of H_2 molecules in similar fashion like O_2 to heme group is desirable for hydrogen storing/operating materials. The primary advantage of such interaction is that each species can exist stable independently thus association and dissociation energy barriers are quite low [27]. The σ-electron pair binds H_2 ligand to Pt by dative occupation of vacant metal orbital [51]. The σ-complex has to be stabilized by backdonation, which results in stronger interaction than physisorbtion or hydrogen bonding. The H_2 is found to be strong π-acceptor, thus σ-complex might easily transform into hydride. Shearing only σ-electron pair can not cause breaking of H—H bond, it is the accompanying overpopulation of dihydride σ* orbital that leads to cleavage of hydrogen molecule [51] due to the strengthening of the Pt—H interaction. The unique feature of H_2 is that it has just one σ-bonding electron pair, thus σ-

bond complex strongly activates dihydrogen, which binds symmetrically, always side-on to the metal. The *trans* ligand has great influence on Pt—H_2 binding nature and strength, particularly a hydride ligand weakness the interaction comparing to Pt specie in trans ligand position.

The corresponding interactions are well known and described in literature [38,51] particularly as a part of catalytic hydrogenation cycle. We were able to visualize the reactive regions of Pt-clusters using electronic chemical potential calculated by RDFT method. Regions of low electronic chemical potential were recognized as "electrophilic" centers characterized by electron withdrawing tensile stress. Through screen of chemical potential of other materials it is possible to quickly determine species able to reversible binding of molecular hydrogen with moderate strengths. Covalent binding of H atoms to Pt significantly lowered electronic chemical potential in *trans* position to Pt—H bond. The relevant regions appeared only in small clusters. The σ-bonding of H_2 stabilizes both Pt—H_2 and *trans*-Pt—H bond. In large clusters surface Pt atoms do not expose to the molecular surface a vacant orbitals with sufficiently low chemical potential to constitute stable σ-bond complex with H_2 due to Pt atom occupies trans ligand position. We anticipate that bulk Pt materials are not able to stabilize the σ-complex. Additionally b_ε and b_μ bond orders picture energetical characteristic of bonding electrons. The Pt—Pt bonds average strength decrease with increasing cluster size and occupancy with hydrogen, the bigger clusters also have weaker terminal Pt—H bonds and stronger 3c/2e interactions. The dihydrogen ligand H—H bond b_ε bond order was higher than any geminal or vicinal Pt—H bond, while b_μ index was similar to that of 3c/2e Pt—H—Pt bridge bonds. The similarity of μ for Pt—Pt and H—H bonds encourage H atoms to occupy the bridging position. Involvement of σ_{PtH}* and σ_{PtH} orbitals in donor-acceptor interactions lead to stronger bonding than engaging σ_{PtH}* and Pt lone pair.

Electronic Supplementary Information available: Fig.S1. Change of energy density (b_ε) and chemical potential (b_μ) bond orders with bond length. The NBO bond orders are also shown for reference. The structures of (a) were optimized in Gaussian03 and of (b) in Dmol3 [27] program packages (details in text).; Fig.S2. Structures, atoms numbering and bonding pattern in Pt-clusters.; Fig.S3. The largest eigenvalue of electronic stress tensor.; Fig.S4. Chemical potential on interface surface of bare Pt-clusters.; Fig.S5. The valence molecular orbitals of Pt_2H_8, Pt_2H_{10} and Pt_2H_{12} clusters.; Table S1. Lagrange point data (Gaussina03: PW91PW91/6-31G**,LanL2DZ optimized structures).

References

[1] Basic Research Needs for the Hydrogen Economy, www.science.doe.gov/bes/Hydrogen.pdf

[2] L. Schlapbach, A. Zuttel, Nature (London), 414, 353 (2001).

[3] R. Coontz, B. Hanson, Science, 305, 957 (2004).

[4] M. Fichtner, Adv. Eng. Mater., 7, 443 (2005).

[5] L. Gagliardi, P. Pyykko, J. Am. Chem. Soc., 126, 15014 (2004).

[6] B. Bogdanovic, M. Felderhoff, A. Pommerin, T. Schuth, N. Spielkamp, Adv. Mater. (Weinheim, Ger.), 18, 1198 (2006).

[7] W.-Q. Deng, X. Xu, W. A. Goddard, Phys. Rev. Lett., 92, 166103 (2004).

[8] T. Yildirim, S. Ciraci, Phys. Rev. Lett., 94, 175501 (2005)

[9] Q. Sun, P. Jena, Q. Wang, M. Marquez, J. Am. Chem. Soc., 128, 9741 (2006).

[10] T. Yildirim, M. R. Hartman, Phys. Rev. Lett., 95, 215504 (2005).

[11] A. Tachibana, Theor. Chem. Acc., 102, 188 (1999).

[12] A. Tachibana, J. Chem. Phys., 115, 3497 (2001).

[13] A. Tachibana, in Stress Induced Phenomena in Metallization, edited by S. P. Baker (American Institute of Physics, New York, 2002), p.205-211.

[14] A. Tachibana, in Reviews in modern quantum chemistry: a celebration of the contributions of Robert Parr, edited by K. D. Sen (World Scientific, Singapore, 2002), Vol 2, p.1327-1366.

[15] A. Tachibana, in Fundamental perspectives in quantum chemistry: a tribute to the memory of Per-Olov Löwdin, edited by E. Brändas, E. Kryachko (Kluwer, Dordrecht, 2003) Vol 2, p.211–239.

[16] A. Tachibana, Int. J. Quantum Chem., 100, 981 (2004).

[17] A. Tachibana, J. Mol. Model., 11, 301 (2005).

[18] P. Szarek, Y. Sueda and A. Tachibana, Electronic Stress Tensor Description of Chemical Bonds Using Non-classical Bond Order Concept (JCP, submitted).

[19] A. Tachibana, Int. J. Quantum Chem., Quantum Chem. Symp., 21, 181 (1987).

[20] A. Tachibana, Int. J. Quantum Chem., 57, 423 (1996).

[21] A. Tachibana, R. G. Parr, Int. J. Quantum Chem., 41, 527 (1992).

[22] A. Tachibana, K. Nakamura, K. Sakata, T. Morisaki, Int. J. Quantum Chem., 74, 669 (1999).

[23] P. Szarek, A. Tachibana, J. Mol. Model., 3, 651 (2007).

[24] A. Tachibana, J. Math. Chem., 7, 95 (1991).

[25] W. A. Sokalski, S. Roszak, K. Pecul., Chem. Phys. Lett., 153,153 (1988).

[26] S. F. Boys, F. Bernardi, Mol. Phys., 19, 553 (1970).

[27] C. Zhou, J. Wu, A. Nie, R.C. Forrey, A Tachibana, H. Cheng, J. Phys. Chem. C, 111, 12773 (2007).

[28] M.J. Frisch, G.W. Trucks, H.B. Schlegel, G.E. Scuseria, M.A. Robb, J.R. Cheeseman, J.A. Montgomery, JrT. Vreven, K.N. Kudin, J.C. Burant, J.M. Millam, S.S. Iyengar, J. Tomasi, V. Barone, B. Mennucci, M. Cossi, G. Scalmani, N. Rega, G.A. Petersson, H. Nakatsuji, M. Hada, M. Ehara, K. Toyota, R. Fukuda, J. Hasegawa, M. Ishida, T. Nakajima, Y. Honda, O. Kitao, H. Nakai, M. Klene, X. Li, J.E. Knox, H.P. Hratchian, J.B. Cross, V. Bakken, C. Adamo, J. Jaramillo, R. Gomperts, R.E. Stratmann, O. Yazyev, A.J. Austin, R. Cammi, C. Pomelli, J.W. Ochterski, P.Y. Ayala, K. Morokuma, G.A. Voth, P. Salvador, J.J. Dannenberg, V.G. Zakrzewski, S.

Dapprich, A.D. Daniels, M.C. Strain, O. Farkas, D.K. Malick, A.D. Rabuck, K. Raghavachari, J.B. Foresman, J.V. Ortiz, Q. Cui, A.G. Baboul, S. Clifford, J. Cioslowski, B.B. Stefanov, G. Liu, A. Liashenko, P. Piskorz, I. Komaromi, R.L. Martin, D.J. Fox, T. Keith, M.A. Al-Laham, C.Y. Peng, A. Nanayakkara, M. Challacombe, P.M.W. Gill, B. Johnson, W. Chen, M.W. Wong, C. Gonzalez, J.A. Pople, 2003, Gaussian 03, Revision C.02, Gaussian, Inc., Wallingford CT

[29] Y. Wang, J. P. Perdew, Phys. Rev. B, 45, 13244 (1992).

[30] P.J. Hay, W.R. Wadt, J. Chem. Phys., 82, 299 (1985).

[31] W. J. Hehre, R. Ditchfield, J. A. Pople, J. Chem. Phys. 56, 2257 (1972).

[32] M. S. Gordon, Chem. Phys. Lett. 76, 163 (1980).

[33] B. Delley, J. Chem. Phys., 92, 508 (1990).

[34] C. W. Bock, M. Trachtman, J. Phys. Chem., 98, 95 (1994).

[35] H. Guo, M. Karplus, J. Chem. Phys., 91, 1719 (1989).

[36] J.A. Sordo, Chem. Phys. Lett., 316, 167 (2000).

[37] A. A. Merkulov, P. Mountford, G. I. Nikonov, in Organosilicon Chemistry V -from Molecules to Materials, edited by N. Auner, J. Weiss (Wiley-VCH, 2003) pp.451-455.

[38] A. Dedieu, Chem. Rev., 100, 543 (2000).

[39] K. Doi, P. Szarek, K. Nakamura, M. Senami and A. Tachibana, Regional DFT program package, ver. 2, Tachibana Lab., Kyoto University, Kyoto (2007)

[40] W. L. DeLano "The PyMOL Molecular Graphics System." DeLano Scientific LLC, San Carlos, CA, USA. (http://www.pymol.org)

[41] W. Humphrey, A. Dalke, K. Schulten, J. Molec. Graphics, 14, 33 (1996), (http://www.ks.uiuc.edu/Research/vmd/).

[42] A. E. Reed and F. Weinhold, J. Chem. Phys., 78, 4066 (1983).

[43] A. E. Reed, R. B. Weinstock, F. Weinhold, J. Chem. Phys., 83, 735 (1985).

[44] L. S. Bartell and B. L. Carrol, J. Chem. Phys., 42, 1135 (1965).

[45] C. G. Van de Walle, P. J. H. Denteneer, Y. Bar-Yam, S. T. Pantelides, Phys. Rev. B, 39, 10791 (1989).

[46] P. E. Blöchl, Phys. Rev. B, 62, 6158 (2000).

[47] J. Kang, E.-C. Lee, K. J. Chang, Y.-G. Jin, Appl. Phys. Lett. 84, 3894 (2004).

[48] R. Bau, et al., Science, 275, 1099 (1997).

[49] A. Janotti, C. G. Van de Walle, Nature, 6, 44 (2007)

[50] Q. Cui, D. G. Musaeev, K. Morokuma, J. Chem. Phys., 108, 8418 (1998).

[51] G. J. Kubas, J. Organometal. Chem., 635, 37 (2001), (and publications cited therein).

[52] M. Brookharta, M. L. H. Green, G. Parkin, PNAS, 104, 6908 (2007).

[53] M. Brookhart, M. L. H. Green, J. Organometal. Chem., 250, 395 (1983).

[54] S. J. La Placa, J. A. Ibers, Inorg. Chem., 4, 778 (1965).

[55] M. Brookhart, M. L. H. Green, G. Parkin, Proceeding of the U.S. National Academy of Sciences, 104, 6908 (2007).

[56] R. A. Henderson, Transition Met. Chem., 13, 474 (1988), (and publications cited therein).

[57] J. Íñiguez, W. Zhou, T. Yildirim, Chem. Phys. Lett., 444, 140 (2007).

Table 1. The RMS of atoms positions of Dmol3 [27] and Gaussian03 optimized hydrogenated platinum clusters.

Cluster	Pt atoms RMS	H atoms RMS	All atoms RMS
Pt_2H_{10}	0.024	0.628	0.584
Pt_3H_{12}	0.010	0.098	0.089
Pt_4H_{16}	0.020	0.095	0.086
Pt_5H_{20}	0.041	0.258	0.236
Pt_7H_{28}	0.120	0.245	0.226
Pt_8H_{30}	0.039	0.076	0.071
Pt_9H_{34}	0.097	0.193	0.178

Table 2. The PW91 interaction energy (ΔE) of Pt_2H_{n-2} with synergistically interacting H_2 molecule.

Cluster	ΔE [kcal/mol]	ΔE_{cc} [kcal/mol] [a]
Pt_2H_{10}	-15.49	-14.36
Pt_2H_{12}	-13.81	-12.58

[a] the counterpoise corrected interaction energy [26]

Table 3. The HOMO-LUMO orbital energies and energy gap of hydrogenated platinum clusters.

Cluster	E_{HOMO} [eV]	E_{LUMO} [eV]	$\Delta_{HOMO-LUMO}$ [eV]
Pt_2H_8	-7.2899	-4.1797	3.1103
Pt_2H_{10}	-7.2382	-3.5973	3.6382
Pt_2H_{12}	-7.1430	-3.0069	4.1361
Pt_3H_{12}	-7.3906	-4.3321	3.0586
Pt_4H_{16}	-7.1321	-4.8246	2.3075
Pt_5H_{20}	-6.7131	-3.9565	2.7565
Pt_7H_{28}	-6.7457	-4.5987	2.1470
Pt_8H_{30}	-5.8069	-4.2504	1.5538
Pt_9H_{34}	-6.2396	-4.4599	1.7769

Figure 1. Change of energy density (b_ε) and chemical potential (b_μ) bond orders with bond length. The NBO bond orders are also shown for reference.

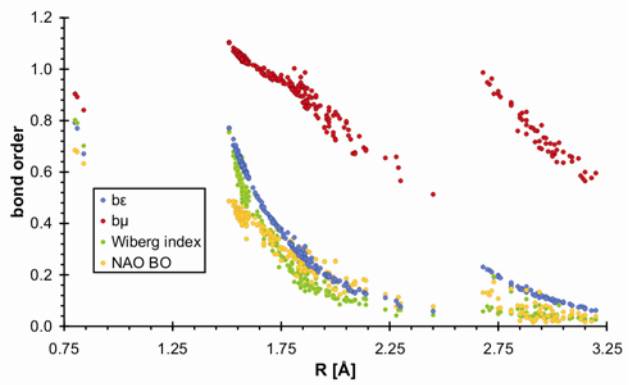

Figure 2. The average bond orders of (a) Pt—Pt bonds (b_ε and b_μ) and (b) Pt—H bonds (b_ε only) with increasing cluster size. In case of 3c/2e bridging Pt(1)—H—Pt(2) bonds the bε indices of Pt(1)—H and Pt(2)—H bonds were first summed and the average of "total" is shown; similarly for tri-fold bonding hydrogen the average of sum of bond orders of the three Pt—H bonds is presented.

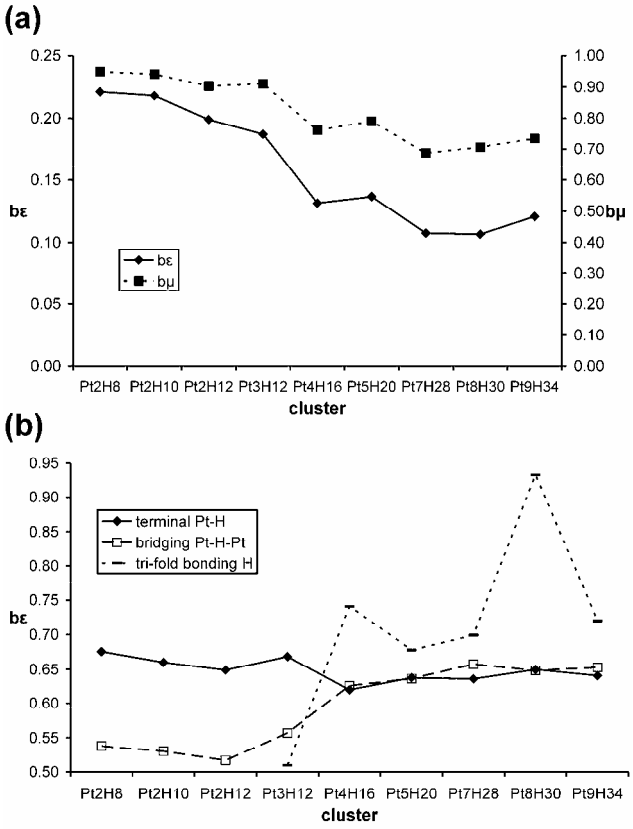

Figure 3. The bond orders (b_ε – left and b_μ – right) of bonds with Lagrange point. The color of bond corresponds to the bond order according to scale. Pt atoms are represented as grey spheres and H atoms are in white.

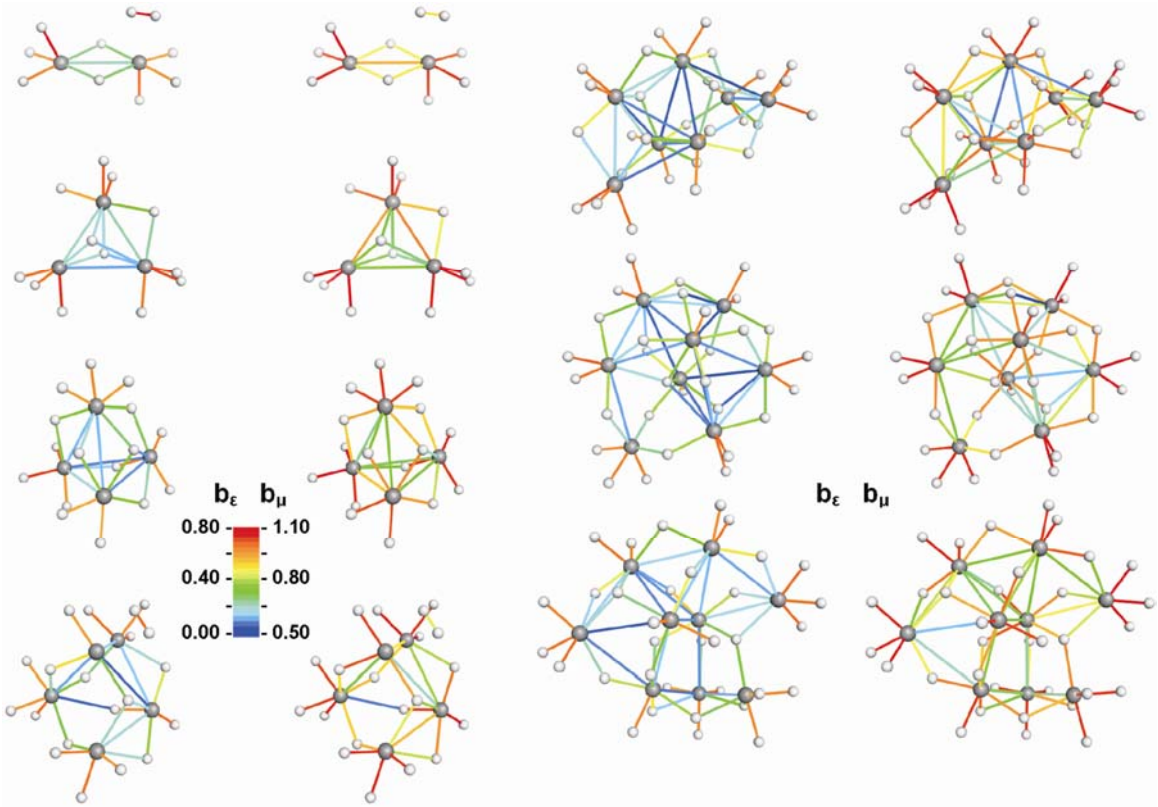

Figure 4. The b_ε bond order and atoms numbering in Pt3H12 cluster.

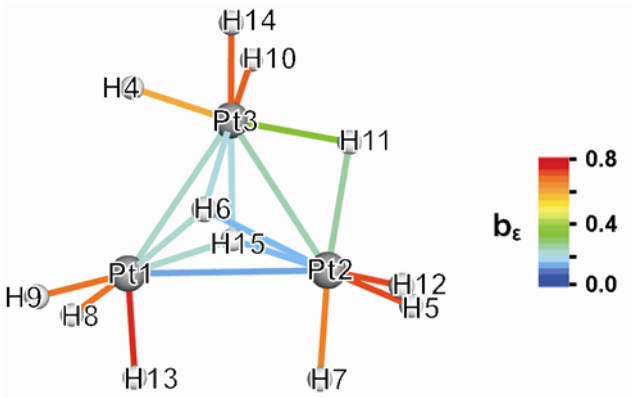

Figure 5. Electronic chemical potential mapped on zero kinetic energy density isosurface.

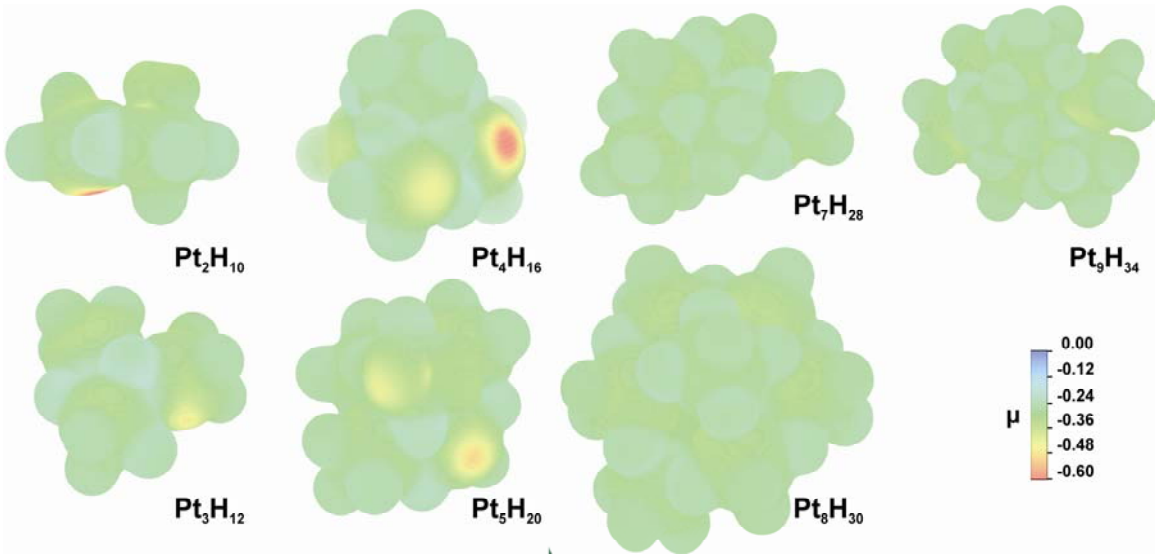

Figure 6. Electronic properties of $Pt_2H_{n=8,10,12}$ clusters. Electronic chemical potential, stress tensor and b_ε and b_μ bond orders.

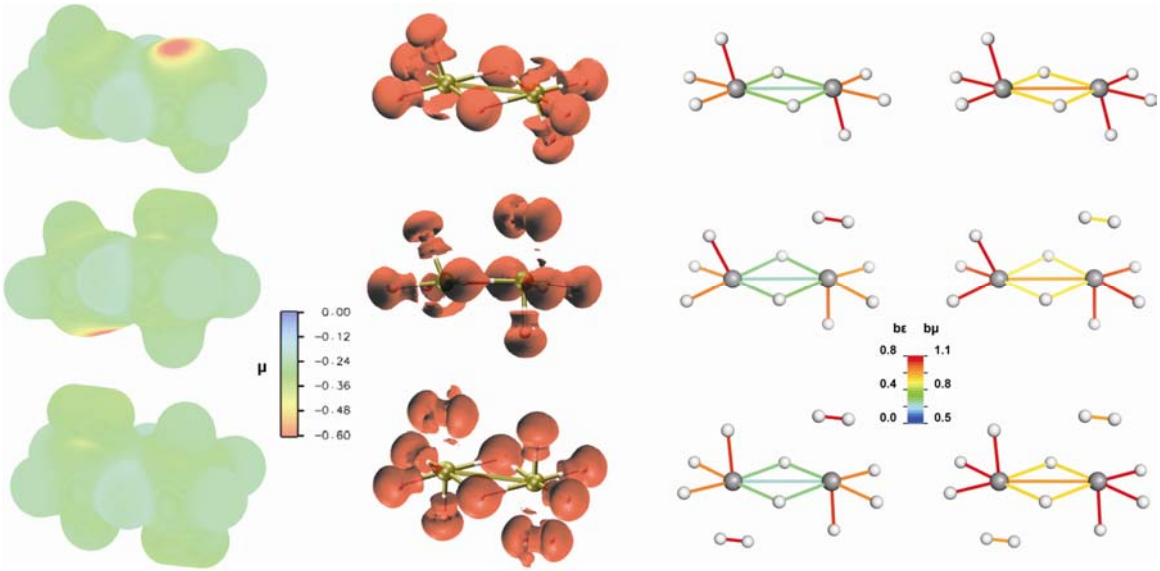

Figure 7. Molecular orbitals with the greatest contribution to H—H bond order. The orbital number and energy is followed by percentage contribution to H—H bε. First row show MOs from Pt_2H_{10}, second row - Pt_2H_{12}, last row - Pt_5H_{20} (all the valence MOs available in supporting data).

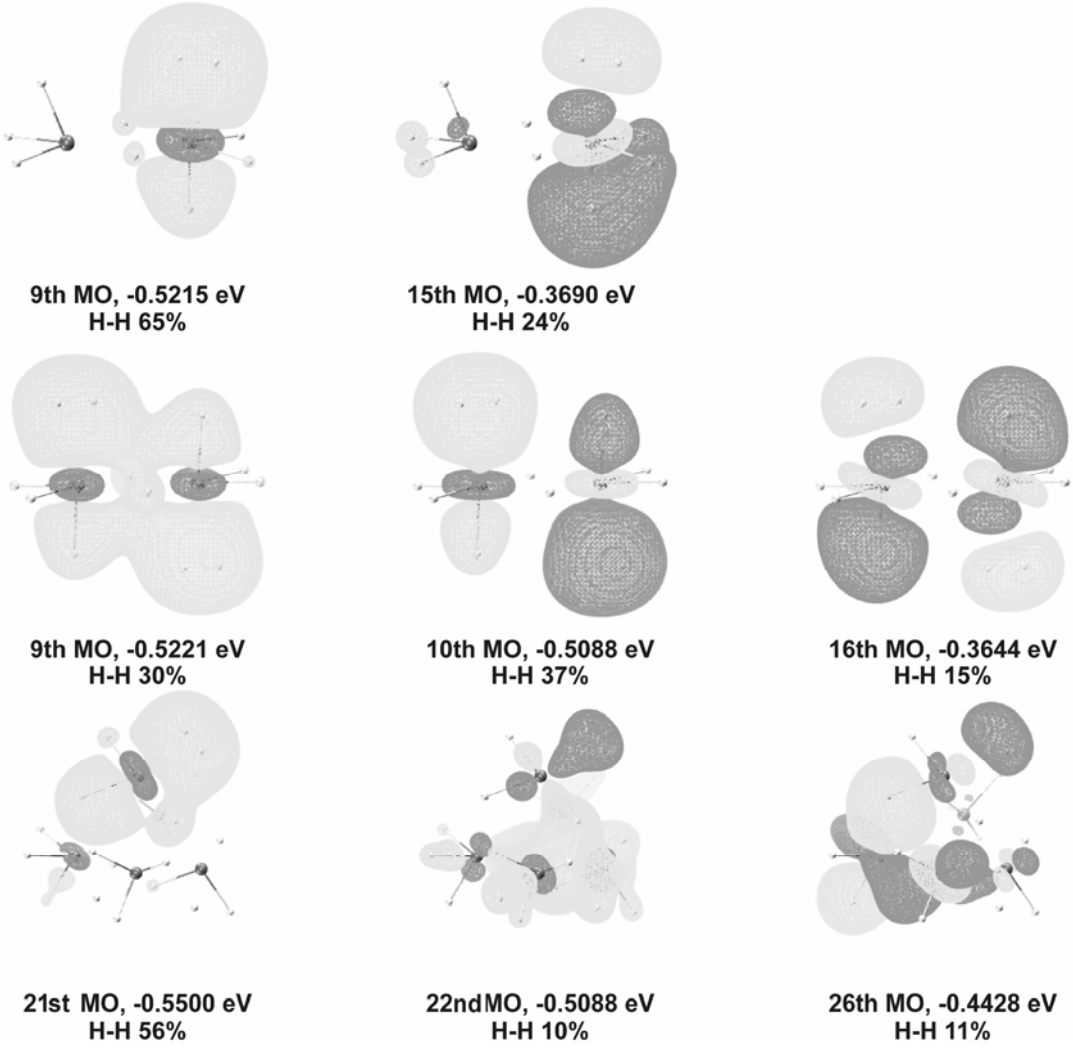

Figure 8. The interaction energy density of Pt_2H_8 and H_2 in Pt_2H_{10} cluster ($Pt_2H_8(H_2)$), Pt_2H_{10} and H_2 in Pt_2H_{12} cluster ($Pt_2H_{10}(H_2)$) and Pt_2H_8 and two H_2 in Pt_2H_{12} cluster ($Pt_2H_8(H_2)_2$).

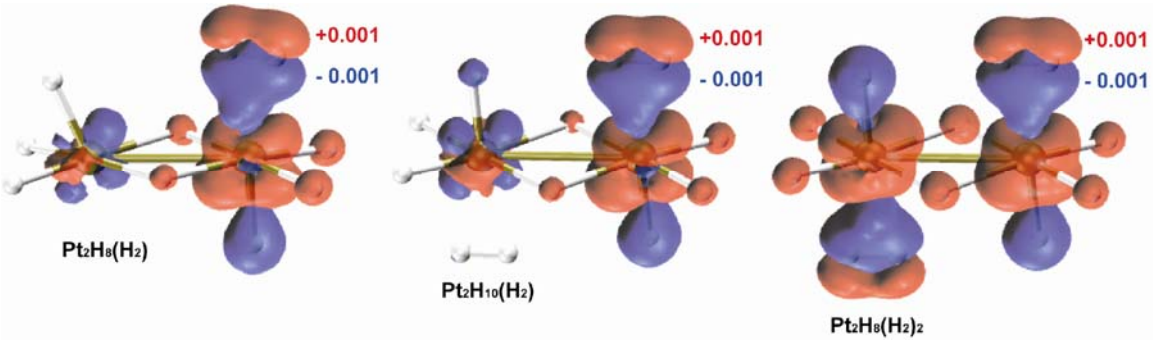

CHAPTER 5

The physical nature of intermolecular interactions within cAMP-dependent protein kinase active site: differential transition state stabilization in phosphoryl transfer reaction.

Introduction

The remarkable enhancement of reaction rates resulting from enzymes action has been a matter of the utmost interest for over a century. Both fundamental and practical importance of unraveling the principal driving force in enzymatic catalysis has fuelled a long-standing debate about the origin of enzyme proficiency [1]. While several proposals have been recently put forward including desolvation, ground-state destabilization and dynamic effects [2], it has been argued that what really contributes to the activation barrier lowering is the preferential transition state binding relative to reactants [3,4]. In other words, the impact of an enzyme environment consists in its improved complementarity toward the transition state which is bound more tightly than the substrates. Therefore, understanding of the catalytic abilities of enzymes could be accomplished by careful examination of the forces exerted by an enzyme active site on the species appearing along a reaction coordinate. Determination of active site residues playing crucial role in a particular reaction provides a useful insight into the molecular mechanism of catalysis. The latter could finally be complemented by detailed analysis of the actual physical nature of noncovalent interactions present in the active site. This can be accomplished within Differential Transition State Stabilization, (DTSS) [5-7] approach using variation-perturbation partitioning of the intermolecular interaction energies [8] based on first principles of quantum mechanics.

Since the electronic and structural changes observed along a reaction path between reactants and the transition state specify the corresponding differential stabilization required for a given reaction, the knowledge of the former should in principle allow for the design of a complementary environment enhancing catalytic activity. Whenever the electrostatic effects are dominant, activation barrier lowering could be approximated by the sum of products of differential electrostatic potential exhibited by transition state compared to reactants and fractional charges of molecular environment. [5] In other words, considering exclusively the aforementioned differential electrostatic characteristics of a transition state/reactants system allows for the straightforward prediction of an influence of a unit charge occupying a specific position on the height of an activation energy barrier. These so called catalytic fields [5-7] have already proven to be a useful tool for the qualitative analysis of an active site (in terms of its evolution-driven complementarity) with a potential to be employed in a catalyst design. Recent spectacular advances in computational *de novo* design of enzymes [9] reflect urgent need for effective and reliable methods of rational design of biocatalysts employing critical

information contained solely in transition state structures. Possibly, such techniques could be augmented by catalytic fields approach [5-7].

Due to their participation in protein phosphorylation and the resulting involvement in cell signaling as well as metabolic regulation, protein kinases have received much attention from the scientific community [10]. Among the most extensively studied is cAMP-dependent protein kinase (PKA) with its catalytic subunit structure and mechanism serving as a prototype for the entire family of eukaryotic protein kinases [11]. PKA-catalyzed process encompasses the transfer of γ-phosphate from ATP to the specific serine residue located on the substrate peptide. Despite numerous experimental [12] and theoretical [13-22] studies, no agreement has been reached regarding all details of PKA catalytic machinery. In particular, the involvement of several highly conserved active site residues (e.g., Asp166, Lys168) along with the functional relevance of magnesium ions has remained unclear. While divalent metal ions are generally thought of as facilitating the phosphorylation processes [23], the mechanism of their participation appears to be complex and, possibly, varying between different metal sites.

X-ray crystallographic data display the presence of two magnesium ions within PKA active site. It has been known, that at least one magnesium ion is essential for PKA action. This metal ion occupies a high affinity metal binding site and chelates the β-, γ-phosphates of ATP as well as Asp184 residues. At high magnesium concentration also the low affinity site is filled with the second Mg^{2+} bridging α-, γ-phosphates and Asp184, Asn171 residues. As shown experimentally, PKA activity decreases with an increasing occupation of the secondary metal site [24]. Accordingly, this particular magnesium ion is termed inhibitory. However, at the limited ATP concentration, the reaction rate is actually accelerated owing to increased ATP binding affinity [10].

Another unresolved issue is the PKA phosphorylation mechanism itself, i.e. the presence and identity of a residue serving as a catalytic base. While many studies suggest that no general-base catalyst is required for the phosphoryl transfer process [13-15,17] other contradict this hypothesis proposing the involvement of Asp166 residue in deprotonation of a hydroxyl group of serine residue prior to its phosphorylation [18,19,25,26]. Moreover, direct Asp166 participation in the general-base catalysis has been supported by the latest high-level computational results [20-22], while the earlier proposals neglecting Asp166 involvement have been put forward based on semiempirical QM (or QM/MM) models [13-15]. Whether this particular residue contributes any more effects to PKA catalytic rate enhancement has yet to be determined.

Since the function of the remaining conserved residues has not been unequivocally ascertained, this work aims at revealing the actual role of PKA active site components in the observed catalytic activity. In particular, the activation barrier lowering resulting from the presence of a given residue will be investigated based on the PKA mechanism and structures demonstrated in Ref. 20. As suggested by classical calculation of the interactions occurring in enzyme-substrate and enzyme-transition state complexes, PKA active site provides stabilization of the transition state [20]. In what follows, these preliminary results will be extended by non-empirical decomposition of interaction energy providing a comprehensive evaluation of the physical nature of catalysis along with the possible involvement of individual active site residues. The overall picture of an enzyme catalytic mechanism could aid prediction of the impact of enzyme mutations on the enzymatic activity.

Computational methods

Sequence and structure alignment

The search for similar protein structures was conducted with FATCAT [27] database searching method based on flexible alignment model. The reactant state of QM/MM-optimized PKA structure [20] was used as a query against SCOP (version 1.73, 90% non-redundant set of 14155 structures) and PDB (June 2007, 90% non-redundant set of 16500 structures) structural databases. Multiple structures of the same protein (if sharing the same source organism) as well as mutant enzymes were excluded from comparison. The structures with statistically meaningful (P-value < $4.5 \cdot 10^{-8}$) structural similarity between spatially superimposed active site residues were selected. The aligned sequences were manually corrected according to spatial correspondence of individual residues. The final set of protein structures was refitted to obtain the best superimposition of active site residues. Visualization of sequence alignments and structural superimposition was performed by means of ClustalW [28] and PyMOL [29], respectively.

DTSS components and catalytic fields

Activation energy lowering Δ representing catalytic activity of a molecular environment could be alternatively expressed as the difference of transition state $\Delta E_{TS.C}$ and substrate $\Delta E_{SC.C}$ interaction energies with active site constituents, C [5-7]:

$$\Delta = \Delta E_{TS.C} - \Delta E_{SC.C} \qquad (1)$$

Differential Transition State Stabilization (DTSS) Δ could be further partitioned into electrostatic Δ_{EL}, exchange Δ_{EX}, delocalization Δ_{DEL} and correlation Δ_{CORR} components defined within hybrid variation-perturbation interaction energy decomposition [8]:

$$\Delta = \overbrace{\Delta_{EL} + \Delta_{EX} + \Delta_{DEL} + \Delta_{CORR}}^{\Delta MP2} \quad \overbrace{\quad\quad\quad}^{\Delta SCF} \quad \overbrace{\quad\quad}^{\Delta HL} \quad \overbrace{\quad}^{\Delta EL} \qquad (2)$$

defining hierarchy of successive approximate models of enzyme catalytic activity

$$\Delta_{MP2} > \Delta_{SCF} > \Delta_{HL} > \Delta_{EL} > \sum_i q_i (V_i^{TS} - V_i^{SC}) \qquad (3)$$

Results of the analysis of the physical nature of catalytic activity for chorismate mutase [6] and 4-methyl-5-β-hydroxyethylthiazole kinase [7] as well as other model systems indicate dominant role of electrostatic term Δ_{EL}, which could be further approximated by the sum of products of differential molecular electrostatic potentials $V_i^{TS} - V_i^{SC}$ and atomic charges q_i, representing a molecular environment. This allows to derive static catalytic field Δ_s *i.e.* general characteristics of the optimal catalytic environment by mapping $\Delta_s = -(V_i^{TS} - V_i^{SC})$ values on electronic isodensity surface. Extremal values of catalytic field determined solely as the difference of molecular electrostatic potentials of superimposed transition state and substrates coincided with the locations of conserved aminoacid residues in aminoacyl t-RNA synthetases [30] and chorismate mutases [6] confirming assumed enzyme reaction mechanism.

Regional DFT electronic chemical potential

The boundaries of chemical species within Regional Density Functional Theory (R-DFT) [31] are represented by the electrons turning point region recognized as isosurface of zero kinetic energy density [32]. The R-DFT kinetic energy density ($n_T(\vec{r})$) divides the reactants space into the electronic drop region (R_D, $n_T(\vec{r}) > 0$) limited by interface surface (S, $n_T(\vec{r}) = 0$), where electron density is accumulated, and the electronic atmosphere region (R_A, $n_T(\vec{r}) < 0$), where classical movement of electrons is not allowed [32]. Within the linear

approximation [33] the regional electronic chemical potential is defined for non-relativistic limit of RQED energy density as:

$$\mu = \frac{\partial E}{\partial N} = \frac{\partial \int \varepsilon(\vec{r})dr}{\partial \int n(\vec{r})dr} = \int \frac{\partial \varepsilon(\vec{r})}{\partial n(\vec{r})} dr \qquad (4a)$$

$$\mu_R = \left(\frac{\partial E_R}{\partial N_R} \right) \Leftrightarrow \frac{\varepsilon(\vec{r})}{n(\vec{r})} \qquad (4b)$$

where is electron density and is the corresponding local energy density at particular point of space. The details of relevant method are described elsewhere [31-33].

Details of calculation

The structures of PKA-bound substrate and transition state were extracted from previous density functional theory QM/MM simulation [20]. The model complexes used for interaction energy calculation were then simplified to include PKA residues in a close vicinity of the reaction site (Figure 1). As the adenosine part of ATP does not change its position and geometry throughout the phosphoryl transfer, ATP molecule was represented by methyl triphosphate only. Similarly, the substrate peptide was limited to serine residue. Whenever justified by significant distance to the substrate/transition state complex, the backbone of selected residues was also removed leaving the respective side chains capped with Cα atoms. Such a treatment was applied to Val44, Lys72, Gln84, Glu91, Lys168, Asn171, and Phe187 residues. All dangling bonds were saturated with hydrogen atoms optimized at HF/6-31G(d) level of theory. The positively charged lysine and negatively charged aspartate and glutamate residues were considered. The model included also several conserved water molecules [34] (Wat410, Wat412, Wat447, Wat459, Wat476, Wat477, Wat597, Wat635) as observed in 1ATP PDB structure, and two water molecules from QM/MM calculation [20] (WatSOL1 and WatSOL2) without any crystallographic counterparts. The first crystallographic information about coordination of the two Mg^{2+} ions has been provided by Zheng et al. [35]. The crystal structures showed metal ions octahedrally coordinated by six oxygen atoms [35,36]. Magnesium ion occupying the high-affinity Mg1 site is surrounded by β- and γ-phosphates of ATP, two oxygen atoms from Asp184 carboxylate group, and two water molecules (WAT447, WAT477). Magnesium ion from the secondary metal site, Mg2, is coordinated by the α- and γ-phosphates, the bridging oxygen located between β- and γ-phosphates, one oxygen atom of Asp184, the side chain carbonyl oxygen of Asn171, and water molecule WAT635. Binding energy was determined in a pairwise fashion encompassing two-body interactions occurring

in dimers composed of substrate/transition state and an individual component of PKA active site. Interaction energy decomposition was performed with 6-31G(d) basis set using a modified version of GAMESS code [37] The MP2/6-31G(d) electron density and electrostatic potentials required for catalytic fields were obtained with Gaussian03 package [38]. All graphics presented herein was prepared by means of PyMOL [29] and VMD [40] software.

Results and Discussion

Sequence and structure alignment

The flexible structure alignment [27] (Figure 2) and the corresponding sequence alignment of serine/threonine and tyrosine kinases (Figure 3) was employed to emphasize the agreement between conserved active site residues and the most catalytically active residues as indicated by DTSS and catalytic fields. Noticeably, all the highly conserved active site residues are charged or at least polar species. Lys72 and Asp166 (according to PKA enumeration) are absolutely conserved in both sequence motifs (Figure 3) and rotamers (Figure 2) in all presented kinases. Although also highly conserved, Lys168 and Asn171 have no fixed sequence position or residue type, *i.e.* Lys168 is often replaced with arginine (Figure 2b) that in case of some members of tyrosine kinases family might be present even two positions further along the sequence (Figure 3).

Catalytic activity of active site components

In order to determine the possible catalytic role of key active site residues, DTSS energy was calculated for particular residues interacting with transition state/substrate complex and further decomposed to reveal the physical nature of DTSS effects. The catalytic contribution of a given residue can be expressed as its ability to lower the activation energy barrier by stronger interaction with transition state in comparison to reactants, i.e. differential transition state stabilization. Accordingly, the presence of such a catalytically active residue results in the reaction rate enhancement and promotes catalysis. Considering partitioning of the system into transition state/substrates and a remaining environment, magnesium ions were arbitrarily assigned to the latter.

Table 1 and Figure 4 provide the catalytic activity of individual active site components in terms of their DTSS energy values calculated at different levels of theory. The residues are

arranged according to decreasing contribution to activation barrier lowering as indicated by the increasing values of DTSS energy. Noticeably, the entire PKA active site provides as much as -51.39 kcal/mol of total differential transition state stabilization (Table 1).

Apart from magnesium ions, the most pronounced catalytic effects seem to be exhibited by absolutely conserved Lys72 and Asp166 residues (Δ_{MP2}=-22.71 and –13.26 kcal/mol, respectively; see Table 1). Lys72 interacting with α- and β-phosphates (Figure 1) has been postulated to facilitate the phosphorylation process without affecting the binding of ATP [10]. Owing to 844-fold decrease in kcat and essentially retained ATP binding properties, alanine-substituted mutants seem to be deficient in ATP transition state binding [41]. In excellent agreement with these experimental results, Lys72 appears to participate in a catalytic step by outstanding preferential stabilization of the transition state (Figure 4). Another strictly conserved active site residue, Glu91, is located behind Lys72 (relative to ATP-serine complex). Instead of being involved in direct contact with any of the substrates, it forms a conserved salt-bridge with Lys72 residue (Figure 1). According to DTSS results, the presence of Glu91 results in a moderate transition state destabilization characterized by Δ_{MP2}=4.96 kcal/mol (Table 1). Presumably, the function of Glu91 consists in a proper positioning of the flexible Lys72 side chain to maximize its favorable interaction with ATP phosphate tail. Relatively large catalytic advantage resulting from the presence of Lys72 cancels destabilizing influence of Glu91 residue.

As confirmed by the results presented in Ref. 20, Asp166 residue serves as a catalytic base that accepts substrate peptide proton during the phosphorylation process. However, the proton transfer step occurs after the transition state which still encompasses deprotonated Asp166 carboxylate and neutral hydroxyl moiety of substrate serine. Therefore, to reveal its possible role in DTSS effects, this particular residue was treated as a part of a catalytic environment. Significant negative value of Asp166 DTSS energy (Δ_{MP2}=-13.26 kcal/mol, Table 1) indicates, that its additional function might indeed consist in preferential stabilization of the transition state.

Both magnesium ions are among the most catalytically effective components of PKA active site (Figure 4). Their contribution to DTSS effects is equal to –32.36 (Mg2) and –15.15 kcal/mol (Mg1; Table 1). Interestingly, magnesium ion occupying the so called inhibitory site, i.e. Mg2, is capable of a greater transition state stabilization than Mg1 located at a high affinity metal binding site. Nonetheless, these results are consistent with preliminary interaction energy analysis from Ref. 20, as well as the results obtained for thiazole kinase [7]. In contrast to magnesium ions themselves, their ligands appear to contribute little if any to

overall transition state stabilization. The most pronounced inhibitory effects result from the presence of Asp184 and Wat447 belonging to Mg1 coordination sphere. These particular residues destabilize the transition state by 3.06 and 2.21 kcal/mol (Table 1). Noteworthily, mutagenesis results show that Asp184 residue is essential for the catalytic function of PKA as yeast cells with Asp184Ala mutation are inviable [41]. Presumably, Asp184 role encompasses the chelation of Mg1 and the lack of the latter is the main reason for impaired PKA action. Considering the overall impact of individual magnesium-ligands complexes, the sum of DTSS energy values associated with a given magnesium ion and its coordination sphere (*i.e.* Asp184, Wat447, and Wat477 or Asn171, and Wat635 for Mg1 and Mg2, respectively) indicates similar influence in terms of transition state stabilization to that exhibited by magnesium ions treated separately. In particular, DTSS energy of Mg1 and Mg2 ions in complexes with their ligands is equal to –10.98 and –33.09 kcal/mol, respectively. It seems that catalytic benefits resulting from the presence of magnesium ions make it worthwhile to employ residues that anchor a magnesium ion even if they exhibit moderate inhibitory effects.

The glycine-rich loop encompassing residues 47-57 constitutes a highly conserved motif within a kinase catalytic core. Owing to its extended "U" shape spatially aligned with ATP triphosphate tail, glycine-rich loop is capable of tightly enfolding the nucleotide by means of both hydrogen bonding and hydrophobic interactions. Accordingly, its primary function appears to involve the positioning of γ-phosphate of ATP for subsequent phosphoryl transfer step [12]. Since mutagenesis studies have revealed no major changes in PKA catalytic competency upon the mutation within this particular region [42,43], it is not clear whether PKA benefits any transition state stabilization due to the presence of glycine-rich loop. Out of the six glycine-rich loop residues present in our model (see Figure 1), only Ser53 exhibits a certain degree of transition state destabilization (Δ_{MP2}=4.72 kcal/mol). This particular residue interacts via its backbone amide hydrogen with γ-phosphate. As shown experimentally [43], it is the presence of a backbone interaction that matters most: side chain modifications do not significantly alter the catalytic features of PKA. Presumably, the role of Ser53 is essentially structural as it involves the optimal positioning of a terminal phosphate group. The catalytic activity of the remaining glycine-rich loop residues is moderate with the most prominent transition state stabilization coming from Gly55 residue (Δ_{MP2}=-4.09 kcal/mol). It is noteworthy, however, that the collective influence of Thr51, Gly52, Ser53, Phe54, Gly55, and Val57 residues encompasses Δ_{MP2} of –6.20 kcal/mol, indicating relatively large contribution to the lowering of activation energy barrier.

Lys168 residue being an important component of a catalytic loop has been suggested to support both the phosphoryl transfer process and peptide binding [10]. Apparently, this residue is not directly involved in the phosphorylation reaction [20], yet the presence of hydrogen bonding interactions between its side chain and both the γ-phosphate as well as the hydroxyl group from substrate serine implies its possible contribution to the catalytic process. Surprisingly enough, the most obvious role consisting in transition state stabilization provided by Lys168 side chain charged oppositely to the reactants is not an issue here, as Lys168 has been found to strongly destabilize the transition state (Table 1 and Figure 4). This result is consistent with interaction energy analysis presented in Ref. 20 and further supports the conclusion stated therein (based on the results of molecular dynamics simulation) that the primary role of Lys168 is to keep the reactants in geometry of the catalytically competent complex. Further discussion of the possible role of Lys168 is given in the next subsection.

The remaining components of PKA active site do not seem to provide an appreciable degree of transition state stabilization or destabilization. Except of water molecule designated as WatSOL1 and Thr201 residue, the absolute contribution of the other residues to the lowering of activation energy barrier does not exceed 1 kcal/mol. WatSOL1 molecule located in the proximity of Lys72 is hydrogen-bonded to α-phosphate. Similarly to Lys72 residue, WatSOL1 seems to promote catalysis providing Δ_{MP2}=-1.81 kcal/mol of transition state stabilization. Since no counterpart of WatSOL1 has been found in PKA X-ray structure, this result should probably be considered as a suggestion that the presence of a water molecule in this particular position would be favorable for catalysis. Thr201 anchors both Asp166 and Lys168 via hydrogen bonds to their side chains. While it has been suggested that such a location of Thr201 residue might imply its involvement in a proton shuttle between Asp166 and Lys168 [12], it has not yet been confirmed. According to DTSS analysis, Thr201 role encompasses additional activation barrier lowering of -1.13 kcal/mol.

In addition to total DTSS contributions to PKA catalytic activity, this analysis aimed at determination of the physical nature of active site interactions. Therefore, binding energy was partitioned into the components with clear physical sense as defined within the variational-perturbational decomposition scheme [8]. Noticeably, such a description of the interactions provides also a convenient way to assess the most suitable level of theory. Since subsequent constituents of interaction energy define a hierarchy of theoretical models differing in both accuracy and computational cost, rational design and validation of approximate models of catalytic activity can be accomplished. The overall quality of consecutive levels of theory applied in analysis of the interactions can be assessed by their

comparison to the most accurate description provided by MP2 calculations. The results of such a comparison encompassing the respective correlation coefficients are presented in Table 1. Only minor decrease in correlation accompanies neglect of subsequent interaction energy corrections. In particular, electron correlation effects appear to be insignificant as the correlation coefficient of SCF results is still equal to 1. Similarly, correlation coefficients of 0.98 and 0.99 indicate minor contribution of delocalization and exchange components. As it can be seen from Figure 4, these two terms tend to cancel each other resulting in a relatively correct description provided by electrostatic energy. Apparently, electrostatic effects play a dominant role in the system under study supporting the general hypothesis about electrostatic origin of enzymatic catalysis [44].

Predicting of the optimal catalytic environment

The fact that PKA active site interactions are mainly electrostatic in nature supports further approximation encompassing the study of differential electrostatic potential generated by transition state relative to reactants. Since the characteristic of a catalyst is inherently related to the reaction subjected to catalysis, it is appealing to derive the optimal catalytic environment entirely from the knowledge of transition and reactant state structures. Implementation of this idea in the form of catalytic fields allows for de novo prediction of the molecular environment that would be the most catalytically active. Alternatively, the comparison of catalytic fields with known catalyst (*e.g.*, enzyme) might aid its redesign toward novel substrate and/or reaction type. Noticeably, catalytic fields-based prediction of the effect of a particular amino acid substitution proved to be successful in case of thiazole kinase [7].

Catalytic fields for PKA-catalyzed phosphoryl transfer reaction are presented in Figure 5. In an excellent agreement with the predicted optimal arrangement of charged moieties are the Asp166 and Lys72 residues as well as both magnesium ions. Similarly to the DTSS results, Lys168 seems to disfavor catalysis as it is present in a region, where the negative charge is expected to be optimal. Nevertheless, Lys168 (or its equivalent arginine) is a highly conserved residue indicating that catalytic machinery of kinases employs its flexible, positively charged side chain. The possible structural role of Lys168 [20] has already been discussed. Another inconsistency between catalytic field predictions and the electrostatic characteristics of PKA active site appears to involve Asp184 residue. Since this particular residue anchors the mandatory magnesium ion, it does not probably affect the catalytic activity as the negative charge of its side chain is screened by the magnesium ion.

Figure 6 shows map of regional electronic chemical potential on the interface surface of isolated TS structure. The regions of lower (red) and higher (blue) chemical potential represent the individual local escaping tendency of charge density around TS atoms. Electrons migrate from regions with higher μ to regions with lower μ. The positive charge of Lys168 attracts electron density of hydrogen bonded γ-phosphate and substrate serine hydroxyl oxygen atoms to less favorable regions with higher chemical potential. Apparently, the unfavorable influence of positive charge of Lys168 as indicated by catalytic fields and DTSS analysis arises from the fact that electrostatic interaction acts against the gradient of specific local electronic chemical potential displayed by isolated TS. The interaction of other active site residues with TS might induce such polarization of charge density on phosphate oxygen atoms which will drain electrons into the regions with lower chemical potential providing thermodynamical stabilization. The binding sites (on phosphate tail) for Mg^{2+} ions display lower chemical potential towards metal atoms position and the same observation can be made regarding the interaction between alpha-phosphate oxygen atom and Lys72 residue. The relatively high μ around serine hydroxyl group proton is associated with significantly electron deficient region thus electrostatic interaction with Asp168 is physically and thermodynamically favorable. It should be noted that in contrast to phosphorus and hydrogen, oxygen atoms display high electron density on the interface surface. The usual trend of electronic energy density is to decrease with increasing electron density. However phosphate oxygen atoms show high μ in electron rich regions which indicates unfavorable electronic energy in that region. All active site residues, except for Lys168, seem to help to rearrange electron distribution in TS so it flows to lower μ regions.

Despite of adverse catalytic effect of Lys168 residue, it plays significant role in binding of the reactants and keeping them in close contact conformation. The positioning of a gamma-phosphate is critical for catalysis. Lys168 is the catalytic loop residue that interacts directly with one of the gamma-phosphate oxygen atoms before and after the phosphoryl transfer [45-49] and is located in a close proximity of hydroxyl group of substrate serine (Figure 1). Mutagenesis studies show the complete loss of catalytic activity of K168A mutant [47] and molecular dynamics simulations performed on wild type and K168A mutant [20] have suggest structural role in the catalytic mechanism. However Lys168 is a major source of TS destabilization in the active site. When considering the local chemical potential on TS, it is not surprising that presence of magnesium cations on phosphate tail can suppress that unfavorable effect by 10 $kcal \cdot mol^{-1}$. It has been proposed that Lys168 makes nucleophilic

attack easier by neutralization of the negative charges developing in the course of catalysis and mainly orients the transferred phosphate [47], which is consistent with our findings.

Conclusions

The phosphoryl transfer reaction catalyzed by protein kinase A has been analyzed in terms of the ability of individual active site components to preferentially stabilize the transition state. Further decomposition of DTSS energy has allowed for elucidation of the major interaction energy components influencing the catalytic activity of PKA. Finally, catalytic fields have been derived and compared to the catalytic surroundings provided by PKA. The main findings can be summarized as follows:

- The overall differential transition state stabilization exhibited by PKA active site model exceeds -50 kcal/mol as calculated at MP2 level of theory.
- Identity of PKA residues exhibiting outstanding catalytic or inhibitory effects matches their sequence and structure conservation. Destabilization of the transition state resulting from the presence of a particular residue suggests a structural role of the latter. Another likely explanation involves the pairwise fashion of interaction energy calculation that entirely neglects any possible many-body contributions.
- PKA active site components with the most significant contribution to differential transition state stabilization include both magnesium ions as well as Lys72 and Asp166 residues. While several magnesium ligands have been found to destabilize the transition state, the total influence of individual complexes involving a magnesium ion along with its coordination sphere is always stabilizing.
- Despite moderate inhibitory effects due to the presence of Ser53 residue, the total DTSS energy of residues building the glycine-rich loop is negative confirming its involvement in transition state stabilization.
- While Lys168 residue appears to provide a certain degree of transition state destabilization, its function probably involves an optimal spatial alignment of the reactants.
- Due to the minor role of electron correlation and mutual cancellation of delocalization and exchange effects, interaction energy within PKA active site is mainly electrostatic in nature.
- The comparison between spatial arrangement of PKA active site components and the catalytic fields representing the electrostatic characteristics of an ideal catalyst provides a

qualitative measure of complementarity of both charge distributions achieved in an evolutionary way.

References

[1] Borman, S. Chem. Eng. News 2004, 82, 35-39

[2] Gao, J.; Ma, S.; Major, D. T.; Nam, K.; Pu, J.; Truhlar, D.G. Chem.Rev. 2006, 106, 3188-3209

[3] Warshel, A.; Sharma, P.K.; Kato, M.; Xiang, Y.; Liu, H.; Olsson M.H.M. Chem. Rev. 2006, 106, 3210-3235

[4] Schramm V.L. J. Biol. Chem. 2007, 282, 28297-28300

[5] Sokalski, W.A. J. Mol. Catalysis 1985, 30, 395-410

[6] Szefczyk, B.; Mulholland, A. J.; Ranaghan, K. E.; Sokalski, W. A. J. Am. Chem. Soc. 2004, 126, 16148-16159

[7] Dyguda-Kazimierowicz, E.; Sokalski, W. A.; Leszczyński, J. J. Mol. Model. 2007, 13, 839-849

[8] Sokalski W. A.; Roszak, S.; Pecul. K. Chem. Phys. Lett. 1988, 153,153-159

[9] Jiang, L.; Althoff, E.A.; Clemente, F.R.; Doyle, L.; Röthlisberger, D.; Zanghellini, A.; Gallaher, J.L.;. Betker, J.L; Tanaka, F.; Barbas III, C.F.; Hilvert, D.; Houk, K.N.; Stoddard, B.L.; Baker D. Science 2008, 319, 1387-1391

[10] Adams, J.A. Chem. Rev. 2001, 101, 2271-2290

[11] Taylor, S. S., Bubis, J., Toner-Webb, J., Sarawat, L. D., First, E. A., Buechler, J. A., Knighton, D. R., and Sowadski, J. FASEB J. 1988, 2, 2677-2685

[12] Johnson, D.A.; Akamine, P.; Radzio-Andzelm, E.; Madhusudan, M.; Taylor, S.S. Chem. Rev. 2001, 101, 2243-2270 and references cited therein

[13] Hart, J. C.; Hillier, I. H.; Burton, N. A.; Sheppard, D. W. J. Am.Chem. Soc. 1998, 120, 13535-13536

[14] Hart, J. C.; Sheppard, D. W.; Hillier, I. H.; Burton, N. A. Chem. Commun. 1999, 79-80

[15] Hutter, M. C.; Helms, V. Protein Sci. 1999, 8, 2728-2733

[16] Hirano, Y.; Hata, M.; Hoshino, T.; Tsuda, M. J. Phys. Chem. B 2002, 106, 5788-5792

[17] Hutter, M. C.; Helms, V. Int. J. Quantum Chem. 2003, 95, 479-486

[18] Valiev, M.; Kawai, R.; Adams, J. A.; Weare, J. H. J. Am.Chem. Soc. 2003, 125, 9926-9927

[19] Diaz, N.; Field, M. J. J. Am.Chem. Soc. 2004, 126, 529-542

[20] Cheng, Y.; Zhang, Y.; McCammon, J. A.; J. Am. Chem. Soc. 2005, 127, 1553-1562

[21] Henkelman, G.; LaBute, M. X.; Tung, C.-S.; Fenimore, P. W.; McMahon, B. H. Proc. Natl. Acad. Sci. U S A. 2005, 102, 15347–15351

[22] Cheng, Y.; Zhang, Y.; McCammon, J. A. Protein Sci 2006, 15, 672-683

[23] Akola, J.; Jones, R.O. J. Phys. Chem. B 2003, 107, 11774-11783

[24] Armstrong, R. N.; Kondo, H.; Granot, J.; Kaiser, E. T.; Mildvan, A. S. Biochemistry 1979, 18, 1230-1238

[25] Yoon, M. Y.; Cook, P. F. Biochemistry 1987, 26, 4118-4125

[26] Cook, A.; Lowe, E. D.; Chrysina, E. D.; Skamnaki, V. T.; Oikonomakos, N. G.; Johnson, L. N. Biochemistry 2002, 41, 7301-7311

[27] Ye, Y.; Godzik, A. Bioinformatics 2003, 19, 246-255

[28] Thompson, J.D.; Higgins, D.G.; Gibson, T.J. Nucleic Acids Res 1994, 22, 4673–4680

[29] DeLano, W.L. The PyMOL Molecular Graphics System 2002, DeLano Scientific, San Carlos, CA, USA

[30] Sokalski, W.A.; Shibata, M.; Barak, D.; Rein, R. J. Mol. Evolution 1991, 33, 405-411

[31] Tachibana A. Theor. Chem. Acc. 1999, 102, 188–195

[32] Tachibana A. J. Chem. Phys. 2001, 115, 3497–3518

[33] Szarek, P.; Tachibana, A. J. Mol. Model. 2007, 13, 651-663 and references cited therein

[34] Shaltiel, S.; Cox, S.; Taylor, S.S. Proc. Natl. Acad. Sci. U S A. 1998, 95, 484–491

[35] Zheng J. et al., Acta Crystallogr., D49, 1993, 362-365

[36] Burk, D.L.; Hon, W.C.; Leung, A.K.-W.; Berghuis, A.M. Biochemistry 2001, 40, 8756-8764

[37] Góra, R.W.; Roszak, S.; Sokalski, W.A.; Leszczyński, J. Jackson State University, JSU preprint 1999

[38] Frisch MJ, Trucks GW, Schlegel HB, Scuseria GE, Robb MA, Cheeseman JR, Montgomery JA, Vreven JrT, Kudin KN, Burant JC, Millam JM, Iyengar SS, Tomasi J, Barone V, Mennucci B, Cossi M, Scalmani G, Rega N, Petersson GA, Nakatsuji H, Hada M, Ehara M, Toyota K, Fukuda R, Hasegawa J, Ishida M, Nakajima T, Honda Y, Kitao O, Nakai H, Klene M, Li X, Knox JE, Hratchian HP, Cross JB, Bakken V, Adamo C, Jaramillo J, Gomperts R, Stratmann \ RE, Yazyev O, Austin AJ, Cammi R, Pomelli C, Ochterski JW, Ayala PY, Morokuma K, Voth GA, Salvador P, Dannenberg JJ, Zakrzewski VG, Dapprich S, Daniels AD, Strain MC, Farkas O, Malick DK, Rabuck AD, Raghavachari K, Foresman JB, Ortiz JV, Cui Q, Baboul AG, Clifford S, Cioslowski J, Stefanov BB, Liu G, Liashenko A, Piskorz P, Komaromi I, Martin RL, Fox DJ, Keith T, Al-Laham MA, Peng CY, Nanayakkara A, Challacombe M, Gill PMW, Johnson B, Chen W, Wong MW, Gonzalez C, Pople JA, (2003) Gaussian 03, Revision C.02, Gaussian, Inc., Wallingford CT.

[39] Doi, K.; Szarek, P.; Nakamura, K.; Senami M.; Tachibana, A. Molecular Regional DFT program package Ver. 2, Tachibana Lab., Kyoto University, Kyoto, 2007

[40] Humphrey, W., Dalke, A. and Schulten, K., J. Molec. Graphics 1996, 14.1, 33-38

[41] Gibbs, C. S.; Zoller, M. J. J. Biol. Chem. 1991, 266, 8923-8931

[42] Hemmer, W.; McGlone, M. L.; Tsigelny, I.; Taylor, S. S. J. Biol. Chem. 1997, 272, 16946-16954.

[43] Aimes, R. T.; Hemmer, W.; Taylor, S. S. Biochemistry 2000, 39, 8325-8332.

[44] Náray-Szabó, G.; Fuxreiter, M.; Warshel, A. In Computational Approaches to Biochemical Reactivity; Náray-Szabó, G.; Warshel, A.; Understanding Chemical Reactivity; Kluwer: Dordrecht, 1997; pp 237-293

[45] Madhusudan, K.R.; Trafny, E.A.; Xuong, N.-h.; Adams, J.A., Ten Eyck, L.F.; Taylor, S.S., Sowadski, J.M.; Protein Science 1994, 3,176-187

[46] Smith, Ch.M.; Radzio-Andzelm, E.; Madhusudan, A. P.; Taylor, S.S.; Progress in Biophysics & Molecular Biology 1999, 71, 313-341

[47] Gonzalez, B.; Schell, M.J.; Letcher, A.J.; Veprintsev, D.B.; Irvine, R.F.; Williams, R.L.; Molecular Cell 2004, 15, 689–701

[48] LaRonde-LeBlanc, N.; Wlodawer, A.; Structure 2004, 12, 1585–1594

[49] Hanks, S.; Quinn, A.M.; Methods Enzymol. 1991, 200, 38-62

Table 1. Differential transition state stabilization (DTSS) energy (kcal/mol) at various levels of theory.

Active-Site Residue	Δ_{EL}	Δ_{HL}	Δ_{SCF}	Δ_{MP2}
Mg2	-28.57	-29.42	-37.20	-32.36
Lys72	-21.83	-16.38	-22.50	-22.71
Mg1	-13.88	-13.12	-16.70	-15.15
Asp166	-19.80	-11.01	-16.02	-13.26
Gly55	-3.64	-1.62	-4.16	-4.07
Thr51	-2.14	-1.82	-2.72	-2.42
Gly52	-1.05	-0.19	-2.66	-2.21
WatSOL1	-2.42	-0.39	-1.95	-1.81
Phe54	-0.91	1.80	-2.1	-1.68
Asn171	-0.69	0.92	-0.58	-1.35
Thr201	-1.82	-2.20	-1.22	-1.13
Wat477	-1.34	-0.36	-1.02	-1.09
Val57	-0.08	0.22	-0.53	-0.51
Gln84	-0.02	-0.02	-0.04	-0.02
Wat412	0.17	0.17	0.14	0.11
Gly200	-0.32	-0.62	-0.24	0.16
Wat410	0.25	0.25	0.29	0.27
Wat476	0.46	0.47	0.52	0.49
Wat635	2.63	0.93	0.87	0.63
Cys199	0.69	0.68	0.87	0.70
WatSOL2	1.11	0.40	0.92	0.73
Wat597	1.03	1.15	0.87	0.78
Wat459	1.09	0.98	1.05	0.81
Phe187	0.61	0.30	1.08	0.97
Wat447	1.54	2.83	2.66	2.20
Asp184	7.04	6.98	4.24	3.06
Ser53	5.17	2.56	4.56	4.72
Glu91	5.90	5.90	5.48	4.96
Lys168	28.21	21.03	27.74	27.83
Sum	-42.60	-29.57	-58.34	-51.39
R	0.985	0.984	0.9969	1

Figure 1. Structure of the PKA active site in complex with substrates (drawn in grayscale). Except of substrates and water molecules, only heavy atoms are shown. The coloring scheme applied to active site components reflects their contribution to differential transition state stabilization (according to the energy scale in a right bottom part of the figure).

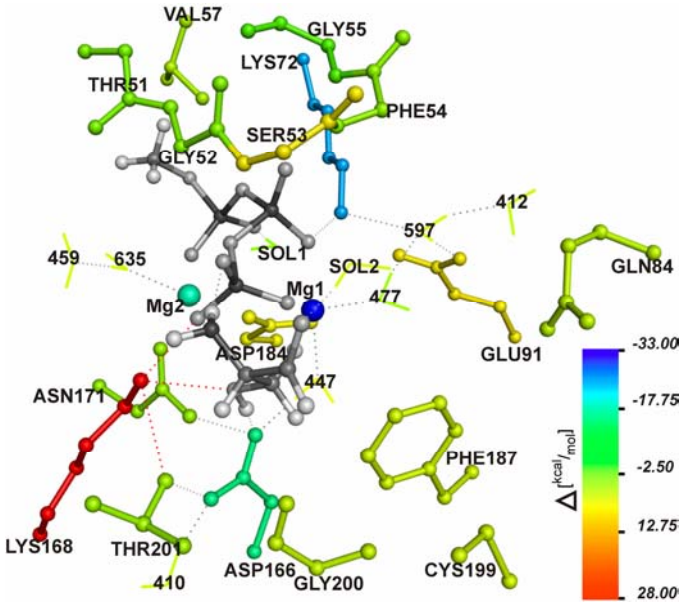

Figure 2. The flexible structure alignment of active site residues highly conserved within protein kinases family. PKA Mg-ATP complex is given in green CPK representation, whereas stick representation is used to show the superimposed amino acid residues extracted from structures with the PDB codes listed below. Thick sticks correspond to PKA residues.

a) Serine/threonine kinases: 1o6l, u5r, 1uu3, 1vyw, 1phk, 1csn, 1jks, 1wmk, 2i0e, 1vjy, 2cn8, 2iwi, 2hw6, 1ig1, 2j90, 2br1, 1na7, 1xws, 2j51, 2a19, 1m2r, 1mru, 2buj. Tyrosine kinases: 1x8b, 2dq7, 1qpc.

b) Tyrosine kinases: 1yvj, 1gag, 1u46, 1xba, 2ivs. The conservative Lys168 residue (distinguished by thicker stick representation) is substituted by arginine residue located two amino acid positions further along the sequence.

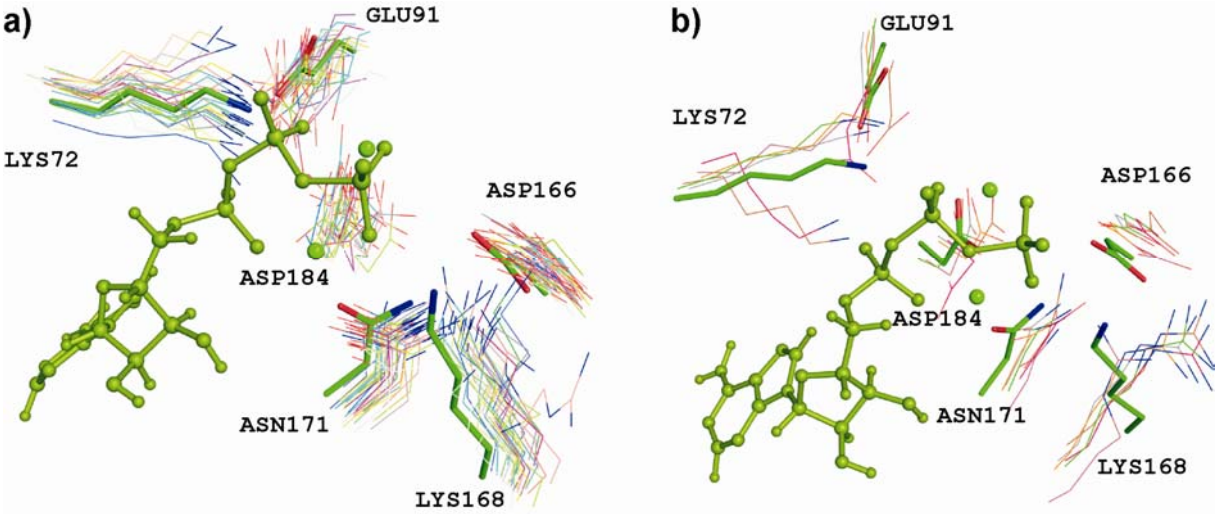

Figure 3. Multiple sequence alignment of highly conserved sequence regions of representative protein kinases. The first sequence belongs to mouse PKA studied herein. Absolutely conserved residues are marked with asterisks in the header row. Background coloring refers to geometrically overlapping residues and indicates their charge (red and pink correspond to positively and negatively charged amino acids, respectively). Histogram in the bottom part of figure indicates quality of the alignment for each residue column. A height of bars represents conservation score associated with each position (high score values indicate a well-conserved position).

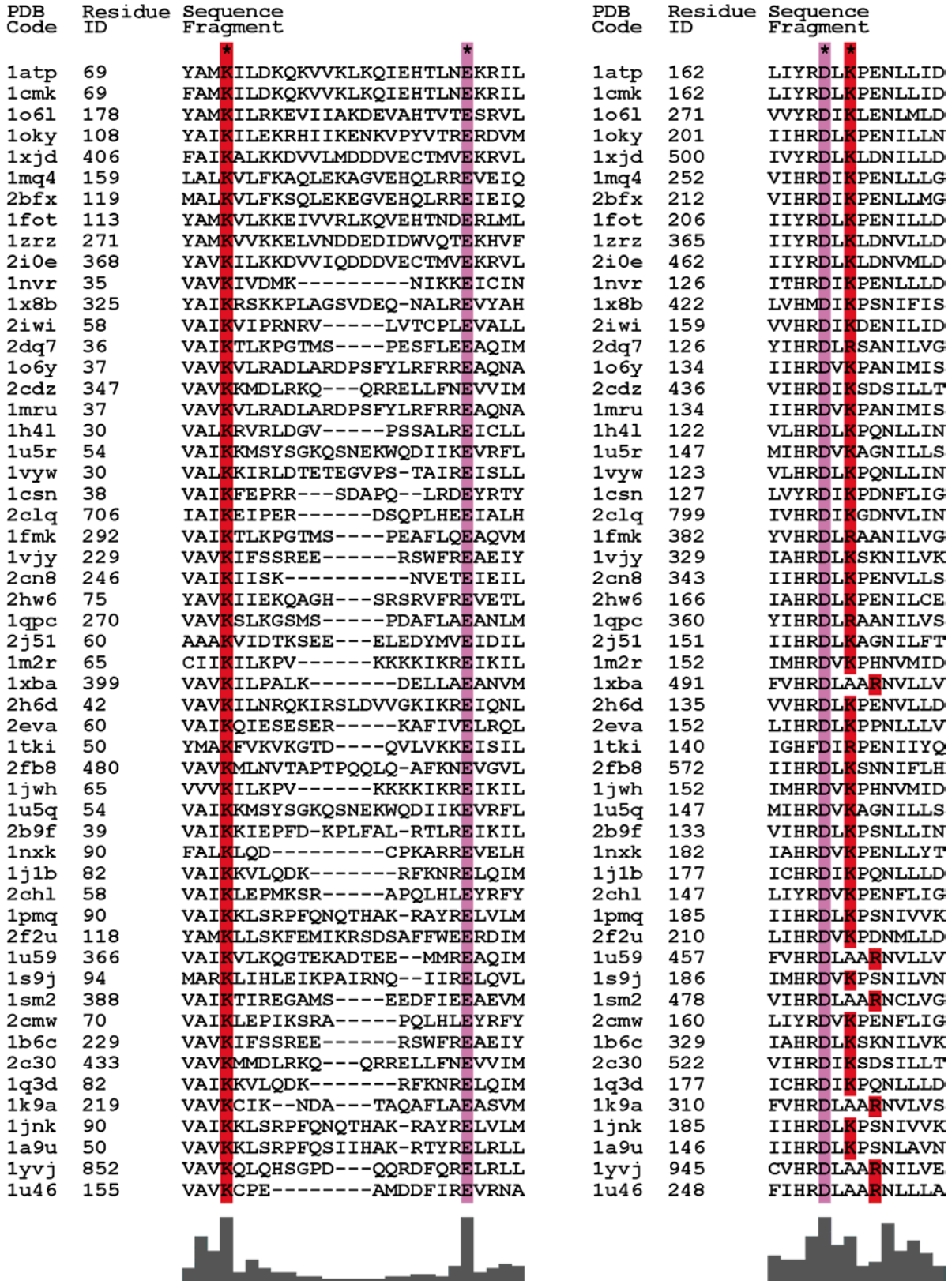
PDB Code
Residue ID
Sequence Fragment
1atp 69 YAMKILDKQKVVKLKQIEHTLNEKRIL
1cmk 69 FAMKILDKQKVVKLKQIEHTLNEKRIL
1o6l 178 YAMKILRKEVIIAKDEVAHTVTESRVL
1oky 108 YAIKILEKRHIIKENKVPYVTRERDVM
1xjd 406 FAIKALKKDVVLMDDDVECTMVEKRVL
1mq4 159 LALKVLFKAQLEKAGVEHQLRREVEIQ
2bfx 119 MALKVLFKSQLEKEGVEHQLRREIEIQ
1fot 113 YAMKVLKKEIVVRLKQVEHTNDERLML
1zrz 271 YAMKVVKKELVNDDEDIDWVQTEKHVF
2i0e 368 YAVKILKKDVVIQDDDVECTMVEKRVL
1nvr 35 VAVKIVDMK---------NIKKEICIN
1x8b 325 YAIKRSKKPLAGSVDEQ-NALREVYAH
2iwi 58 VAIKVIPRNRV-----LVTCPLEVALL
2dq7 36 VAIKTLKPGTMS----PESFLEEAQIM
1o6y 37 VAVKVLRADLARDPSFYLRFRREAQNA
2cdz 347 VAVKKMDLRKQ---QRRELLFNEVVIM
1mru 37 VAVKVLRADLARDPSFYLRFRREAQNA
1h4l 30 VALKRVRLDGV-----PSSALREICLL
1u5r 54 VAIKKMSYSGKQSNEKWQDIIKEVRFL
1vyw 30 VALKKIRLDTETEGVPS-TAIREISLL
1csn 38 VAIKFEPRR---SDAPQ--LRDEYRTY
2clq 706 IAIKEIPER------DSQPLHEEIALH
1fmk 292 VAIKTLKPGTMS----PEAFLQEAQVM
1vjy 229 VAVKIFSSREE------RSWFREAEIY
2cn8 246 VAIKIISK----------NVETEIEIL
2hw6 75 YAVKIIEKQAGH---SRSRVFREVETL
1qpc 270 VAVKSLKGSMS-----PDAFLAEANLM
2j51 60 AAAKVIDTKSEE---ELEDYMVEIDIL
1m2r 65 CIIKILKPV------KKKKIKREIKIL
1xba 399 VAVKILPALK-------DELLAEANVM
2h6d 42 VAVKILNRQKIRSLDVVGKIKREIQNL
2eva 60 VAIKQIESESER-----KAFIVELRQL
1tki 50 YMAKFVKVKGTD----QVLVKKEISIL
2fb8 480 VAVKMLNVTAPTPQQLQ-AFKNEVGVL
1jwh 65 VVVKILKPV------KKKKIKREIKIL
1u5q 54 VAIKKMSYSGKQSNEKWQDIIKEVRFL
2b9f 39 VAIKKIEPFD-KPLFAL-RTLREIKIL
1nxk 90 FALKLQD---------CPKARREVELH
1j1b 82 VAIKKVLQDK-------RFKNRELQIM
2chl 58 VAIKLEPMKSR-----APQLHLEYRFY
1pmq 90 VAIKKLSRPFQNQTHAK-RAYRELVLM
2f2u 118 YAMKLLSKFEMIKRSDSAFFWEERDIM
1u59 366 VAIKVLKQGTEKADTEE--MMREAQIM
1s9j 94 MARKLIHLEIKPAIRNQ--IIRELQVL
1sm2 388 VAIKTIREGAMS----EEDFIEEAEVM
2cmw 70 VAIKLEPIKSRA-----PQLHLEYRFY
1b6c 229 VAVKIFSSREE------RSWFREAEIY
2c30 433 VAVKMMDLRKQ---QRRELLFNEVVIM
1q3d 82 VAIKKVLQDK-------RFKNRELQIM
1k9a 219 VAVKCIK--NDA---TAQAFLAEASVM
1jnk 90 VAIKKLSRPFQNQTHAK-RAYRELVLM
1a9u 50 VAVKKLSRPFQSIIHAK-RTYRELRLL
1yvj 852 VAVKQLQHSGPD---QQRDFQRELRLL
1u46 155 VAVKCPE--------AMDDFIREVRNA
PDB Code
Residue ID
Sequence Fragment
1atp 162 LIYRDLKPENLLID
1cmk 162 LIYRDLKPENLLID
1o6l 271 VVYRDIKLENLMLD
1oky 201 IIHRDLKPENILLN
1xjd 500 IVYRDLKLDNILLD
1mq4 252 VIHRDIKPENLLLG
2bfx 212 VIHRDIKPENLLMG
1fot 206 IIYRDLKPENILLD
1zrz 365 IIYRDLKLDNVLLD
2i0e 462 IIYRDLKLDNVMLD
1nvr 126 ITHRDIKPENLLLD
1x8b 422 LVHMDIKPSNIFIS
2iwi 159 VVHRDIKDENILID
2dq7 126 YIHRDLRSANILVG
1o6y 134 IIHRDVKPANIMIS
2cdz 436 VIHRDIKSDSILLT
1mru 134 IIHRDVKPANIMIS
1h4l 122 VLHRDLKPQNLLIN
1u5r 147 MIHRDVKAGNILLS
1vyw 123 VLHRDLKPQNLLIN
1csn 127 LVYRDIKPDNFLIG
2clq 799 IVHRDIKGDNVLIN
1fmk 382 YVHRDLRAANILVG
1vjy 329 IAHRDLKSKNILVK
2cn8 343 IIHRDLKPENVLLS
2hw6 166 IAHRDLKPENILCE
1qpc 360 YIHRDLRAANILVS
2j51 151 IIHRDLKAGNILFT
1m2r 152 IMHRDVKPHNVMID
1xba 491 FVHRDLAARNVLLV
2h6d 135 VVHRDLKPENVLLD
2eva 152 LIHRDLKPPNLLLV
1tki 140 IGHFDIRPENIIYQ
2fb8 572 IIHRDLKSNNIFLH
1jwh 152 IMHRDVKPHNVMID
1u5q 147 MIHRDVKAGNILLS
2b9f 133 VIHRDLKPSNLLIN
1nxk 182 IAHRDVKPENLLYT
1j1b 177 ICHRDIKPQNLLLD
2chl 147 LIYRDVKPENFLIG
1pmq 185 IIHRDLKPSNIVVK
2f2u 210 LIHRDVKPDNMLLD
1u59 457 FVHRDLAARNVLLV
1s9j 186 IMHRDVKPSNILVN
1sm2 478 VIHRDLAARNCLVG
2cmw 160 LIYRDVKPENFLIG
1b6c 329 IAHRDLKSKNILVK
2c30 522 VIHRDIKSDSILLT
1q3d 177 ICHRDIKPQNLLLD
1k9a 310 FVHRDLAARNVLVS
1jnk 185 IIHRDLKPSNIVVK
1a9u 146 IIHRDLKPSNLAVN
1yvj 945 CVHRDLAARNILVE
1u46 248 FIHRDLAARNLLLA

Figure 4. The components of differential transition state stabilization (DTSS) energy (kcal/mol). For each residue, the transition state stabilization energy (relative to substrates) is given at subsequent levels of theory. Vertical arrows show the mutual cancellation of correlation, delocalization, and exchange corrections to the MP2 interaction energy.

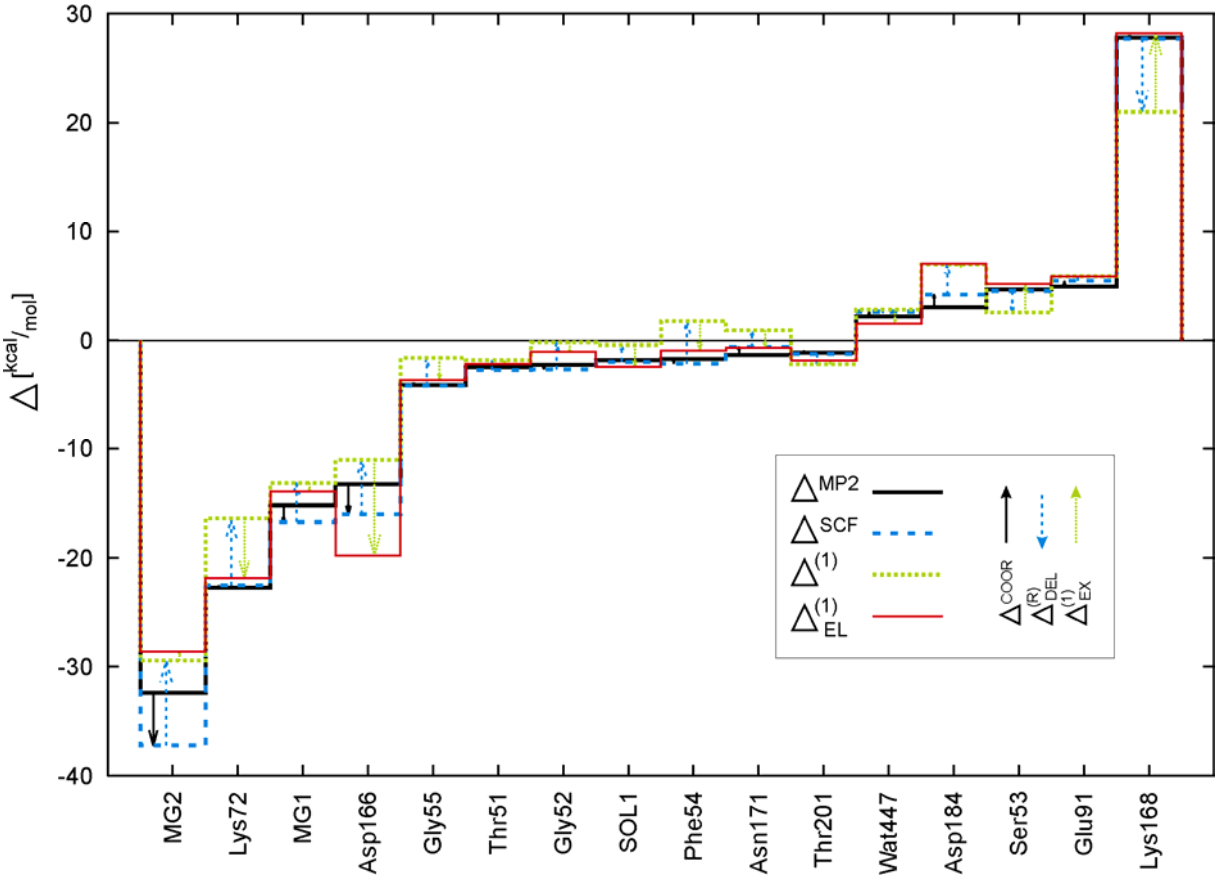

Figure 5. Catalytic fields for the PKA-catalyzed phosphorylation reaction. The color of electronic isodensity surface represents differential electrostatic potential around transition state/substrates with red and blue regions corresponding to negative and positive charges, respectively. The sign of differential potential is inverted to show electrostatic properties of an optimal catalytic environment. Superimposed with the latter is the actual arrangement of the most proximate PKA residues.

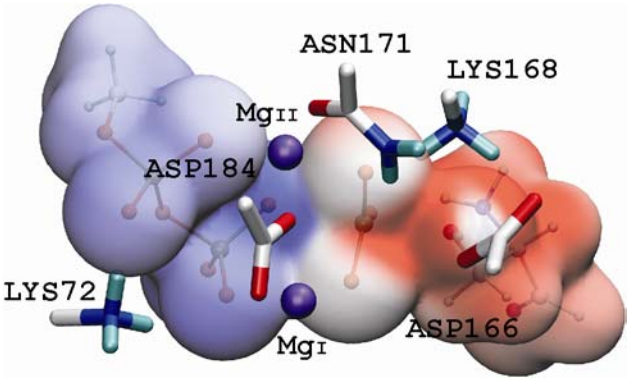

Figure 6. Electronic chemical potential on the zero isosurface of RDFT kinetic energy density around isolated TS structure. The regions of high and low chemical potential are mapped using color scale. Selected active site residues are shown in grayscale.

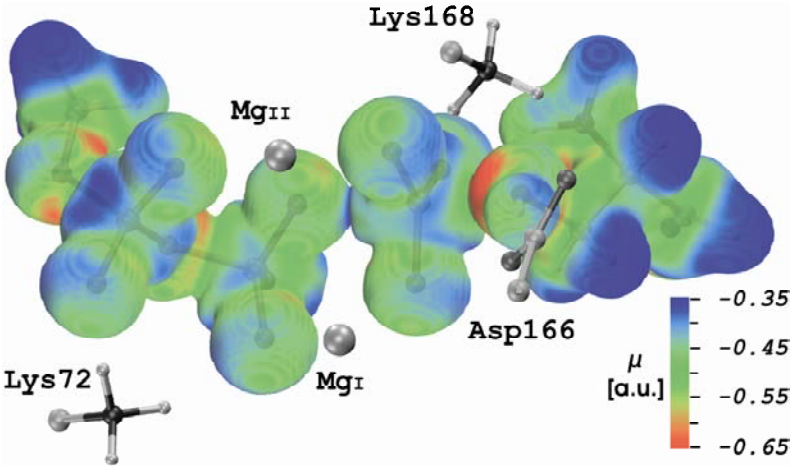

CHAPTER 6

Theoretical studies of the transition states along the reaction coordinates of [NiFe] hydrogenaze.

1. Introduction

With the growing need to develop alternative energy resources, hydrogen has attracted attention as a candidate fuel and the manufacturing and application technologies of low-cost hydrogen have been developed for the commercialization of fuel cells. Hydrogenases are considered to be a useful material in this application. [1–9] Hydrogenases are enzymes that catalyze under anaerobic conditions by the reaction

$$2H^+ + 2e^- \rightleftarrows H_2 \ . \qquad (1)$$

The hydrogenases, [NiFe] hydrogenase, [NiFeSe] hydrogenase and [Fe] hydrogenase, have been studied. [NiFe] hydrogenase has Ni and Fe atoms at its active site, which play a central role in the catalytic reaction. It is found in anaerobic bacteria, such as Desulfovibrio gigas (Dg) and Desulfovibrio vulgaris Miyazaki F (DvMF). The structure of [NiFe] hydrogenase from Dg has been investigated by several groups [10–14] and that from DvMF by Higuchi et al. [15–17] Groups [18–20] have investigated [NiFe] hydrogenase from other bacteria by X-ray crystallography and EPR spectroscopy. [NiFeSe] hydrogenase (with a selencysteine in the place of a cysteine residue at the active site) from Desulfomicrobium baculatum [21] and [Fe] hydrogenase (with a $[Fe_4S_4]$ cluster and a [2Fe] cluster at the active site, very similar to the active site of [NiFe] hydrogenase) from Clostridium pasteurianum [22] and Desulfovibrio desulfuricans [23] have also been crystallized and investigated by X-ray crystallography.

We have focused our study on [NiFe] hydrogenase from Dg and DvMF. Figure 1-1 shows the entire structure of [NiFe] hydrogenase from Dg. The active site is shown in the magnified part of Figure 1-1 and its structure is shown in Figure 1-2. These figures show the three diatomic ligands L1, L2, and L3 coordinated to the Fe atom and a bridging atom X between the Ni and Fe atoms. The ligand X in Dg is assigned to μ-O and in DvMF to μ-S. [11–17] The diatomic ligands L1, L2 and L3 are also different between Dg and DvMF; two of the ligands have been identified as CN and one as CO for Dg, [11–14,24–26] while it has been proposed that L1 can be identified as SO, CO, or CN and L2 and L3 as CN or CO for DvMF. [15–17] The bacteria Allochromatium vinosum has a similar active center and same ligand pattern as Dg. [27] The SO ligand in DvMF is considered an important factor in characterizing the properties of DvMF as it causes a peculiar function of the enzyme.

Studies of synthetic active sites of [NiFe] hydrogenase and [Fe] hydrogenase have been conducted [28–35] and breakthroughs are expected for the mass production of hydrogen

molecules. For this purpose, a more basic study of real hydrogenases in bacteria is required. Theoretical studies have been taken place for investigating the catalytic mechanism inside these large proteins by DFT, semi empirical study, QM/MM study and so on. Unfortunately, we can only compute the small part of the entire protein by DFT since the current computers do not have the adequate ability. Therefore, we have to determine the model system which has been calculated by DFT. We usually define the active site of the [NiFe] hydrogenase as the model system. For [NiFe] hydrogenases, many mechanisms of the catalytic reaction have been suggested. [36,37] One of these schemes is shown in Figure 1-3. [37,38] One of these schemes is shown in Figure 1-3. [37,38] The oxidized system (Ni-A and Ni-B) is reduced under an atmosphere of H_2 and switches to a reduced system. This scheme has four paramagnetic states: Ni-A, Ni-B, Ni-C and Ni-L and three EPR-silent states: Ni-SU, Ni-SI and Ni-R. Volbeda et al. have found that Ni-SI has the two different states, denoted by Ni-SII and Ni-SIII. [10,11] The Ni-A and Ni-B states have been obtained under aerobic conditions. The oxidized system is considered to be catalytically inactive and the reduced system is considered to be active. Ni-A can be activated slowly while Ni-B can be activated rapidly and these forms are called the unready and ready forms, respectively. [39,40] [NiFe] hydrogenase in the reduced system catalyzes the H_2 production process effectively. Ni-C has a central role in the catalyzation and is changed into Ni-L under illumination at low temperature (<100 K). Competing with H_2 production, CO inhibits the activation process to give a Ni-CO state. [41-45] Researchers are divided in their views of the structures of the EPR-silent states, such as Ni-SU, Ni-SI and Ni-R. [36,37] Volbeda et al. propose that there are two different states in NI-SI [10–12] and that these EPR-silent states are one part of the catalytic cycle. Lately, DvMF in the oxidized system has been activated by H_2S elimination under an atmosphere of H_2. [15,16] We have found that the reverse cycle of the activation process can be a H_2 production process itself. That is, [NiFe] hydrogenase has two H_2 production processes: one is the normal process in the reduced system as mentioned above and the other is the reverse reaction of the initial stage of H_2S elimination in the oxidized system. This novel mechanism will be discussed in detail in section 2-2.

Several groups have investigated the catalytic system of [NiFe] hydrogenase and their findings are not yet consistent. Some light has been shed on this complicated puzzle by excellent review articles focusing on experimental investigations, [34,46–50] synthetic studies of hydrogenase [34,46] and theoretical studies. [37,51,52] In this paper we review the published studies, comparing the characteristics of the proposed catalytic mechanisms, focusing especially on the transition states. Identification of the transition state and the

activation energy barrier is critical to determining which reaction coordinate plays a crucial role. However, none of the reviews have focused on transition states in relation to the catalytic reaction coordinates.

2. Theoretical Investigations of [NiFe] hydrogenase

2.1 Active site of DG

Dg has been investigated by several groups and the structure of the active site determined by experimental investigations is consistent among these groups. In this section we review the mechanisms proposed by these groups. In section 2.1.1 we summarize the computational details of each of the studies. In section 2.1.2 we review the optimized structure of each state, the paramagnetic states, Ni-A, Ni-B, Ni-C, and Ni-L, as shown in Figure 2-1, and the EPR-silent states, Ni-SU, Ni-SI and Ni-R, as shown in Figure 2-2. In the section 2.1.3 we show each group's reaction mechanism.

2.1.1 Computational details

We detail here the functional and basis set of each groups' density functional calculations.

(i) Pavlov et al. [53–55] performed B3LYP [56,57] energy calculations with the large 6-311+G-(2d, 2p) basis set. They used the LANL2DZ [58-60] set in the B3LYP [56,57] geometry optimizations in Gaussian94. [61]

(ii) Hall et al. [62–64] optimized the geometries with the B3LYP [56,57] functional and the double-ζ basis set. They used the modified version of the Hay and Wadt effective core potentials (ECPs) [65] in Gaussian98. [61]

(iii) Gioia et al. [66,67] optimized the geometries with the BLYP [56,68] functional and the double- ζ basis set (D95) [69] on the first-row atoms and Los Alamos ECPs [58-60] on the S, Fe and Ni atoms in Gaussian94. [61]

(iv) We optimized the geometries with the B3LYP [56,57] functional. We used the LanL2DZ basis set [56–60] with the Huzinaga polarization function [70] for Fe, Ni and S and with the Dunning [69] function for the other atoms. In the QM/MM study, [71–75] we used the same functional and basis set for the QM region and used the UFF method for the MM region. We used the ONIOM method [76–79] in Gaussian03. [61]

(v) Stein et al. in ref. 80 used the BLYP [56,68] functional and the DZVP basis set in DGauss4.0. [81]

(vi) Stein et al. in ref. 82 optimized the geometries with the BP86 [68,83–85] functional and the non-relativistic Slater-type DZP basis set and used a g- and hyperfine-tensor study with the relativistic Slater-type DZP basis set and TZP basis set. In refs. 38, 52, 82, and 86 Stein et al. used the Amsterdam Density Functional package (ADF). [87,88]

(vii) Stein et al. in refs. 38 and 86 optimized the geometries with the BP86 [68,83–85] functional and the double-ζ Slater-type basis set and examined a g- and hyperfine-tensor study by the zero-order regular approximation (ZORA) [89-92] implemented in ADF [87,88] with the same basis set as in ref. 80.

(viii) Amara et al. [93] performed QM/MM [71–75] calculations. They used the B3LYP [56,57] functional with the double-ζ basis set for the QM region. They used the Hay and Wadt ECPs for the non-metal atoms [58–60] and the Dunning ECPs for the Ni and Fe atoms. [69] For the MM region, they used the potential energy due to covalent interactions accounting for the bonds, bond angles, proper and improper dihedral angles, and the potential energy due to the nonbonding interactions (Coulomb and Lennard-Jones). This calculation was performed using the quantum mechanical CADPAC program. [94]

2.1.2 The structure of each state

Several groups have proposed structures of each state from theoretical analysis based on experimental studies. There is good agreement for the structures of the paramagnetic states Ni-A, Ni-B, Ni-C and Ni-L, while the proposed structures of the EPR-silent states do not agree. In contrast to the other groups, Pavlov et al. and Hall et al. have proposed that H2 attacks the Fe atom in the first step of the mechanism. Hence we show their paramagnetic states in Figure 2-1(a) and their EPR-silent states in Figure 2-2(a). The paramagnetic and EPR-silent states of the other groups are shown in Figure 2-1(b) and Figure 2-2(b), respectively.

Ni-A is more stable than Ni-B, and Ni-A is reduced slowly into the activated state Ni-SU. Ni-A has been considered to have $O2^-$ as the bridging ligand X. Hall et al. [51,62–64] compared the optimized structure of each candidate for the structure of Ni-A and determined that X is OH^-, as shown in Figure 2-1(a). Ni-B is reduced faster than Ni-A and is activated into Ni-SI. With theoretical and experimental data for Ni-B, Gioia et al. proposed that there is no bridging ligand X in the structure of Ni-B. [66,67] However, Stein et al. concluded that the ligand X for Ni-B is OH^- by comparing the experimental structure by X-ray crystallography with the optimized structure of DFT. [52,80,82] They also calculated the structural and spectroscopic data of the Ni-B state by the relativistic DFT study with the ZORA and

compared them with the experimental data of the hyperfine- and g-tensors, [38,86] and thus confirmed that X is OH−. Other groups have also investigated Ni-A and Ni-B with ZORA. [95,96]

The paramagnetic Ni-C state is a part of the catalytic cycle and has the redox state Ni(III)Fe(II). Hall et al. proposed that the ligand X in Ni-C is an H atom and one of the cysteine residues is protonated, based on a comparison between their DFT study and experimental data. [51,62–64] Other groups have come to the same conclusion. [51,52,55] Recently, however, Stein et al. have stated a slightly different opinion. Based on g- and hyperfine-tensor experimental data and their relativistic DFT calculations, Stein et al. conclude that Ni-C has no protonated cysteine residue. [38] In addition, Pavlov and Siegbahn et al. propose that one of the bridging cysteine ligands is liberated from the Ni atom, accompanying a H atom. [53–55] Ni-L has not been examined much because it is not important to the catalytic cycle. Stein et al. consider that Ni-L has a vacancy at X and has no protonated ligand. [38,52,80,82,86]

We next review the EPR-silent states Ni-SU, Ni-SI, and Ni-R. The proposed structures of these states by each group are shown in Figure 2-2. The determination of the structures of EPR-silent complexes is harder than for those of the paramagnetic complexes and hence the structures are still controversial. Ni-SU is produced by the reduction of Ni-A. Ni-SI is produced by the reduction of Ni-B or Ni-SU. As mentioned above, Ni-B is reduced and transformed into Ni-SI faster than Ni-A into Ni-SI. Ni-SU and Ni-SI have the same redox state Ni(II)Fe(II), resulting in their EPR-silent properties. Stein has investigated the structure of Ni-SI and proposed that the Fe atom of Ni-SI is coordinated by H_2O. [38,52,80,82,86] Gioia et al. and Hall et al. propose that there is no atom at the position of the ligand X in Ni-SI. [51,62-64,66,67] Hall et al. suggest structures for two Ni-SI states, based on the experimental data by Volbeda et al., [10,11] called Ni-SIa and Ni-SIb. They state that Ni-SIa is transformed into NI-SIb by protonation at the S atom of a cysteine residue. [51] Amara et al. suggest a rather unique structure by QM/MM study [93] and called the two Ni-SI states Ni-SI1 and Ni-SI2, again based on Volbeda et al. [10,11] They suggest that NI-SI1 and Ni-SI2 have a H atom as the bridge ligand X. The structure of NI-SI2 with a H atom added is in surprisingly good agreement with the experimental structure. [93]

Ni-R is also an EPR-silent state and has the redox state Ni(II)Fe(II). Hall et al. have shown that Ni-R has H_2 bound to the Fe atom by DFT calculations and considering the electronic states. [51,62–64] Gioia et al. and Stein et al. propose similar structures. [66,67] Both groups state that the bridging ligand X is a H atom and Ni-R has another coordinated H

atom. Gioia et al. propose that the H atom coordinates to one of the cysteine residues bound to the Ni atom and Stein proposes that it coordinates to the Ni atom directly.

We have to admit subtlety for the local spin state of Ni. Hall et al. suggest that Ni-SIa and Ni-R are high-spin Ni(II) states based on L-edge XAS data [98] and on this assumption they optimized the structures, giving a distorted tetrahedral coordination of the Ni atom. They found that high-spin structures were in better agreement with the experimental structure than the low-spin structures, confirming their prediction that Ni-SIa and Ni-R are high-spin complexes. However, other groups consider Ni-SIa and Ni-R to be low-spin Ni(II) complexes. [37,98] The low-spin states have square planar coordination. Further theoretical studies are clearly required on this point. Stein et al. and Gioia et al. have recently investigated the Ni-S4 complexes as a model of the [NiFe] hydrogenase active site together to lead the conclusion that the Ni-SIa and Ni-R is spin-crossover state and the density functional BP86 is the most suited functional to describe the structural features and Ni-SI and Ni-R are spin crossover states. [99] They suggested that high-spin states with B3LYP have too stable energy, compared with the calculations with BP86 or B3LYP*. [100-102]

Recently we calculated the energy of Ni-SIa by QM/MM calculations. We considered the active site as a QM region, the atoms within 7.0 Å of the active site as an MM-free region and the other atoms within 13.0 Å of the active site as an MM-fixed region, as shown in Figure 2-3. Atoms in the MM-free region can move during the optimization process, while atoms in the MM-fixed region cannot move. The total energy of the low-spin state was 1.5 kcal/mol less than that of the high-spin state. The QM region of the low-spin state was 10.2 kcal/lmol less stable than the high-spin state, while the energy of the MM region was 11.7 kcal/mol more stable than the high-spin state. Based on this calculation, we conclude that Ni-SI is a low-spin complex. This difference of 1.5 kcal/mol is small and hence we did not attempt to make a more accurate calculation. A similar calculation for Ni-R is currently underway.

2.1.3 Catalytic mechanism of hydrogen production

Several groups have proposed catalytic cycles, [38,42,53,54,62,66,67,80] each characterized by the atom that coordinates to the Ni atom, Fe atom or cysteine residues and each cycling through the paramagnetic state Ni-C and the EPR-silent states Ni-SIa and Ni-R. The first of these proposed cycles, by Pavlov et al., simulated the catalytic mechanism with a relatively small model of the active site. Figure 2-4(a) [53] shows the mechanism of Pavlov et al. The transition states are also calculated and the activation energy is found to be 7.9 cal/mol,

as shown in Figure 2-5(a). [53] The mechanism is unique compared with the results of the other groups in that the bond between the bridging cysteine residue and Ni atom is cut and the bimetallic CN ligand of the Fe atom moves toward the vacant position between the Fe and Ni atoms. Pavlov et al. later slightly modified the mechanism, as shown in Figure 2-4(b). [54] Again the transition states are calculated and the activation energy is found to be 3.1 kcal/mol, as shown in Figure 2-5(b). [54] Including the solvent effect, the energy is 6.4 kcal/mol. As in the unmodified mechanism, [53] the bond between the bridging cysteine residue and Ni atom is cut. However, it has been commented that this result is achieved because the model is too small. Amara et al. claim that the small size of the model allows the bridging cysteine ligands to move too much; [93] the ligands are bonded to amino acid chains and cannot move freely.

The proposed catalytic mechanism of Hall et al. is shown in Figure 2-6. [51,62–64] They calculated the transition states using the same model as Pavlov et al. The activation energy is 14.2 kcal/mol when the model of the active site has a neutral charge and is 12.4 kcal/mol when the model has a minus charge, as shown in Figure 2-7. [63]

The proposed mechanism of Dole et al. is shown in Figure 2-8 [42] and has been confirmed by Gioia et al. [66,67] They calculated the optimized structure by DFT and performed frontier orbital analysis. From their analysis, they proposed that H_2 reacts with the Ni atom to give two seperate H atoms. Recently we have simulated this mechanism and have found the transition state in the low-spin state. The energy diagram and the structure of the calculation model are shown in Figure 2-9. The Mulliken atomic charge densities of the Fe, Ni, three S atoms and two H atoms are shown in Table 2-1. The three S atoms and two H atoms are identified by suffixes in Figure 2-8. The Mulliken atomic charge is known to be unreliable for the transition metals and hence we pay careful attention to it. At the first step, H2 is bonded to the Ni atom or S3 atom. Next, H1 is trapped between the Fe and Ni atoms, which is indicated by the Mulliken atomic charge of H1 and H2.

Finally, the charge is absorbed by the Fe atom. The electron density on the S1 atom also increases between the transition state and Ni-R, which is consistent with the findings of Gioia et al., [67] and hence it has an active role in the H_2 cleavage. The activation energy is 29.3 kcal/mol, while the reverse reaction, that is, the hydrogen production, requires only 10.4 kcal/mol.

The suggested catalytic mechanism of Stein et al. is shown in Figure 2-10. [38,52,86] This mechanism is more complicated than the others. In this reaction, the solvent H_2O has an important role in the heterolytic cleavage of H_2. One of the H atoms of H_2 is attracted to the O atom of H_2O, forming an H_3O+ ion. This results in the bridging ligand X being a H atom.

These considerations are based on relativistic DFT research with ZORA and the experimental g- and hyperfine-tensors. [38,86]

Amara et al. suggested a rather unique mechanism, as shown in Figure 2-11. NI-SI2 of this mechanism has a μ-H^-, based on a QM/MM study. The structure of NI-SI2 with μ-H^- is in good agreement with the experimental structure. [93]

To conclude, several controversial mechanisms have been proposed based on theoretical investigations. To characterize a mechanism it is necessary to calculate the reaction path including the transition states. The transition states and activation energies will then specify the catalytic mechanism.

2.2 Active site of DVMF

Unlike Dg, the structure of the active site of DvMF is still controversial. Higuchi et al. have investigated the structure by X-ray crystallography [15–17] and Tüker et al. have performed semi-empirical calculations. [103,104] Stein et al. investigated the structure of [NiFe] hydrogenase from DvMF by DFT calculations and g- and hyperfine-tensor calculations as well as for Dg. [38,80] The active site of DvMF is shown in Figure 1-2. It has been proposed that the L1 ligand is SO, CO or CN and the L2 and L3 ligands are CN or CO, but the exact nature of the ligands has not been determined. The widely accepted ligand pattern is SO for L1, CN for L2 and CO for L3. We have made a theoretical investigation of the pattern: CO for L1, CN for L2 and CO for L3. We assumed that there exists a mechanism holding the bridge ligand X during the catalytic reaction. Amara et al. [93] suggested a fixed bridge ligand of a H atom during the reaction. We considered a bridge ligand S atom fixed during the catalytic cycle, as shown in Figure 2-12, because it is experimentally found to be the most probable bridge ligand in DvMF. [15,16] We introduce our preliminary results in this section. Other patterns are being studied, incorporating possible ligands of bridging and nonbridging characters with various redox and spin states under the influence of the environment.

2.2.1 The optimized structure of the DvMF model

We have devised a DvMF model by substituting a methyl group for cysteine (Cys) in the structural formula shown in Figure 2-12, where S1 is the bridging atom between the Fe atom and Ni atom, S2 is one of the bridging S atoms of the cysteine amino acids and S3 is one of the S atoms of the cysteine amino acids coordinated to the Ni atom only. We then optimized the structure. The optimized atomic distances and angles of the DvMF model in the

low-spin and high-spin oxidized states (1a and 1b, where the suffixes a and b denote the low-spin state and the high-spin state, respectively) are tabulated in Table 2-2.

Model 1b is less stable by 19.46 kcal/mol than 1a, but 1b closely resembles the structure derived from X-ray crystallography; [15,16] the optimized structural parameters of 1b agree with the X-ray structural parameters, except for the Ni-Fe distance. On the other hand, the distance between the Ni atom and S2 atom of 1a is 3.25 Å while the distance measured in the X-ray structure is 2.37 Å. The Ni-Fe distances of both calculated spin states do not agree with the X-ray measured distance; the Ni-Fe distance of the X-ray structure is 2.55 Å while that of 1a is 3.41 Å and that of 1b is 2.92 Å. The differences are too large to be regarded as uncertainties in the calculation. The same differences were reported by Stein et al. [80] The differences are due to deviations of the bond angles of S1-Ni-S2 and Si-Fe-S2. In fact, there is not much interaction between the Fe and Ni atoms. Therefore, the differences hardly affect the reaction mechanism.

2.2.2 Transition states of the activation process in the oxidized system

We examined the reaction mechanism of the activation process in the oxidized system and performed a more detailed investigated of DvMF [17] (which has a S atom at the bridging ligand of the active site). We defined the following mechanism (shown in Eq. (2)) based on the work of Higuchi et al. [15–17] As already mentioned, an oxidized system of DvMF can be activated by H_2S elimination under an atmosphere of H_2. The origin of the S atom in H_2S is not yet known, however, Higuchi et al. have assumed that it is a bridging S atom. [15,16] In the initial stage of H_2S elimination, DvMF model 1, which is called the Ni-A state in general, makes a complex with H_2 (complex 2). Then, the intermediary 3, with one of the hydrogen atoms abstracted by the S1 atom, is obtained through the transition states TS as follows:

$$\begin{aligned} &\mathbf{1a}(\mathrm{d}) + \mathrm{H_2} \rightarrow \mathbf{2a}(\mathrm{d}) \rightarrow [\mathbf{TSa}](\mathrm{d}) \rightarrow \mathbf{3a}(\mathrm{d}); \\ &\mathbf{1b}(\mathrm{q}) + \mathrm{H_2} \rightarrow \mathbf{2b}(\mathrm{q}) \rightarrow [\mathbf{TSb}](\mathrm{q}) \rightarrow \mathbf{3b}(\mathrm{q}), \end{aligned} \qquad (2)$$

where d and q in the parentheses denote doublet and quartet states respectively. Each low-spin state is more stable than the corresponding high-spin state. The activation energy in the low-spin states is 34.33kcal/mol. That of the high-spin states is 21.39kcal/mol. Therefore, the activation process such as the H_2S elimination is not easy to take place to some extent in the low-spin state, but the reaction become easier to happen after the low-spin state is excited and transferred to the high-spin state.

It is important to also consider the reverse cycle of the reaction shown in Eq. (2). This reverse cycle can generate H_2 with very low activation energy. We describe this reverse cycle

in detail, presenting the structures, electron states and energy diagrams of the complexes and transition states in the reaction of Eq. (2) in the next section, section 2.2.3.

2.2.3 H_2 production in the oxidized system

Here, we consider the reaction cycle of the H_2 production process in the oxidized system based on the reverse reaction of that given in Eq. (2), as shown in Figure 2-12,

$$\begin{aligned}
&\mathbf{1a}(\mathrm{d}) + 2\mathrm{H} \rightarrow \mathbf{4a}(\mathbf{4a'})(\mathrm{s}) + \mathrm{H} \\
&\qquad \rightarrow \mathbf{3a}(\mathrm{d}) \rightarrow [\mathbf{TSa}](\mathrm{d}) \rightarrow \mathbf{2a}(\mathrm{d}) \rightarrow \mathbf{1a}(\mathrm{d}) + \mathrm{H}_2\,; \\
&\mathbf{1b}(\mathrm{q}) + 2\mathrm{H} \rightarrow \mathbf{4b}(\mathbf{4b'})(\mathrm{t}) + \mathrm{H} \\
&\qquad \rightarrow \mathbf{3b}(\mathrm{q}) \rightarrow [\mathbf{TSb}](\mathrm{q}) \rightarrow \mathbf{2b}(\mathrm{q}) \rightarrow \mathbf{1b}(\mathrm{q}) + \mathrm{H}_2,
\end{aligned} \tag{3}$$

In the reaction of Eq. (3), protons and electrons are added to the system from outside the hydrogenase or from ferredoxins along the transport chain of the amino acids. This has been discussed by Pavlov et al. [53–55] The optimized species in the low- and high-spin states are shown in Figure 2-13(a) and (b), respectively. The DvMF models 1a and 1b can capture H radicals easily. After one H radical is adsorbed on S1 (4a and 4b), S3 (4a', 4b') or Ni (4b") atoms, the complex 2 is formed by capturing another H radical through the complex 3 and TS by the counterclockwise cycle in Figure 2-12. Energy diagrams for the reaction of Eq. (3) are shown in Figure 2-14. The reaction can generate H_2 with a very low activation energy; the activation energy is 6.74 kcal/mol for the reverse cycle in the high-spin states (3b → TSb → 2b) and is 16.94 kcal/mol in the low-spin states (3a → TSa → 2a).

For all models, the configuration of the ligands coordinated to the Ni atom is tetrahedral in the high-spin state and square planar in the low-spin state. The Mulliken atomic spin densities and charges of each state are shown in Table 2-3. In the high-spin state, the S1, S3 and Ni atoms have 0.5−0.8 spin densities, while the S1 and Ni atoms in 1a have hardly any spin. In addition, each of the S1, S3 and Ni atoms in 4b, 4b', and 4b" have 0.4−0.9 spin densities except the atoms abstracting the first H radical. The second H radical is captured easily on atoms with large spin density.

2.2.4 String model of the catalytic mechanism

In [NiFe] hydrogenase, catalyzation does not necessarily occur in the neutral state of the active site. Therefore we have to consider electron transfer during catalyzation. Hence, we calculated the energy of the anion and dianion complexes in the catalytic reaction, where the structures of each state are assumed to be optimized structures and transition states of the neutral state. This is the starting point in the analysis of the string model. [105–107] The

energy diagram is shown in Figure 2-15. From this diagram, we can see that the reaction occurs easily in the anion and dianion states. In the anion state, especially, the activation energy of the low-spin state is lower than the high-spin state and the complex $3a^-$ is the most stable of the other complexes. In the dianion states the energy of TSb^{2-} is lower than that of $3b^{2-}$, which indicates that the catalytic mechanism proceeds with no potential barrier if 3b and $3b^-$ get two or one electron respectively. Therefore, we suggest two catalytic mechanisms of the reduced system of DvMF:

$$\mathbf{3a^-} \rightarrow [\mathbf{TSa^-}] \rightarrow \mathbf{2a^-}, \qquad (4)$$

$$\mathbf{3b^-} \xrightarrow{+e^-} \mathbf{3b^{2-}} \longrightarrow [\mathbf{TSb^{2-}}] \xrightarrow{-e^-} \mathbf{2b^-}. \qquad (5)$$

These mechanisms need to be optimized for each electric state and the activation energies need to be calculated. The mechanisms proceed more readily than the mechanism of Eq. (3) in the neutral state.

2.2.5 Other patterns of ligands at Fe atom

We have investigated other patterns of ligands, such as L1=CN, L2=CO, L3=CN. This is identical to the active site of Dg with an S atom as the bridge ligand X. Figure 2-16 shows the energy diagram. The low-spin state of this model has a similar catalytic mechanism and energy diagram; the high-spin state is currently under investigation. We are also currently calculating other ligand patterns, such as the most probable pattern, L1=SO, L2=CN, L3=CO.

2.2.6 Quantum energy density

The electronic interaction in the H_2 production process in section 2.2.3 can be expressed in terms of the quantum energy densities [108–113] based on the regional DFT. [108–114] The electronic kinetic energy density $n_T(\vec{r})$ is defined as

$$n_T(\vec{r}) = \frac{1}{2}\sum_i v_i \left[\left\{ -\frac{\hbar^2}{2m}\Delta\psi_i^*(\vec{r}) \right\} \psi_i(\vec{r}) + \psi_i^*(\vec{r}) \left\{ -\frac{\hbar^2}{2m}\Delta\psi_i(\vec{r}) \right\} \right] \qquad (6)$$

where m is the mass of an electron, $\psi_i(\vec{r})$ is the natural orbital and v_i is the occupation number of $\psi_i(\vec{r})$. [108–111] $n_T(\vec{r})$ is important to the discussion on bond formation because the sign of $n_T(\vec{r})$ has a physical meaning with respect to electronic interaction; in the region $n_T(\vec{r}) > 0$ (electronic drop region, R_D) electrons can move freely in a classical fashion, whereas electrons cannot enter the region $n_T(\vec{r}) < 0$ (electronic atmosphere region, R_A) in a classical sense. [108–111] The total electronic force density $\vec{F}^S(\vec{r})$ is given by

$$\vec{F}^S(\vec{r}) = \vec{\tau}^S(\vec{r}) + \vec{X}^S(\vec{r}) \qquad (7)$$

where $\vec{\tau}^S(\vec{r})$ and $\vec{X}^S(\vec{r})$ denote the electronic tension density and electronic external force density, respectively. [108–111] $\vec{\tau}^S(\vec{r})$ has a quantum mechanical origin and is given by $\vec{\tau}^S(\vec{r}) = \left(\tau^{Sk}(\vec{r})\right)$ with

$$\tau^{Sk}(\vec{r}) = \frac{\hbar^2}{4m}\sum_i \nu_i \left\{ \psi_i^*(\vec{r}) \frac{\partial \Delta\psi_i(\vec{r})}{\partial x^k} - \frac{\partial \psi_i^*(\vec{r})}{\partial x^k} \Delta\psi_i(\vec{r}) + \frac{\partial \Delta\psi_i^*(\vec{r})}{\partial x^k}\psi_i(\vec{r}) - \Delta\psi_i^* \frac{\partial \psi_i(\vec{r})}{\partial x^k} \right\} \qquad (8)$$

for k = 1, 2, 3. In the stationary state, $\vec{\tau}^S(\vec{r})$ balances $\vec{E}(\vec{r})$, the electric field acting on an electron. [108–111] The detail of each bond can be expressed in terms of the stress tensor density, which is given by a 3×3 matrix $\vec{\tau}^S(\vec{r}) = (\tau^{Skl}(\vec{r}))$ with

$$\tau^{Skl}(\vec{r}) = \frac{\hbar^2}{4m}\sum_i \nu_i \left\{ \psi_i^*(\vec{r}) \frac{\partial^2 \psi_i(\vec{r})}{\partial x^k x^l} - \frac{\partial \psi_i^*(\vec{r})}{\partial x^k}\frac{\partial \psi_i(\vec{r})}{\partial x^l} + \frac{\partial^2 \psi_i^*(\vec{r})}{\partial x^k \partial x^l}\psi_i(\vec{r}) - \frac{\partial \psi_i^*}{\partial x^l}\frac{\partial \psi_i(\vec{r})}{\partial x^k} \right\} \qquad (9)$$

for k, l = 1, 2, 3. $n_T(\vec{r})$, $\vec{\tau}^S(\vec{r})$, the largest eigenvalues of $\vec{\tau}^S(\vec{r})$ and their eigenvectors in the formation and cleavage of chemical bonds in the TS can be calculated using the MR DFT program, [115] as shown in Figure 2-16.

As shown in Figure 2-17(a), in the low-spin state, the R_D due to the Ni atom is not directly connected to the R_D due to H atoms in TSa. This means that electrons cannot transfer classically between the Ni atom and H atoms. The area between S3 and the H atoms is filled with continuous R_D, but the compressive stress, for which the largest eigenvalue of $\vec{\tau}^S(\vec{r})$ is negative, [112,113] is distributed widely in the S3-H area, as shown in Figure 2-17(b), that is, the chemical-bond interaction in the S3-H area has been lost in TSa. On the other hand, in the high-spin state, not only is classical electron transfer allowed between the Ni and H atoms in TSb in terms of the continuous R_D, as shown in Figure 2-17(c), but Figure 2-17(d) also shows that the eigenvectors of the tensile stress, where the largest eigenvalue of $\vec{\tau}^S(\vec{r})$ is positive, [112,113] in the Ni-H area have a "spindle structure." [112,113] Such a spindle structure is observed in typical covalent bonds, [112,113] and therefore it is considered that the character of the Ni-H covalent bond seen in 3b remains strong even in TSb and that the height of the energy barrier from 3b to TSb is greatly suppressed due to the large covalent-bond-like interaction in TSb.

3. Conclusion

[NiFe] hydrogenase has received much attention as a material for use in hydrogen production. However, the catalytic mechanism is still controversial and the structures of some states have not yet been determined. Therefore further experimental and theoretical investigations are required. It is certain that the active site receives or gives electrons to other parts of the hydrogenase and the environment. There is also no consensus among research groups on a value of the activation energy of hydrogen cleavage. Catalytic mechanisms for Dg have been proposed, shown in Figures 2-4, 2-6, 2-8, 2-10 and 2-11, with activation energies of 3.1–29.3 kcal/mol. [NiFe] hydrogenase of DvMF has catalytic mechanisms in both the oxidized state and the reduced state. Further theoretical investigations are required because this reaction might occur more readily by electron transfer under the well-ordered control of the redox states.

References

[1] R. Cammack, Nature 397, 214–215 (1999).

[2] S. P. J. Albracht, Biochim. Biophys. Acta 1188, 167–204 (1994).

[3] M. W. W. Adams, Biochim. Biophys. Acta 1020, 115–145 (1990).

[4] E.-G. Graf and R. K. Thauer, FEBS Lett. 136, 165–169 (1981).

[5] Y. Nicolet, B. J. Lemon, J. C. Fontecilla-Camps, and J. W. Peters, Trends Biochem. Sci. 25, 138–143 (2000).

[6] J. W. Peters, Curr. Opin. Struct. Biol. 9, 670–676 (1999).

[7] D. S. Horner, B. Heil, T. Happe, and T. M. Embley, Trends Biochem. Sci. 27, 148–153 (2002).

[8] Y. Nicolet, C. Cavazza, and J. C. Fontecilla-Camps, J. Inorg. Biochem. 91, 1–8 (2002).

[9] E. J. Lyon, S. Shima, G. Buurman, S. Chowdhuri, A. Batschauer, K. Steinbach, and R. K. Thauer, Eur. J. Biochem. 271, 195–204 (2004).

[10] A. Volbeda, M.-H. Charon, C. Piras, E. C. Hatchikian, M. Frey, and J. –C. Fonticilla-Camps, Nature 373, 580–587 (1995).

[11] A. Volbeda, E. Garcin, C. Piras, A. L. de Lacey, V. M. Fernandez, E. C. Hatchikian, M. Frey, and J. C. Fontecilla-Camps, J. Am. Chem. Soc. 118, 12989–12996 (1996).

[12] D. L. Hallahan, V. M. Fernandez, E. C. Hatchikian, and R. Cammack, Biochim. Biophys. Acta. 874, 72–75 (1986).

[13] A. Volbeda and J. C. Fontecilla-Camps, Dalton Trans. 2003, 4030–4038 (2003).

[14] M. Teixeira, I. Moura, A. V. Xavier, J. J. G. Moura, J. LeGall, D. V. DerVartanian, H. D. Peck Jr., and B. H. Huynh, J. Biol. Chem. 264, 16435–16450 (1989).

[15] Y. Higuchi, T. Yagi, and N. Yasuoka, Structure 5, 1671–1680 (1997).

[16] Y. Higuchi, H. Ogata, K. Miki, N. Yasuoka, and T. Yagi, Structure 7, 549–556 (1999).

[17] H. Ogata, Y. Mizoguchi, N. Mizuno, K. Miki, S. Adachi, N. Yasuoka, T. Yagi, O. Yamauchi, S. Hirota, and Y. Higuchi, J. Am. Chem. Soc. 124, 11628–11635 (2002).

[18] M. Rousset, Y. Montet, B. Guigliarelli, N. Forget, M. Asso, P. Bertrand, J. C. Fontecilla-Camps, and E. C. Hatchikian, Proc. Natl. Acad. Sci. USA 95, 11625–11630 (1998).

[19] A. Volbeda, Y. Montet, X. Vernede, E. C. Hatchikian, and J. C. Fontecilla-Camps, Int. J. Hydrogen Energy 27, 1449–1461 (2002).

[20] P. M. Matias, C. M. Soares, L. M. Saraiva, R. Coelho, J. Morais, J. Le Gall, and M. A. Carrondo, J. Biol. Inorg. Chem. 6, 63–81 (2001).

[21] E. Garcin, X. Vernede, E. C. Hatchikian, A. Volbeda, M. Frey, and J. C. Fontecilla-Camps, Structure 7, 557–566 (1999).

[22] J. W. Peters, W. N. Lanzilotta, B. J. Lemon, and L. C. Seefeldt, Science 282, 1853–1858 (1998).

[23] Y. Nicolet, C. Piras, P. Legrand, E. C. Hatchikian, and J. C. Fontecilla-Camps, Structure 7, 13–23 (1999).

[24] K. A. Bagley, E. C. Duin, W. Roseboom, S. P. J. Albracht, and W. H. Woodruff, Biochemistry 34, 5527–5535 (1995).

[25] R. P. Happe, W. Roseboom, A. J. Pierik, S. P. Albracht, and K. A. Bagley, Nature 385, 126 (1997).

[26] A. L. de Lacey, E. C. Hatchikian, A. Volbeda, M. Frey, J. C. Fontecilla-Camps, and V. M. Fernandez, J. Am. Chem. Soc. 119, 7181–7189 (1997).

[27] B. Bleijlevens, B. W. Faber, and S. P. Albracht, J. Bio. Inorg. Chem. 6, 763–769 (1997).

[28] D. Sellmann, F. Geipel, F. Lauderbach, and F. W. Heinemann, Angew. Chem. Int. Ed. 41, 632–634 (2002).

[29] T. B. Rauchfuss, Inorg. Chem. 43, 14–26 (2004).

[30] M. Y. Darensbourg, E. J. Lyon, and J. J. Smee, Coord. Chem. Rev. 206–207, 533–561 (2000).

[31] F. Osterloh, W. Saak, D. Haase, and S. Pohl, Synthesis, Chem. Commun. 1997, 979–980 (1997).

[32] S. C. Davies, D. J. Evans, D. L. Hughes, S. Longhurst, and J. R. Sanders, Chem. Commun. 1999, 1935–1936 (1999).

[33] M. C. Smith, J. E. Barclay, S. P. Cramer, S. C. Davies, W.-W. Gu, D. L. Hughes, S. Longhurst, and D. J. Evans, Dalton Trans. 2002, 2641–2647 (2002).

[34] A. C. Marr, D. J. E. Spencer, and M. Schröder, Coord. Chem. Rev. 219–221, 1055–1074 (2001).

[35] S. J. George, Z. Cui, M. Razavet, and C. J. Pickett, Chem. Eur. J. 8, 4037–4046 (2002).

[36] R. Cammack, M. Frey, and R. Robson, Hydrogen as Fuel-Learning from Nature (Taylor and Francis, London, 2001).

[37] M. Bruschi, G. Zampella, P. Fantucci, and L. De Gioia, Coord. Chem. Rev. 249, 1620–1640 (2005).

[38] M. Stein and W. Lubitz, J. Inorg. Biochem. 98, 862–877 (2004).

[39] V. M. Fernandez, E. C. Hatchikian, D. S. Patil, and R. Cammack, Biochim. Biophys. Acta 883, 145–154, (1986).

[40] V. M. Fernandez, E. C. Hatchikian, and R. Cammack, Biochim. Biophys. Acta 832, 69–79 (1985).

[41] L. M. Roberts and P. A. Lindahl, Biochemistry 33, 14339–14350 (1994).

[42] F. Dole, A. Fournel, V. Magro, E. C. Hatchikian, P. Bertrand, and B. Guigliarelli, Biochemistry 36, 7847–7854 (1997).

[43] A. L. de Lacey, C. Stadler, V. M. Fernandez, E. C. Hatchikian, H. -J. Fan, S. Li, and M. B. Hall, J. Biol. Inorg. Chem. 7, 318–326 (2002).

[44] R. P. Happe, W. Roseboom, and S. P. J. Albracht, Eur. J. Biochem. 259, 602–608 (1999).
[45] G. Davidson, S. B. Choudbury, Z. Gu, K. Bose, W. Roseboom, S. P. J. Albracht, and M. J. Maroney, Biochemistry 39, 7468–7479 (2000).
[46] E. Bouwman and J. Reedijk, Coord. Chem. Rev. 249, 1555–1581 (2005).
[47] S. P. Best, Coord. Chem. Rev. 249, 1536–1554 (2005).
[48] A. L. de Lacey, V. M. Fernández, and M. Rousset, Coord. Chem. Rev. 249, 1596–1608 (2005).
[49] A. Volbeda and J. C. Fontecilla-Camps, Coord. Chem. Rev. 249, 1609–1619 (2005).
[50] D. J. Evans and C. J. Pickett, Chem. Soc. Rev. 32, 268–275 (2003).
[51] H.-J. Fan and M. B. Hall, J. Biol. Inorg. Chem. 6, 467–473 (2001).
[52] M. Stein and W. Lubitz, Curr. Opin. Chem. Biol. 6, 243–249 (2002).
[53] M. Pavlov, P. E. M. Siegbahn, M. R. A. Blomberg, and R. H. Crabtree, J. Am. Chem. Soc. 120, 548–555 (1998).
[54] M. Pavlov, M. R. A. Blomberg, and P. E. M. Siegbahn, Int. J. Quant. Chem. 73, 197–207 (1999).
[55] P. E. M. Siegbahn, M. R. A. Blomberg, M. Pavlov, and R. H. Crabtree, J. Biol. Inorg. Chem 6, 460–466 (2001).
[56] C. Lee, W. Yang, and R.G. Parr, Phys. Rev. B 37, 785–789 (1988).
[57] A.D. Becke, J. Chem. Phys. 98, 5648–5652 (1993).
[58] P. J. Hay and W. R. Wadt, J. Chem. Phys. 82, 270–283 (1985).
[59] W. R. Wadt and P. J. Hay, J. Chem. Phys. 82, 284–298 (1985).
[60] P. J. Hay and W. R. Wadt, J. Chem. Phys. 82, 299–310 (1985).
[61] M. J. Frisch, G. W. Trucks, H. B. Schlegel, G. E. Scuseria, M. A. Robb, J. R. Cheeseman, J. A. Montgomery, Jr., T. Vreven, K. N. Kudin, J. C. Burant, J. M. Millam, S. S. Iyengar, J. Tomasi, V. Barone, B. Mennucci, M. Cossi, G. Scalmani, N. Rega, G. A. Petersson, H. Nakatsuji, M. Hada, M. Ehara, K. Toyota, R. Fukuda, J. Hasegawa, M. Ishida, T. Nakajima, Y. Honda, O. Kitao, H. Nakai, M. Klene, X. Li, J. E. Knox, H. P. Hratchian, J. B. Cross, C. Adamo, J. Jaramillo, R. Gomperts, R. E. Stratmann, O. Yazyev, A. J. Austin, R. Cammi, C. Pomelli, J. W. Ochterski, P. Y. Ayala, K. Morokuma, G. A. Voth, P. Salvador, J. J. Dannenberg, V. G. Zakrzewski, S. Dapprich, A. D. Daniels, M. C. Strain, O. Farkas, D. K. Malick, A. D. Rabuck, K. Raghavachari, J. B. Foresman, J. V. Ortiz, Q. Cui, A. G. Baboul, S. Clifford, J. Cioslowski, B. B. Stefanov, G. Liu, A. Liashenko, P. Piskorz, I. Komaromi, R. L. Martin, D. J. Fox, T. Keith, M. A. Al-Laham, C. Y. Peng, A. Nanayakkara, M. Challacombe, P. M. W. Gill, B. Johnson, W. Chen, M. W. Wong, C. Gonzalez, and J. A. Pople, Gaussian 03, Revision C.02 (Gaussian, Inc., Wallingford CT, 2004).
[62] S. Niu, L. M. Thomson, and M. B. Hall, J. Am. Chem. Soc. 121, 4000–4007 (1999).
[63] S. Niu, and M. B. Hall, Inorg. Chem. 40, 6201–6203 (2001).
[64] S. Li, and M. B. Hall, Inorg. Chem. 40, 18–24 (2001).
[65] M. Couty and M. B. Hall, J. Comput. Chem. 17, 1359–1370 (1996).
[66] L. De Gioia, P. Fantucci, B. Guigliarelli, and P. Bertrand, Int. J. Quant. Chem. 73, 187–195 (1999).
[67] L. De Gioia, P. Fantucci, B. Guigliarelli, and P. Bertrand, Inorg. Chem. 38, 2658–2662 (1999).
[68] A. D. Becke, Phys. Rev. A 38, 3098–3100 (1988).
[69] T. H. Dunning Jr. and P. J. Hay, in: Modern Theoretical Chemistry vol. 3, edited by H. F. Schaefer III (Plenum, New York, 1976), pp. 1–27.

[70] S. Huzinaga, Gaussian Basis Sets for Molecular Calculations, (Elsevier, New York, 1984), pp. 23–24.
[71] A. Warshel and M. Levitt, J. Mol. Biol. 103, 227–249 (1976).
[72] U. C. Singh and P. A. Kollman, J. Comput. Chem. 7, 718–730 (1986).
[73] M. J. Field, P. A. Bash, and M. Karplus, J. Comput. Chem. 11, 700-733 (1990).
[74] J. Gao, in: Reviews in Computational Chemistry, Vol. 7, edited by K. B. Lipkowitz and D. B. Boyd (VCH Publishers: New York, 1996), pp. 119-185.
[75] T. Z. Mordasini and W. Thiel, Chimia 52, 288-291 (1998).
[76] F. Maseras and K. Morokuma, J. Comput. Chem. 16, 1170-1179 (1995).
[77] M. Svensson, S. Humbel, R. D. J. Froese, T. Matsubara, S. Sieber, and K. Morokuma, J. Phys. Chem. 100, 19357-19363 (1996).
[78] S. Dapprich, I. Komáromi, K. S. Byun, K. Morokuma, and M. J. Frisch, J. Mol. Struct. (Theochem) 461–462, 1–21 (1999).
[79] T. Vreven and K. Morokuma, J. Comput. Chem. 16, 1419–1432 (2000).
[80] M. Stein and W. Lubitz, Phys. Chem. Chem. Phys. 3, 5115–5120 (2001).
[81] Dgauss4.0 (Cray Res. Inc., San Diego, 1995).
[82] M. Stein and W. Lubitz, Phys. Chem. Chem. Phys. 3, 2668–2675 (2001).
[83] A. D. Becke, J. Chem. Phys. 84, 4524–4529 (1986).
[84] J. P. Perdew, Phys. Rev. B 33, 8822–8824 (1986).
[85] J. P. Perdew, Phys. Rev. B 34, 7406–7406 (1986).
[86] M. Stein, E. van Lenthe, E. J. Baerends, and W. Lubitz, J. Am. Chem. Soc. 123, 5839–5840 (2001).
[87] Theoretical Chemistry Amsterdam Density Functional (ADF) Rev. 2000.02 (Vrije Universiteit De Boelelaan, Amsterdam, 2000).
[88] G. te Velde, F. M. Bickelhaupt, E. J. Baerends, C. Fonseca Guerra, S. J. A. van Gisbergen, J. G. Snijders, and T. Ziegler, J. Comp. Chem. 22, 931–967 (2001).
[89] E. van Lenthe, E. J. Baerends, and J. G. Snijders, J. Chem. Phys. 99, 4597–4610 (1993).
[90] R. van Leeuwen, E. van Lenthe, E. J. Baerends, and J. G. Snijders, J. Chem. Phys. 101, 1272–1281 (1994).
[91] E. van Lenthe, E. J. Baerends, and J. G. Snijders, J. Chem. Phys. 101, 9783–9792 (1994).
[92] A. J. Sadlej, J. G. Snijders, E. van Lenthe, and E. J. Baerends, J. Chem. Phys. 102, 1758–1766 (1995).
[93] P. Amara, A. Volbeda, J. C. Fontecilla-Camps, and M. J. Field, J. Am. Chem. Soc. 121, 4468–4477 (1999).
[94] R. D. Amos, I. L. Alberts, J. S. Andrews, S. M. Colwell, N. C. Handy, D. Jayatilaka, P. J. Knowles, R. Kobayashi, K. E. Laidig, G. Laming, A. M. Lee, P. E. Maslen, C. W. Murray, J. E. Rice, E. D. Simandiras, A. J. Stone, M. -D. Su, and D. J. Tozer, The Cambridge Analytic Derivatives Package Issue 6 (Cambridge University, Cambridge, 1995).
[95] C. Stadler, A. L. de Lacey, B. Hernandez, V. M. Fernandez, and J. C. Conesa, Inorg. Chem. 41, 4417–4423 (2002).
[96] C. Stadler, A. L. de Lacey, Y. Montet, A. Volbeda, J. C. Fontecilla-Camps, J. C. Conesa, and V. M. Fernandez, Inorg. Chem. 41, 4424–4434 (2002).
[97] H.-J. Fan and M. B. Hall, J. Am. Chem. Soc. 124, 394–395 (2002).
[98] C.-P. Wang, R. Franco, J. J. G. Moura, I. Moura, and E. P. Day, J. Biol. Chem. 267, 7378–7380 (1992).

[99] M. Bruschi, L. De Gioia, G. Zampella, M. Reiher, P. Fantucci, and M. Stein. J. Biol. Inorg. Chem. 9, 873–884 (2004).
[100] M. Reiher, O. Salomon, and B. A. Hess, Theor. Chem. Acc. 107, 48–55 (2001).
[101] M. Reiher, Inorg. Chem. 41. 6928–6935 (2002).
[102] O. Salomon, M. Reiher, and B. A. Hess, J. Chem. Phys. 117, 4729-4737 (2002).
[103] L. Tüker, J. Mol. Struct. (Theochem) 664–665, 175–181 (2003).
[104] L. Tüker, I. Eroglu, M. Yücel, and Y. Gündüz, J. Mol. Struct. (Theochem) 672, 169–174 (2004).
[105] A. Tachibana, H. Fueno, E. Tanaka, M. Murashima, M. Koizumi, and T. Yamabe, Int. J. Quant. Chem. 39, 561–583 (1991).
[106] A. Tachibana, H. Fueno, M. Yamato, and T. Yamabe, Int. J. Quant. Chem. 40, 435–456 (1991).
[107] A. Tachibana, J. Math. Chem. 7, 95–110 (1991).
[108] A. Tachibana, J. Chem. Phys. 115, 3497–3518 (2001).
[109] A. Tachibana, in: Stress Induced Phenomena in Metallization, edited by S. P. Baker, (American Institute of Physics, New York, 2002), pp. 105–116.
[110] A. Tachibana, in: Fundamental Perspectives in Quantum Chemistry, A Tribute to the Memory of Per-Olov Löwdin, Vol. 2, edited by E. J. Brändas and E. S. Kryachko, (Kluwer Academic Publishers, Dordrecht, 2002), pp. 211–239.
[111] A. Tachibana, in: Reviews in Modern Quantum Chemistry: A Celebration of the Contributions of Robert Parr, Vol. 2, edited by K. D. Sen (World Scientic, Singapore, 2002), pp. 1327–1366.
[112] A. Tachibana, Int. J. Quant. Chem. 100, 981–993 (2004).
[113] A. Tachibana, J. Mol. Modeling 11, 301–311 (2005).
[114] A. Tachibana, Theor. Chem. Acc. 102, 188–195 (1999).
[115] K. Nakamura, K. Doi, and A. Tachibana, Molecular Regional DFT program package, ver. 1 (Tachibana Lab., Kyoto University, Kyoto, 2004).

Table 2-1. Mulliken atomic charge densities in all states in Fig. 2-7. The positions of the three S atoms and two H atoms are shown in Fig. 2-6, distinguished by the suffixes.

	Fe	Ni	S1	S2	S3	H1	H2
Ni-SI $^{+}$ H_2	-0.44	-0.01	-0.05	-0.28	-0.28	-0.07	0.09
TS	-0.86	0.02	0.02	-0.31	-0.18	0.00	0.27
Ni-R	-0.89	0.04	-0.19	-0.09	-0.31	0.14	0.19

Table 2-2. Atomic distances and angles in 1a and 1b.

distance (Å)	**1a**	**1b**	exp.[15,16]
Ni-Fe	3.409	2.919	2.55
Ni-S1	2.288	2.263	2.16
Ni-S2	3.252	2.432	2.37
Fe-S1	2.418	2.284	2.22
Fe-S2	2.363	2.387	2.37
angle (deg)	**1a**	**1b**	exp.[15,16]
S1-Ni-S2	41.0	88.0	91.1
S1-Fe-S2	53.1	88.6	89.7

Table 2-3. Mulliken atomic spin densities and charge densities in all complexes.

spin densities	Ni	Fe	S1	S2	S3	H1	H2
1a	-0.04	0.01	0.01	0.00	0.49		
1b	0.67	0.28	0.80	0.35	0.48		
2a	-0.04	0.01	0.01	0.00	0.49	0.00	0.00
2b	0.67	0.29	0.80	0.35	0.48	0.00	0.00
3a	-0.03	0.00	0.04	0.00	0.48	0.00	0.00
3b	0.67	0.82	0.26	0.07	0.53	-0.08	-0.01
4a	0.00	0.00	0.00	0.00	0.00	0.00	
4a'	0.00	0.00	0.00	0.00	0.00	0.00	
4b	0.75	-0.02	0.05	0.34	0.44	0.00	
4b'	0.93	0.28	0.80	0.29	0.04	0.00	
4b''	-0.11	0.04	0.85	0.21	0.49	0.01	
TSa	-0.05	-0.01	0.00	0.22	0.16	0.06	-0.04
TSb	0.61	0.45	0.86	0.06	0.43	-0.03	0.22
charge densities	Ni	Fe	S1	S2	S3	H1	H2
1a	0.09	-0.57	-0.06	0.12	-0.03		
1b	0.16	-0.88	0.00	0.05	-0.02		
2a	0.07	-0.57	-0.06	0.12	-0.03	0.00	0.02
2b	0.14	-0.89	0.00	0.05	-0.02	0.03	-0.01
3a	-0.33	-0.80	-0.10	0.01	0.04	0.23	0.20
3b	-0.06	-0.95	-0.16	0.05	-0.03	0.18	0.22
4a	0.20	-0.79	-0.34	0.01	0.07	0.19	
4a'	0.08	-0.54	-0.11	0.12	-0.08	0.25	
4b	0.15	-0.81	-0.17	0.03	-0.03	0.20	
4b'	0.18	-0.86	-0.06	0.06	-0.10	0.22	
4b''	-0.34	-0.80	0.08	0.04	0.05	0.24	
TSa	0.08	-0.65	-0.13	0.05	-0.03	0.04	0.08
TSb	-0.02	-0.81	-0.08	0.05	0.01	0.11	0.01

Table 2-4. ulliken atomic spin densities and charge densities in anion complexes ($2a^-$, $2b^-$, $3a^-$, $3b^-$, TSa^-, TSb^-) and dianion complexes ($2a^{2-}$, $2b^{2-}$, $3a^{2-}$, $3b^{2-}$, TSa^{2-}, TSb^{2-}).

spin densities	Ni	Fe	S1	S2	S3	H1	H2
$2a^-$	0.00	0.00	0.00	0.00	0.00	0.00	0.00
$2b^-$	0.66	-0.02	0.10	0.27	0.51	0.00	0.00
$3a^-$	0.00	0.00	0.00	0.00	0.00	0.00	0.00
$3b^-$	0.62	-0.01	0.11	0.00	0.62	0.00	-0.10
TSa^-	0.00	0.00	0.00	0.00	0.00	0.00	0.00
TSb^-	0.37	0.04	0.28	0.09	0.46	-0.07	0.30
$2a^{2-}$	0.01	0.75	0.12	0.13	-0.01	0.00	0.00
$2b^{2-}$	1.31	0.02	0.08	0.04	0.61	0.21	0.00
$3a^{2-}$	0.60	-0.01	0.06	0.00	0.18	0.00	-0.11
$3b^{2-}$	1.21	0.05	0.10	0.05	0.59	0.00	0.20
TSa^{2-}	0.74	0.02	0.06	0.00	0.06	0.00	0.00
TSb^{2-}	1.22	0.01	0.14	0.13	0.60	-0.02	0.17
charge densities	Ni	Fe	S1	S2	S3	H1	H2
$2a^-$	-0.07	-0.64	-0.06	0.10	-0.18	-0.04	0.06
$2b^-$	0.08	-0.91	-0.21	-0.02	-0.07	0.07	-0.05
$3a^-$	-0.31	-0.80	-0.18	-0.04	-0.12	0.18	0.21
$3b^-$	-0.29	-0.87	-0.20	-0.02	-0.08	0.17	0.21
TSa^-	0.00	-0.71	-0.14	-0.01	-0.06	-0.01	0.07
TSb^-	-0.08	-0.84	-0.34	0.00	-0.04	0.09	0.02
$2a^{2-}$	-0.13	-0.66	-0.17	0.02	-0.22	-0.06	0.00
$2b^{2-}$	-0.19	-1.04	-0.33	-0.08	-0.10	0.01	0.17
$3a^{2-}$	-0.38	-0.87	-0.24	-0.06	-0.23	0.17	0.18
$3b^{2-}$	-0.41	-0.98	-0.22	-0.07	-0.11	0.14	0.06
TSa^{2-}	-0.14	-0.79	-0.19	-0.04	-0.12	-0.04	0.06
TSb^{2-}	-0.08	-0.91	-0.45	-0.07	-0.13	0.12	-0.05

Figure 1-1. Structure of the [NiFe] hydrogenase of Desulfovibrio gigas, showing an enlargement of its active site.

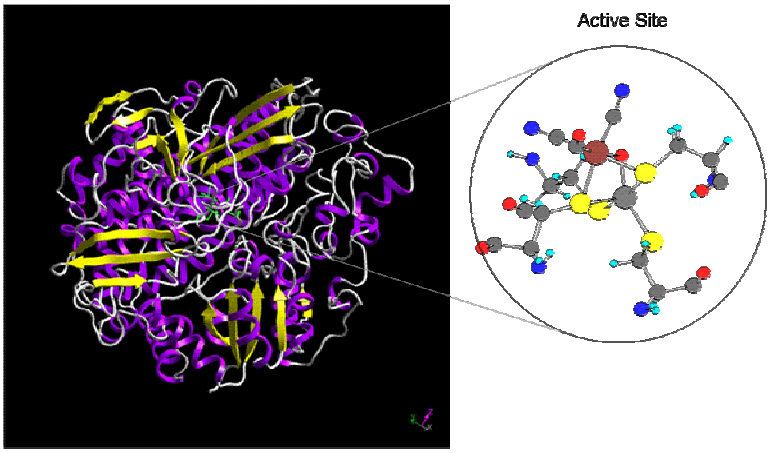

Figure 1-2. Computational model of the active site.

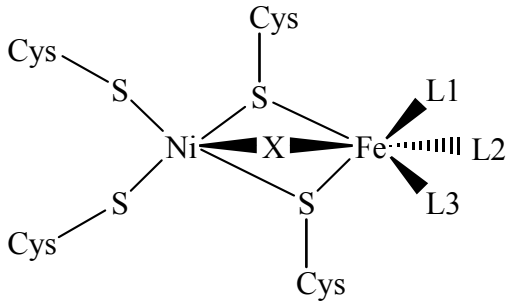

Figure 1-3. Reduction scheme showing the relation of each state. [37,38]

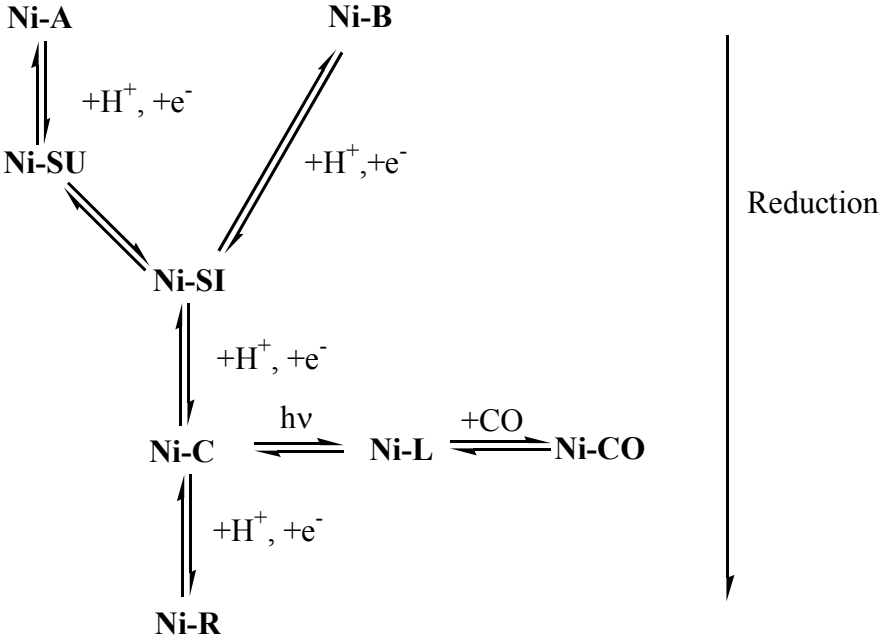

Figure 2-1. **a)** Structure of the paramagnetic states, such as Ni-A, Ni-B and Ni-C of Pavlov et al. and Hall et al. from the theoretical investigations.

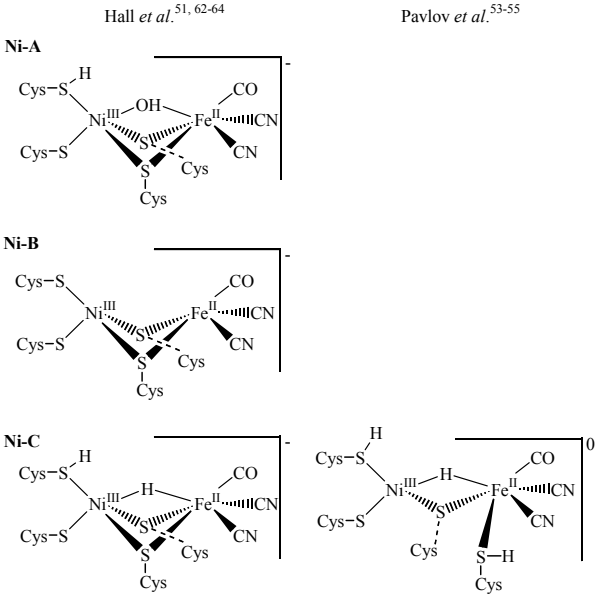

b) Structure of the paramagnetic states, such as Ni-A, Ni-B, Ni-C, and Ni-L of Gioia et al., Stein et al. and Amara et al. from the theoretical investigations.

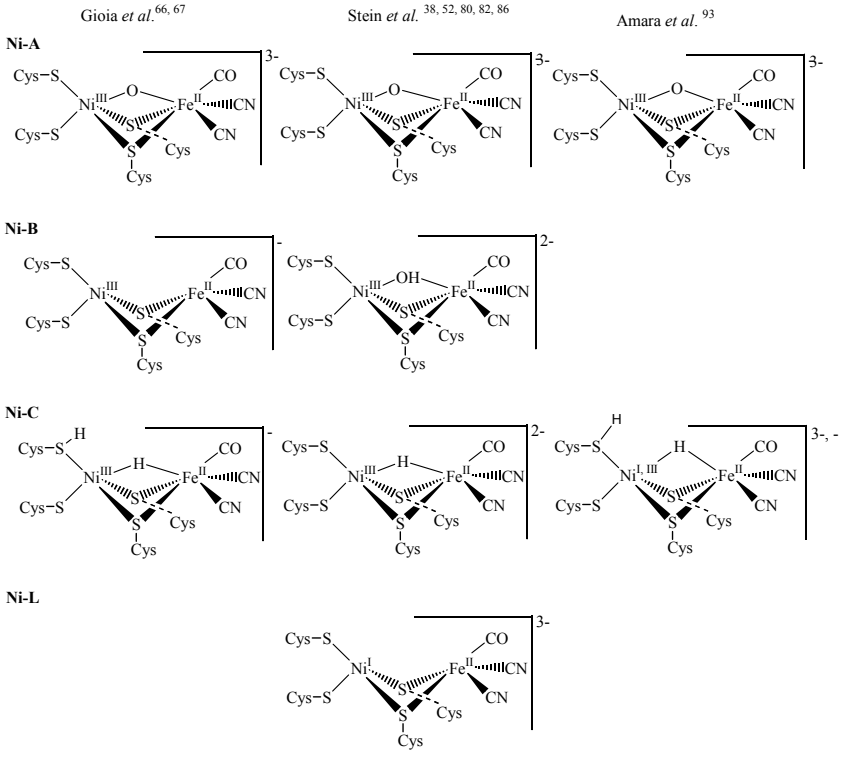

Figure 2-2. **a)** Structure of the EPR-silent states, such as Ni-SU, Ni-SI, and Ni-R of Pavlov et al. and Hall et al. from theoretical investigations. Note that Hall et al. suggest the existence of two Ni-SI states, Ni-SIa and Ni-SIb.

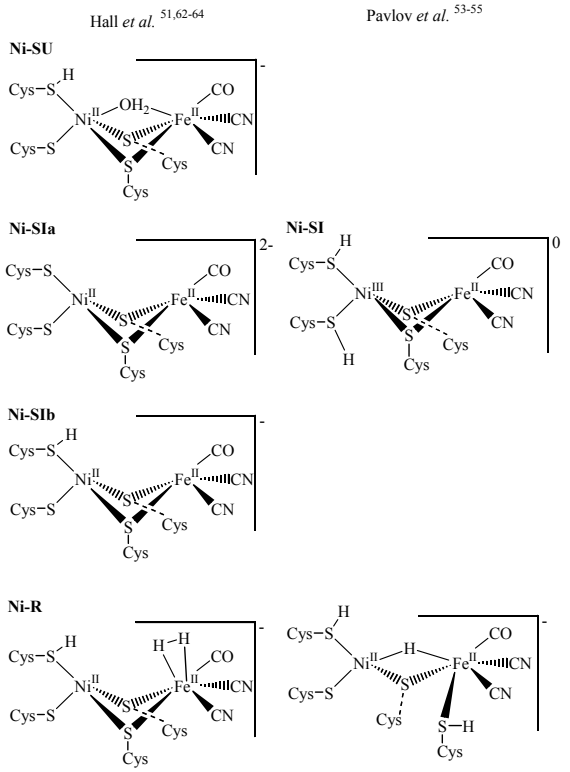

b) Structure of the EPR-silent states, such as Ni-SU, Ni-SI, and Ni-R of Gioia et al., Stein et al. and Amara et al. by theoretical investigations.

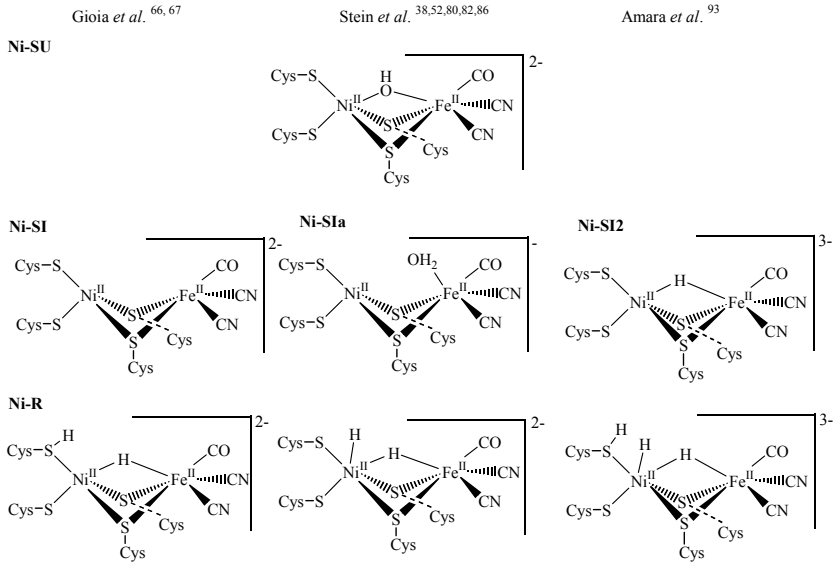

Figure 2-3. Scheme of the QM, MM-free, and MM-fixed regions.

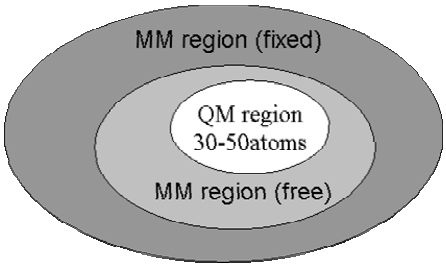

Figure 2-4. **a)** Catalytic mechanism of Pavlov et al. All of the states are calculated as quartet states. [53]

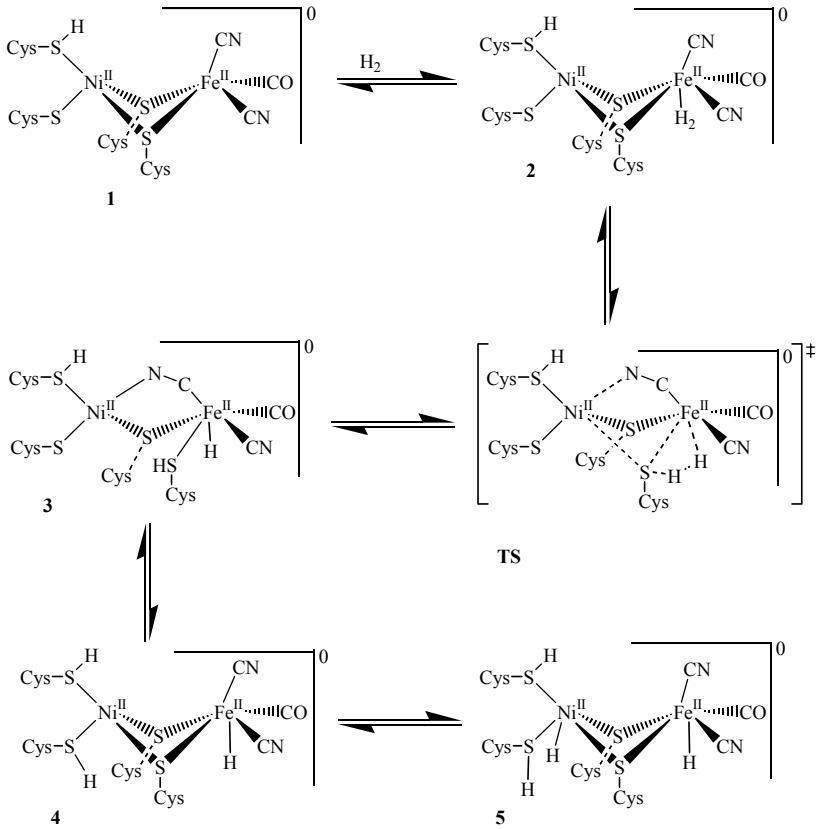

Figure 2-4. **b)** Modified catalytic mechanism of Pavlov et al. All of the states were calculated as quartet states. [54,55]

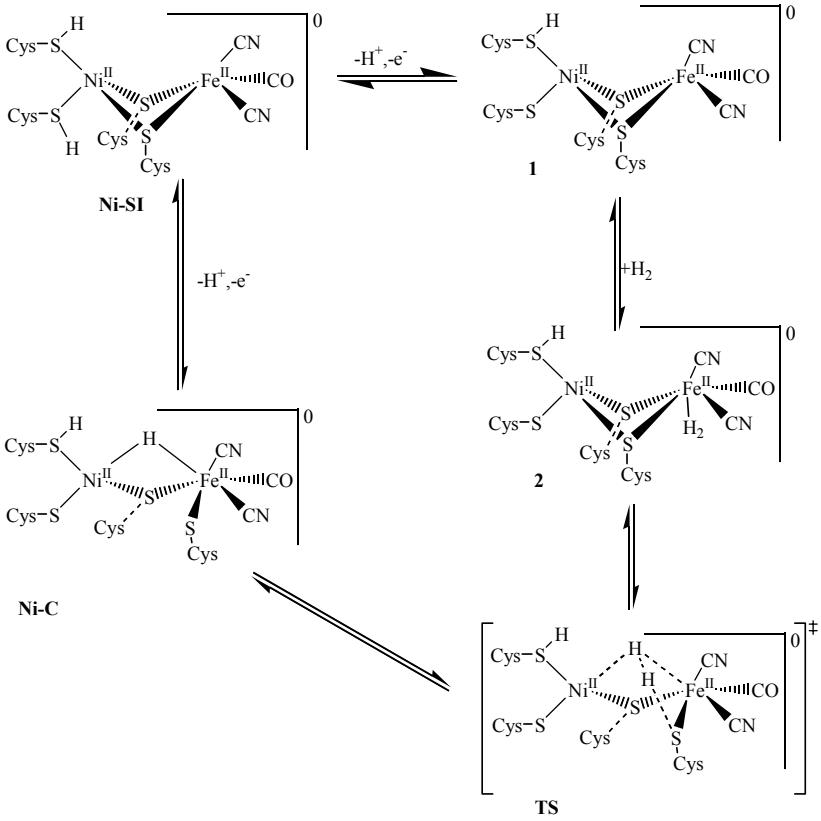

Figure 2-5. **a)** Energy diagram corresponding to the catalytic mechanism of Pavlov et al. shown in Fig. 2-4(a). [53] The unit of energy is kcal/mol.

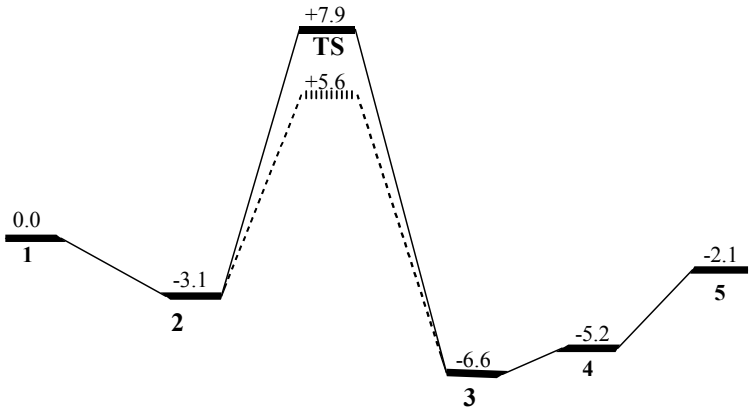

Figure2-5. **b)** Energy diagram corresponding to the modified catalytic mechanism of Pavlov et al. shown in Fig. 2-4(b). Here 2', TS' and Ni-C' include solvent effect. [54] The unit of energy is kcal/mol.

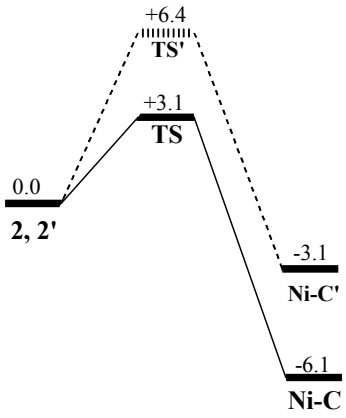

Figure 2-6. Catalytic mechanism of Hall et al. The states are calculated as low-spin states. There are two catalytic cycle. One cycles through the neutral states including the transition state, while the other includes only the anion states during the cycle. [51,62-64] The Ni-R state is denoted by 1^- , which releases one electron to become 1^0. State 2^0 is an intermediate complex and receives one electron to become 2^-.

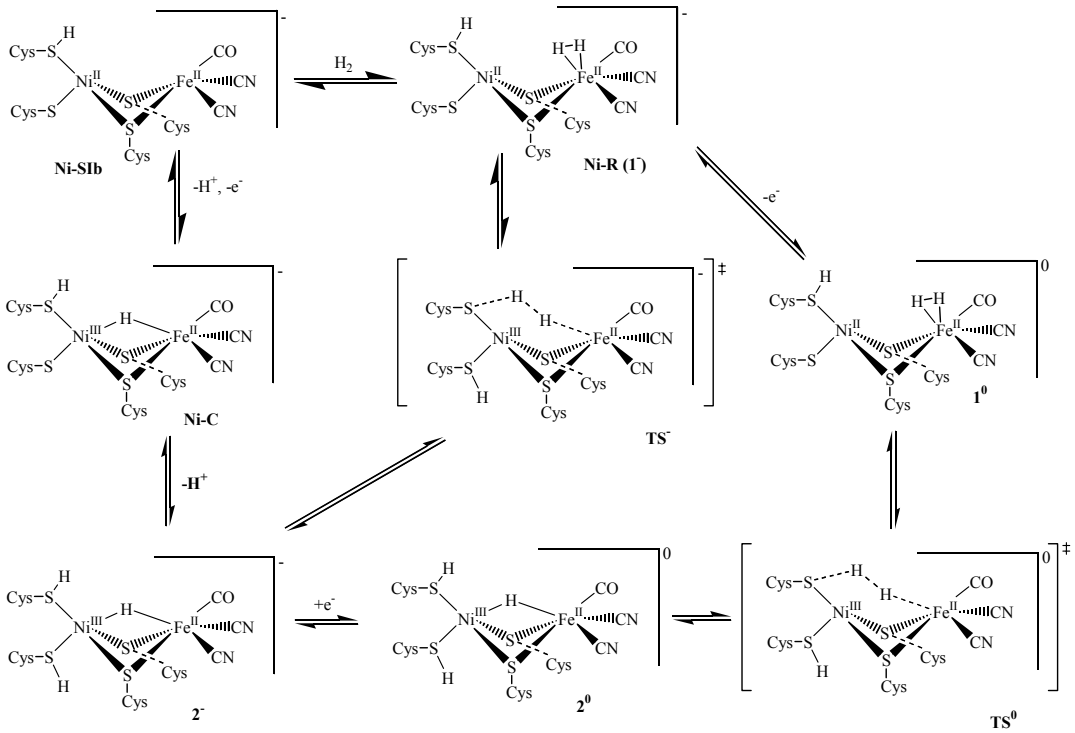

Figure 2-7. Energy diagram of Hall et al, shown in Fig. 2-6. [63] Each state corresponds to a state in Fig. 2-6. The unit of energy is kcal/mol.

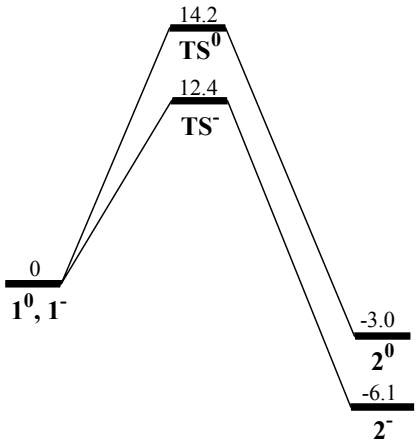

Figure 2-8. Mechanism of Dole et al. and Gioia et al. Our transition state is inserted into it. All the states are were calculated as low-spin states. [42,66,67]

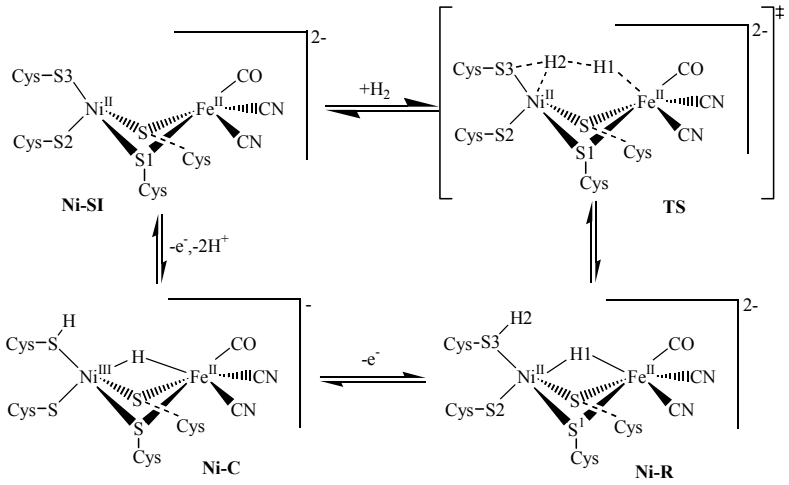

Figure 2-9. Our energy diagram based on the mechanism shown in Fig. 2-8. This diagram is only for the low-spin states. The unit of energy is kcal/mol.

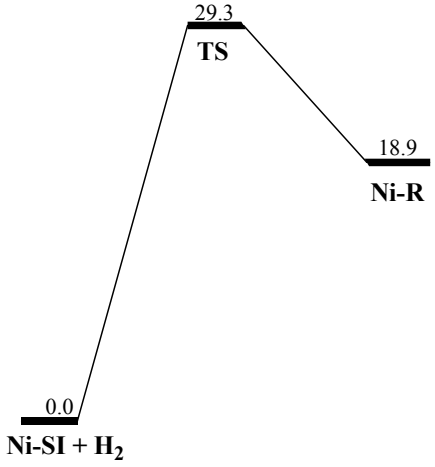

Figure 2-10. Catalytic mechanism of Stein et al. characterized by the mediation of H2O. [38,52,80,82,86] All the complexes are calculated as the low-spin states. [80]

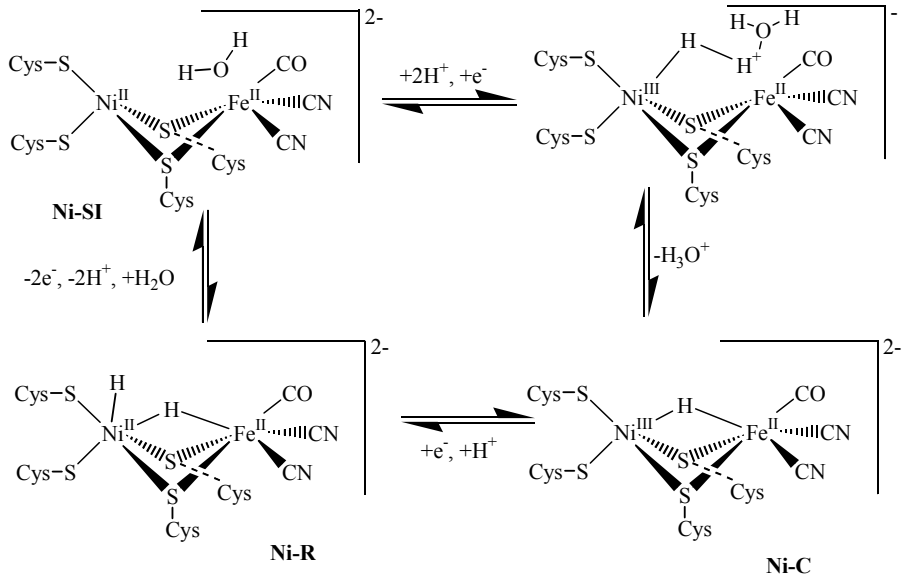

Figure 2-11. Mechanism of Amara et al. All the states are calculated as low- and high-spin states. [93]

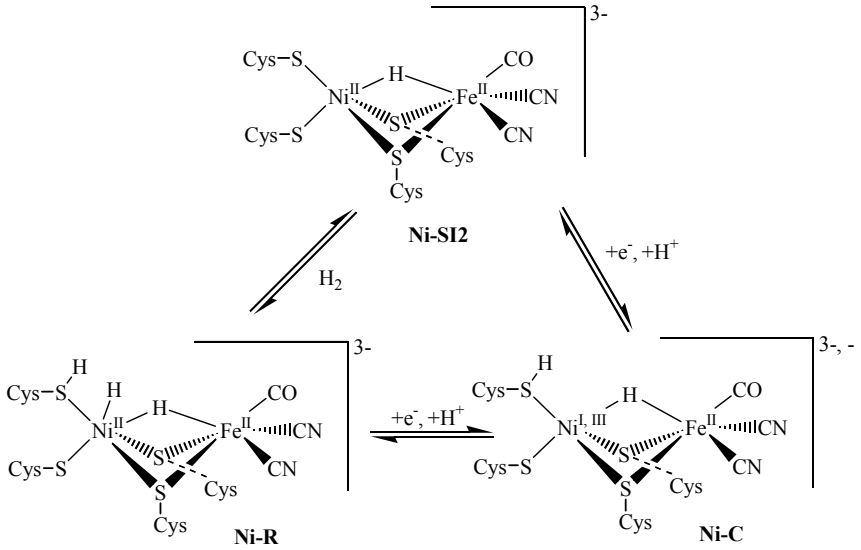

Figure 2-12. Reaction of Eq. (2) (clockwise) and reverse reaction, Eq. (3) (counterclockwise).

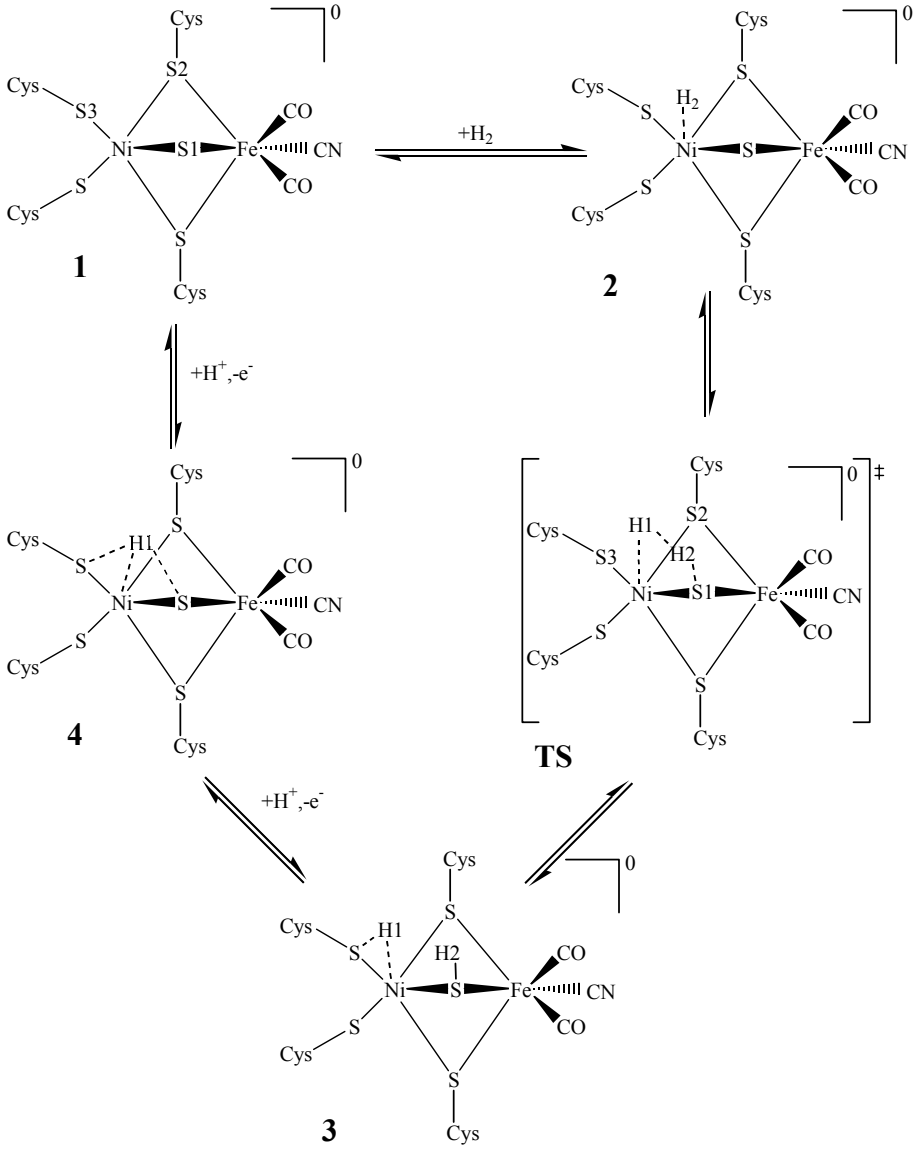

Figure 2-13. **a)** Optimized species in the low spin state.

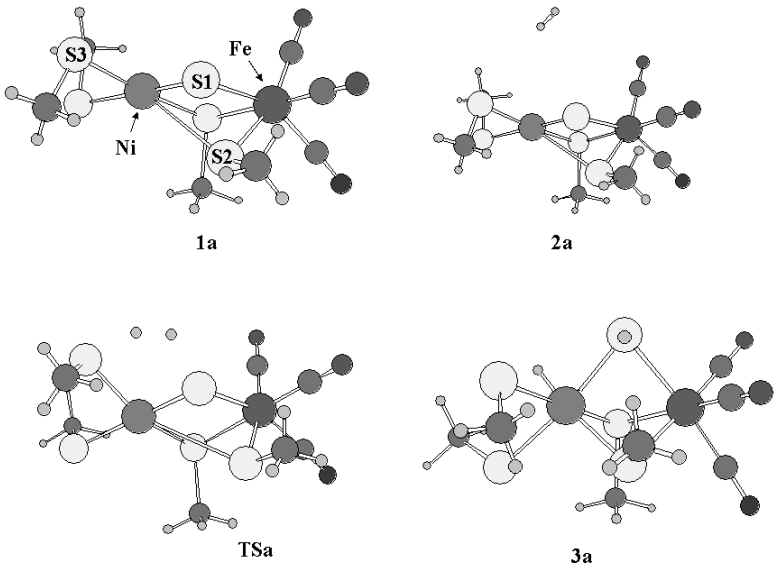

b) Optimized species in the high spin state.

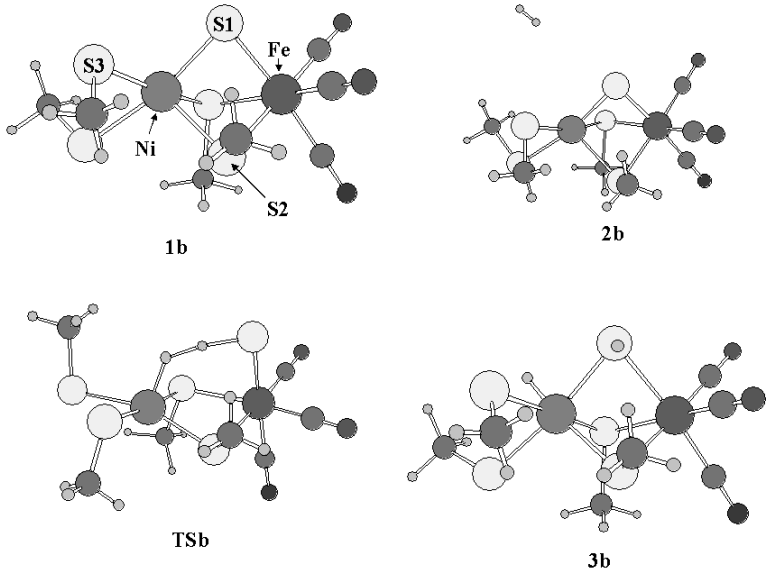

Figure 2-14. Energy diagram of the catalytic cycle. The unit of energy is kcal/mol. where s and t in the parentheses respectively denote singlet and triplet states.

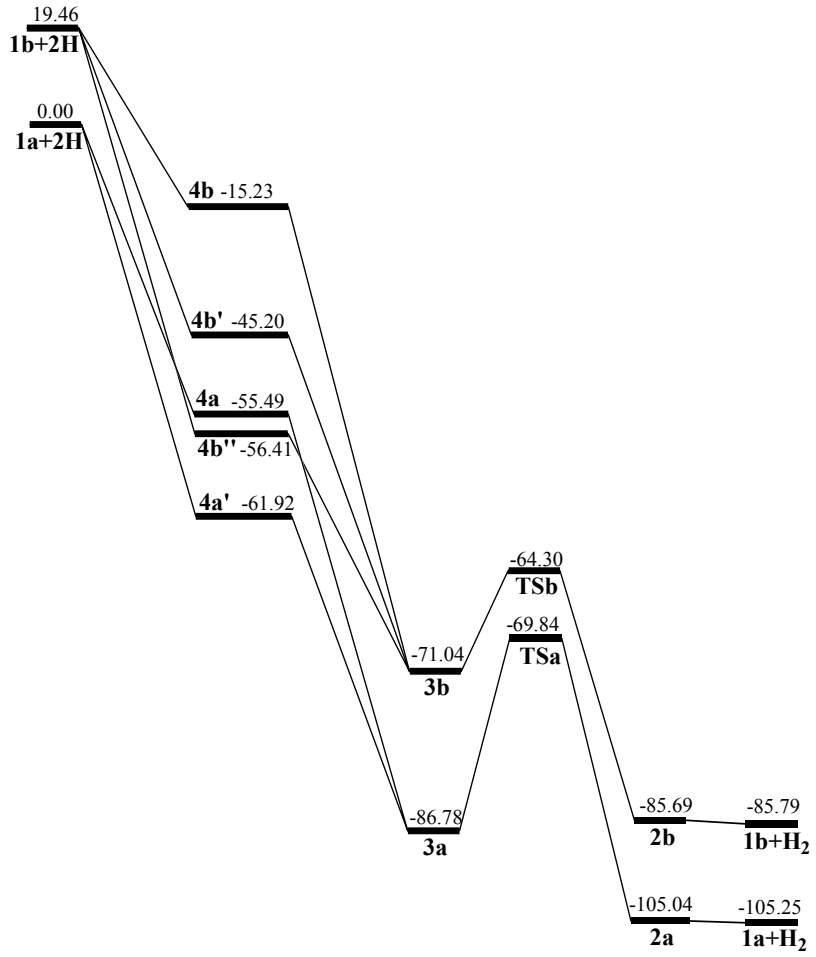

Figure 2-15. String model of the catalytic mechanism in the oxidized system of DvMF. The unit of energy is kcal/mol. The energies in this diagram do not include the zero-point energy.

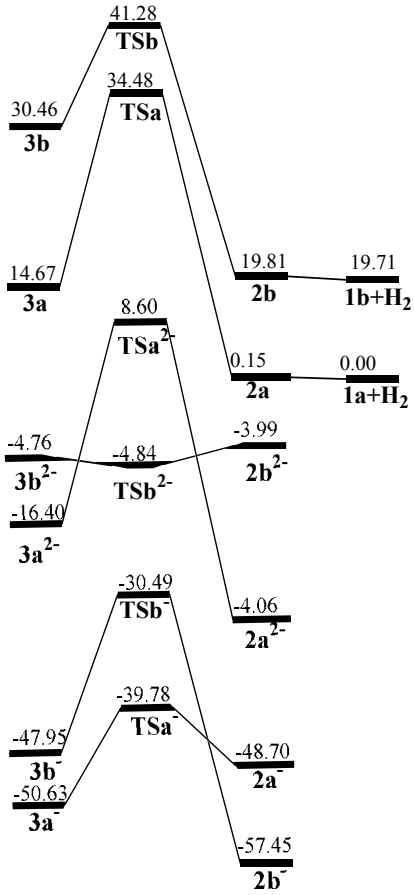

Figure 2-16. Energy diagram of the catalytic cycle for L1=CN, L2=CO, and L3=CN. The mechanism is the same as that in Fig. 2-12 and the diagram shows only about low spin states. The unit of energy is kcal/mol.

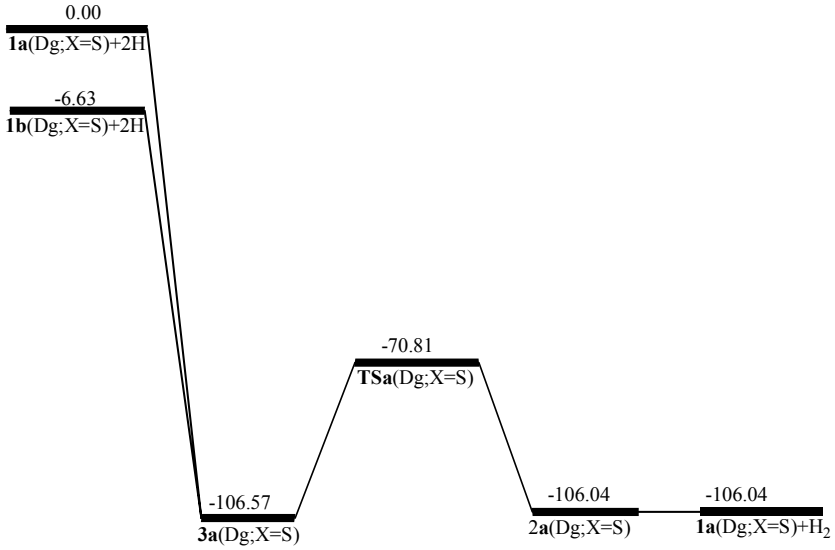

Figure 2-17. Maps of the quantum energy densities: **a)** $n_T(\vec{r})$ (background shading), $\vec{\tau}^S(\vec{r})$ (arrows), **b)** The largest eigenvalues of $\vec{\tau}^S(\vec{r})$ (background shading) and their eigenvectors (short lines) in TSa; The cross section of TSa is displayed above (a) and (b), with the centers of the Ni atom and two H atoms are included. **c)** $n_T(\vec{r})$ (background shading), $\vec{\tau}^S(\vec{r})$ (arrows), **d)** The largest eigenvalues of $\vec{\tau}^S(\vec{r})$ (background shading) and their eigenvectors (short lines) in TSb. The cross section of TSb is displayed above (c) and (d), with the centers of the Ni atom and two H atoms are included. The gray areas in (a) and (c) denote R_D regions and those in (b) and (d) denote the tensile stresses. The contours in (b) and (d) denote the values of -0.01, 0.0, and 0.01.

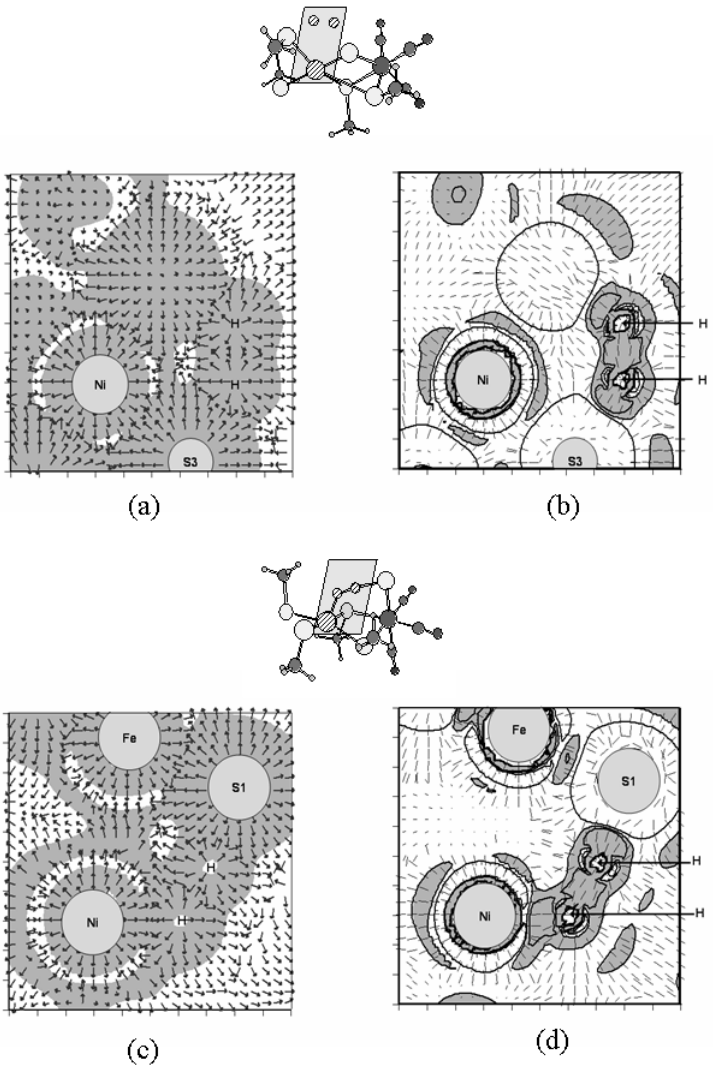

CHAPTER 7

Electronic Structure Study of Local Dielectric Properties of Lanthanoid Oxide Clusters.

Introduction

Significant improvements of electronic devices have been supported by rapid progress in ultralarge-scale integrated (ULSI) circuits. Many studies of complementary metal-oxide-semiconductor (CMOS) gate insulators have been performed in academic and industrial fields of material research. The dielectric breakdown of insulators, however, is a serious problem in reliability of advanced electric devices. Recently, the search for advanced materials superior to SiO_2 and the renewal of MOS structures have attracted much attention because the pursuit of device performance, which requires the downsizing of the gate insulators, leads to the loss of device reliability.[1] These problems require urgent solutions for the generation of new CMOS. Many candidate substitutes for SiO_2, that shows desirable dielectric properties has been proposed. Some oxides and silicates, e.g., CeO_2, [2] Pr_2O_3, [3] Al_2O_3, [4] and Zr and Hf silicates, [5-8] are known to maintain thermodynamical and chemical stabilities on Si substrates. In recent years, lanthanoid-oxide dielectrics have been considered to be good gate insulators because of their high dielectric constants and wide band gaps. La_2O_3, for example, showed a dielectric constant of 27 [9] and a band gap of 5.5 eV. [10] Furthermore, some lanthanoid (Ln) elements, e.g., Ce and Sm, have been reported to work as catalysts in the oxidation of Si substrates. [11–14]

In order to obtain computational results consistent with experimental results of Ln compounds, careful treatment of valence electrons of Ln elements is required for electronic structure calculations. [15–17] In the calculation of cerium oxide, for example, Ce 4f in Ce_2O_3 is treated as part of the inner core, but that in CeO_2 should be treated as a valence electron. [15] Moreover, the composition of lanthanoid oxide films on Si substrates is very complicated and so are their electronic structures. [11–14,18,19] Transition layers composed of an oxide layer, a silicate layer, and an interfacial layer are observed between the oxide surface and the substrate. Ln atoms are stable as mixed states in the transition layer, and the complicated structure of the oxide layer procuces a complex electronic structure. [11–14] The characteristics of lanthanoid oxides are further reviewed in ref. 10.

In this work, we focus on some oxides, such as La_2O_3, Ce_2O_3, Gd_2O_3, HfO_2, and SiO_2, and calculate their electronic structures and local dielectric properties using the densityfunctional molecular-orbital (MO) method. In our previous calculation, we emphasized the importance of the treatment of the valence electrons of Gd. [20] We reported that electrons in the $5s^2$, $5p^6$, $4f^7$,

$6s^2$, and $5d^1$ states should be treated as valence electrons. We follow this treatment in this work. This is because we want to get more precise and detailed dielectric response of valence electrons than the conventional Clausius–Mossotti (CM) relation. [21] The analysis is based on the Rigged QED theory described elsewhere. [22–28]

Computational Methods

2.1 Electronic structure calculation

We have performed quantum chemical calculations for several small cluster models of lanthanoid monoxides (i.e., LaO, CeO, and GdO) and several tetrahydroxides, such as $La(OH)_4$, $Hf(OH)_4$, and $Si(OH)_4$ using the density functional theory [29] with the Molecular Regional DFT (MRDFT) program package. [30] The calculations for small clusters can clarify details of the chemical-bonding characteristics of metallic species and O atoms. However, these calculations are not sufficient to understand the electronic structures of the condensed phase. Therefore, the electronic structure of a large-scale model has also been treated in this work using a combined quantum mechanics/molecular mechanics (QM/MM) method. Following our previous results, [20] the electronic configurations of La, Ce, and Gd have been taken as $5s^25p^65d^16s^2$, $4f^15s^25p^65d^16s^2$, and $4f^75s^25p^65d^16s^2$ for valence electrons with 46 core electrons, respectively. On the other hand, the 4f, 5s, and 5p states of Hf are located at levels so deep that these states do not contribute to bonding interactions and can be treated as core states. The core electrons are substituted by effective core potentials (ECPs) using the CEP-31G basis set of Stevens et al. [31,32] Additionally, the f-type polarization function of La is optimized. The exponent of the f function that minimizes the total energy of LaO is determined to be 0.525. The contribution of the f orbital to the interaction between Ln and O has also been studied by many researchers, [11-17] employing the 6-31G* basis set for O and Si, and the 6-31G** set for H. In DFT calculations, the Lee–Yang–Parr (LYP) [33] gradient-corrected functionals for correlation interaction are employed, and Becke's hybrid three parameters [34] for generalized-gradient-approximation (GGA) exchange-correlation functionals (B3LYP) are adopted. This condition provided accurate results for gadolinium oxide clusters in our previous work. [20] In this work, geometric optimizations and electronic structure calculations for each cluster model are carried out using the GAUSSIAN 03 program package. [35]

2.2 Electron energy density and local dielectric constant

Using electron wave functions, local electronic properties such as the electronic stress tensor density and local dielectric constant are calculated. According to the Rigged QED theory, [22-28] the electronic stress tensor density $\vec{\tau}^{S}(r)$ is given by a 3x3 matrix described as

$$\tau^{Skl}(r)=\frac{\hbar^2}{4m}\sum_{i}^{occ}\nu_i\left[\psi_i^*(\vec{r})\frac{\partial^2\psi_i(\vec{r})}{\partial x^k\partial x^l}-\frac{\partial\psi_i^*(\vec{r})}{\partial x^k}\frac{\partial\psi_i(\vec{r})}{\partial x^l}+\frac{\partial^2\psi_i^*(\vec{r})}{\partial x^k\partial x^l}\psi_i(\vec{r})-\frac{\partial\psi_i^*(\vec{r})}{\partial x^l}\frac{\partial\psi_i(\vec{r})}{\partial x^k}\right] \quad (2.1)$$

where {k,l}={1, 2, 3}, m is the electron mass, ν_i is the occupation number of the i^{th} state, and $\psi_i(r)$ is the electron wave function. [27,28] The dielectric constant density $\vec{\varepsilon}(r)$ is locally defined as a 3x3 matrix described as

$$\vec{\varepsilon}(r)=(1-4\pi\vec{\alpha}(r))^{-1} \quad (2.2)$$

where $\vec{\alpha}(r)$ is the local polarizability tensor density that satisfies

$$P(r)=\vec{\alpha}(r)D(r) \quad (2.3)$$

In eq. (2.3), *D(r)* is the electric displacement of the external environment filled with medium M, and *P(r)* is the polarization of system A embedded in medium M. [28] The local dielectric properties are related to the polarization of the system induced by the electric displacement of the external medium. The polarization *P(r)* is represented as

$$P(r)=\frac{1}{4\pi}grad\,A_{0_A}(r) \quad (2.4)$$

$$A_{0_A}(r)=\int_A d^3s\frac{\rho(s)}{|r-s|} \quad (2.5)$$

where A_{0_A} is the gauge potential at *r*, obtained by integrating the charge density in system A. The response of electrons against the external electric field *D(r)* is calculated by the self-consistent-.eld method. In this work, electronic structure calculations are carried out under the condition of homogeneous *D(r)* such as *D(r)=De* composed of the magnitude *D* and the unit vector *e*. Electronic polarization is calculated using eqs. (2.4) and (2.5), and then the local dielectric constant is derived from eqs. (2.2) and (2.3). As a result of these calculations, the relationship between chemical bonding properties and local dielectric constants are determied because these quantities are derived from the same electron wave functions. [28] The electronic stress tensor density and the local dielectric constant are calculated using the MRDFT program package. [30]

Results and Discussion

3.1 Electronic structures of LnO

The optimized bond lengths of LaO, CeO, and GdO are shown in Table I. The calculated bond lengths of CeO and GdO show good agreement with the experimental data. [36,37] The calculated bond length of LaO was improved with the basis set that contains the f-type polarization function. According to the increase in atomic number, the radius of lanthanoid atoms ends to decrease because the addition of electrons to the 4f orbitals does not shield the atomic nucleus. This is known as lanthanoid contraction. In the case of the lanthanum oxide, the unoccupied f function is considered in the electronic structure calculations as the polarization function, and the overlap between La 4f and O 2p stabilizes the chemical bond. Thus, hereafter, the electronic structures of lanthanum oxide are obtained using the CEP-31G plus f-type polarization function. The MO interaction diagrams of LaO, CeO, and GdO are shown in Fig. 1. The 5p and 5d orbitals are delocalized and contribute to the interaction between Ln and O. On the other hand, the 4f and 5s orbitals remain intact in the Ln atom. In the case of LaO, the MO levels are divided into two bands, with each band showing a different property. In the lower energy band, the interaction between La 5p and O 2s generates bonding and antibonding MOs because of the close energy levels of these two atomic orbitals (AOs), -0.881 (-23.968) and -0.897 a.u. (-24.419 eV), respectively, and their nonzero overlap interaction. In the higherenergy band, MO levels composed of La 5p,5d and O 2p are in.uenced by the bonding interaction of La 5d–O 2p and the antibonding interaction of La 5p–O 2p. In the cases of CeO and GdO, the orbital interactions are explained as in the case of LaO.

3.2 Electronic structures of $La(OH)_4$, $Hf(OH)_4$, and $Si(OH)_4$

Next, the electronic structures of $La(OH)_4$, $Hf(OH)_4$, and $Si(OH)_4$ are calculated in order to analyze the bonding states between metallic species and O atoms in oxygen ligand systems. This discussion is motivated by the interest for the many folded Ln–O interactions. In the calculations, all molecules were fixed in tetragonal symmetry (T_d). In the ground state, the bond lengths of La–O, Hf–O, and Si–O were optimized at 2.24, 1.92, and 1.60Å, respectively. The angles <M–O–H (M = La, Hf, and Si) were fixed at 180º. Figure 2 shows MO interaction diagrams of $La(OH)_4$, $Hf(OH)_4$, and $Si(OH)_4$. In the cases of $La(OH)_4$, La 6s and O 2s,2p interact and generate a

bonding orbital. The singly occupied molecular orbital (SOMO) is a nonbonding O 2p orbital. The bonding state of La–O, however, shows almost the same characteristics as those of LaO. It is interesting to understand the similarities and differences between La_2O_3 and HfO_2 because HfO_2 is known as a good candidate gate insulator, so that HfO_2 has reference properties as an advanced insulator. In HfO_2, the interactions between Hf 5p and O 2s, 2p are considered to be weak because the calculated Hf 5p level of -1.408 a.u. (-38.327 eV) is deeper than O 2s at -0.897 a.u. (-24.419 eV). The differences in bonding properties between La–O and Hf–O clearly shown in Fig. 2. In $Hf(OH)_4$, the O 2s level is weakly influenced by Hf 5p. The bonding orbital generated from Hf 5d–O 2p is more stable than that generated from La 5d–O 2p in $La(OH)_4$ because of the weak contribution of the antibonding element caused by the Hf 5p orbital. On the other hand, in the case of $Si(OH)_4$, the bond between Si and O is caused by the interactions of Si 3s–O 2s and Si 3s,3p–O 2p, as observed in the SiO_2 bulk system.

3.3 Stress tensor density

The stress tensor density represented by eq. (2.1) explains local electronic stresses and bonding characteristics. Figures 3(a) and 3(b) show maps of the stress tensor density for $La(OH)_4$ and $Hf(OH)_4$, respectively. In these figures, one Hf or La atom and two O atoms are located on the same cross section, and the third principal eigenvalues and eigenvectors of the diagonalized stress tensor density are plotted at each point. The positive or negative quantities around the La, Hf, and O atoms explain the tensile and compressive stresses of the electron density, respectively. The tensile stress observed between the La or Hf and O atoms connected to each other is called the ‘‘spindle structure’’. [27] The stress tensor density is calculated from the derivatives of the electron wave functions, and the chemical bonding properties contained in the wave functions are clarified on the basis of the stress tensor density as the dimension of energy density. In particular, in covalent bonds, electron density experiences tensile stress because of the attractive interactions between atoms. In this work, only the third principal axis, which corresponds to the largest eigenvalue, is only focused on because the characteristics of chemical bonds are clarified best on this axis. More details and some examples of the stress tensor density are shown elsewhere. [27] The difference shown in Hf–O and La–O is caused by the interaction between La or Hf and O atoms, as described above using MO interaction diagrams. The electron density between Hf and O atoms in $Hf(OH)_4$ experiences more compressive stress than that between La and O in $La(OH)_4$.

This is because the chemical bond Hf–O is mainly composed of bonding orbitals formed by Hf 5d–O 2p and Hf 6s–O 2p, and in this case, the contribution of Hf 5p is very weak. On the other hand, in $La(OH)_4$, La 5p interacts with O 2s, 2p and causes antibonding components. Therefore, the electron density that contributes to the Hf–O bond shows a more compressive property. The MO diagram is spatially visualized using the stress tensor density. In $Si(OH)_4$, as shown in Fig. 3(c), the electron density between Si and O atoms experiences tensile stress in the regions represented by positive quantities. The bonding character of Si–O in $Si(OH)_4$ shows different images from those of $La(OH)_4$ and $Hf(OH)_4$. One of the reasons for this difference is the difference in the number of electrons that contribute to the bonds. Mulliken atomic charges [38] in these molecules are shown in Table II. As a result, the charge transfer between metallic species and an O atom is the greatest in $Hf(OH)_4$ and least in $Si(OH)_4$, so that electrons are exchanged most prominently between Hf and O atoms and that the chemical bonds between them become stronger.

3.4 Local dielectric constant

The local properties of dielectric constants are calculated using eqs. (2.2)–(2.5) and the results are shown in Fig. 4. The local dielectric constant depends on the electronic polarization *P(r)* defined by eq. (2.3), and the responses of such polarization to the external electric fields *D(r)* are attributed to the polarizability $\vec{\alpha}(r)$. Therefore, the local dielectric tensor represented by eq. (2.2) is calculated from the polarizability at each point. In this work, polarizability was calculated from numerical finite differences. The response of electrons to the external electric field calculated using the Schrödinger equation shows quantum mechanical perspectives. The electron density derived from the Schrödinger equation is drawn using continuous wave functions and not discrete values, so that the dielectric constant that depends on electronic polarization is defined at each point in a function space. The absolute largest eigenvalues and eigenvectors of the diagonalized dielectric constants are shown on the same cross sections in Fig. 3. In this discussion, the largest dielectric constants are only focused on because the distribution of the largest eigenvalues clearly describes the relationship between electrodynamics and chemical bonding properties.

The distributions of the dielectric constants clearly differ between $La(OH)_4$, $Hf(OH)_4$, and $Si(OH)_4$. High dielectric constants were obtained between Hf and O atoms in $Hf(OH)_4$, as shown in Fig. 4(b). On the other hand, no such result was obtained in $La(OH)_4$ [Fig. 4(a)]. In the case of

$Si(OH)_4$, as shown in Fig. 4(c), large values were observed between O atoms, not between Si and O atoms. The dielectric constant originates from the response of electrons to the external electric field *D(r)*, so that the inner electric field *E(r)* changes as a function of *D(r)*. In the regions where the dielectric constant is larger than 1.0, it is concluded that polarization caused by electron displacements is easily induced by *D(r)*. In $Hf(OH)_4$, in particular, electrons that contribute to the bond between Hf and O atoms responded to *D(r)*, generated polarization, and caused a high dielectric constant.

Furthermore, Fig. 4(d) shows the result of an anionic state $La(OH)_4^-$. In an ideal ionic crystal of La_2O_3, La, and O are considered to be ionized as La^{3+} and O^{2-}, respectively. Therefore, anionic lanthanum tetrahydroxide, $LaO_4H_4^-$, was calculated in order to realize the valence charges in its solid state. In this case, the length between La and O atoms was optimized at 2.26Å. The distribution of the dielectric constants of $La(OH)_4^-$ showed the same tendency as that of $Hf(OH)_4$. An added electron responded to *D(r)* and the polarization appeared around a center La atom. As shown in Table II, the calculated Mulliken atomic charges of La and O atoms in $La(OH)_4^-$ are 1.164 and -0.793, respectively, which proves that the added electron occupied atomic orbitals of La and O and contributed to the La–O bond similarly to the Hf–O bond in $Hf(OH)_4$.

In order to confirm the results presented above, the local dielectric constant was calculated for a large-cluster model of lanthanum silicate. The electronic structure of this large cluster was calculated using the QM/MM method. In the QM region, electron wave functions were expanded by the same basis set as those in LaO and $La(OH)_4$. However, in the MM region, atomic force fields were represented by the universal force field (UFF). The silicate model was composed of 234 Si and 394 O atoms in the MM region and 7 Si and 8 O atoms in the QM region. As a result, in the optimized structure, the coordination number was 8, and 8 O atoms existed within 3.0Å from a La atom. Several cross sections in which one La atom and two O atoms were located showed the distribution of the dielectric constant in the disordered condensed phase. As shown in Fig. 5, high dielectric constants were observed between La and O atoms. These distributions explain a tendency similar to that in the anionic state such as $La(OH)_4^-$, so that charges from the environment are accepted in the interactions between La and O atoms, thereby causing high dielectric constants.

It is concluded that La atoms in silicate or interfacial layers where charge transfer is easily result in high dielectric constants, which neutral 4-coordinated lanthanum oxides do not show.

Conclusion

In this work, we investigated the local properties of dielectric constants, focusing on La, Hf, and Si oxides. Local dielectric constant is defined as a field quantity. The differences in bonding characteristics between La–O, Hf–O, and Si–O were visualized using the stress tensor density, and the origin of high dielectric constants was revealed. Electrons that contribute to La–O bonds in $La(OH)_4$ were found to be not sensitive to the external electric field, so that no high dielectric constant was observed in $La(OH)_4$. The local properties of a lanthanum silicate were investigated using a QM/MM method, in which charge transfer from the environment to La–O bonds resulted in high dielectric constants, as observed in $La(OH)_4^-$ and $Hf(OH)_4$.

In our future work, the dielectric constant will be calculated taking into account the molecular vibrational effect. Ionic polarizations will also be calculated to obtain accurate dielectric properties.

References

[1] J. H. Stathis and D. J. Dimaria, IEDM Tech. Dig., 1998, p. 167.

[2] M. Yoshimoto, T. Maeda, T. Ohnishi, G. H. Lee, and H. Louinuma, Mater. Res. Soc. Symp. Proc. 41 (1996) 210.

[3] J. P. Liu, P. Zaumseil, E. Bugiel, and H. J. Osten, Appl. Phys. Lett. 79 (2001) 671.

[4] E. P. Gusev, M. Copel, E. Cartier, I. J. R. Baumvol, C. Krug, and M. A. Cribelyuk, Appl. Phys. Lett. 76 (2000) 176.

[5] G. D. Wilk, R. M. Wallace, and L. M. Anthony, J. Appl. Phys. 89 (2001) 5243.

[6] G. D. Wilk and R. M. Wallace, Appl. Phys. Lett. 74 (1999) 2854.

[7] G. D. Wilk, R. M. Wallace, and J. M. Anthony, J. Appl. Phys. 87 (2000) 484.

[8] G. D. Wilk and R. M. Wallace, Appl. Phys. Lett. 76 (2000) 112.

[9] Y. Kim, S. Ohmi, K. Tsutsui, and H. Iwai, Proc. 34th European Solid-State Device Research Conf. (ESSDERC2004), Leuven, 2004, p. 81.

[10] G. Adachi and N. Imanaka, Chem. Rev. 98 (1998) 1479.

[11] F. U. Hillebrecht, M. Ronay, D. Rieger, and F. J. Himpsel, Phys. Rev. B 34 (1986) 5377.

[12] S. Chang, P. Philip, A. Wall, A. Raisanen, N. Toullier, and A. Franciosi, Phys. Rev. B 35 (1987) 3013.

[13] J. Onsgaard, J. Ghijsen, R. L. Johnson, M. Christiansen, F. Řrskov, and P. J. Godowiski, Phys. Rev. B 43 (1991) 4216.

[14] P. Patsalas, S. Logothetidis, L. Sygellou, and S. Kennou, Phys. Rev. B 68 (2003) 035104.
[15] N. V. Skorodumova, R. Ahuja, S. I. Simak, I. A. Abrikosov, B. Johansson, and B. I. Lundqvist, Phys. Rev. B 64 (2001) 115108.
[16] L. Marsella and V. Fiorentini, Phys. Rev. B 69 (2004) 172103.
[17] L. Petit, A. Svane, Z. Szotek, and W. M. Temmerman, Phys. Rev. B 72 (2005) 205118.
[18] T. Hattori, T. Yoshida, T. Shiraishi, K. Takahashi, H. Nohira, S. Joumori, K. Nakajima, M. Suzuki, K. Kimura, I. Kashiwagi, C. Ohshima, S. Ohmi, and H. Iwai, Microelectron. Eng. 72 (2004) 283.
[19] H. Nohira, T. Shiraishi, K. Takahashi, T. Hattori, I. Kashiwagi, C. Ohshima, S. Ohmi, H. Iwai, S. Joumori, K. Nakajima, M. Suzuki, and K. Kimura, Appl. Surf. Sci. 234 (2004) 493.
[20] K. Doi, K. Fujitani, N. Kadowaki, K. Nakamura, and A. Tachibana, Jpn. J. Appl. Phys. 44 (2005) 6115.
[21] K. Nakamura, K. Doi, K. Fujitani, and A. Tachibana, Phys. Rev. B 71 (2005) 045332.
[22] A. Tachibana, Theor. Chem. Acc. 102 (1999) 188.
[23] A. Tachibana, J. Chem. Phys. 115 (2001) 3497.
[24] A. Tachibana, in Stress Induced Phenomena in Metallization, ed. S. P. Baker (American Institute of Physics, New York, 2002) p. 105.
[25] A. Tachibana, in Reviews of Modern Quantum Chemistry, A Celebration of the Contributions of Robert G. Parr, ed. K. D. Sen (World Scientific, Singapore, 2002) Vol. 2, Chap. 45, p. 1327.
[26] A. Tachibana, in Fundamental World of Quantum Chemistry, A Tribute to the Memory of Per-Olov Löwdin, ed. E. J. Brändas and E. S. Kryachko (Kluwer Academic, Dordrecht, 2003) Vol. 2, p. 211.
[27] A. Tachibana, Int. J. Quantum Chem. 100 (2004) 981.
[28] A. Tachibana, J. Mol. Model. 11 (2005) 301.
[29] R. G. Parr and W. Yang, Density-Functional Theory of Atoms and Molecules (Oxford University Press, New York, 1989).
[30] K. Nakamura, K. Doi, and A. Tachibana, Molecular Regional DFT program package, ver. 1, Tachibana Lab., Kyoto University, Kyoto, 2004.
[31] W. J. Stevens, M. Krauss, H. Bausch, and P. G. Jasien, Can. J. Chem. 70 (1992) 612.
[32] T. R. Cundari and W. J. Stevens, J. Chem. Phys. 98 (1993) 5555.
[33] C. Lee, W. Yang, and R. G. Parr, Phys. Rev. B 37 (1988) 785.
[34] A. D. Becke, J. Chem. Phys. 98 (1993) 5648.
[35] M. J. Frisch et al., Gaussian 03, Revision B.05, Gaussian, Inc., Pittsburgh, PA, 2003.
[36] K. P. Huber and G. Herzberg, Molecular Spectra and Molecular Structure, Constants of Diatomic Molecules (Van Nostrand Reinhold, New York, 1979).
[37] B. R. Yadav, S. B. Rai, and D. K. Rai, J. Mol. Spectrosc. 89 (1981) 1.
[38] R. S. Mulliken, J. Chem. Phys. 23 (1955) 1833.

Table I. Bond lengths of lanthanoid monoxides: LaO with f and LaO without f mean the calculations performed with and without f-type polarization function, respectively. The calculations were performed with a CEP-31G basis set and a LanL2DZ basis set.

	Bond length (Å)			
	LaO without f	LaO with f	CeO	GdO
CEP-31G	1.947	1.903	1.828	1.844
LanL2DZ	1.965	1.914	—	—
Exp.	1.826		1.820	1.812

Table II. Mulliken atomic charges in $La(OH)_4$, $La(OH)_4^-$, $Hf(OH)_4$, and $Si(OH)_4$.

	$La(OH)_4$	$La(OH)_4^-$	$Hf(OH)_4$	$Si(OH)_4$
M (= La, Hf or Si)	1.467	1.164	1.721	1.099
O	-0.683	-0.797	-0.767	-0.599

Figure 1. MO interaction diagrams of (a) LaO, (b) CeO, (c) GdO at B3LYP/(CEP-31G, 6-31G**) level. Closed circles represent the occupied levels and dashed lines indicate atomic-orbital contributions to the MOs. Values are written in atomic unit.

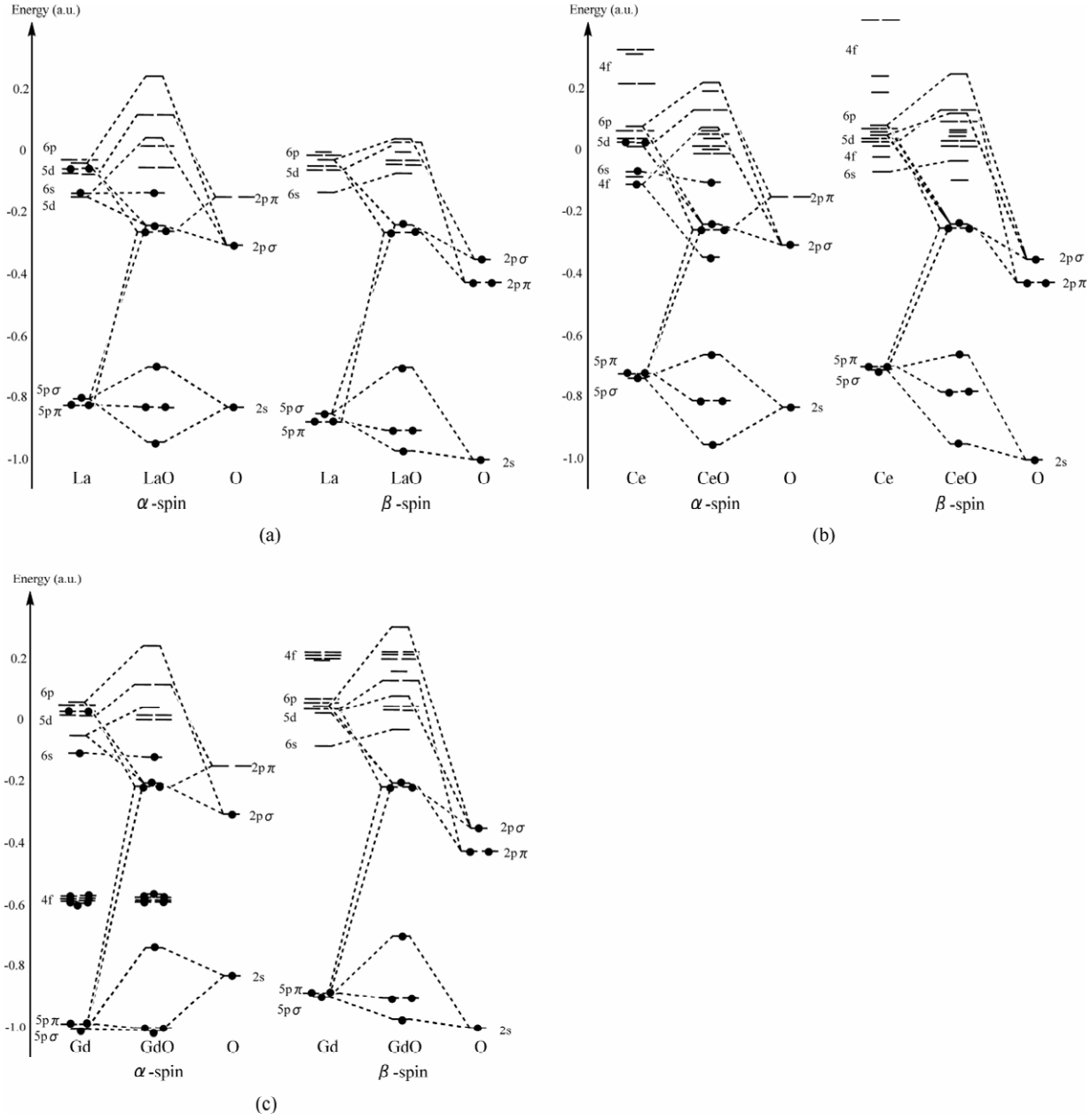

Figure 2. MO interaction diagrams of (a) $La(OH)_4$, (b) $Hf(OH)_4$, and (c) $Si(OH)_4$. Values are written in atomic unit.

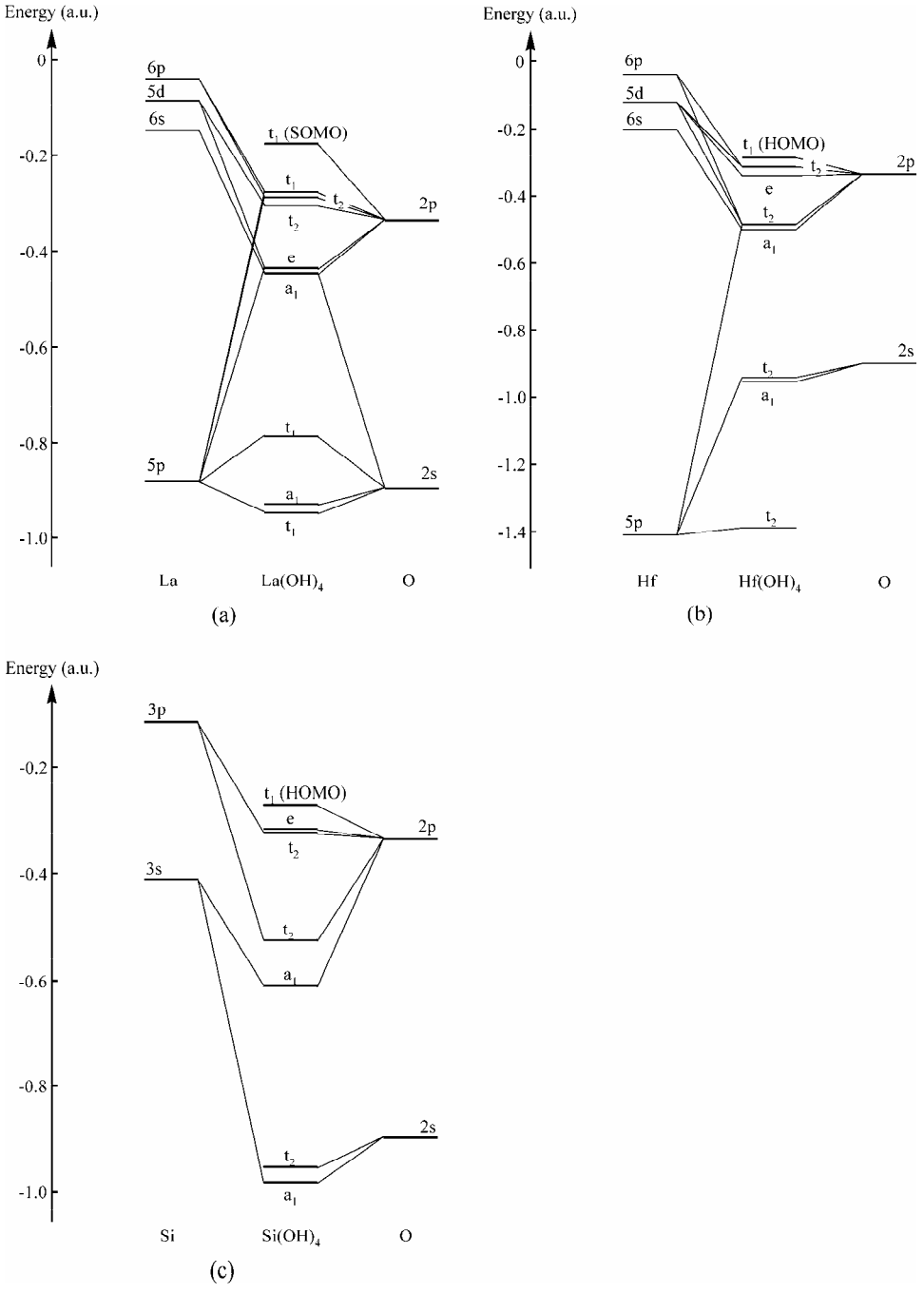

Figure 3. Maps of the electronic stress tensor density for (a) $La(OH)_4$, (b) $Hf(OH)_4$, and (c) $Si(OH)_4$. One metallic atom (La, Hf, or Si) and two O atoms are located on the cross sections. The short lines denote the eigenvectors of the third principal axis corresponding to the largest eigenvalue of the stress tensor density. Contours denote the values of -0.05, -0.01, 0.0, 0.01, and 0.05.

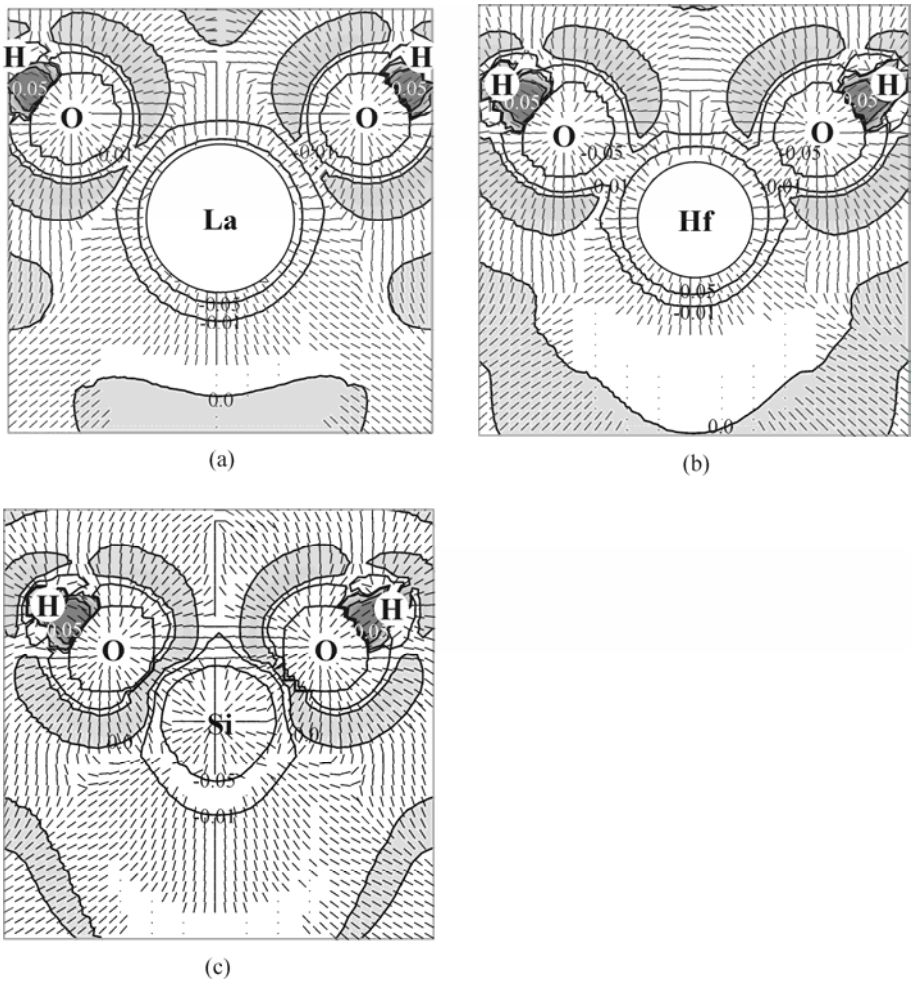

Figure 4. Maps of the dielectric constant for (a) $La(OH)_4$, (b) $Hf(OH)_4$, (c) $Si(OH)_4$, and (d) $La(OH)_4^-$. The cross sections are the same as those in Fig. 3. The inverse of dielectric constant is plotted.

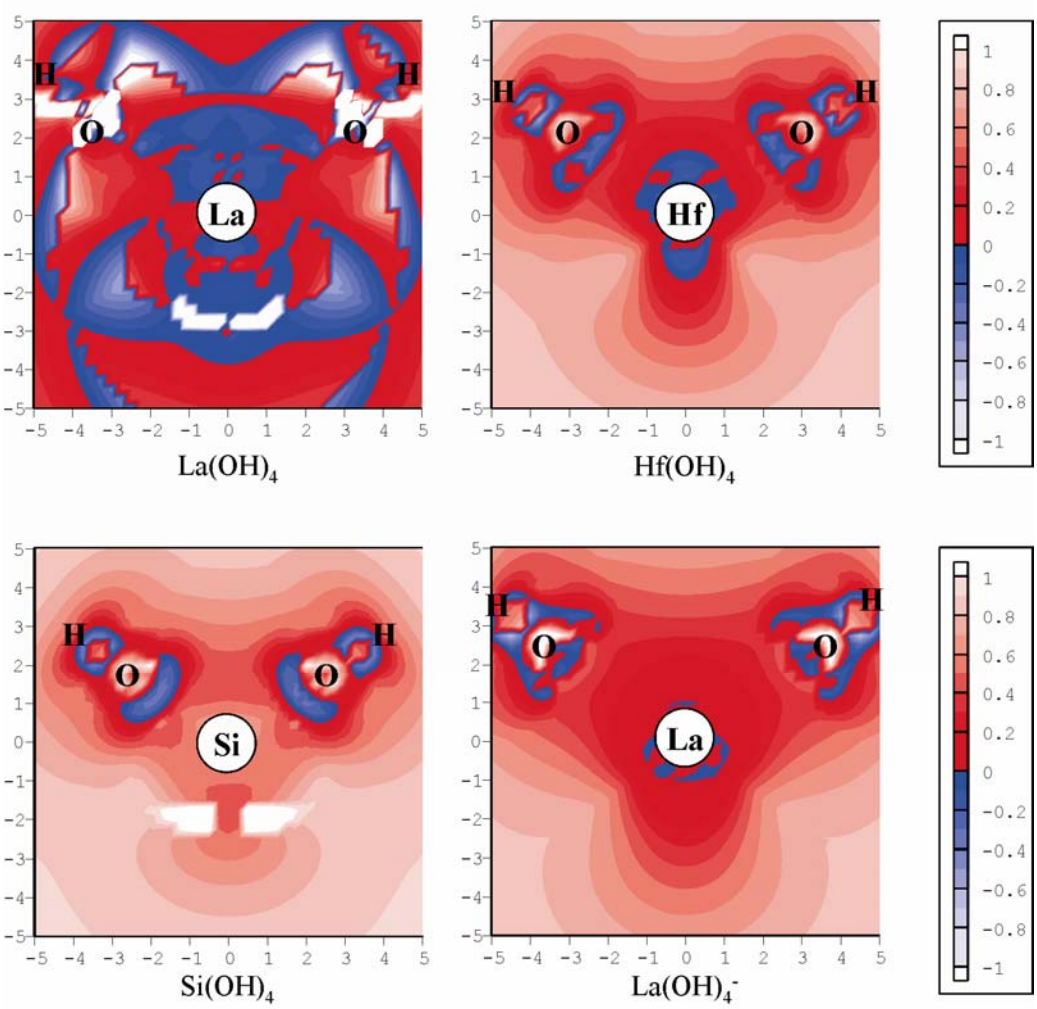

Figure 5. Maps of the dielectric constant for large-cluster model of lanthanum silicate. There are eight O atoms within 3.0Å from a La atom. One La atom and two O atoms are located on the cross sections. The inverse of dielectric constant is plotted.

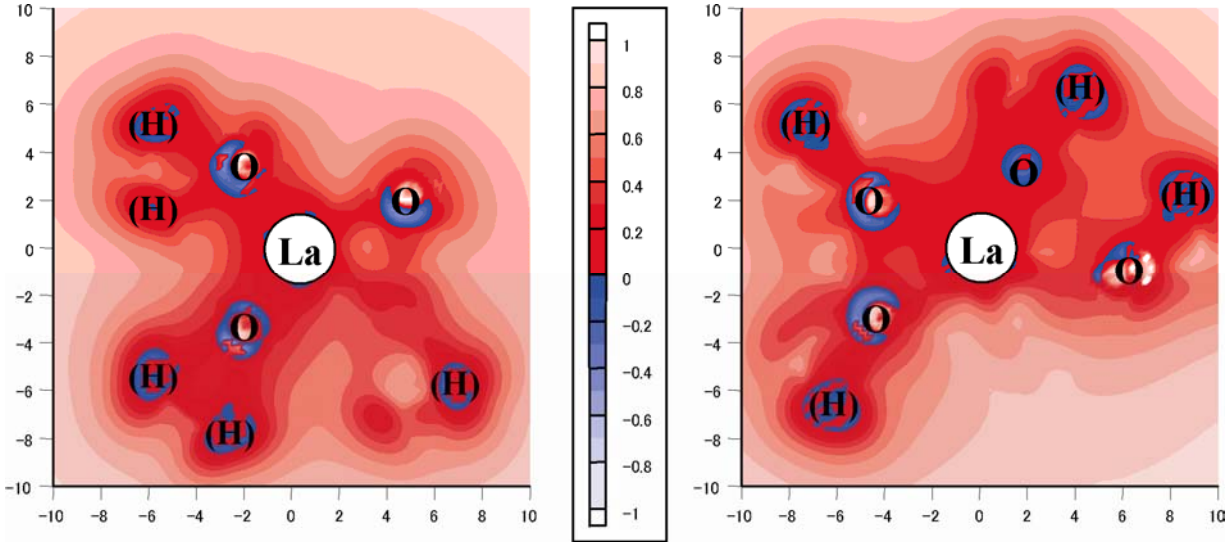

CHAPTER 8

Conclusions.

The molecular properties that affect stability and reactivity of molecules on the frame of nonrelativistic limit of rigged quantum electrodynamics have been characterized. The different elements of theory: kinetic energy density distribution, regional electronic stress tensor, local chemical potential, bond indices and local dielectric properties allow extracting plenty essential information about chemical system. The nonpositive-definite kinetic energy density defines shape of molecules in the course of reaction and separates core electron regions from valence electrons in molecules. The electronic stress tensor provides information on the system that is the most valuable to chemist – about the bonding nature. The effective electric potential of a set of nuclei is described by regional electronic chemical potential and the electron screening effects are visualized by local dielectric constant and local polaryzability. The new bond orders express bond strengths using body forces acting on electrons in interatomic region. The new bond orders, despite its simplicity, show remarkable performance. The method can provide both qualitative and quantitative description of physical-chemical properties of molecules. The method benefits from ability for real three-dimensional space representation of all properties.

Additionally, which is not a part of this thesis yet gives important insight on the subject, author was able to approximate (with good accuracy) combustion heats of large group of organic molecules using chemical potential bond order indices of isolated “standard” reactants and products species, optimized at the same level of theory. It is worth noting that the new bond order, in a sense, satisfies the Hess low, since commonly used indices do not, but instead they follow the rule, which might be called “bond order conservation rule” [1]. However the results require further study to estimate entropic contribution, which is substantial for correct prediction of reaction heats for chemical processes with significant entropic factor. Moreover, based on similar assumptions as former, the dissociation constants

of hydroxyl group proton in alcohols, phenols, carboxylic and inorganic acids, from gas phase calculations were obtained. However, also in this case the estimation of entropic contribution, in certain cases is necessary in order to produce more accurate results. This information were brought to emphasize that the electronic properties exhibited by stationary charge density at Lagrange point express the representative features that characterize interatomic interactions in molecules, and might be translated into more general (thermodynamic/macroscopic) properties.

References

[1] Lendvay, G. J Phys Chem 1989, 93, 4422, Lendvay, G. J Phys Chem 1994, 98, 6098.

List of publications

P. Szarek and A. Tachibana, *The field theoretical study of chemical interaction in terms of the Rigged QED: new reactivity indices*, J. Mol. Model 13, 651-663 (2007)

H. Nakano, P. Szarek, K. Doi and A. Tachibana, *Reaction Path of the catalytic reaction in [NiFe] hydrogenase by QM and QM/MM study*, in *Molecular meterials with specific interactions - modeling and design*, edited by W.A. Sokalski (Springer, Dordrecht 2007) pp. 399-432

K. Doi, Y. Mikazuki, S. Sugino, T. Doi, P. Szarek, M. Senami, K. Shiraishi, H. Iwai, N. Umezawa, T. Chikyo, K. Yamada and A. Tachibana, *Electronic Structure Study of Local Dielectric Properties of Lanthanoid Oxide Clusters*, Jap. J. App. Phys. 47, 205-211 (2008) and Erratum

P. Szarek, Y. Sueda and A. Tachibana, *Electronic Stress Tensor Description of Chemical Bonds Using Non-classical Bond Order Concept*, J. Chem. Phys. (2008, accepted)

P. Szarek, E. Dyguda-Kazimierowicz, A. Tachibana and W.A. Sokalski, *The physical nature of intermolecular interactions within cAMPdependent protein kinase active site: differential transition state stabilization in phosphoryl transfer reaction*, J. Phys. Chem. B (2008, accepted)

P. Szarek, K. Urakami, C. Zhou, H. Cheng and A. Tachibana, *On reversible bonding of H_2 molecules on Pt-clusters*, J. Chem. Phys. (submitted)

Conference appearances

- *Application of DTSS and Rigged QED in Protein Engineering.*

P.Szarek, E.Dyguda-Kazimierowicz, W.A.Sokalski, H.Nakano, A.Tachibana, Y.Cheng, Y.Zhang, J.A.McCammon, XIIth International Congress of Quantum Chemistry, May 21-26 2006 Kyoto, Japan

- *Intermolecular bonding by Rigged QED and hybrid variation-perturbation conceptual models.*

P.Szarek, E.Dyguda-Kazimierowicz, W.A.Sokalski, H.Nakano, A.Tachibana, Y.Cheng, Y.Zhang, J.A.McCammon, XIIth International Congress of Quantum Chemistry, May 21-26 2006 Kyoto, Japan

- *The catalyst – reactants interactions, the physical and chemical outlook on enzyme active site.*

P.Szarek, E.Dyguda-Kazimierowicz, W.A.Sokalski, H.Nakano, A.Tachibana, Y.Cheng, Y.Zhang, J.A.McCammon, 20th IUBMB International Congress of Biochemistry and Molecular Biology and 11th FAOBMB Congress, June 18-23 2006 Kyoto, Japan

- *Properties of molecular structures by quantum energy density analysis.*

P.Szarek, W.A.Sokalski, A.Tachibana, Symposium of Molecular Structure, September 20-23 2006 Shizuoka, Japan

- *Investigation of supramolecular bonding.*

P.Szarek, W.A.Sokalski, A.Tachibana, Symposium of Molecular Structure, September 20-23 2006 Shizuoka, Japan

- *Theoretical study of stable structure and electronic states of AlB nanowire.*

A. Fukushima, K. Doi, P. Szarek, A. Tachibana, Symposium of Molecular Structure, September 20-23 2006 Shizuoka, Japan

- *Stress Tensor Description of Chemical Bonds – New Bond Order Concept.*

K. Doi, Y. Mikazuki, S. Sugino, T. Doi, P. Szarek, A. Tachibana, 12th Workshop on Gate Stack Technology and Physics, 2-3 February 2007, Mishima, Japan

- *Theoretical Study of Hydrogen Adsorption Processes of Al and AlB Nanowires.*

K. Doi, A. Fukushima, Y. Kitagawa, K. Hirai, P. Szarek, A. Tachibana, The CSJ 87th Spring Metteing, 25-28 March 2007, Osaka, Japan

- *Theoretical Study of Influence of Oxygen Atoms on Metallic Atoms in Gate Insulators.*

K. Doi, S. Sugino, Y. Mikazuki, P. Szarek, A. Tachibana, The 54th Spring Meeting, JSAP and Related Societies, 27-30 March 2007, Tokyo, Japan

- *Theoretical Study on Dissociation Reaction of Ga.Ga Bond on GaN(0001) Surface.*

K. Doi, N. Ohmori, N. Maida, P. Szarek, A. Tachibana, The 54th Spring Meeting, JSAP and Related Societies, 27-30 March 2007, Tokyo, Japan

- *Theoretical Study on Electronic Structures of GaN-Nanowire/Si(111) Interface.*

K. Doi, K. Kimura, Y. Asano, P. Szarek, A. Tachibana, The 54th Spring Meeting, JSAP and Related Societies, 27-30 March 2007, Tokyo, Japan

- *The field theoretical study of chemical interaction in terms of the Rigged QED: new reactivity indices.*

P.Szarek, A.Tachibana, 10th Theoretical Chemistry Symposium, 14-16 May 2007 Nagoya, Japan

- *The Rigged QED density interpretation of physical-chemical properties of molecules and chemical processes.*

P.Szarek, Y.Sueda, A.Tachibana, 10th Theoretical Chemistry Symposium, 14-16 May 2007 Nagoya, Japan

- *The covalent bond formation between Al atoms in Al-cluster hydrides.*

P.Szarek, K.Watanabe, A.Tachibana, 1st Symposium of Molecular Science, 16-20 September 2007 Sendai, Japan

- *Theoretical investigation of mechanism of light emission of GaN with defect.*

K. Kimura, Y. Asano, P. Szarek, K. Doi, A. Tachibana, 1st Symposium of Molecular Science, 16-20 September 2007 Sendai, Japan

- *Theoretical study of interatomic interaction in High-k Materials.*

S. Sugino, Y. Mikazuki, P. Szarek, K. Doi, A. Tachibana, 1st Symposium of Molecular Science, 16-20 September 2007 Sendai, Japan

- *Theoretical study of effects of Al nanowire on Hydogen Adsorption on graphene.*

A. Fukushima, K. Doi, P. Szarek, A. Tachibana, 1st Symposium of Molecular Science, 16-20 September 2007 Sendai, Japan

- *Theoretical Study on Dissociation Reaction of Ga.Ga Bond on GaN(0001) Surface.*

N. Ohmori, N. Maida, P. Szarek, K. Doi, A. Tachibana, 1st Symposium of Molecular Science, 16-20 September 2007 Sendai, Japan

- *Estimate of chemical bond by new bond order.*

Y. Sueda, P. Szarek, A. Tachibana, 1st Symposium of Molecular Science, 16-20 September 2007 Sendai, Japan

- *Stress Tensor Description of Chemical Bonds – New Bond Order Concept.*

P.Szarek, A.Tachibana, 11th Theoretical Chemistry Symposium, 22-24 May 2008 Yokohama, Japan

- *QED Stress Tensor Description of Chemical Bonds – Formulation of Non-classical Bond Order Concept.*

P.Szarek, Y.Sueda, A.Tachibana, Modeling and Design of Molecular Materials, June 23-28 2008 Piechowice, Poland

- *Theoretical Study of Electronic States of Chemical Bonds.*

P.Szarek, A.Tachibana, The 2nd International Symposium on Molecular Theory for Real Systems, 4-6 August 2008 Okazaki, Japan

- *QED Stress Tensor Description of Chemical Bonds – Formulation of Non-classical Bond Order Concept.*

P.Szarek, Y.Sueda, A.Tachibana, WATOC, 14-19 September 2008 Sydney, Australia

- *Stress Tensor Description of Chemical Bonds and New Bond Order Concept.*

P.Szarek, A.Tachibana, 2nd Symposium of Molecular Science, 24-27 September 2008 Fukuoka, Japan

- *Theoretical research of adsorption of hydrogen on Al cluster.*

P.Szarek, K. Watanabe, A.Tachibana, 2nd Symposium of Molecular Science, 24-27 September 2008 Fukuoka, Japan

- *On reversible bonding of H_2 molecules on Pt-clusters.*

P. Szarek, K. Urakami, C. Zhou, H. Cheng and A. Tachibana, 2nd Symposium of Molecular Science, 24-27 September 2008 Fukuoka, Japan